Semiconductors, Vol. 38, No. 3, 2004, pp. 245–252. Translated from Fizika i Tekhnika Poluprovodnikov, Vol. 38, No. 3, 2004, pp. 257–264.

ATOMIC STRUCTURE AND NONELECTRONIC PROPERTIES OF SEMICONDUCTORS

Genesis of Nanoscale Defects and Damage in GaAs Subjected to Multipulse Quasi-Static Photostrains in Micrometer-Sized Regions of Semiconductor

S. V. Vintsents*, A. V. Zaĭtseva, V. B. Zaĭtsev**, and G. S. Plotnikov****

**Institute of Radio Engineering and Electronics, Russian Academy of Sciences (Fryazino Branch), pl. Vvedenskogo 1, Fryazino, Moscow oblast, 141120 Russia*

e-mail: vintsents@mail.ru

***Moscow State University (Faculty of Physics), Vorob'evy gory, Moscow, 119899 Russia*

Submitted May 13, 2003; accepted for publication May 19, 2003

Abstract—Atomic-force microscopy and analysis of both photothermal (quasi-static) strains of surfaces and the kinetics of intensity of specularly reflected light were used to study special features of defect production in GaAs in relation to the number N of focused laser pulses incident on the surface. Irradiation of the semiconductor was accompanied by its electronic excitation, local heating, and deformation of surface layers. It is shown for the first time that the genesis of surface defects and damage in semiconductors (within the laser spot with a micrometer diameter) has a multistage character in the vicinity of the plasticity threshold. The defect-induced and plastic nanometer-scale surface displacements ΔU_z increase with increasing N only if the shearing surface strains φ exceed the previously determined values $10^{-5} < \varphi_0 < 10^{-4}$ for deformation-related elasticity (quasi-elasticity) limits in GaAs. The origination of nanoscale defects and their self-organization at the early stages of photostrains in the semiconductor is discussed. The possible relation between the defects observed and the subsequent catastrophic damage to micrometer-sized regions of GaAs at large values of N is considered.

1. INTRODUCTION

The interaction of pulsed laser radiation with a GaAs surface has been studied for more than 20 years. The persistent interest in this interaction is caused by the wide use of gallium arsenide in modern microelectronics and optoelectronics [1] and also, in particular, by the fact that nonequilibrium pulsed laser irradiation can initiate various phase transformations in semiconductors and affect a number of properties of the surface layer within the irradiated zone [2, 3]. When interacting with GaAs, optical radiation irreversibly changes the chemical composition and microstructure of this compound [2–6], as well as its luminescent [3, 7, 8] and electrical [6, 7, 9] characteristics, and it stimulates the generation of point and extended defects [7, 10, 11] and affects the properties of oxide layers [2, 3, 12] and the surface profile [13, 14].

The single-shot irradiation of semiconductors with nanosecond laser pulses (or laser pulses with other widths) in the spectral region of the band-to-band absorption of light was used in the majority of early studies; the density W of the incident energy was varied. The irradiated areas were comparatively large (typically, larger than 1–10 mm^2); the distribution of optical-radiation intensity was quasi-uniform throughout the irradiated area, which ensured that there were no shearing strains within this area. Variations in the semiconductor properties were caused mainly by the generation of defects and were observed near the surface; for these variations to occur, the incident-energy density W in the pulses should have been close to the calculated thresholds W_m for the formation of the surface (metastable) liquid phase [2, 3]. The results were predominantly explained by the thermal effect of illumination [2–6] or the combined effect that involved (for $W < W_m$) electronic excitations in the semiconductor [7, 10].

In order to gain insight into the contribution of photostrains to the production of defects, we carried out direct photostrain studies of semiconductors and metals using a different approach. This is based on the use of localized and multiple moderate-energy focused single-mode irradiation events with controlled and almost Gaussian light-intensity distribution [15–18]; i.e., we have $I(r, t) = W\exp(-r^2/\omega^2)(t/\tau^2)\exp(-t/\tau_0)$, where W = 10–100 mJ/cm^2 $\ll W_m$ is the incident-energy density at the laser-spot center, ω = 10–100 μm is the laser-spot radius at the sample surface, and τ = 0.1–1 μs is the characteristic width of the pulses. As expected, we observed an appreciable increase in the strain-related effects. Specifically, we observed the low-threshold effect of shearing strains and stresses that arise due to local irradiation on point-defect production in the surface layers of germanium and silicon [19–22].

Naturally, controlled photodeformation effects in the vicinity of previously detected deformation-related

limits of elasticity (quasi-elasticity) in semiconductors $\varphi_0(W_0)$ [21–25] attract particular interest. Our previous publications concerned with the aforementioned effects included primarily electrical and optical studies of Ge and Si under conditions of laser scanning of actual surfaces. The number of laser pulses was maintained constant ($N \approx 10^3$), whereas the value of W was varied [19–22]. At the same time, the number N of laser pulses can be considered as one of the most natural control parameters (along with the energy density W). Therefore the study of the earliest stages of defect production (when N is still small) is of most interest. In order to simplify the interpretation of the results, it is appropriate to carry out the measurements in the absence of laser scanning, i.e., when the laser-beam position at the surface is fixed.

Previously, we used X-ray and chemical microanalysis, electron microscopy, and Auger spectroscopy to study the situation where the laser-beam position at the GaAs surface was fixed and the value of N was large ($N \approx 10^5$–10^6) [26]. We found that GaAs was a more complex object than Ge or Si, mainly due to the volatility of arsenic [2, 3] and possible development of various low-threshold phenomena [26, 27]. Note, for example, that nonsteady (acoustic) strains initiated by localized irradiation induced decomposition of GaAs in a thin (~4–7 nm) surface layer. This decomposition gave rise to a nearly equal number of unbonded Ga and As atoms even at fairly large distances (on the order of millimeters) from the irradiated zone with a radius of $\omega \approx$ 20 μm [26]. The long-range effect of laser pulses observed by Barskov *et al.* [26] was not related (as in [28]) to a nonsteady thermal field localized in the vicinity of the irradiated region. Indeed, some processes that vary quite slowly with time and are mainly related to the temperature gradients are dominant on the microsecond time scale within the laser-spot area; these processes are quasi-static and are referred to as photothermal strains of solid-state surfaces [16–25]. These slow shearing strains in pulsed photoacoustic spectroscopy of the laser-beam deflection [15–18] are typically characterized by the values of local inclinations of the strained surface $\varphi \equiv (dU_z/dr)$, where U_z is the effective normal displacement of the surface and r is the distance from the beam center. When $\varphi > \varphi_0 \approx (5–6) \times 10^{-5}$ and, accordingly, energy densities $W > W_0 \approx 100$ mJ/cm^2 [22], macrodamage (structural catastrophe) was previously observed in micrometer-scale GaAs regions [26]. Microcraters of regular circular shape with a depth of ~(1–5) μm and radius ω = ~20 μm were formed (mainly due to noncongruent evaporation of arsenic) at the GaAs surfaces within the laser spot at large values of N [26]. We emphasize that the genesis of earlier (initial) stages of defect production in local GaAs regions as the value of N increased has not yet been studied.

In this study, we used atomic-force microscopy (AFM) and analysis of both photothermal surface strains (PTSSs) and the intensity of specularly reflected light to gain insight for the first time into the process of formation of finer, nanoscale variations in the GaAs surface profile as a result of multiple quasi-static photostrains in micrometer-sized regions of semiconductors in the vicinity of thresholds $\varphi_0(W_0)$ [22] with wide ranges of variations in N (from unity to 10^5).

This study may be useful to justify the boundaries of nondestructive modes in GaAs laser microscopy [29] and to simulate the degradation processes in small-sized (1–10 μm) semiconductor optoelectronic devices (for example, those designed for millimeter-region wavelengths) subjected to local overheating [30, 31] and, as a consequence, to strains [32].

2. EXPERIMENTAL

The samples were 5×5 mm^2 in area, had a (100) orientation of the surface, and were cut from a single epitaxial GaAs structure composed of a 2.4-μm-thick film with electron concentration $n \approx 10^{16}$ cm^{-3}. The film was grown by liquid-phase epitaxy on a heavily doped substrate ($n^+ \approx 10^{18}$ cm^{-3}) with a thickness of ~250 μm. Details of the preliminary preparation of the surface for irradiation were described in [26].

The GaAs samples were irradiated with focused laser pulses (without scanning the beam) in atmospheric air at room temperature. The second harmonic of a pulsed Nd:YAG laser with wavelength $\lambda = 0.53$ μm and characteristic pulse width $\tau \geq 0.4$–0.5 μs was used for irradiation. The total pulse width at a 0.1 level of I_{max} was no smaller than 1.5 μs. The pulse-repetition rate was f = 10–25 kHz; the pulse train could be interrupted using a shutter with the exposure time Δt_i ranging from 0.005 to 10 s. The single-mode laser radiation was focused on GaAs samples to a spot with a regular shape and Gaussian radius $\omega \approx 20$ μm. The spot size was monitored during irradiation using the PTSS method [16] to reveal characteristic profiles of arising quasi-elastic strains; an SOK-1-01 optical microscopy accessory was also used [23].

The incident-energy density $W = E/\pi\omega^2$ (E is the total energy in a pulse) ranged from 10 to 350 mJ/cm^2 at the laser-spot center; the range of variations in W was chosen so that the previously ascertained thresholds for the origination of inelastic strains in GaAs surface layers ($W_0 \approx 100$ mJ/cm^2 [22]) were within this range. We emphasize that, for the microsecond laser pulses used in this study, the calculated [3] melting thresholds for GaAs $W_m \geq 1$–1.2 J/cm^2 were much higher than those for pulses with well-studied nanosecond-scale values of τ ($W_m \approx 200$ mJ/cm^2) [2, 3].

In order to study the kinetics of large-scale damage within the laser spot (0.1–1 μm), we used the PTSS method [16, 23] and relied on the time dependence of integrated intensity $I_p(t)$ of the probe He–Ne laser beam reflected specularly from the semiconductor surface under a continuous train of focused laser pulses. We paid special attention (as in [33]) to steady-state values of $I_p(t)$ attained in the time intervals between the pulses.

The point in time t_0 at which the ratio $I_p(t_0)/I_p(0)$ decreased irreversibly to the level of 0.9 was considered as the onset of catastrophic damage. A new (undamaged) GaAs region was chosen each time for repeated recording of the $I_p(t)$ kinetics, which was monitored using an SOK-1-01 microscope. The method for determining t_0 and, accordingly, the critical number of irradiating laser pulses $N_0 = ft_0$ was also described previously [34, 35].

In order to study the earlier stages of defect production in GaAs (i.e., at $N \ll N_0$), we used an AFM system and an optical microscope, which were incorporated into the equipment supplied with a Nanoscope-111a (Digital Instruments) scanning probe microscope. Individual areas of the semiconductor (with a small number of pulses N) were subjected to local pulsed irradiation with fixed energy densities W_i, where $W_i/W_0 = 0.1$, 0.9, 1.15, 1.35, 1.6, 2.0, 2.6, 3.0, and 3.5. In this case, the number of pulses N was varied by varying the irradiation time Δt_i (see above). An array of photoirradiated GaAs regions obtained on a single epitaxial structure made it possible to study special features of the defect-producing surface strains and the nanoscale damage that formed in relation to both W at N = const and the number of laser pulses N at a fixed energy density W_i.

The resolution of the optical microscope made it possible to observe only the most radical variations in the surface profile at a level of irreversible displacements $\Delta U_z \approx 1$ μm. Atomic-force microscope was used to study a finer evolution of the surface nanoprofile ($\Delta U_z \approx 1$ nm) at the early stages of deformation (small N and $W \approx W_0$). The AFM measurements were performed in atmospheric air. The microscope operated in the contact mode; the rigidity of levers was 0.01–0.2 N/m. The AFM images were processed and analyzed using a FemtoSkan-0.01 special software package [36].

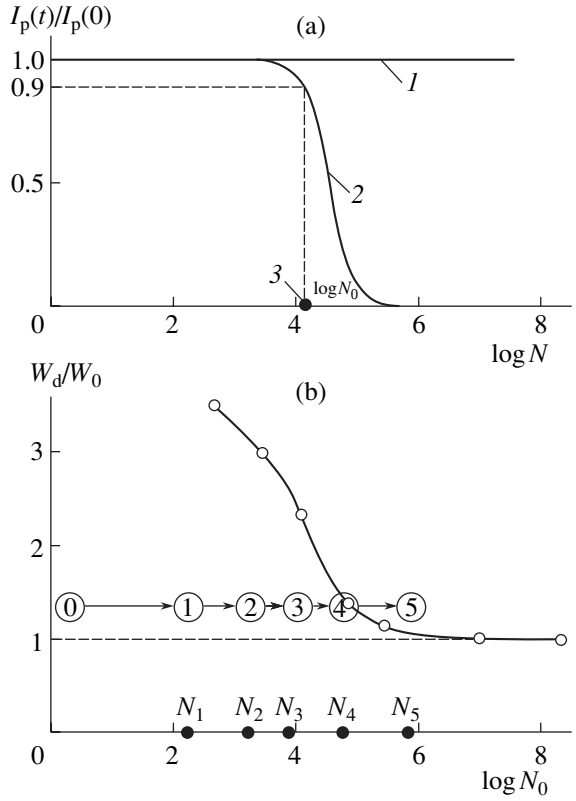

Fig. 1. (a) Kinetics $I_p(t)$ of the intensity for a continuous probing laser beam reflected specularly from the semiconductor (normalized to the initial intensity $I_p(0)$): (*1*) in the mode of nondestructive quasi-elastic photostrains in GaAs, $\varphi < \varphi_0$ ($W < W_0$); (*2*) with destructive irradiation of the semiconductor, $\varphi > \varphi_0$ ($W > W_0$); and (*3*) the scheme for determining the critical number of laser pulses N_0. (b) Dependence of the damage thresholds W_d (in units of $W_0 = 90$–100 mJ/cm^2) on $\log(N_0)$ for GaAs at $\omega \approx 20$ μm. The numbers 0–5 illustrate the trend for an increase in N at $W/W_0 \approx 1.35$. Numerical values of N_i are listed in the table.

3. RESULTS AND DISCUSSION

3.1 Boundaries of Defect-Producing Inelastic Strains

As noted previously [22–25], the controlled inelastic processes initiated in semiconductors by multiple pulsed laser irradiation of micrometer-sized areas are limited from below in the energy density W by the region of reversible linear photoacoustics (thresholds W_0), and are limited from above by uncontrolled damage-forming processes (W_d thresholds). At $W_0 < W < W_d$ and $\omega = 10$–100 μm, the number N of laser pulses becomes an important parameter of inelastic effects [22].

In this context, we studied in GaAs primarily the dependences of the upper thresholds W_d on N using the methods described previously [34, 35] (Fig. 1). To this end, we measured the kinetics $I_p(t)$ at $W < W_0 = 90$–100 mJ/cm^2 (case 1, Fig. 1a, curve *1*) and at $W > W_0$ (case 2, Fig. 1a, curve *2*). In case 1, we failed to detect appreciable variations in $I_p(t)$ for $N \geq 10^7$–10^8 in the intervals between the pulses. In case 2, we determined the critical number of pulses N_0^i (Fig. 1a, curve *3*) and then plotted the dependences of W_d^i on N_0^i for several (i) fixed destructive levels of the energy density $W_0 < W_d^i < 3.5W_0$ (Fig. 1b). We emphasize that appreciable degradation and catastrophic damage in micrometer-sized irradiated semiconductor regions always developed when N exceeded N_0; furthermore, we had $I_p(t) \longrightarrow 0$ when $N \longrightarrow \infty$ (Fig. 1a).

It can be seen from the experimental dependence $W_d(N)$ shown in Fig. 1b that there is a sharp boundary that is located at $W \approx W_0$ and separates the irradiation-induced regions of degradation of the semiconductor from relatively nondestructive irradiation levels. In order to make certain that precisely the mode of quasi-elastic strains in GaAs was realized under the conditions of our experiments at $W < W_0 = 90$–100 mJ/cm^2, we used (as in [22, 26]) the PTSS method (Fig. 2a). Using this method, we managed to confirm the view that, at $\varphi \equiv (dU_z/dr)_{max} < \varphi_0 \approx 5$–$6 \times 10^{-5}$, the photo-

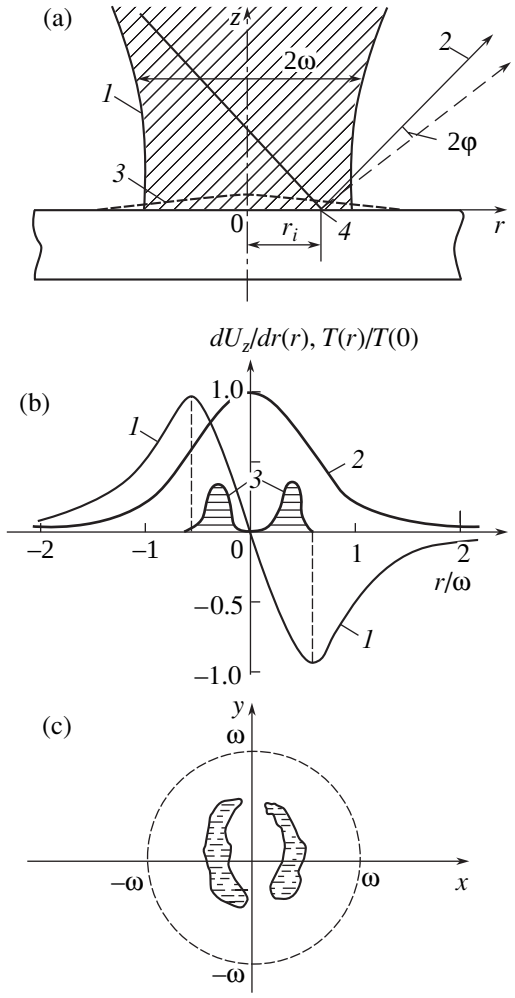

Fig. 2. (a) Schematic representation of the PTSS method [16, 22]: (*1*) a pulsed single-mode "heating" laser beam with a diameter of ~2ω, (*2*) a continuous probing laser beam whose deflection $2\varphi(r, t)$ from the strained surface *3* is measured at various points (*4*) of the surface r_i. (b) Typical distributions of (*1*) quasi-static shearing strains $\varphi(r) \equiv dU_z/dr(r)$ arising in GaAs at $W \le W_0$ [26] and (*2*) normalized calculated temperature $T(r)/T(0)$ over the cross section of the "heating" beam; (*3*) radial distribution of primary damaged regions detected at $W \ge W_0$. (c) Schematic representation of damaged regions within the irradiated zone of GaAs; this scheme was derived on the basis of the combined data obtained using the AFM method.

strains $\varphi(t)$ in GaAs are indeed completely reversible in time, and the features of the photostrain's kinetics do not vary from pulse to pulse up to $N \ge 10^7$–10^8 [22].

Since the shearing strains dU_z/dr may play a significant role in the mechanisms of point defect production and catastrophic damage in monatomic semiconductors and metals [19–25], we used the PTSS method [16] to study the features of the $\varphi(r)$ distribution over the beam cross section for GaAs (Fig. 2b, curve *1*). The largest strains were observed at the time instants that corresponded to the completion of laser pulses $t = 1.5$–2.0 μs, i.e., to the time instants that corresponded to the completion of the main heat release in the semiconductor [2, 3]. The maximal values of φ were shifted in reference to the beam cross-section center by $r_{max} \approx \omega/\sqrt{2} =$ 12–15 μm. Note that the similar distribution $\varphi(r)$ in metals at early stages of strain development was previously related to a partial accomplishment of "quasi-single-mode" conditions of displacements $U_z(r)$ [17, 18].

Thus, the preliminary study of the kinetics $I_p(t, W)$ and strains $\varphi(t, r, W)$ made it possible to correctly choose the modes of studying the early stages of defect production and nanodamage in GaAs in coordinates (W, N). Defect production under the aforementioned conditions ($W/W_0 \ge 1$ and $N/N_0 \ll 1$) for various values of N was thereafter studied using the AFM method.

The genesis of nanometer-sized defects and damage in GaAs was studied for various combinations of the values of W and N. As an example, we used the numbers from 0 to 5 to illustrate the trajectory of the increase in N for $W/W_0 \approx 1.35$. The corresponding AFM results are shown in Figs. 3a–3d and are listed in the table. We managed to separate several different stages in the development of defect and damage production. Below, we describe the main characteristics of these stages in order of increasing N (numerical values of N_i for $W/W_0 \approx 1.35$ are listed in the table).

3.2. Time Interval Corresponding to the Latent Buildup of Defects

It is found that, with the smallest number of laser pulses ($N < N_1$), the latent buildup of point defects is dominant and the nanometer-scale amplitudes ΔU_z^0 of the random surface profile are retained; this profile is characteristic of unirradiated GaAs with $\Delta U_z^0 < 1$ nm. The method of dynamic indentation has been previously applied to certain semiconductors (among them, GaAs) to show [37] that, at short durations (≤1–10 ms) of pulsed contact loading, the dislocation-unrelated mechanisms of microplasticity in the surface layers with preferential point migration (rather than extended) defects near the surface are dominant. The defect-diffusion mechanisms of microplasticity are characteristic of relatively small near-surface stresses in semiconductors [19–22] and can be in effect at comparatively low temperatures (including 295 K) [38].

3.3. Stage 1

At $N_1 < N < N_2$, clusters of point defects are formed in the semiconductor regions shifted by $r = 6$–7 μm to the periphery in reference to the irradiation-spot center (Fig. 2b, curves *3*). These clusters are not oriented spatially and are related by the AFM method to a preferential reduction in the initial surface-profile amplitude in the semiconductor (Fig. 3a). The complex profile features are observed with a certain increase at the nanocrater center within each nanocrater. The difference in

heights ΔU_z for these defects amounts to 1.5–2.0 nm, and the characteristic dimension of surface-profile features is 10–50 nm (see table). The results of comparing the aforementioned characteristics of the defects with the previous data obtained using X-ray microanalysis [26] suggest that the detected local nanometer-scale depressions in the GaAs surface profile are mainly caused by an escape of arsenic from the semiconductor. Further development of early damage-formation stages and origination of new types of defects occurred mainly within the aforementioned peripheral regions (i.e., near the boundaries of the laser spot) (Fig. 1c) and was accompanied by the extension of these regions as N increased.

3.4. Stage 2

Spatial self-organization of unoriented clusters composed of nanometer-sized defects along one of the crystallographic axes in GaAs was observed at $N_2 < N < N_3$ (Fig. 3b). Depression regions (with ΔU_z = 5–7 nm) in the profile merge into fairly thin (50–100 nm) and extended (400–600 nm) lines with a spatial period of 100–200 nm (Fig. 3b, table). We emphasize that the above processes continue to be predominant at distances r_0 = 5–10 nm from the laser-spot center (Fig. 2b, curve *3*, Fig. 2c) rather than at the center itself, where a photoinduced increase in the temperature $\Delta T(r)$ and the concentration of nonequilibrium electrons are maximal [2, 3, 15–18, 23] (Fig. 2b, curve *2*). These observations clearly indicate that not only the temperature $\Delta T(r)$ and electronic excitation of semiconductors but also local shearing quasi-static strains $\varphi \equiv dU_z/dr$ contribute significantly to the processes of defect production and redistribution under investigation (Fig. 2b, curve *1*). Indeed, the regions of origination (stage 1) and primary self-organization (stage 2) of the defects under conditions of local photodeformation of GaAs were always found between the peaks of $\Delta T(r)$ and $\varphi(r)$ (Fig. 2b, curves *1–3*). Such a multifactorial character of point defect formation was previously studied in detail for quasi-single-mode conditions of irradiation of semiconductor with nanosecond laser pulses; an electronic–deformational–thermal model was suggested to interpret the experimental data [39–41]. The effects of self-organization of defects are much less pronounced in radial directions (the *y* axis in Fig. 2c), which are perpendicular to the observed extended lines of defect clusters (Fig. 3b). This fact suggests that the defect clusters migrate (and then merge together) more easily along a certain crystallographic direction, which was detected using the AFM method; the above orientational behavior can be attributed, e.g., to the piezoelectric effect [1–3]. The aforementioned directions can correspond to projections of piezoelectric axes onto the (100) plane. Apparently, the shearing strains dU_z/dr and subsurface stresses σ_{zr} [23–25] that are perpendicular to these directions (Fig. 2c) may be much less efficient.

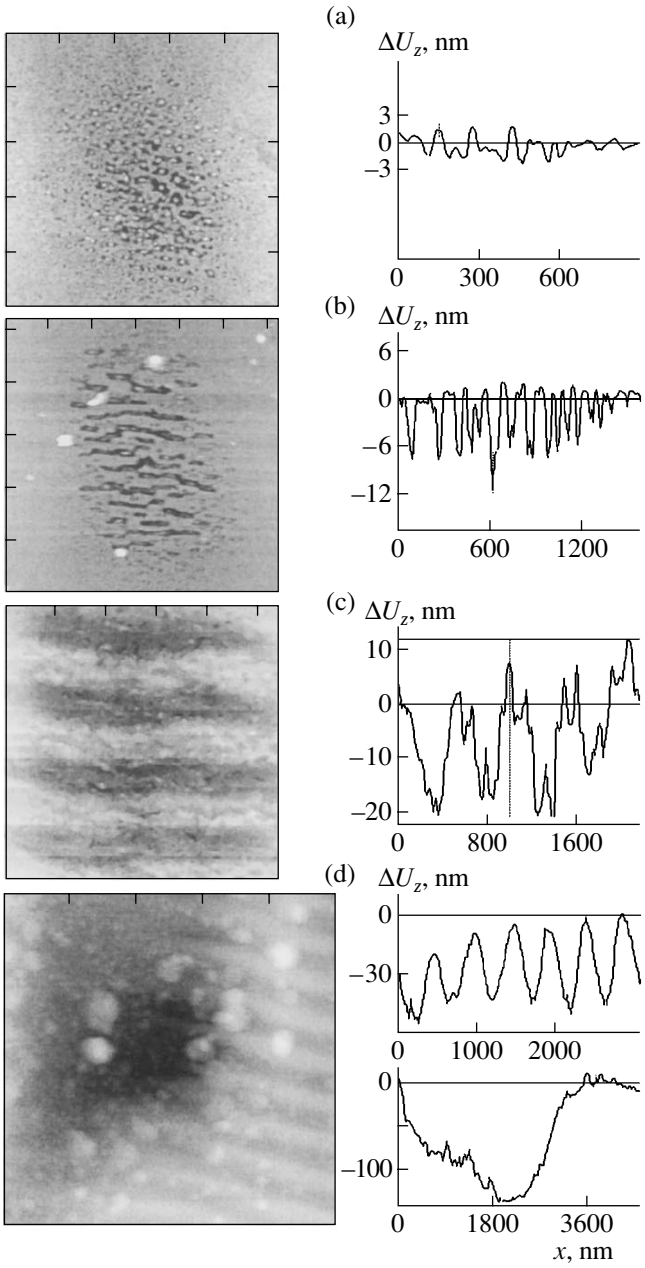

Fig. 3. AFM images of GaAs surface areas at various stages of defect formation under conditions of multiple quasi-static deformation of the semiconductor. The size of the imaged area is (a–c) 2×2 μm^2 and (d) 4.5×4.5 μm^2. The profiles of the normal surface displacements $\Delta U_z(x)$ along the vertical direction *z* are shown on the right (*x* is the coordinate in the surface plane).

3.5. Stage 3

Enlargement of oriented bands in the GaAs surface profile occurs when $N_3 < N < N_4$ (Fig. 3c). A one-dimensional (1D) wavelike profile with a height difference ΔU_z = 15–20 nm a transverse (lateral) dimension of 200–250 nm, and a period of 400–500 nm is formed on a larger scale without changing the spatial orienta-

Consecutive stages of genesis of nanometer-sized defects in GaAs with increasing number N of destructive ($W/W_0 \approx 1.35$) quasi-static photostrains in the micrometer-sized regions of GaAs

Stage no.	The number N of pulsed quasi-static photostrains	The dominant type of generated defects	Characteristic sizes		
			the height difference ΔU_z, nm	lateral dimension, nm	the structure period, nm
0 (latent)	$1 < N < N_1$	Latent buildup of point defects at amplitudes of the displacement fluctuations $\Delta U_z < 1$ nm	$\Delta U_z^0 < 1$	-	–
1	$N_1 < N < N_2$	Unoriented clusters of nanodepressions at the surface	1.5–2	10–50	–
2	$N_2 < N < N_3$	Merging of the clusters into oriented bands of depressions	5–7	50–100	100–200
3	$N_3 < N < N_4$	Enlarged oriented waves of the surface nanoprofile	15–20	20–250	400–500
4	$N_4 < N < N_5$	Deepened waves of depressions in the surface nanoprofile	30–40	~250	~500
		Local pitting (erosion) of GaAs, individual microcraters	100–150	≤1000	–
5	$N > N_5$	A unified macroscopic crater (a catastrophe)	1–5	$(1–3) \times 10^4$	–

Note: The values of N were equal to $N_1 \approx (2–5) \times 10^2$, $N_2 \approx 2.5 \times 10^3$, $N_3 \approx 10^4$, $N_4 \approx (5–10) \times 10^4$, and $N_5 \geq 10^5$–10^6 under conditions of local pulsed laser irradiation of GaAs at $\omega \approx 20$ μm and $W/W_0 \approx 1.35$ (see text).

tion of the bands (see table). In our opinion, although the period of the wavelike structures in stage 3 almost coincides with the wavelength λ, this period is not related to the phenomena of optical interference [2, 3, 29], since the period of similar structures observed in stage 2 was much shorter than λ (see text above and table). A predominant lowering of the surface profile (formation of depressions) occurs in stage 3 (as in previous stages); this lowering is apparently related to the continuing escape of arsenic from the semiconductor. Two established facts count in favor of this hypothesis. First, damage to the GaAs surface with a diameter of 10–15 μm is accompanied by the formation of sharp edges of the profile, with the height of these edges equal to 15–20 nm. It will be recalled that a similar effect was previously attributed to noncongruent evaporation of arsenic, which was corroborated by the observation of blue cathodoluminescence using an optical microscope in the microanalyzer in the region of the forming profile edge due to the origination of Ga_2O_3 in this region as a result of oxidation of unbonded gallium. Second, according to the AFM data, the remaining portion of unbonded gallium is involved in the formation of nanometer-sized drops in stage 3 in the direction of the y axis (Fig. 2c), which was predicted previously on the basis of stoichiometric data obtained by Auger spectroscopy of GaAs [26].

3.6. Stage 4

As the number N of the laser pulses incident on GaAs increased ($N_4 < N < N_5$), individual defects in the form of craters appeared at several sites of the semiconductor surface, mainly at distances $r \approx r_0$ from the laser-spot center. One such defect has a fairly regular (circular) shape with a bottom depth of $\Delta U_z = 120$–150 nm and a transverse dimension of ~1 μm and is shown in Fig. 3d. It was ascertained by the AFM method that such local pitting (erosion) of GaAs occurs only against a background of oriented enlarged profile bands with height difference $\Delta U_z \geq 30$–40 nm (Fig. 3d). These bands were already formed at stage 3 and are additionally developed in stage 4. Comparison of the AFM data on $N = N_4$ and the dependences $W_d(N)$ at $W/W_0 \approx 1.35$ in Fig. 1 suggests that it is the observed stage 4 that should be identified with the onset of catastrophic degradation of GaAs. It should be recalled that the thresholds W_d of the aforementioned damage were conventionally determined previously in semiconductors and metals either from irreversible decrease in the intensity of specularly reflected light or using various versions of optical microscopy [23–25, 29, 34, 35]. In this study, we used the AFM method on the nanometer scale of surface displacements to monitor for the first time the earlier stages (stages 1–3) of defect production in micrometer-sized regions of GaAs.

3.7. Stage 5

Individual microcraters that had arisen at stage 4 merged into a single macroscopic defect at $N > N_5 = 10^5$–10^6. As a result, a "giant" circular crater was formed. This crater had a depth of $\Delta U_z = 1$–5 μm and a transverse dimension of 10–30 μm; the latter was close to the diameter 2ω of the laser spot at the semiconductor surface. Previously, we studied such final stages of damage production in GaAs using electron microscopy and X-ray and chemical microanalysis [26]. The AFM

measurements of the array of laser-irradiated GaAs areas showed that the features of nanometer-sized damaged surface regions depended on both the energy density of incident radiation (for $W > W_0$) and the number N of pulsed quasi-static photostrains in the semiconductor. Similar results could be obtained not only by varying N at W = const but also by increasing W under conditions of N = const. Indeed, an increase in W inevitably resulted in a shift of the aforementioned stages of the defect formation in GaAs to smaller values of N.

4. CONCLUSION

The results obtained make it possible to consider the process of catastrophic damage in micrometer-sized GaAs regions exposed to multiple laser pulses from a unified standpoint; i.e., this process is considered as multistage. The earliest (initial) stages of defect formation in a semiconductor subjected to inelastic deformation ($W > W_0$ [22]) feature the latent buildup of mainly point defects (arsenic vacancies, excess of gallium [26]) from pulse to pulse. As N increases, individual defects merge into nanometer-sized clusters and, thus, form chaotic local depressions in the surface profile and are subsequently involved in orientational self-organization of these clusters. We used the PTSS and AFM methods to show that not only the elevated temperatures or electronic excitation but also the shearing strains $dU_z/dr(r)$ and subsurface stresses contribute significantly to the mechanisms of the defect formation and the clusters' migration [23–25]. The results obtained are consistent with both the quasi-1D electronic–deformational–thermal model of the laser-induced defect production in semiconductors [39–41] and the strain-stimulated "dimensional" effects [23–25, 34, 35].

The consecutive stages of defect formation (monitored for the first time by the AFM method in micrometer-sized GaAs regions) at increasing nanometer-scale surface displacements ΔU_z show clearly (as in the case of Ge [42]) that the processes of self-organization of the defect clusters are gradually transformed into subsequent nanoscale and microscale damage in the semiconductor. We believe that similar mechanisms of defect generation in GaAs can also be encountered in the case of other methods for heating the micrometer-sized semiconductor regions, for example, by passing the electric current through the sample. Thus, the processes studied may give rise to fundamental limitations on the standard operation modes of commercial small-sized devices (Gunn and Schottky diodes and other devices) with local heat release [30] and, correspondingly, with local strains [32] in the active semiconductor layers.

ACKNOWLEDGMENTS

We thank I.E. Sapozhnikov and A.G. Barskov for their help with preparation of some of the samples and with maintenance of the probing lasers.

REFERENCES

1. M. Shur, *GaAs Devices and Circuits* (Plenum, New York, 1987; Mir, Moscow, 1991).
2. A. V. Dvurechenskiĭ, G. A. Kachurin, E. V. Nidaev, and L. S. Smirnov, *Pulse Annealing of Semiconductor Materials* (Nauka, Moscow, 1982).
3. *Semiconductors and Semimetals*, Vol. 23: *Pulsed Laser Processing of Semiconductors*, Ed. by R. F. Wood, C. W. White, and R. T. Young (Academic, New York, 1984).
4. N. G. Dzhumamukhambetov and A. G. Dmitriev, Pis'ma Zh. Tekh. Fiz. **17** (13), 21 (1991) [Sov. Tech. Phys. Lett. **17**, 467 (1991)].
5. V. D. Andreeva, M. I. Anisimov, N. G. Dzhumamukhambetov, and A. G. Dmitriev, Fiz. Tekh. Poluprovodn. (Leningrad) **24**, 1010 (1990) [Sov. Phys. Semicond. **24**, 635 (1990)].
6. B. G. Gribov, G. M. Gusakov, T. N. Kondratova, *et al.*, Dokl. Akad. Nauk SSSR **314**, 618 (1990) [Sov. Phys. Dokl. **35**, 847 (1990)].
7. A. I. Efimova, P. K. Kashkarov, V. I. Petrov, and V. Yu. Timoshenko, Poverkhnost, No. 8, 94 (1990).
8. N. G. Dzhumamukhambetov and A. G. Dmitriev, Fiz. Tekh. Poluprovodn. (Leningrad) **22**, 1880 (1988) [Sov. Phys. Semicond. **22**, 1192 (1988)].
9. G. M. Gusakov, T. N. Kondratova, K. S. Kapskiĭ, and A. I. Laryushin, Fiz. Tekh. Poluprovodn. (Leningrad) **23**, 1864 (1989) [Sov. Phys. Semicond. **23**, 1154 (1989)].
10. P. K. Kashkarov, V. I. Petrov, D. V. Ptitsyn, and V. Yu. Timoshenko, Fiz. Tekh. Poluprovodn. (Leningrad) **23**, 2080 (1989) [Sov. Phys. Semicond. **23**, 1287 (1989)].
11. G. D. Ivlev, F. M. Koshchanov, V. L. Malevich, and E. A. Tyavlovskaya, Pis'ma Zh. Tekh. Fiz. **16** (6), 42 (1990) [Sov. Tech. Phys. Lett. **16**, 222 (1990)].
12. C. Cohen, J. Siejka, and D. Pribat, J. Phys. Colloq. C5 (Paris) **44** (10), 179 (1983).
13. K. K. Dzhamanbalin, A. G. Dmitriev, É. N. Sokol-Nomokonov, and Yu. I. Ukhanov, Fiz. Khim. Obrab. Mater., No. 2, 20 (1990).
14. A. G. Dmitriev, Fiz. Tekh. Poluprovodn. (St. Petersburg) **27**, 582 (1993) [Semiconductors **27**, 323 (1993)].
15. F. A. McDonald, R. J. Gutfield, and R. W. Dreyfus, Proc.–IEEE Ultrason. Symp., 403 (1986).
16. S. V. Vintsents and S. G. Dmitriev, Zh. Tekh. Fiz. **67**, 105 (1997) [Tech. Phys. **42**, 216 (1997)].
17. S. V. Vintsents, S. G. Dmitriev, and O. G. Shagimuratov, Fiz. Tverd. Tela (St. Petersburg) **38**, 993 (1996) [Phys. Solid State **38**, 552 (1996)].
18. S. V. Vintsents, S. G. Dmitriev, and K. I. Spiridonov, Fiz. Tverd. Tela (St. Petersburg) **39**, 2224 (1997) [Phys. Solid State **39**, 1985 (1997)].
19. S. V. Vintsents, S. G. Dmitriev, R. A. Zakharov, and G. S. Plotnikov, Fiz. Tekh. Poluprovodn. (St. Petersburg) **31**, 513 (1997) [Semiconductors **31**, 433 (1997)].
20. S. V. Vintsents, V. B. Zaitsev, A. V. Zoteyev, *et al.*, in *Proceedings of 3rd International Conference on Physics of Low-Dimensional Structures* (Chernogolovka, 2001), Vol. 3, p. 69.

21. S. V. Vintsents, V. B. Zaĭtsev, A. V. Zoteev, *et al.*, Fiz. Tekh. Poluprovodn. (St. Petersburg) **36**, 947 (2002) [Semiconductors **36**, 883 (2002)].
22. S. V. Vintsents, A. V. Zoteev, and G. S. Plotnikov, Fiz. Tekh. Poluprovodn. (St. Petersburg) **36**, 902 (2002) [Semiconductors **36**, 841 (2002)].
23. A. G. Barskov and S. V. Vintsents, Fiz. Tverd. Tela (St. Petersburg) **36**, 2590 (1994) [Phys. Solid State **36**, 1411 (1994)].
24. S. V. Vintsents and S. G. Dmitriev, Pis'ma Zh. Tekh. Fiz. **21** (19), 1 (1995) [Tech. Phys. Lett. **21**, 767 (1995)].
25. S. V. Vintsents, S. G. Dmitriev, and O. G. Shagimuratov, Pis'ma Zh. Tekh. Fiz. **22** (8), 8 (1996) [Tech. Phys. Lett. **22**, 602 (1996)].
26. A. G. Barskov, S. V. Vintsents, G. G. Dvoryankina, *et al.*, Poverkhnost, No. 3, 79 (1995).
27. D. V. Lioubtchenko, I. A. Markov, and T. A. Briantseva, Appl. Surf. Sci. **195**, 42 (2002).
28. A. Blazhis, S. Zhilenis, and G. Tautvaĭshas, Zh. Tekh. Fiz. **58**, 2237 (1988) [Sov. Phys. Tech. Phys. **33**, 1359 (1988)].
29. W. W. Duley, *Laser Processing and Analysis of Materials* (Plenum, New York, 1983).
30. V. I. Borisov, V. E. Lyubchenko, and A. S. Rogashkov, Élektron. Tekh., Ser. 1: Élektron. SVCh **10**, 404 (1987).
31. V. E. Lyubchenko, Radiotekhnika (Moscow), No. 2, 16 (2002).
32. A. L. Polyakova, *Deformation of Semiconductors and Semiconductor Devices* (Énergiya, Moscow, 1979).
33. P. K. Kashkarov, M. V. Rusina, and V. Yu. Timoshenko, Fiz. Tekh. Poluprovodn. (St. Petersburg) **26**, 1835 (1992) [Sov. Phys. Semicond. **26**, 1030 (1992)].
34. C. S. Lee, N. Koumvakalis, and M. Bass, Appl. Phys. Lett. **41**, 625 (1982); Opt. Eng. **22**, 419 (1983); J. Appl. Phys. **54**, 5727 (1983).
35. S. S. Cohen, J. B. Bernstein, and P. W. Wyatt, J. Appl. Phys. **71**, 630 (1992).
36. A. S. Filonov and I. V. Yaminskiĭ, *User's Manual for FemtoSkan-001* (TsPT, Moscow, 1999).
37. Yu. I. Golovin and A. I. Tyurin, Fiz. Tverd. Tela (St. Petersburg) **42**, 1818 (2000) [Phys. Solid State **42**, 1865 (2000)].
38. V. P. Alekhin, *Physics of Strength and Plasticity of Surface Layers of Materials* (Nauka, Moscow, 1983).
39. V. I. Emel'yanov and P. K. Kashkarov, Poverkhnost, No. 2, 77 (1990).
40. V. I. Emel'yanov and P. K. Kashkarov, Appl. Phys. A **55**, 161 (1992).
41. P. K. Kashkarov and V. Yu. Timoshenko, Poverkhnost, No. 6, 5 (1995).
42. S. V. Vintsents, A. V. Zaĭtseva, and G. S. Plotnikov, Fiz. Tekh. Poluprovodn. (St. Petersburg) **37**, 134 (2003) [Semiconductors **37**, 124 (2003)].

Translated by A. Spitsyn

Semiconductors, Vol. 38, No. 3, 2004, pp. 253–257. Translated from Fizika i Tekhnika Poluprovodnikov, Vol. 38, No. 3, 2004, pp. 265–269.

ATOMIC STRUCTURE AND NONELECTRONIC PROPERTIES OF SEMICONDUCTORS

Effects of Predoping and Implantation Conditions on Diffusion of Silicon in Gallium Arsenide Subjected to Electron-Beam Annealing

M. V. Ardyshev*^, V. M. Ardyshev*, and Yu. Yu. Kryuchkov**

**Kuznetsov Physicotechnical Institute, pl. Revolyutsii 1, Tomsk, 634050 Russia*

^e-mail: ard.rff@elefot.tsu.ru; detector@mail.tomsknet.ru

***Tomsk Polytechnical University, Tomsk, 634050 Russia*

Submitted May 16, 2003; accepted for publication June 3, 2003

Abstract—Measurements of capacitance–voltage characteristics and Rutherford backscattering were used to study the parameters of silicon diffusion from preliminarily formed *n*-type layers into semi-insulating GaAs under electron-beam annealing and conventional heat treatment. The layers were doped with either sulfur or silicon. The degree of ^{28}Si electrical activation and ^{28}Si diffusion coefficient are found to depend on the dopant used to form the *n*-type layer and on the implantation conditions (continuous or pulsed-repetitive, with a pulse width of 1.3×10^{-2} s and duty factor of 100). © *2004 MAIK "Nauka/Interperiodica".*

1. INTRODUCTION

The in-diffusion of ^{28}Si implanted into GaAs was observed previously after postimplantation electron-beam annealing [1]. It was shown that this phenomenon was caused by lowering of potential barriers to migration and activation of silicon impurity and depended on the conditions at the semiconductor surface [2] and on the degree of imperfection of the initial material [3]. Internal electric fields and implantation conditions (in particular, it is known that the diffusion coefficient depends on the implantation dose of impurities) can often affect the impurity diffusion. In this context, we studied silicon diffusion in GaAs as a result of electron-beam annealing; the diffusion proceeded from preliminarily formed *n*-type layers into the material with intrinsic conductivity.

2. EXPERIMENTAL

In our studies, we used wafers of single-crystal semi-insulating GaAs with a resistivity higher than 10^7 Ω cm and dislocation density no higher than 5×10^4 cm^{-2}; we also used n–n_i epitaxial structures with an electron concentration in the *n*-type layer equal to $\sim 1.1 \times 10^{17}$ cm^{-3} and with a thickness of ~0.22 μm. The epitaxial layers were doped with sulfur and were formed by the gas-transport method on the semi-insulating GaAs substrates. The wafers were oriented in the (100) plane. The wafers were first treated in an $H_2SO_4 : H_2O_2 : H_2O = 1 : 1 : 100$ etchant; the ^{28}Si ions were then implanted at room temperature in the pulsed-repetitive mode (pulse width of 1.3×10^{-2} s and duty factor of 100) and in the continuous mode, consecutively with an ion energy of 50 keV and dose of 5.62×10^{12} cm^{-2}, energy of 75 keV and dose of 1.88×10^{12} cm^{-2}, and energy of 100 keV and dose of 1×10^{14} cm^{-2} for the single-crystal material; the ion energies were 50 and 100 keV with the respective doses of 5×10^{13} and 5.62×10^{12} cm^{-2} in the case of epitaxial material. The ion-current density was no higher than 0.1 μA cm^{-2}. We took measures to suppress the axial and planar channeling effects during implantation (see [4]). An SiO_2:Sm film with a thickness of 0.1–0.2 μm was deposited onto the substrate surface from the film-forming solution using the method described elsewhere [5]. The electron-beam annealing was carried out using a Modul' system (Institute of High-Current Electronics, Siberian Division, Russian Academy of Sciences, Tomsk) with an electron energy of 10 keV in the beam and power density of 8.2 W cm^{-2} in a vacuum chamber with a residual pressure of 10^{-5} Pa; the annealing duration ranged from 10 to 16 s. The thermal annealing was carried out for 30 min at a temperature of 800°C.

After the layers with *n*-type conductivity were formed near the GaAs surface, the wafers were cut into two parts. The second parts of the wafers were subjected to an additional electron-beam annealing.

After annealing and removal of the insulator, we determined the electron-concentration profiles by measuring the capacitance–voltage characteristics (see [1]). We used the method of Rutherford backscattering of channeled 1.86-MeV helium ions to determine the degree of imperfection of the material after implantation and after annealing. Experimental doping profiles were approximated using the expression [6]

$$n(x, t) = \frac{\eta F}{\sqrt{2\pi}\sigma} \exp\left[-\frac{(x - R_p)^2}{2\sigma^2}\right], \qquad (1)$$

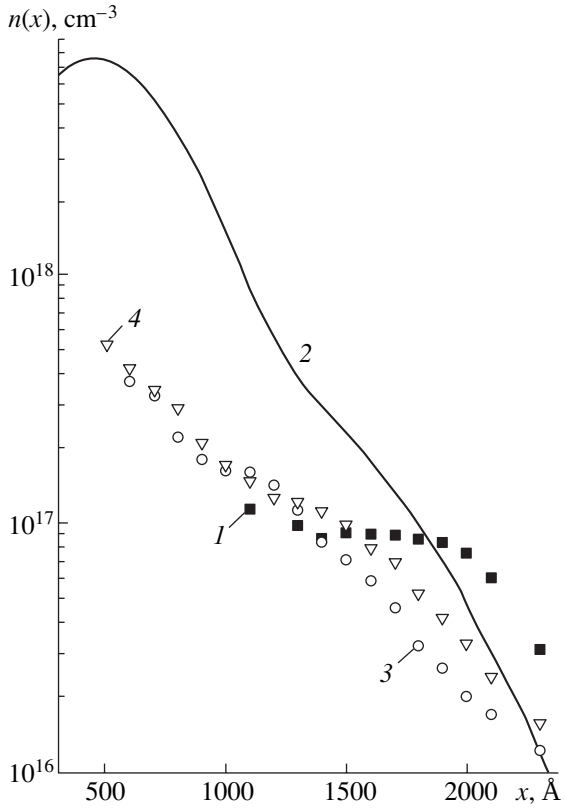

Fig. 1. Concentration profiles of silicon implanted in continuous mode into an n–n_i epitaxial structure: (*1*) the initial electron-concentration profile in the n-type layer; (*2*) calculated profile for silicon implantation with ion energy of first 50 keV at 5×10^{13} cm^{-2} and then 100 keV at 5.62×10^{12} cm^{-3}; (*3*, *4*) electron-concentration profiles obtained after electron-beam annealing for (*3*) 10 and (*4*) 16 s.

where $\sigma^2 = \Delta R_p^2 + 2Dt$ is the concentration-profile variance; F, R_p, and ΔR_p are the implantation dose, the projected range of ions, and the projected-range standard deviation, respectively; D and η are the diffusion coefficient and the degree of electrical activation of the impurity, respectively; x is the coordinate; and t is time.

Table 1. Characteristics of electron-concentration profiles in the n–n_i GaAs:S structures after ^{28}Si implantation and subsequent electron-beam annealing with various durations ($x > 1100$ Å)

Annealing duration, s	n_{max}, cm^{-3}	η, %	σ^2, Å^2	D, cm^2 s^{-1}
10	1.42×10^{17}	34	2.9×10^5	4.33×10^{-13}
16	3.9×10^{17}	42	3.84×10^5	5.64×10^{-13}
10*	No data	78*	No data	$(2.0 \pm 0.2) \times 10^{-12}$*

Note: Parameters marked by an asterisk (*) are taken from [1] and correspond to the ^{28}Si migration from the implanted layer into semi-insulating GaAs rather than into epitaxial structure.

When using expression (1), we assumed that there is no diffusion of impurity through the semiconductor boundary and that the experimental impurity-concentration profile can be described analytically. In the case of profiles that cannot be described analytically, we used the Boltzmann–Motano method (see, for example, [7]) to determine the diffusion coefficient; i.e.,

$$D_i = -N_i(x_i - R_p)\left[2t\frac{dN}{dx}\bigg|_{x = x_i}\right]^{-1}, \qquad (2)$$

where N_i and $dN/dx|_{x = x_i}$ are the concentration and the concentration gradient at the depth x_i, respectively.

3. RESULTS AND DISCUSSION

3.1. The Effect of Preliminary Doping

In Fig. 1, we show the experimental electron-concentration profiles in the structure under consideration before and after silicon implantation and after subsequent electron-beam annealing; the calculated concentration profile of implanted silicon is also shown. It can be seen that, as the duration of the electron-beam annealing increases, the depth to which silicon atoms migrate increases (curves *3*, *4*). It is significant that two portions can be identified in the silicon concentration profiles: one portion extends from the surface to a depth $x \approx 1100$ Å and the other portion extends to depths greater than $x < 1100$ Å. Redistributions of the impurity and electron concentrations with respect to the profile of implanted silicon (curve *2*) do not occur as a result of annealing for 10 or 16 s at depths $x > 1100$ Å. The maximum of electron concentration n_{max} in the layers and the degree of electrical activation of the impurity are found to be in the ranges of $(4–5) \times 10^{17}$ cm^{-3} and 4.3–4.6%, respectively (curves *3*, *4*). For $x > 1100$ Å, the diffusion and activation parameters of the doping profiles differ for the annealing duration of 10 and 16 s (Table 1).

The results of electron-beam annealing (case 1) also differ from those obtained for implanted semi-insulating GaAs (case 2); in particular, in case 1 compared to case 2, the value of η is two times smaller and the diffusion coefficient is smaller by an order of magnitude. It is also noteworthy that the quantity $D/t \cong 4.3 \times 10^{-14}$ cm^2 s^{-2} in the case of electron-beam annealing for 10 s is larger ($D/t \cong 3.5 \times 10^{-14}$ cm^2 s^{-2}) than in the case of similar annealing for 16 s; i.e., we observe a decrease of about 20% for the diffusion coefficient per unit time. It is also worth noting that there is no "shoulder" in the concentration profiles measured after electron-beam annealing (curves *3*, *4*) in contrast to what is observed in the initial (prior to annealing) electron-concentration profile (curve *1*). Since sulfur is the dopant in the n-type layer of the epitaxial structure, it is likely that a redistribution of sulfur closer to the surface (to the region with a high concentration of radiation defects) occurs in the course of implantation and electron-beam annealing. It

is also possible that radiation defects (along with silicon atoms) migrate into the semiconductor bulk; in particular, these defects can include gallium vacancies V_{Ga}, with which, as is known, sulfur forms neutral complexes. Formation of neutral complexes consisting of sulfur and V_{Ga} should result, on the one hand, in a decrease in the degree of electrical activation of silicon in the layers at depths smaller and larger than 1100 Å and, on the other hand, in a decrease in the diffusion coefficient of ^{28}Si if silicon diffuses via gallium vacancies. This is exactly what is observed experimentally (Table 1, Fig. 1).

In Fig. 2, we show experimental electron-concentration profiles after implantation of silicon and subsequent consecutive electron-beam anneals; the calculated profile of implanted silicon is also shown. The parameters of silicon concentration profiles are listed in Table 2.

It can be seen that a somewhat deeper penetration of silicon into GaAs is observed after the second electron-beam annealing (Fig. 2); in addition, the electron concentration and the degree of electrical activation of silicon increase compared to what is observed after the first electron-beam annealing. The diffusion coefficient increases insignificantly, although silicon migration occurs from the *n*-type layer to intrinsic GaAs; i.e., the diffusion occurs in fact in the electric field of the n–n_i junction. The band bending at the boundary of this junction gives rise to the built-in negative charge on the side of intrinsic GaAs; this charge is neutralized in the *n*-type layer. Accumulation of V_{Ga} vacancies can occur in this negatively charged region of the n–n_i junction; as is known [8], these vacancies can be singly, doubly, or triply negatively charged. An increase in the V_{Ga} concentration should result in an increase in the diffusion coefficient D according to the expression [8]

$$D_{\text{eff}} = D_0 + D_-\left(\frac{n}{n_i}\right) + D_{2-}\left(\frac{n}{n_i}\right)^2 + D_{3-}\left(\frac{n}{n_i}\right)^3, \qquad (3)$$

where the subscripts of corresponding components of D denote the charge state of vacancies.

It is noteworthy that expression (3) is valid only if the charge-carrier concentration is controlled solely by the concentration of charged vacancies.

However, one should display great reservations with respect to the processes under consideration. The point is that nonequilibrium charge carriers and ionized atoms of the semiconductor host with concentrations of $\sim 10^{19}$ cm^{-3} are generated in the material irradiated with high-energy electrons. Calculations performed using the method described elsewhere [10] showed that the thickness of the ionized layer greatly exceeded the depth of the n–n_i junction for the energy of electrons (10 keV) used for annealing. Therefore, all the processes under investigation take place in the highly ionized material. The observed phenomena are mainly caused by the ionization- and thermal-induced decrease in the barrier heights for the impurity migration and

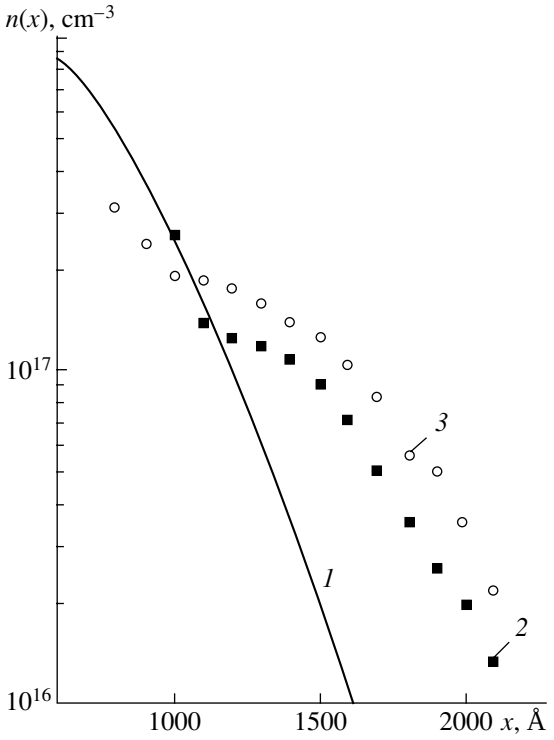

Fig. 2. The concentration profiles of silicon implanted in continuous mode into semi-insulating GaAs: (*1*) calculated profile for combined implantation of 50-keV ions (5.62×10^{13} cm^{-2}) and 75-keV ions (1.88×10^{12} cm^{-3}), and the electron-concentration profiles obtained after (*2*) the first and (*3*) the second electron-beam annealing for 10 s.

activation [1] (as in the case of the first electron-beam annealing) rather than by the effect of the electric field of the n–n_i junction, whose potential does not exceed 0.5 eV at the temperature of annealing. In particular, this inference is confirmed by the fact that the values of

Table 2. The most important diffusion parameters of silicon in semi-insulating GaAs after electron-beam annealing (EBA) for 10 s

Annealing	n_{max}, cm^{-3}	η, %	σ^2, Å^2	D, cm^2 s^{-1}
The first EBA	2.24×10^{17}	54.2	5.275×10^5	1.88×10^{-12}
The second EBA	2.59×10^{17}	76.0	7.753×10^5	3.12×10^{-12}

Table 3. The diffusion coefficients of silicon in semi-insulating GaAs for different ion-implantation conditions with subsequent thermal annealing (TA) or electron-beam annealing (EBA)

Implantation mode	Diffusion coefficient, cm^2 s^{-1}	
	TA	EBA
Continuous	1.6×10^{-15}	4.5×10^{-13}
Pulsed-repetitive	3.0×10^{-15}	3.1×10^{-12}

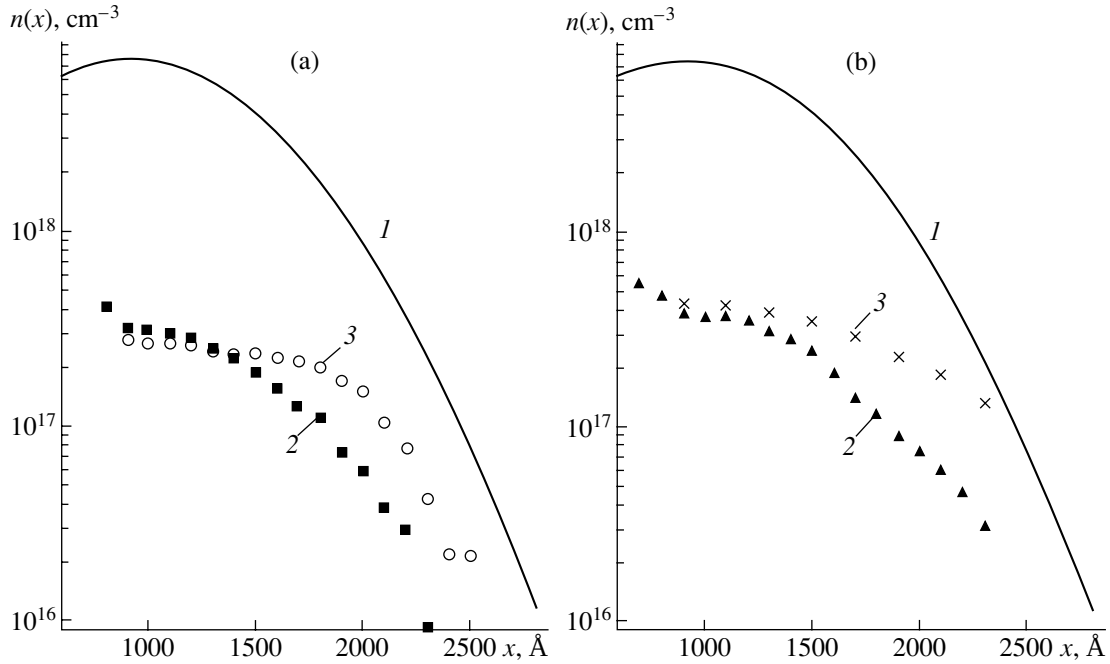

Fig. 3. Concentration profiles of silicon implanted in the (a) continuous and (b) pulsed-repetitive modes of implantation into semi-insulating GaAs: (*1*) calculated profile for implantation of 100-keV Si ions (1×10^{14} cm^{-2}) and (*2*, *3*) electron-concentration profiles obtained after (*2*) thermal annealing and (*3*) subsequent electron-beam annealing.

the diffusion coefficient for both annealing durations almost coincide (Table 2).

3.2. The Effect of Implantation Conditions

In Figs. 3a and 3b, we show the electron-concentration profiles after the thermal and subsequent electron-beam anneals for two conditions of implantation. The concentration profile of implanted silicon is also shown. The values of the silicon diffusion coefficient after annealing are listed in Table 3.

It follows from Fig. 3 and Table 3 that the redistribution of silicon is more pronounced in the pulsed-repetitive mode of implantation than in the continuous mode after both thermal annealing and electron-beam annealing of implanted layers, which is confirmed by the corresponding values of the diffusion coefficient D. The most plausible cause of observed differences in the behavior of ^{28}Si for the implantation conditions under investigation is related to differences in the degree of imperfection of the material both after implantation of the impurity and after thermal annealing.

In Fig. 4, we show the spectra of Rutherford backscattering for GaAs samples. In Table 4, the values of the lowest backscattering yield χ_{min} and the degree of imperfection of the material are listed. We calculated the relative concentration of defects in the ion-implanted layer [11]; i.e.,

$$\frac{N_D}{N_0} = \frac{\chi_{min}^{ex} - \chi_{min}^{in}}{1 - \chi_{min}^{in}}, \qquad (4)$$

where N_D and N_0 are the defect concentration and the atom density of GaAs, respectively, and χ_{min}^{in} and χ_{min}^{ex} are the values of χ_{min} before and after implantation, respectively. The range of integration in calculation of χ_{min}^{ex} was chosen beyond the defect peak at a depth of $R_p + 2\Delta R_p$. The values of theoretical yield χ_{min}^{th} for helium ions are also listed in Table 4.

As can be seen (Fig. 4, Table 4), the degree of the material's imperfection is much higher after implantation in the continuous mode than after pulsed-repetitive

Table 4. The degree of imperfection of GaAs after ion implantation with subsequent thermal annealing (TA)

Implantation mode	After implantation				After TA	
	χ_{min}^{ex}	χ_{min}^{in}	χ_{min}^{th}	N_d/N_0, at %	N_d/N_0, at %	N_d/N_0, at % (after removal of a 150-nm-thick layer)
Continuous	0.29	0.06	0.035	25	~0.10	~0.09
Pulsed-repetitive	0.13	0.06	0.035	8	0.00	0.00

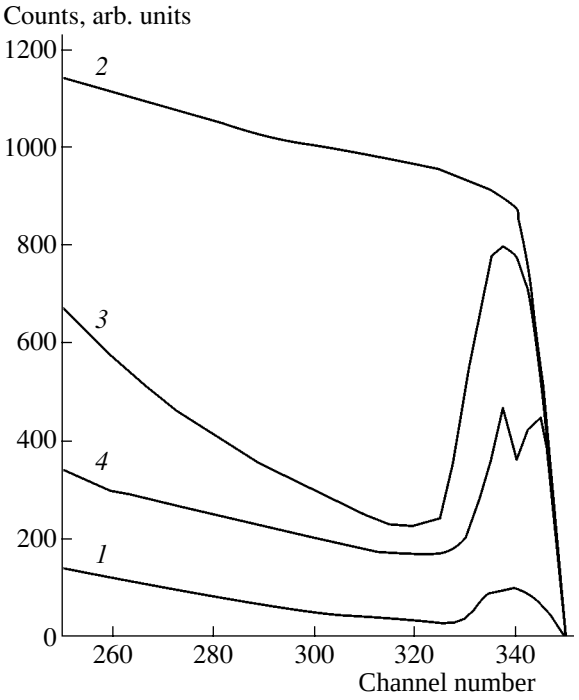

Fig. 4. Energy spectra of helium ions (E = 1.86 MeV) backscattered by a ⟨100⟩ GaAs crystal implanted with 100-keV silicon ions with a dose of 10^{14} cm^{-2} and an ion-current density of 0.1 μA cm^{-2} at 300 K in the (*3*) continuous and (*4*) pulsed-repetitive modes of implantation: (*1*) the initial aligned (axial) spectrum and (*2*) the initial random spectrum.

implantation, although the energy, dose, and ion-current density were the same in both cases. Defects are not completely annealed out after heat treatment (Table 4); it is noteworthy that removal of a 150-nm-thick layer from the semiconductor surface has virtually no effect on the residual damage in the material. The latter fact indicates that defects penetrate beyond the implanted layer. By comparing the data listed in Tables 3 and 4, we may conclude that, after implantation and thermal annealing, residual defects manifest themselves as traps for silicon atoms and thus retard the migration of these atoms into the GaAs bulk. These defects also do not anneal out during subsequent electron-beam annealing. Taking into account the results of recent studies [1–3] where the implantation doses were on the order of ~10^{13} cm^{-2}, we may state that this stability of defects also manifests itself at comparatively high doses of implantation (≥10^{14} cm^{-2}).

4. CONCLUSIONS

(i) Electron-beam annealing of GaAs:S n–n_i epitaxial structures doped with the silicon isotope ^{28}Si using ion implantation in the continuous mode with a dose of $\leq 5 \times 10^{13}$ cm^{-2} results in a decrease in the silicon diffusion coefficient and in a decrease in the degree of electrical activation of silicon compared to similar characteristics of diffusion in semi-insulating GaAs implanted with ^{28}Si.

(ii) If the n–n_i structure where the n-type layer was formed by continuous implantation of ^{28}Si with a dose $<10^{13}$ cm^{-2} and by electron-beam annealing is subjected to a second electron-beam annealing, the silicon diffusion coefficient increases insignificantly compared to what was observed after the first annealing, although silicon migrates in the electric field of the n–n_i junction. As a result of the second electron-beam annealing, the degree of electrical activation of silicon increases approximately by a factor of 1.5.

(iii) If the pulsed-repetitive implantation of ^{28}Si (with a pulse width of 1.3×10^{-2} s and duty factor of 100) is used with subsequent thermal annealing, a much lower concentration of residual defects is formed in GaAs compared to what is observed after continuous implantation. The damaged layer extends to a GaAs depth that exceeds the thickness of the n-type layer after thermal annealing. The presence of this layer reduces the silicon diffusion coefficient both after thermal annealing and after electron-beam annealing. It is noteworthy that, in the latter case, silicon diffuses in the electric field of the n–n_i junction.

ACKNOWLEDGMENTS

This study was supported by the Russian Foundation for Basic Research, project no. 02-02-16280.

REFERENCES

1. M. V. Ardyshev and V. M. Ardyshev, Fiz. Tekh. Poluprovodn. (St. Petersburg) **32**, 1153 (1998) [Semiconductors **32**, 1029 (1998)].
2. M. V. Ardyshev, V. M. Ardyshev, and S. S. Khludkov, Fiz. Tekh. Poluprovodn. (St. Petersburg) **34**, 70 (2000) [Semiconductors **34**, 70 (2000)].
3. M. V. Ardyshev, V. M. Ardyshev, and S. S. Khludkov, Fiz. Tekh. Poluprovodn. (St. Petersburg) **34**, 28 (2000) [Semiconductors **34**, 27 (2000)].
4. M. V. Ardyshev and V. M. Ardyshev, Izv. Vyssh. Uchebn. Zaved., Fiz. **41** (11), 44 (1998).
5. V. M. Ardyshev, V. A. Selivanova, O. N. Korotchenko, and A. P. Mamontov, Inventor's Certificate No. 235,899 (1 April 1986).
6. H. Ryssel and I. Ruge, *Ionenimplantation* (Teubner, Stuttgart, 1978; Nauka, Moscow, 1983).
7. A. Bakowski, J. Electrochem. Soc.: Solid State Sci. Technol. **127**, 1644 (1980).
8. E. L. Allen, M. D. Deal, and J. D. Plummer, J. Appl. Phys. **67**, 3311 (1990).
9. M. V. Ardyshev, V. M. Ardyshev, and S. S. Khludkov, in *Proceedings of 5th International Conference on Actual Problems in Electron Instrument Making* (Novosibirsk, 2000), Vol. 2, p. 119.
10. I. A. Abroyan, A. N. Andronov, and A. I. Titov, *Physical Foundations of Electron- and Ion-Beam Technology* (Vysshaya Shkola, Moscow, 1984).
11. J. W. Mayer, L. Eriksson, and J. A. Davies, *Ion Implantation in Semiconductors: Silicon and Germanium* (Academic, New York, 1970; Mir, Moscow, 1973).

Translated by A. Spitsyn

Semiconductors, Vol. 38, No. 3, 2004, pp. 258–261. Translated from Fizika i Tekhnika Poluprovodnikov, Vol. 38, No. 3, 2004, pp. 270–273.

ATOMIC STRUCTURE AND NONELECTRONIC PROPERTIES OF SEMICONDUCTORS

Simulation of the Concentration Dependence of Boron Diffusion in Silicon

O. V. Aleksandrov

St. Petersburg Electrotechnical University, St. Petersburg, 197376 Russia

e-mail: Aleksandrov@svs.ru

Submitted May 27, 2003; accepted for publication June 18, 2003

Abstract—Boron diffusion in silicon with a high surface concentration was simulated on the basis of the dual pair mechanism. The calculations were compared with experimental data and the calculations using the SUPREM-3 code. It was shown that the model proposed allows us to describe the concentration profiles and the concentration dependence of the boron diffusivity in a wide temperature range: 800–1100°C. © *2004 MAIK "Nauka/Interperiodica".*

Boron is in fact a single acceptor impurity used as a main dopant in planar technology of silicon devices and integrated circuits. As other basic dopants for silicon (P, As, Sb), boron is characterized by a concentration dependence of its diffusivity. The dependence of the boron diffusivity on the local concentration of majority carriers was determined from an analysis of the concentration profiles and experiments on isoconcentration diffusion [1–3] as

$$D = D^0 + D^+ = D_i^0 + D_i^+\left(\frac{p}{n_i}\right), \quad (1)$$

where D^0 and D^+ are the partial coefficients of boron diffusion via neutral and positively charged intrinsic point defects (IPDs), p is the hole concentration, n_i is the intrinsic carrier concentration, and the subscript i indicates intrinsic silicon. The dependence in the form of (1) provides a quite satisfactory description of boron diffusion at temperatures $\gtrsim$1000°C and is used in the SUPREM-3 code for simulation of physical processes and technology of fabrication [4].

At moderate diffusion temperatures (T < 1000°C) and sufficiently high surface concentrations ($C_s > n_i$), the concentration dependence of the diffusivity deviates from dependence (1) at low concentrations ($C < n_i$) of the profile [5]. Moreover, some additional diffusion features arise, which are characteristic of another basic dopant (phosphorus), but more weakly pronounced. In particular, at lower diffusion temperatures (800–900°C), the boron concentration profiles exhibit an kink and a tail [5–7], in which case the temperature dependence of the boron concentration is similar to that of phosphorus in the kink region [6].

To describe the boron diffusion, Anderson and Gibbons [8] proposed a mechanism of diffusion via neutral pairs consisting of boron atoms and vacancies BV^0 (B^-V^+). This mechanism made it possible to explain the concentration dependence of diffusivity (1), $D \propto p/n_i$. The tail in the concentration profile was associated in [6] with two-flux diffusion of a dopant through sites (via impurity–vacancy pairs) at high concentrations and through interstices at low concentrations. According to the estimates of [6], the formation energy (1.5 eV) of interstitial boron atoms is significantly lower than the formation energy of self-interstitials. However, we should note that the two-flux models do not allow us to attain invariance of the concentration profiles with respect to the reduced depth $x/\sqrt{t}$ (x is the depth and t is the diffusion time) for weak interaction between fluxes; in the case of strong interaction, these models yield no kink. Attempts were made to simulate the boron diffusion on the basis of quasi-equilibrium pair models involving (i) impurity–self-interstitial pairs in different charge states [9] and (ii) impurity–self-interstitial (BI) and impurity–vacancy (BV) pairs simultaneously [10]. In both papers, some assumptions were made, restricting the model applicability, and a number of fitting parameters were used. Nevertheless, the agreement with experimental boron profiles was not entirely satisfactory. Many-particle models [11–13] considered all possible interactions of ionized impurity atoms with IPDs of both types (vacancies and self-interstitials) in different charge states (0, ±1, ±2), the formation of impurity–defect pairs of both types, the interaction of IPDs of both types with impurity–defect pairs and IPDs of opposite sign, and the recharging of all components involved in the diffusion. This consideration necessitates solving a set of a large number of partial differential equations (up to 20) with a large number of undetermined parameters (up to 134) [13]. In this case, the problem of adequacy and uniqueness of the solution arises since the same parameters determined within various models differ from each other and often differ from the known experimental ones.

The objective of this study is to simulate boron diffusion in silicon within a rather simple model based on the dual pair mechanism, which we previously developed for the case of phosphorus diffusion in silicon [14]. In terms of the model [14], a substitutional impurity diffuses according to the dual pair mechanism, i.e., via pairs formed by an ionized impurity (boron in the case under consideration) and IPDs of both types (vacancies (BV) and self-interstitials (BI)),

$$D_{\mathrm{B}} = D_{\mathrm{B}V} + D_{\mathrm{B}I} = D^*_{\mathrm{B}V}a_V + D^*_{\mathrm{B}I}a_I, \quad (2)$$

where $D_{\mathrm{B}V}$ and $D_{\mathrm{B}I}$ are the components of the coefficient of boron diffusion via BV and BI pairs, respectively, and $a_V = C_V/C^*_V$ and $a_I = C_I/C^*_I$ are, respectively, the ratios of the vacancy and self-interstitial concentrations to the corresponding thermodynamic equilibrium concentrations (the superscript (*) means the condition of thermodynamic equilibrium with respect to IPDs ($a_V = a_I = 1$)). We assume that the condition of local equilibrium between vacancies and self-interstitials, C_VC_I = const, is satisfied; hence, $a_V = 1/a_I$.

IPDs and IPD–ionized-impurity pairs are in different charge states, whose contribution to boron diffusion is directly taken into account using relative fractions of diffusion via vacancies (f_V) and self-interstitials (f_I) in corresponding charge states ($f^0_V + f^0_I = 1$, $f^+_V + f^+_I = 1$):

$$D^*_{\mathrm{B}V} = f^0_V D^0 + f^+_V D^+, \quad D^*_{\mathrm{B}I} = f^0_I D^0 + f^+_I D^+. \quad (3)$$

Within the model [14], the IPD concentrations deviate from the thermodynamic equilibrium ones due to the diffusion of neutral impurity–self-interstitial pairs from the region with high concentrations of pairs and impurity into the region with low concentrations. Further decomposition of pairs is accompanied by release of self-interstitials, which are excess ($a_I > 1$) in the region of low concentration. In the case of one-stage diffusion with a constant impurity concentration at the surface (C_s = const), the self-interstitial supersaturation is determined by the expression (see [14])

$$a_I(x) = \frac{1 + k_{IF}C_s p_s}{1 + k_{IF}Cp}, \quad (4)$$

where $k_{IF} = k_I k_F$, k_I is the equilibrium constant of the self-interstitial-recharge reaction ($I^0 + h^+ \longleftrightarrow I^+$), $1/k_I = N_V\exp[-(E^+_I - E_V)/kT]$, N_V is the effective density of states in the valence band, $(E^+_I - E_V)$ is the energy of the level of a positively charged self-interstitial with respect to the top of the valence band, k_F is the equilibrium constant of the reaction of generation of neutral BI pairs ($\mathrm{B}^- + I^+ \longleftrightarrow \mathrm{B}I^0$), $k_F = k_{F0}\exp(E_b/kT)$, and E_b is the binding energy. In this case, boron diffusion can be described by the ordinary diffusion equation

$$\frac{\partial C}{\partial t} = \frac{\partial}{\partial x}\left(hD\frac{\partial C}{\partial x}\right), \quad (5)$$

where h is the factor of diffusion enhancement by the internal electric field, with the diffusivity defined by expressions (2)–(4); this factor depends not only on the local impurity and carrier concentrations but also on the corresponding surface concentrations.

Parameters. The data on the isoconcentration boron diffusion [1–3] were used in the SUPREM-3 code [4] to find $D^0_i = 0.037\exp(-3.4/kT)$ and $D^+_i = 0.23\exp(-3.4/kT)$. Even at low boron concentrations ($C_{\mathrm{B}} < n_i$), the second term, corresponding to the diffusion via positively charged IPDs, dominates in expression (1). The self-diffusion coefficient of boron at low concentrations was refined in [15]: $D_i = 7.87\exp(-3.75/kT)$. The relative fraction (f^+_I) of the interstitial component in the boron diffusion at low concentrations was estimated at 0.5–0.98 in [16–18]. Preferring the results of later studies [17, 18], we assumed f^+_I and f^+_V to be 0.9 and 0.1, respectively. The energy level of positively charged self-interstitials in the silicon band gap is estimated as $E^+_I - E_V = 0.4$ eV with respect to the top of the valence band [19] or $E_c - E^+_I = 0.86$ eV with respect to the bottom of the conduction band E_c [20]. Preferring the results of the later study [20], we assumed that $E^+_I - E_V + 0.24$ eV. Thus, among all the parameters used, only k_F remains undetermined; this parameter was chosen by the best fit of the calculations to the experimental data of [5]. We disregard the boron clustering since the boron diffusion in the experiment [5] was carried out under isothermal conditions with the surface concentration $C_s \approx 7 \times 10^{19}$ cm^{-3}, which does not exceed the solubility limit.

Diffusion equation (5) with the diffusivity defined by expressions (2) and (3), taking into account expressions (1) and (4), was solved numerically using the implicit finite-difference (sweep) method [21]. The boundary condition was the condition of constant boron concentration at the surface, $C_s = 7 \times 10^{19}$ cm^{-3}, which corresponds to the experimental conditions of [5]. The boron distributions calculated within this model are shown in Fig. 1 by solid lines for $k_F = 5.5 \times 10^{-21}$ and $k_F = 4.4 \times 10^{-21}$ cm^3 (at 850 and 1000°C, respectively). The dashed curves correspond to the calculation using the SUPREM-3 code and the concentration dependence of the diffusivity (1). As can be seen in Fig. 1, the model calculation adequately describes the experimental profiles at 850°C and 1000°C, in contrast to the calculation using the SUPREM-3 code, which yields an underestimated diffusion depth, especially at a lower temperature.

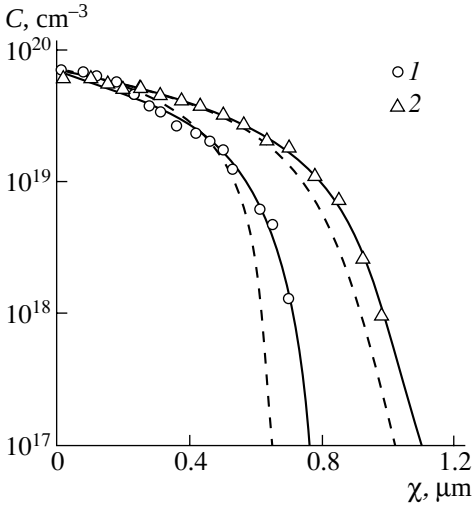

Fig. 1. Boron concentration profiles for the diffusion temperatures (*1*) 850 and (*2*) 1000°C; the diffusion time is (*1*) 48 and (*2*) 4 h; (*1*, *2*) experiment [5]; the solid and dashed curves correspond to the calculations within the model proposed and using the SUPREM-3 code, respectively.

Figure 2 compares the concentration dependences of the diffusivity determined from the experimental concentration profiles obtained in [5] with those calculated within the model with the temperature dependence of k_F in the form $k_F = 9.4 \times 10^{-22}\exp(0.17/kT)$. For comparison, Fig. 2 also shows the dependence $D(C)$ calculated at $a_V = a_I = 1$, which corresponds to dependence (1). As can be seen in Fig. 2, the model calculation satisfactorily describes the experimental dependences in the entire temperature range (800–1100°C), whereas dependence (1) yields good correspondence only at high diffusion temperatures ($T >$ 1000°C).

Comparison of the temperature dependences of the formation constants k_F of neutral impurity–interstitial pairs for boron with the temperature dependences of k_F previously determined for other dopants (phosphorus [14] and arsenic [22]) shows that the binding energy of impurity–interstitial pairs for boron (acceptor impurity) is significantly lower than that for phosphorus and arsenic (donor impurities) (0.17 and 1.65 eV, respectively). The parameter k_F for boron is of the same order of magnitude as for phosphorus at high temperatures (900–1100°C) and of the same order of magnitude as for arsenic at low temperatures (500–600°C). Taking into account the lower boron solubility in silicon in comparison with phosphorus and arsenic, this result accounts for identical features in the boron diffusion and phosphorus diffusion at high temperatures and the absence of boron diffusion from heavily doped silicon surface layers at low temperatures.

Thus, the boron diffusion in silicon at a high surface concentration was simulated on the basis of the dual pair mechanism. It was shown that the model allows one to describe both concentration profiles and the concentration dependence of the boron diffusivity, including the case of moderate temperatures (below 1000°C), at which the calculation using the SUPREM-3 code yields an underestimated diffusion depth.

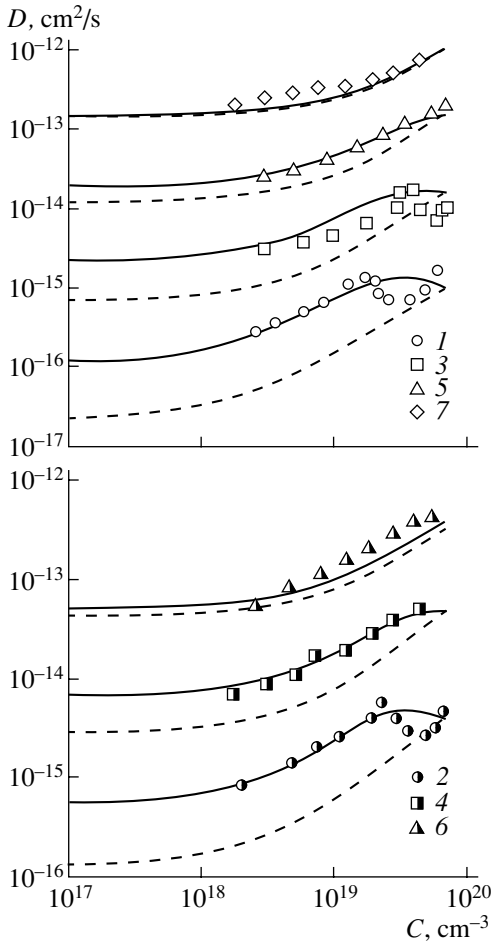

Fig. 2. Concentration dependences of the boron diffusivity for the diffusion temperatures (*1*) 800, (*2*) 850, (*3*) 900, (*4*) 950, (*5*) 1000, (*6*) 1050, and (*7*) 1100°C. Symbols *1–7* represent the experimental data of [5], and the solid and dashed curves correspond to the model calculations and dependence (1) ($a_V = a_I = 1$), respectively.

REFERENCES

1. R. B. Fair and P. N. Pappas, J. Electrochem. Soc. **122**, 1241 (1975).
2. R. B. Fair, in *Impurity Doping Processes in Silicon*, Ed. by F. F. Y. Wang (North-Holland, New York, 1981), p. 315.
3. A. F. W. Willoughby, A. G. R. Evans, P. Champ, *et al.*, J. Appl. Phys. **59**, 2392 (1986).
4. C. P. Ho, J. D. Plummer, S. E. Hansen, and R. W. Dutton, IEEE Trans. Electron Devices **30**, 1438 (1983).
5. S. Matsumoto, Y. Ishikawa, Y. Shirai, and T. Niimi, J. Appl. Phys. **19**, 217 (1980).

6. V. A. Panteleev, V. I. Okulich, A. S. Vasin, and V. A. Gusarov, Izv. Akad. Nauk SSSR, Neorg. Mater. **21**, 1253 (1985).
7. B. Garben, W. A. Orr Arienzo, and R. F. Lever, J. Electrochem. Soc. **133**, 2152 (1986).
8. J. R. Anderson and J. F. Gibbons, Appl. Phys. Lett. **28**, 184 (1976).
9. W. A. Orr Arienzo, R. Glang, R. F. Lever, and R. K. Lewis, J. Appl. Phys. **63**, 116 (1988).
10. J. Mulvaney and W. B. Richardson, Appl. Phys. Lett. **51**, 1439 (1987).
11. D. Mathiot and S. Martin, J. Appl. Phys. **70**, 3071 (1991).
12. B. Baccus, T. Wada, N. Shiguo, *et al.*, IEEE Trans. Electron. Devices **39**, 648 (1992).
13. K. Ghaderi and G. Hobler, J. Electrochem. Soc. **142**, 1654 (1995).
14. O. V. Aleksandrov, Fiz. Tekh. Poluprovodn. (St. Petersburg) **35**, 1289 (2001) [Semiconductors **35**, 1231 (2001)].
15. Y. M. Haddara, B. T. Folmer, M. E. Law, and T. Buyuklimanli, Appl. Phys. Lett. **77**, 1976 (2000).
16. P. M. Fahey, P. B. Griffin, and J. D. Plummer, Rev. Mod. Phys. **61**, 289 (1989).
17. P. A. Packan and J. D. Plummer, J. Appl. Phys. **68**, 4327 (1990).
18. A. Ural, P. B. Griffin, and J. D. Plummer, J. Appl. Phys. **85**, 6440 (1999).
19. W. Frank, Inst. Phys. Conf. Ser. **23**, 23 (1975).
20. V. V. Luk'yanitsa, Fiz. Tekh. Poluprovodn. (St. Petersburg) **37**, 422 (2003) [Semiconductors **37**, 404 (2003)].
21. A. A. Samarskiĭ, *The Theory of Difference Schemes* (Nauka, Moscow, 1977).
22. O. V. Aleksandrov, Fiz. Tekh. Poluprovodn. (St. Petersburg) **36**, 392 (2002) [Semiconductors **36**, 370 (2002)].

Translated by A. Kazantsev

Semiconductors, Vol. 38, No. 3, 2004, pp. 262–265. Translated from Fizika i Tekhnika Poluprovodnikov, Vol. 38, No. 3, 2004, pp. 274–277.

ATOMIC STRUCTURE AND NONELECTRONIC PROPERTIES OF SEMICONDUCTORS

Chromium Diffusion in Gallium Arsenide

S. S. Khludkov*, O. B. Koretskaya, and A. V. Tyazhev

Kuznetsov Physicotechnical Institute, pl. Revolyutsii 1, Tomsk, 634050 Russia

**e-mail: kanc@spti.tsu.ru*

Submitted March 3, 2003; accepted for publication June 25, 2003

Abstract—Chromium diffusion in GaAs was studied by measuring the thickness of high-resistivity layers formed during diffusion of chromium (a deep acceptor) in *n*-GaAs. The dependence of the chromium diffusivity in GaAs on the temperature, arsenic-vapor pressure, conductivity type, and carrier density was determined. The temperature dependence of the diffusivity is described by the Arrhenius equation with the parameters $D_0 = 8 \times 10^9$ cm^2/s and $E = 4.9$ eV. The dependence of the diffusivity on the arsenic-vapor pressure is described by the expression $D \propto P_{\mathrm{As}_4}^{-m}$, where $m \approx 0.4$. The experimental data obtained are interpreted in terms of the concept of the dissociative mechanism of migration of Cr atoms in GaAs. © *2004 MAIK "Nauka/Interperiodica".*

Chromium impurity atoms in GaAs form deep acceptor centers with an energy level near the midgap, which makes it possible to obtain semi-insulating GaAs with a conductivity that is close to intrinsic. GaAs-based structures doped by diffusion of Cr find application in the production of many devices, such as avalanche diodes; photodetectors; and detectors of high-energy charged particles, X-rays, and gamma-ray photons [1–4].

Chromium diffusion in GaAs was studied in [5–10]. However, the published data on chromium diffusion in GaAs are notable for their wide spread and ambiguous interpretation. In this paper, we report the results of studies of Cr diffusion in *n*-GaAs over a wide range of diffusion parameters (diffusion from an infinite source is considered). The diffusivity was determined by measuring the thickness of high-resistivity layers formed by diffusion of chromium into GaAs. The mechanism of migration of Cr atoms in GaAs is discussed.

We studied samples of GaAs grown by the Czochralski method from flux. The electron density n at room temperature ranged from 10^{16} to 3×10^{17} cm^{-3}. Chromium diffusion was carried out from a deposited layer in evacuated quartz cells. The diffusion temperature was varied within T = 900–1180°C, and the arsenic-vapor pressure was P_{As_4} = 0.01–3 atm. The arsenic-vapor pressure in a cell was set by the value of arsenic weight calculated from the ideal-gas equation under the assumption that arsenic tetramers dominate in vapor.

The condition for producing high-resistivity Cr-compensated GaAs can be written as

$$N_{\mathrm{Cr}} \geq N_D,$$

where N_{Cr} is the concentration of electrically active Cr atoms,

$$N_D = N_D^{\Sigma} - N_A^{\Sigma} = n$$

is the concentration of uncompensated shallow donors at $T \approx 300$ K, N_D^{Σ} is the total donor concentration, and N_A^{Σ} is the total concentration of background acceptors. The diffusion conditions were such that the Cr concentration at the diffusion-layer surface would have exceeded the concentration of uncompensated shallow donors in GaAs. As a result, Cr diffusion resulted in high-resistivity layers with a resistivity up to 10^9 Ω cm and a thickness d from several to 1000 μm. The thickness of the high-resistivity layer was determined by anodic oxidation of a transverse cleavage in wafers and by measuring the breakdown voltage of a contact probe on an angle lap. Chromium diffusion into GaAs at each temperature was carried out for various times with various electron densities n. The data obtained were used to construct the dependences of the thickness of the high-resistivity layer on the diffusion time ($d = f(t^{1/2})$) and on the electron density ($d = f(n)$).

The diffusivity D was determined using two methods: from the time dependence of the diffusion-layer thickness (using the expression $d = 2\sqrt{Dt}$) and from the dependence of d on the concentration of uncompensated donors, $d = f(N_D = n)$. We should note that the dependence $d = f(n)$ is a diffusion profile of electrically active Cr atoms, $N_{\mathrm{Cr}} = f(x)$. As an example, Fig. 1 shows one of such profiles. We can see in Fig. 1 that the experimental points satisfactorily fall on the theoretical curve in the case of diffusion from an infinite source (the erfc function), which makes it possible to determine the diffusivity from the dependence $N_{\mathrm{Cr}} = f(x)$. Both methods yielded similar values of diffusivity.

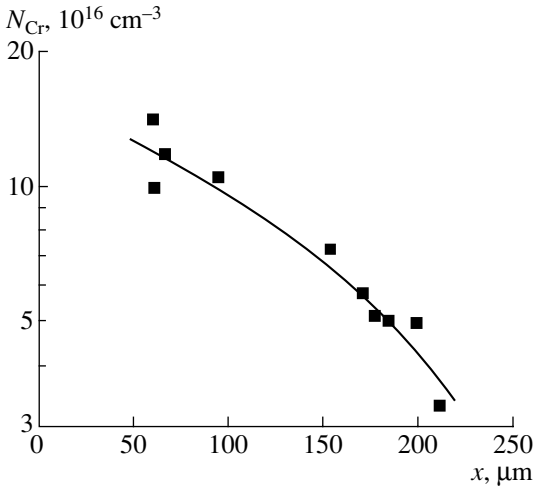

Fig. 1. Diffusion concentration profile of electrically active Cr atoms in GaAs. The diffusion parameters are T = 1100°C, t = 1 h, and P_{As_4} = 1 atm. Squares represent the experimental data, and the curve is the erfc(x) function.

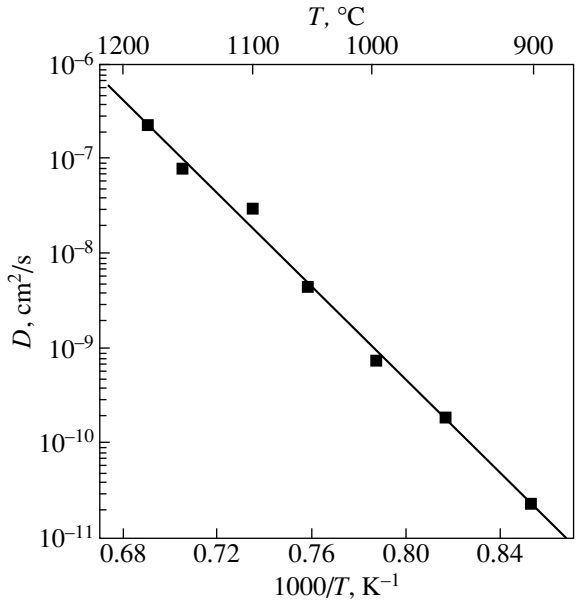

Fig. 2. Temperature dependence of the Cr diffusivity in GaAs at the arsenic-vapor pressure P_{As_4} = 1 atm.

The temperature dependence of the Cr diffusivity in GaAs at P_{As_4} = 1 atm, determined using the aforementioned technique, is shown in Fig. 2. Each experimental point in Fig. 2 is an average over ten (or more) experimental values. The experimental points fall nicely on the Arrhenius curve

$$D = D_0 \exp(-E/kT) \quad (1)$$

with $D_0 = 8 \times 10^9$ cm^2/s and E = 4.9 eV.

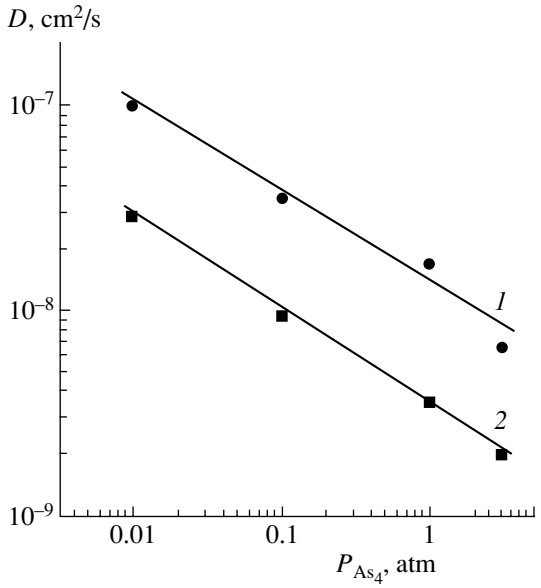

Fig. 3. Dependences of the Cr diffusivity on the arsenic-vapor pressure at T = (*1*) 1100°C and (*2*) 1050°C.

The dependence of the Cr diffusivity in GaAs on the arsenic-vapor pressure, determined at 1050 and 1100°C, is shown in Fig. 3. We can see that the diffusivity decreases as the arsenic-vapor pressure increases as

$$D \propto P_{As_4}^{-m}, \quad (2)$$

where $m \approx 0.4$. If the GaAs wafer was covered by a SiO_2 film, the diffusivity was almost independent of the arsenic-vapor pressure at which chromium diffusion was carried out, and the diffusivity corresponded to a low pressure of arsenic vapor.

An analysis of the diffusion profiles obtained for chromium diffusion in GaAs with various electron densities made it possible to determine the solubility limit of electrically active Cr atoms in GaAs. Its value corresponds to the surface concentration of the bulk region of the diffusion profile; it is equal to $\sim 1.5 \times 10^{17}$ cm^{-3} at T = 1100–1150°C and P_{As_4} = 1 atm.

The diffusion of Cr was studied in p^+–n structures by analogy with [11]. The chromium diffusivity in p^+-GaAs was determined. To this end, we used a set of structures with different thicknesses of the p^+-layer, prepared by Zn diffusion, with the following parameters:

$$d_{p^+} = 20\text{–}80\ \mu\text{m}, \quad p^+ \approx 10^{20}\ \text{cm}^{-3}, \quad n = 10^{17}\ \text{cm}^{-3}.$$

Chromium diffusion was carried out from the p^+-layer side at 1050°C and P_{As_4} = 1 atm. The technique described in [11] was used to determine the ratio of the Cr diffusivities in p^+-GaAs (D_p) and n-GaAs (D_n), which was found to be $D_p/D_n = 2$. These data allow us to ascertain the migration mechanism of Cr atoms in GaAs.

Let us analyze the data on the Cr diffusion in GaAs obtained in this study and [5–10].

According to [7, 8], the diffusion profile of Cr in GaAs, determined by the isotopic method and mass spectrometry, consists of two regions (bulk and surface). Each of them can be approximately described by the erfc function. The surface-region thickness is about 10–20% of the total thickness of the diffusion layer. The surface Cr concentration for the bulk region at T = 1100°C is ~5×10^{16} cm^{-3} [7, 8] and ~1.5×10^{17} cm^{-3} (this study); for the surface region, this value is (3–5) × 10^{17} cm^{-3} [8] and 10^{18}–10^{19} cm^{-3} [7]. The values of the Cr diffusivity in GaAs at the same temperature reported in [5–10] differ by three orders of magnitude. The corresponding activation energies of diffusion are also substantially different. This data spread can be explained by the fact that the experimental conditions of [5–10] were not completely listed (or met).

The main experimental parameters for GaAs should include the temperature, time, arsenic-vapor pressure, and dopant source (from a surface metal layer or gas phase). The method and conditions of the crystal growth, which control the GaAs stoichiometry, as well as the method (radioisotopic or electric) for determining the impurity distribution, should also be taken into account.

The spread of the diffusivity values in the literature can also be caused by the fact that this parameter was determined in different regions (bulk or surface). Moreover, "jumps" from one region to another could occur in various temperature ranges in some studies. The data spread could also be caused by the following factor. In the case of layer-by-layer measurements of the Cr distribution, one more diffusion region (with a corresponding diffusivity) may arise in the diffusion layer due to the deeper penetration of Cr into the regions containing dislocation clusters.

Let us now consider the mechanism of Cr diffusion in GaAs. In many studies [11–17], it was convincingly shown that acceptor impurities substituting group-III atoms in III–V compounds, including impurities of transition elements Zn, Cu, Fe, and Mn in GaAs, migrate via the dissociative mechanism. In this case, a major portion of impurity atoms are located in sites, but a certain minor portion of them are in interstices. The ratio of the numbers of atoms in sites and interstices is controlled by the impurity type; the semiconductor-lattice properties; and the diffusion conditions: arsenic-vapor pressure, Fermi level position in the semiconductor at the diffusion temperature, and some other factors. When the impurity diffusion is not limited by vacancy migration and the atomic flux via interstices significantly exceeds that via sites, the effective diffusivity of impurity atoms in the case of the dissociative diffusion mechanism can be written in the form (see [12])

$$D = \frac{D_i}{1 + \alpha}, \qquad (3)$$

where D_i is the coefficient of diffusion via interstices and $\alpha = N_s/N_i$ is the ratio of the concentrations of impurity located in sites and interstices. The dynamic equilibrium between the charged impurity atoms in sites (N_s) and interstices (N_i) shifts, depending on the Fermi level position in a semiconductor. Hence, for singly charged impurity atoms in a p-type semiconductor, we can write (see [12, 16])

$$N_s = N_s^i \frac{n_i}{p}, \quad N_i = N_i^i \frac{p}{n_i}, \quad \alpha = \alpha_i \left(\frac{n_i}{p}\right)^2, \qquad (4)$$

where n_i and p are the carrier densities in the intrinsic and p-type semiconductors, respectively, at the diffusion temperature; N_s^i and N_i^i are the concentrations of impurity atoms in sites and interstices in the intrinsic semiconductor, respectively; and $\alpha_i = N_s^i/N_i^i$. It follows from formulas (3) and (4) that, in the case of the dissociative mechanism of impurity diffusion in the p-type semiconductor, the coefficient α should decrease and the diffusivity should increase in comparison with the intrinsic semiconductor (at the diffusion temperature). Formulas (3) and (4) were used to estimate the coefficients α and α_i for Cr in GaAs under the aforementioned experimental conditions (1050°C, P_{As_4} = 1 atm) using the values

$$D_{p^+}/D_n = 2, \quad N_s = 2 \times 10^{17} \text{ cm}^{-3},$$
$$p^+ = 10^{20} \text{ cm}^{-3}, \quad D_i = 10^{-5} \text{ cm}^2/\text{s}.$$

Here, the diffusivity corresponds to Cu diffusion via interstices in GaAs [12]. In this case, GaAs with n = 10^{17} cm^{-3} at the diffusion temperature takes on the intrinsic conductivity type with the carrier density n_i = 10^{18} cm^{-3}. An estimate showed that $\alpha_i = 10^7$ and $\alpha = 10^3$ for Cr in GaAs. Thus, a certain redistribution of Cr atoms (increase in the interstitial component) and a certain enhancement of Cr diffusion occur in p^+-GaAs, which is in agreement with the dissociative diffusion mechanism.

In the case of the dissociative mechanism, a change in the arsenic-vapor pressure should lead to the following dependence of the concentration of interstitial impurity atoms and the diffusivity (see [6, 17]):

$$N_i \propto P_{As_4}^{-1/4} \text{ and } D \propto P_{As_4}^{-1/4}. \qquad (5)$$

The experimental dependence of the Cr diffusivity in GaAs on the arsenic-vapor pressure (Fig. 3) qualitatively agrees with the theoretical dependence in the case of the dissociative mechanism.

The independence of the Cr diffusivity on P_{As_4} in the case of GaAs wafers covered by a SiO_2 film suggests the following. Experimental data on diffusion in the Si–SiO_2 system show that SiO_2 is a good mask for As impurity. Therefore, in our experiment, the SiO_2

film on GaAs should prevent penetration of As into the GaAs wafer and, as a result, retain the ratio of Ga and As vacancies established during the crystal growth. The crystal growth, most likely, was accompanied by a deviation from stoichiometry (arsenic deficiency), and the vacancy equilibrium corresponded to that occurring upon annealing at a low arsenic-vapor pressure.

Thus, the studies carried out allowed us to determine the dependence of the Cr diffusivity in GaAs on temperature, arsenic-vapor pressure, conductivity type, and charge density in the case of diffusion from a deposited layer at strictly controlled parameters of the diffusion process. The data on the effect of the conductivity type, carrier density, and arsenic-vapor pressure on the Cr diffusivity in GaAs suggest the dissociative mechanism of Cr impurity diffusion in GaAs.

ACKNOWLEDGMENTS

This study was supported by the Russian Foundation for Basic Research, project no. 00-02-17930, and the International Scientific and Technical Center, project no. 1107.

REFERENCES

1. C. S. Khludkov and O. P. Tolbanov, Fiz. Tekh. Poluprovodn. (Leningrad) **14**, 1624 (1980) [Sov. Phys. Semicond. **14**, 963 (1980)].
2. C. S. Khludkov, O. P. Tolbanov, and D. L. Budnitskiĭ, Izv. Vyssh. Uchebn. Zaved., Fiz. **41** (8), 39 (1998).
3. S. S. Khludkov, O. P. Tolbanov, and V. E. Stepanov, J. Phys. D: Appl. Phys. **29**, 1559 (1996).
4. G. I. Ayzenshtat, N. N. Bakin, D. L. Budnitsky, *et al.*, Nucl. Instrum. Methods Phys. Res. A **466**, 25 (2001).
5. C. S. Khludkov, G. A. Prikhod'ko, and T. N. Karelina, Izv. Akad. Nauk SSSR, Neorg. Mater. **8**, 1044 (1972).
6. N. C. Casey, in *Atomic Diffusion in Semiconductors*, Ed. by D. Shaw (Plenum, London, 1973; Mir, Moscow, 1975).
7. N. V. Gontar', L. B. Gorodnik, A. V. Emel'yanov, *et al.*, in *Properties of Doped Semiconductors* (Nauka, Moscow, 1977), p. 31.
8. B. Tuck and A. Adegboyega, J. Phys. D: Appl. Phys. **12**, 1895 (1979).
9. J. Kasahara and N. Watanabe, Jpn. J. Appl. Phys. **19** (3), L15 (1980).
10. M. D. Deal and D. A. Stevenson, J. Appl. Phys. **59**, 2398 (1986).
11. C. S. Khludkov and N. V. Chaldysheva, Izv. Vyssh. Uchebn. Zaved., Fiz. **25** (5), 115 (1982).
12. R. H. Hall and J. H. Raccete, J. Appl. Phys. **35**, 379 (1964).
13. B. I. Boltaks, S. I. Rembeza, and M. K. Bakhadyrkhanov, Fiz. Tekh. Poluprovodn. (Leningrad) **10**, 432 (1968).
14. B. I. Boltaks, G. S. Kulikov, I. M. Nikulina, and F. S. Shishiyanu, Izv. Akad. Nauk SSSR, Neorg. Mater. **11**, 348 (1975).
15. *Atomic Diffusion in Semiconductors*, Ed. by D. Shaw (Plenum, London, 1973; Mir, Moscow, 1975).
16. W. Shockley and J. L. Moll, Phys. Rev. **119**, 1480 (1960).
17. B. I. Boltaks, *Diffusion and Point Defects in Semiconductors* (Nauka, Leningrad, 1972).

Translated by A. Kazantsev

Semiconductors, Vol. 38, No. 3, 2004, pp. 266–272. Translated from Fizika i Tekhnika Poluprovodnikov, Vol. 38, No. 3, 2004, pp. 278–284.

ATOMIC STRUCTURE AND NONELECTRONIC PROPERTIES OF SEMICONDUCTORS

Special Features of Sb_2 and Sb_4 Incorporation in MBE-Grown AlGaAsSb Alloys

A. N. Semenov*^, V. S. Sorokin, V. A. Solov'ev*, B. Ya. Mel'tser*, and S. V. Ivanov***

**Ioffe Physicotechnical Institute, Russian Academy of Sciences, Politekhnicheskaya ul. 26, St. Petersburg, 194021 Russia*
^e-mail: semenov@beam.ioffe.rssi.ru
***St. Petersburg Electrotechnical University, St. Petersburg, 197376 Russia*
Submitted July 14, 2003; accepted for publication July 16, 2003

Abstract—AlGaAsSb and GaAsSb alloys of different composition were grown by molecular-beam epitaxy (MBE) on GaSb, InAs, and GaAs substrates, using both conventional and cracker antimony effusion cells. The incorporation coefficients of dimer and tetramer antimony molecules, which totally describe the kinetic processes on the growth surface, were calculated. The differences in the incorporation of Sb_2 and Sb_4 molecules in MBE-grown GaAsSb alloys are shown. The effect of the MBE-growth parameters (substrate temperature and incident fluxes of group-V and group-III elements) on the composition of (Al,Ga)AsSb alloys and the incorporation coefficient of Sb was studied in detail. The incorporation coefficients of tetramer and dimer antimony molecules were found to vary over a wide range, depending on the substrate temperature and the ratio between the arrival rates of the group-III and the group-V elements. © *2004 MAIK "Nauka/Interperiodica".*

1. INTRODUCTION

A conventional Knudsen effusion cell used in molecular-beam epitaxy (MBE) of III–V compounds provides atomic fluxes only for group-III elements, whereas group-V elements are evaporated in the form of tetramers. However, it is well known that the growth of III–V compounds using dimers of metal components has certain advantages [1]. Therefore, in order to obtain fluxes of dimers of group-V elements in modern MBE systems, cracker effusion cells are used, which provide dissociation of tetramers in an additional high-temperature zone of special design.

The use of cracker effusion cells makes it possible to attain more intense interaction of molecules with the growth surface and substantially improve the electric and optical characteristics of semiconductor heterostructures. These advantages are especially pronounced in the case of heterostructures on the basis of antimonides of group-III elements [2]. As is well known, nominally undoped GaSb layers have *p*-type conductivity, which is, most likely, due to intrinsic defect complexes (a Ga vacancy and a Ga atom substituting a Sb atom in the Sb sublattice). As a rule, the residual hole density is no less than 10^{16} cm^{-3}. In conventional epitaxy, antimony tetramers (Sb_4), which are dominant upon evaporation of elemental antimony, have low mobility on the growth surface and tend to form clusters and precipitates. This circumstance leads, on the one hand, to an increase in the number of unoccupied Sb sites on the growth surface, which are occupied by Ga atoms [3], and, on the other hand, to the appearance of local areas with a rather high concentration of Ga vacancies. Hence, the use of more mobile dimers (Sb_2) or Sb atoms leads to a decrease in the concentration of point defects. However, the effect of the composition of fluxes of group-V elements on the composition of multicomponent alloys and the incorporation coefficients of metal components has not been adequately studied.

In this study, we get insight into the physicochemical aspects of the MBE of multicomponent AlGaAsSb and GaAsSb alloys (which have the same period as InAs and GaSb) grown using both conventional arsenic and antimony effusion cells (As_4 and Sb_4) and a cracker antimony effusion cell (Sb_2). It is noteworthy that the problem of the composition control as applied to (Al,Ga)AsSb alloys was studied previously in [4–13], but, in these studies, combinations of either cracker (As_2 and Sb_2) [4–8] or conventional (As_4 and Sb_4) [11–14] effusion cells were used. The features of the epitaxy of (Al,Ga)AsSb alloys using a conventional source of Sb_4 and a cracker source of As_2 were also studied [9, 10], but the reverse combination (a cracker source of Sb_2 and a conventional source of As_4) has not been investigated. Here, we studied experimentally the distinctive features of the incorporation of Sb_2 and Sb_4 molecules in MBE-grown (Al,Ga)AsSb alloys and estimated the incorporation coefficients of these molecules in (Al,Ga)AsSb alloys grown using an As_4 source.

2. METHOD FOR ESTIMATING INCORPORATION COEFFICIENTS

The difficulties in controlling the composition of multicomponent solid solutions containing two volatile group-V components are due to their strong competition upon incorporation in a metal sublattice. In this case, the search for the regularities in controlling the

composition of AlGaAsSb alloys can be performed only in terms of kinetic concepts. The main parameters determining the composition of the metal sublattice of an alloy are the incorporation coefficients of antimony and arsenic. The incorporation coefficient is defined as the ratio of the number of atoms of the *i*th element incorporated in the crystal lattice to the total number of incident atoms of this element. It should be noted that direct measurements of the incorporation coefficients are not always possible since they require one to adapt the growth chamber and replace one of the sources of molecular beams with a mass spectrometer to measure fluxes of particles desorbed from the substrate. At the same time, it is well known that the composition of the metal sublattice of an MBE-grown $Al_xGa_{1-x}As_ySb_{1-y}$ alloy is determined by the ratio of the incorporation rate of As to the total incorporation rate of metal atoms. The latter parameter, in turn, is determined by the incorporation rate of group-III atoms. Taking into account this circumstance, the relationship between the content of As in the metal sublattice *y* with the incorporation coefficient of Sb, α_{Sb}, can be written as

$$y = 1 - \frac{\alpha_{Sb_j} J_{Sb_j}}{J_{III}}, \quad (1)$$

where J_{Sb_j} is the incident flux of Sb molecules ($j = 2$ and 4 for Sb dimers and tetramers, respectively) and J_{III} is the flux of group-III atoms. In this case, $\alpha_{Sb}J_{Sb}$ can be considered as an effective flux of Sb atoms, thermalized on the growth surface. The incorporation coefficients of group-III atoms at MBE-growth temperatures typical of antimonides (480–550°C) can be assumed equal to unity [15]. Readings of an ionization sensor used to measure fluxes are proportional to the intensity of molecular fluxes at a substrate:

$$P_i^* = \eta_i K_i^* P_i = K^* \eta_i J_i \sqrt{2\pi m_i k T_i}, \quad (2)$$

where P_i^* is the equivalent molecular-beam pressure measured by a Bayard–Alpert gauge, η_i is the relative sensitivity of the gauge, P_i is the partial vapor pressure, m_i is the mass of evaporated particles, T_i is the evaporator temperature, k is the Boltzmann constant, and K^* is the empirical constant taking into account the specific features of the gauge used. In this study, the constant K^*, which was carefully determined from the layer-growth rate, amounted to 0.158. The relative sensitivity of the Bayard–Alpert gauge, according to the data of [16], is determined by the empirical expression

$$\eta_i = \frac{0.6Z_i}{14} + 0.4, \quad (3)$$

where Z_i is the number of electrons in the *i*th atom (or molecule). The sensitivity of the Bayard–Alpert gauge, calculated according to (3), is $\eta_{Sb_2} \approx 4.77$ for Sb dimers, $\eta_{Sb_4} \approx 9.14$ for Sb tetramers, $\eta_{Al} \approx 0.96$ for Sb atoms, and $\eta_{Ga} \approx 1.73$ for Ga atoms.

With regard to these data, the incorporation coefficient of antimony can be determined from the measured values of equivalent pressures in molecular beams and the alloy composition as

$$\alpha_{Sb_j} = (1-y)\frac{\eta_{Sb_j}}{\eta_{III}}\frac{P_{III}}{P_{Sb}}\frac{\sqrt{m_{Sb_j}T_{Sb}}}{\sqrt{m_{III}T_{III}}}. \quad (4)$$

3. EXPERIMENTAL

The structures under investigation were grown on an MBE RIBER 32P system equipped with conventional effusion cells for all sources, except for the Sb source. To evaporate antimony, we used both a conventional effusion cell and an RB-075-Sb cracker source, which provides, depending on the temperature in the cracker zone, fluxes of Sb tetramers, dimers, or atoms. Before the growth, fluxes were calibrated by a Bayard–Alpert gauge for each structure.

The (Al,Ga)AsSb alloys were MBE-grown on InAs(100) and GaSb(100) substrates and, in some cases, on GaAs. The thickness of epitaxial layers was generally about 1 μm. Three sets of experiments were performed using a cracker Sb source. In the first set (*A*), the epitaxial layers were grown in different arsenic fluxes, with the other parameters being constant; in the second set (*B*), only the Sb flux was changed; and, in the third set (*C*), epitaxy was performed at different substrate temperatures T_s. The cracking-zone temperature was maintained at 920°C, which provided almost complete dissociation of Sb tetramers into dimers. In addition, layers of (Al,Ga)AsSb alloys were grown using a conventional Sb effusion cell (Sb_4). The fluxes of group-III elements were constant (1.35×10^{14} cm^{-2} s^{-1}) for all the structures and corresponded to a deposition rate of ~0.25 monolayers per second for both Ga and Al. The equal intensities of incident Ga and Al fluxes provided identical contents of these elements in the grown layers.

The composition of the grown alloys was determined using a CAMEBAX X-ray spectral microanalyzer and by double-crystal X-ray diffractometry (XRD). The microanalysis data on the composition of the metal components were used in the analysis and simulation of the XRD rocking curves for more exact determination of the lattice mismatch between an epitaxial layer and a substrate: we chose the composition of the metal sublattice providing the best agreement between the experimental and calculated XRD rocking curves. The simulation was performed under the assumption of pseudomorphic phase matching or complete relaxation of elastic stresses, depending on the ratio between the real thickness of an epitaxial layer and the critical thickness for the given lattice mismatch $\Delta a/a$. The critical thicknesses were calculated by the

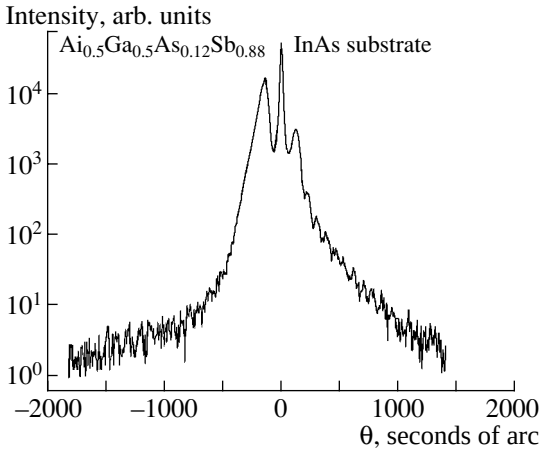

Fig. 1. θ–2θ-XRD rocking curve for a AlGaAsSb layer grown on an InAs(100) substrate at T_s = 480°C.

equilibrium-strain model [17] and corrected with regard to the experimental data in the literature.

A typical XRD rocking curve is shown in Fig. 1. Along with the substrate peak, the curve contains a peak located at $\theta \approx -200$ ($\Delta a/a \approx 10^{-3}$), which is due to the diffraction from the $Al_{0.5}Ga_{0.5}As_ySb_{1-y}$ layer. Along with the small lattice mismatch, comparable values of the intensities and half-widths of the peaks from the epitaxial layer and the substrate, as well as the presence of thickness oscillations, indicate the absence of relaxation of elastic stresses in the $Al_{0.5}Ga_{0.5}As_ySb_{1-y}$ layer. The simulation of the XRD rocking curve under the assumption of pseudomorphic matching between the layer and substrate yields the value $y = 0.12$.

4. EXPERIMENTAL RESULTS

Measurements of the composition of the samples from set *A*, grown in different As fluxes, showed that, when the Sb-flux density is sufficient for stabilization of the growth surface of the AlGaSb layer by group-V atoms, changes in the As flux over a fairly wide range do not lead to a noticeable change in the composition of the metal sublattice of the AlGaAsSb alloy. The content of arsenic in the AlGaAsSb epitaxial layers amounts to ~(1–4)% in this case, depending on the growth temperature. Such a content of arsenic in epitaxial layers is typical of most Sb-containing structures grown without using a valved As effusion cell and, in essence, is the background content. We should also note that the samples grown at a ratio of the effective fluxes of the group-V and group-III elements $J_V/J_{III} > 10$ (i.e., at high As-flux densities) had a dull surface with worse morphology in comparison with the samples grown at $J_V/J_{III} \sim 1$. Along with the deterioration of the surface morphology at $J_V/J_{III} > 10$, we also observed an increase in the half-width and a decrease in the intensity of diffraction peaks on the X-ray rocking curves. A more significant deterioration of the morphology and structural quality was observed for samples grown on InAs substrates at T_s = 540°C. Apparently, 540°C is too high for the InAs buffer layer and a significant increase in the As flux is required to maintain the stoichiometry on the growth surface. At this temperature and the As pressure corresponding to $J_V/J_{III} \approx 1$ at $T_s < 500$°C, the surface of the InAs buffer layer begins to degrade, and the initial stages of the epitaxial growth of AlGaAsSb run under nonoptimal conditions. Therefore, the samples from sets *B* and *C* were grown under the following conditions: $J_{Sb}/J_{III} \leq 0.5$–1.5, $J_{As}/J_{Sb} \approx 2$, and T_s = 480–520°C.

The equivalent Sb-flux pressures corresponding to the minimum pressure P_{Sb}^{min} necessary for the growth of $Al_{0.5}Ga_{0.5}Sb$ on a surface enriched in Sb at T_s = 480 and 520°C amounted to $\sim 1.4 \times 10^{-6}$ and $\sim 1.7 \times 10^{-6}$ Torr, respectively. This difference is due only to a change in α_{Sb} since the above temperatures are not sufficient for substantial decomposition of GaSb [18]. The values of P_{Sb}^{min} were determined from the changes in the surface reconstruction observed by high-energy electron diffraction during the epitaxy of AlSb test layers. The Sb-flux pressure determined in this way was doubled since, in the case of epitaxial growth of $Al_{0.5}Ga_{0.5}Sb$, aluminum and gallium have the same deposition rates.

For MBE-grown (Al,Ga)AsSb alloys, the material-balance equation takes the form

$$J_{III} = \alpha_{As}J_{As} + \alpha_{Sb}J_{Sb};$$

i.e., the total incorporation rate of arsenic and antimony corresponds to the incorporation rate of the group-III element. The ratio of the incorporation coefficients α_{As}/α_{Sb} depends on the intensities of the fluxes and the substrate temperature. The experimental data on the composition of the samples from sets *B* and *C* are shown in Figs. 2 and 3 as the dependences of the As content y in $Al_{0.5}Ga_{0.5}As_ySb_{1-y}$ on the equivalent Sb pressure and the growth temperature.

The experimental dependences obtained by us show that the incorporation of arsenic into the structure is significantly hindered in comparison with antimony, especially at low substrate temperatures. These results are in good agreement with data on the interchange reactions between As and Sb atoms at the InAs/GaSb interface [19–24], which indicates a significant difference in the efficiency of the As–Sb substitution when InAs and GaSb surfaces are exposed to fluxes of Sb and As atoms, respectively. It is noteworthy that, when an InAs surface is exposed to a Sb flux, an InSb layer is always formed, independent of the molecular composition of the Sb vapor. At the same time, when a GaSb surface is exposed to an As flux, a GaAs layer is formed only when the incident flux consists of As dimers [20]. Hence, the activity of Sb molecules significantly exceeds that of As molecules, not only when there is competition between the processes of incorporation of arsenic and antimony, but also when the epitaxial

growth is interrupted, except for the case when the arsenic flux consists of As_2 molecules. At the same time, analysis of the change in the composition of the solid phase as a function of the ratio of incident fluxes in terms of the thermodynamic model [25] predicts a significant dominance of arsenic in the grown layer even when the As-flux density is insignificant.

As can be seen from Fig. 2, when the Sb-flux pressure exceeds the minimum equivalent pressure required for the growth of AlGaSb on a Sb-enriched surface ($P^*_{Sb} > P^{min}_{Sb}$) in the temperature range T_s = 480–520°C, the content of As in $Al_xGa_{1-x}As_ySb_{1-y}$ layers is equal to 1–4% and, in fact, is the background content corresponding to the rather high background As pressure in the growth chamber. In this case, the background content depends mainly on the growth temperature rather than the As-flux density. This parameter is equal to 1–2% at low temperatures (~480°C) and may be as high as 8–10% at T_s = 520°C. When the Sb-flux pressure decreases below P^{min}_{Sb}, an abrupt increase in the As content in the grown layer is observed. The reason is that the effective Sb flux is now insufficient to maintain the general stoichiometry (equal contents of group-III and group-V atoms: $N_{III} = N_V$) on the growth surface in an invariable flux of group-III atoms. In this case, the growth stabilized with respect to the group-V elements is maintained by the As flux.

It is noteworthy that relaxation of elastic stresses might occur in $Al_xGa_{1-x}As_ySb_{1-y}$ layers about 1 μm thick with the As content exceeding 20% due to the large mismatch with the substrate lattice. In addition, the these compositions are within the immiscibility region characteristic of AlGaAsSb alloys at the temperatures under consideration. However, we did not observe any decomposition of alloys with compositions within the immiscibility region or any changes in the conditions for Sb incorporation in the epitaxial layers under study. No significant effect of the substrate material on the alloy composition was observed either since the samples grown under the same conditions on lattice-matched InAs and GaSb substrates and on highly mismatched GaAs substrates were of the same composition. Thus, the main factor determining the alloy composition is the Sb-incorporation coefficient.

No alloy decomposition was observed in [9] either; however, the solubility limitations manifested themselves in the hindered incorporation of arsenic in the lattice, which made it difficult to attain the center of the composition diagram of the four-component system. Apparently, for the configuration of the As_2 and Sb_4 effusion cells used in [9], the activity and reaction ability of As dimers and Sb tetramers are comparable, and epitaxial growth occurs under conditions closer to equilibrium, when the kinetic factors are not dominant and the effects of lattice-period stabilization, as well as elastic stresses, manifest themselves.

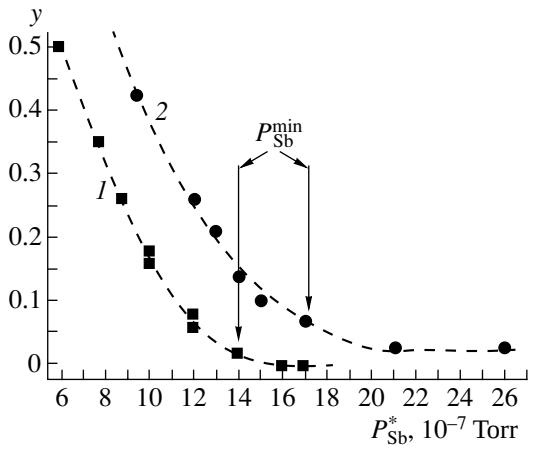

Fig. 2. Experimental dependences of the composition of an $Al_{0.5}Ga_{0.5}As_ySb_{1-y}$ alloy on the effective Sb-flux pressure at the substrate temperature T_s = (*1*) 480 and (*2*) 520°C. The vertical lines indicate the minimum Sb pressure required to stabilize the growth surface of $Al_{0.5}Ga_{0.5}Sb$ layers by the group-V elements: $P^{min}_{Sb} = 1.4 \times 10^{-6}$ and 1.7×10^{-6} Torr at 480 and 520°C, respectively. The dashed curves connect the experimental points for each temperature.

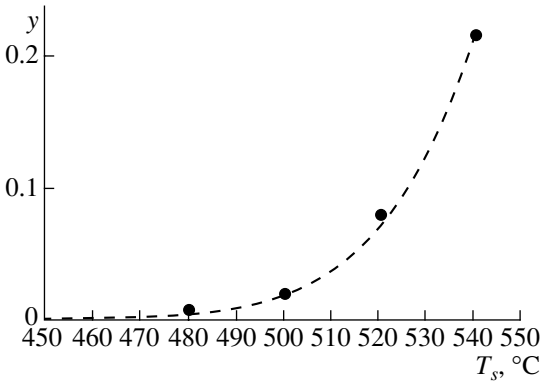

Fig. 3. Dependence of the composition of an $Al_{0.5}Ga_{0.5}As_ySb_{1-y}$ alloy on the growth temperature at constant Sb- and As-beam pressures: $P^*_{Sb} = 1.6 \times 10^{-6}$ Torr and $P^*_{As} = 4 \times 10^{-6}$ Torr; the growth rate is 0.5 monolayer/s.

The experiments show that the As content in AlGaAsSb layers can be increased by increasing the density of the fluxes of Al and Ga atoms. The reason is that, as the flux of group-III atoms increases, the antimony shortage at the interface increases and, therefore, the incorporation of excess As in unoccupied lattice sites is enhanced. The dependence of the As content on the flux of group-III atoms is described well by expression (1). These results are also in agreement with the data of [11, 12], where a similar dependence was revealed.

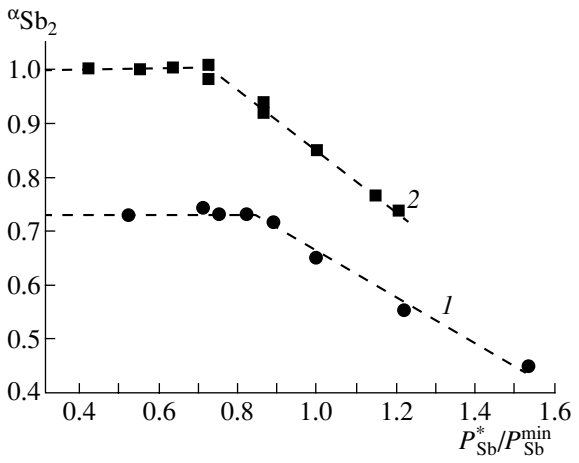

Fig. 4. Dependence of the incorporation coefficient of Sb on the P^*_{Sb}/P^{min}_{Sb} ratio for the case of MBE of AlGaAsSb alloys using Sb dimers at T_s = (*1*) 520 and (*2*) 480°C.

In the case of MBE growth of GaAsSb, significant quantitative differences in the behavior of Sb_2 and Sb_4 molecules were observed, despite the fact that the qualitative dependences of the alloy composition on the Sb flux were similar to those for AlGaAsSb (Fig. 2). The GaAsSb layers grown under the same conditions contained more arsenic when Sb_4 molecules were used. Most likely, the dissociation rate of Sb_4 molecules is significantly lower than that of Sb_2 molecules; therefore, more arsenic atoms become incorporated in the lattice in this case.

The temperature dependence of the alloy composition at fixed Sb, As, Al, and Ga fluxes is shown in Fig. 3. With an increase in T_s, an abrupt increase in the As content in the grown layer is observed. This fact can be explained as follows. Due to the lower binding energy of Sb_4 (or Sb_2) molecules, their dissociation rate significantly exceeds that of As_4 molecules. Therefore, antimony is incorporated much faster than arsenic at low temperatures, which limits the As incorporation. In this case, there are almost no unoccupied sites on the growth surface for As atoms appearing due to the dissociation (except for cases when there is a shortage of antimony). The increase in the temperature equalizes the dissociation rates of Sb_4 and As_4 molecules (since the latter have a higher activation energy). Hence, an increase in temperature leads to an increase in the number of As atoms that have time to incorporate, along with Sb atoms, in the crystal lattice. In addition, the desorption rate of antimony also increases with increasing T_s.

5. RESULTS OF CALCULATIONS

The dependences of the incorporation coefficients of Sb_2 and Sb_4 molecules on the Sb flux and the substrate temperature (the MBE parameters that determine the alloy composition in the case under consideration) are of prime interest.

It is convenient to represent the results of calculations carried out on the basis of the analysis of the experimental data and the simple model (see Section 2) in the form of the dependence of the Sb-incorporation coefficient on the ratio of the equivalent flux pressure to the minimum pressure required for the MBE growth of AlGaSb under stoichiometric conditions on the growth surface, P^*_{Sb}/P^{min}_{Sb}, rather than on P^*_{Sb}. Figure 4 shows these dependences for the coefficients of incorporation of dimers (α_{Sb2}) in AlGaAsSb alloys at two temperatures.

When the Sb flux density is low ($P^*_{Sb}/P^{min}_{Sb} \ll 1$), the incorporation coefficient of Sb, α_{Sb2}, is constant and close to unity (at low T_s). The incorporation coefficient begins to decrease at flux pressures of about (0.7–0.8)P^{min}_{Sb}. Probably, this decrease accounts for the dependence of the incorporation coefficient of Sb on the degree of coating of the layer surface by Sb atoms. Under conditions of As excess (the Sb flux amounted to ~20–30% of the general flux of group-V elements) and sufficiently high growth rates, only some of the Sb atoms have time to occupy stable positions in the metal sublattice, while the rest are occupied by As atoms. With a further increase in the Sb flux ($P^*_{Sb} > P^{min}_{Sb}$), the alloy composition does not change, being governed by the background As content (see Fig. 2); hence, the Sb incorporation coefficient decreases proportionally to the ratio P^*_{Sb}/P^{min}_{Sb}. The coefficient α_{Sb2} changes in a similar way with increasing ratio P^*_{Sb}/P^{min}_{Sb} at higher substrate temperatures as well; however, the maximum value of α_{Sb2} is significantly smaller (only ~0.73 at T_s = 520°C).

It is obvious that the incorporation coefficient of antimony, determined under conditions of its shortage on the growth surface stabilized by metal atoms, is of practical interest. In this case, α_{Sb} attains the maximum value α^{max}_{Sb} at a given temperature and is independent of the flux of antimony molecules and group-III atoms. The dependence of the maximum incorporation coefficient of Sb_2 molecules, $\alpha^{max}_{Sb_2}$, on the substrate temperature is shown in Fig. 5. At temperatures below 500°C, the coefficient $\alpha^{max}_{Sb_2}$ is close to unity. With an increase in temperature, α^{max}_{Sb} decreases. The data obtained are in good agreement with the results of [12, 13], where the behavior of antimony was analyzed and the temperature dependence of the alloy composition was studied. The characteristic activation energy is about 1.5 eV.

It is noteworthy that the Sb incorporation coefficient for Sb_4 molecules in the case of epitaxial growth of AlGaAsSb behaves in a similar way. Nevertheless, the epitaxy of GaAsSb alloys is characterized by significantly different behavior of Sb tetramers. For dimers,

the dependence of the incorporation coefficient on the ratio P^*_{Sb}/P^{min}_{Sb} in the case of epitaxial growth of GaAsSb quantitatively and qualitatively coincides with the dependence shown in Fig. 4 for the epitaxy of AlGaAsSb; i.e., α_{Sb2} is independent of the flux of group-III atoms and is close to unity over a wide range of fluxes at low temperatures. However, the results obtained using Sb tetramers indicate a decrease in the incorporation coefficient of Sb in the case of the MBE of GaAsSb (the maximum coefficient $\alpha^{max}_{Sb_4} \approx 0.6$) in comparison with the MBE of AlGaAsSb ($\alpha^{max}_{Sb_4} \approx 1$). Notably, the decrease in the incorporation coefficient is not related to the decrease in the flux of group-III atoms (see (4)) since the experiments were performed under conditions where $P^*_{Sb}/P^{min}_{Sb} < 1$ (the leveling-off portion of the α_{Sb} (P^*_{Sb}/P^{min}_{Sb}) dependence). The effect of the flux of group-III atoms on the alloy composition in the metal sublattice has not been adequately studied and requires more detailed analysis. However, with regard to the data of [8, 11], we can suggest that the decrease in the incorporation coefficient of Sb in MBE-grown GaAsSb is due to the decrease in the growth rate rather than the effect of aluminum.

The numerical values of $\alpha^{max}_{Sb_4}$ obtained in this study are, on the one hand, in good agreement with the data of [12], where it was shown that the incorporation coefficient of Sb_4 in the case of MBE of AlGaAsSb at temperatures below 500°C is close to unity. On the other hand, our results are consistent with the data of [13], where the incorporation coefficient of Sb_4 was found to be equal to 0.42 for MBE-grown GaAsSb.

The results obtained for AlGaAsSb samples grown using different As fluxes (set *A*) can be explained as follows. Since the incorporation coefficient of Sb is close to unity at low temperatures ($T_s < 500$°C) and $P^*_{Sb}/P^{min}_{Sb} < 1$, almost all incident Sb atoms are incorporated in the lattice and As atoms are incorporated only in unoccupied sites in the metal sublattice. In this case, an increase in the As flux even by an order of magnitude does not change the alloy composition, while a significant decrease in the As flux may break the epitaxial growth since the stoichiometric conditions on the grown-layer surface (the equality of the surface concentrations of group-V and group-III elements: $N^s_V/N^s_{III} \approx 1$) are no longer valid. Therefore, when As_4 molecules along with Sb_2 or Sb_4 molecules are used in the MBE growth of $Al_xGa_{1-x}As_ySb_{1-y}$ and $GaAs_ySb_{1-y}$ alloys, the most effective control of the metal-sublattice composition is obtained by changing the Sb flux at fixed values of the Al, Ga, and As fluxes and the substrate temperature.

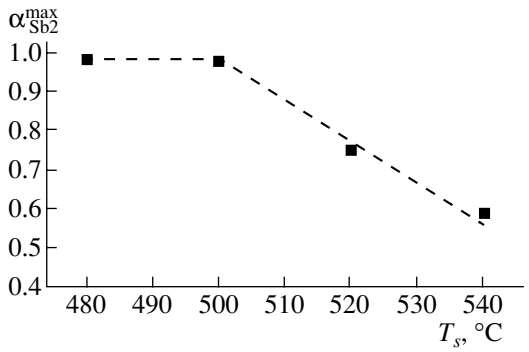

Fig. 5. Temperature dependence of the Sb_2 incorporation coefficient ($\alpha^{max}_{Sb_2}$) for the MBE of AlGaAsSb alloys. $P^*_{Sb} = 1.6 \times 10^{-6}$ Torr, $P^*_{As} = 4 \times 10^{-6}$ Torr, and the growth rate is 0.5 monolayer/s.

6. CONCLUSIONS

In this study, we report the results of studying (Al,Ga)AsSb alloys grown by MBE using both conventional and cracker Sb effusion cells. It is found that the kinetics of the surface processes, described on the whole in terms of the incorporation coefficients, most significantly affects the composition of the metal sublattice of alloys. In the range of growth temperatures from 480 to 520°C, the incorporation of antimony is dominant, which is in obvious contradiction with the thermodynamic estimates. It is shown that, when As_4 molecules are used, the alloy composition can be most effectively controlled by changing the Sb flux at fixed Al, Ga, and As fluxes and substrate temperature. The results of the calculations of the incorporation coefficients of metal components for the case of low-temperature (below ~500°C) MBE of AlGaAsSb alloys showed that, using either cracker or conventional Sb effusion cells, the incorporation coefficient of Sb is close to unity. For the MBE of GaAsSb alloys, it is found that the incorporation coefficient of Sb tetramers is smaller than that of Sb dimers. It is shown that the value of the incident flux of group-III elements significantly affects the incorporation coefficient of Sb tetramers.

ACKNOWLEDGMENTS

We are grateful to M.V. Baĭdakova for carrying out the X-ray diffraction measurements.

This study was supported by the Russian Foundation for Basic Research, project no. 01-02-17933, and the Volkswagen Foundation.

REFERENCES

1. S. A. Barnet and I. T. Ferguson, in *Handbook of Thin Film Process Technology*, Ed. by D. A. Glocker and S. I. Shah (Inst. Phys., Bristol, 1995), p. A2.0:1.

2. X. Qianghua, J. E. Van Nostrand, R. L. Jones, *et al.*, J. Cryst. Growth **207**, 255 (1999).
3. D. Effer and P. J. Etter, J. Phys. Chem. Solids **25**, 451 (1964); M. Ichimura, K. Higuchi, Y. Hattori, and T. Wada, J. Appl. Phys. **68**, 6153 (1990).
4. E. Hall, H. Kroemer, and L. A. Coldren, J. Cryst. Growth **203**, 447 (1999).
5. S. Simanowski, M. Walther, J. Schmitz, *et al.*, J. Cryst. Growth **201–202**, 849 (1999).
6. G. Almuneau, E. Hall, S. Mathis, and L. A. Coldren, J. Cryst. Growth **208**, 113 (2000).
7. P. Gopaladasu, J. L. Cecchi, K. J. Malloy, and R. Kaspi, J. Cryst. Growth **225**, 556 (2001).
8. E. Selvig, B. O. Fimland, T. Skauli, and R. Haakenaasen, J. Cryst. Growth **227**, 562 (2001).
9. H. R. Blank, S. Mathis, E. Hall, *et al.*, J. Cryst. Growth **187**, 18 (1998).
10. L. R. Dawson, J. Vac. Sci. Technol. B **4**, 598 (1986).
11. A. Bosacchi, S. Franchi, P. Allegri, *et al.*, J. Cryst. Growth **201–202**, 858 (1999).
12. K. R. Evans, C. E. Stutz, P. W. Yu, and C. R. Wie, J. Vac. Sci. Technol. B **8**, 271 (1990).
13. H. Zhao, A. Z. Li, J. Jeong, *et al.*, J. Vac. Sci. Technol. B **6**, 627 (1988).
14. M. Yano, M. Ashida, A. Kawaguchi, *et al.*, J. Vac. Sci. Technol. B **7**, 199 (1989).
15. C. T. Foxon and B. A. Joyce, Surf. Sci. **50**, 434 (1975); J. R. Tsao, T. M. Brennan, J. F. Klem, and B. E. Hammons, J. Vac. Sci. Technol. A **7**, 2138 (1989).
16. V. V. Preobrazhenskii, M. A. Putyato, O. P. Pchelyakov, and B. R. Semyagin, J. Cryst. Growth **201–202**, 170 (1999).
17. J. W. Matthews and A. E. Blakeslee, J. Cryst. Growth **27**, 118 (1974).
18. S. Ivanov and P. Kop'ev, in *Antimonide-Related Strained Layer Heterostructures*, Ed. by M. O. Manasreh (Gordon and Breach Sci., Amsterdam, 1997), Ser. Optoelectronic Properties of Semiconductors and Superlattices, Vol. 3, Chap. 4, p. 95.
19. D. A. Collins, M. W. Wang, R. W. Grant, and T. C. McGill, J. Appl. Phys. **75**, 259 (1994).
20. B. Z. Nosho, B. R. Bennett, L. J. Whitman, and M. Goldenberg, J. Vac. Sci. Technol. B **19**, 1626 (2001).
21. N. Georgiev and T. Mozume, J. Cryst. Growth **209**, 247 (2000).
22. Qianghua Xie, J. E. Van Nostrand, J. L. Brown, and C. E. Stutz, J. Appl. Phys. **86**, 329 (1999).
23. B. R. Bennett, B. V. Shanabrook, and M. E. Twigg, J. Appl. Phys. **85**, 2157 (1999).
24. R. Kaspi, J. Cryst. Growth **201**, 864 (1999).
25. H. Seki and A. Koukitu, J. Cryst. Growth **78**, 342 (1986).

Translated by Yu. Sin'kov

Semiconductors, Vol. 38, No. 3, 2004, pp. 273–276. Translated from Fizika i Tekhnika Poluprovodnikov, Vol. 38, No. 3, 2004, pp. 285–288.

ELECTRONIC AND OPTICAL PROPERTIES OF SEMICONDUCTORS

Determination of Gallium Concentration in Germanium Doped Using Neutron-Induced Nuclear Transmutation from Measurements of Resistivity in the Region of Hopping Conductivity

O. P. Ermolaev* and T. Yu. Mikul'chik

Belarussian State University, ul. Leningradskaya 14, Minsk, 220050 Belarus

**e-mail: ermolaev@bsu.by*

Submitted April 21, 2003; accepted for publication June 2, 2003

Abstract—Methods for determining the concentration of gallium in germanium doped using nuclear transmutations induced by thermal and epicadmium neutrons from measurements of resistivity in the region of low (liquid-helium) temperatures are considered. In order to evaluate the gallium concentration, it is suggested to use the concentration dependences of hopping resistivity ρ_3 and the resistivity measured at a temperature of 2.5 K.

1. INTRODUCTION

The method of neutron-induced nuclear-transmutation doping of semiconductors [1] attracts the attention of researchers because this method features advantages over conventional methods of doping. These advantages consist in a high precision of doping and a high uniformity of the impurity distribution. Germanium with *p*-type conductivity (gallium is the major impurity) is obtained as a result of neutron-induced transmutation doping; the degree of compensation (K) is controlled by the energy spectrum of reactor neutrons and by its hardness (see, for example, [2]). Germanium doped using neutron-induced nuclear transmutations is a convenient object for studying the basic problems of conductivity in the impurity band and of insulator–metal transition and is also the most important material for fabrication of low-temperature resistance thermometers and detectors of high-energy particles.

In this context, it is important to solve the problem of determining the concentration of transmutation-introduced impurities. Study of the Hall effect is one of the conventional methods for determining the impurity concentration. However, degeneracy of the germanium valence band (i.e., the presence of light- and heavy-hole bands) and the dependences of the Hall factor on the impurity concentration and a magnetic field make it difficult to determine the gallium concentration (N_A). The contribution of light holes to the Hall effect and the dependence of this contribution on the doping level were studied by Alekseenko *et al.* [3]. Experimental determination of the Hall coefficient is a time-consuming procedure. The gallium concentration can be evaluated from an analysis of temperature dependences of the concentration of free charge carriers. Interaction between impurities when their concentration exceeds 1×10^{16} cm^{-3} is one of the causes that limit the use of the aforementioned method. An analysis of temperature dependences of resistivity in the region of hopping conductivity is a simpler method. As is well known, the resistivity is described by the following expression in the case of moderately low temperatures and in the region of hopping conductivity with a constant activation energy (ε_3):

$$\rho = \rho_3 \exp\frac{\varepsilon_3}{kT}. \quad (1)$$

Here, k is the Boltzmann constant; T is temperature; and ρ_3 is an exponential factor defined as [4]

$$\rho_3 \propto \exp\frac{\alpha(K)}{aN_A^{1/3}}, \quad (2)$$

where $\alpha(K)$ is a function that depends on the degree of compensation and a is the Bohr radius of the impurity. According to expression (2), the hopping conductivity is very sensitive to a variation in the concentration of the majority impurity. The energy ε_3 is independent of temperature and is expressed as [4]

$$\varepsilon_3 = \left(\frac{e^2 N_A^{1/3}}{\chi}\right)F(K), \quad (3)$$

where e is the elementary charge, χ is the permittivity, and $F(K)$ is a universal function of the degree of compensation.

In this study, we consider methods for determining the gallium concentration in germanium doped using nuclear transmutations induced by thermal and epicad-

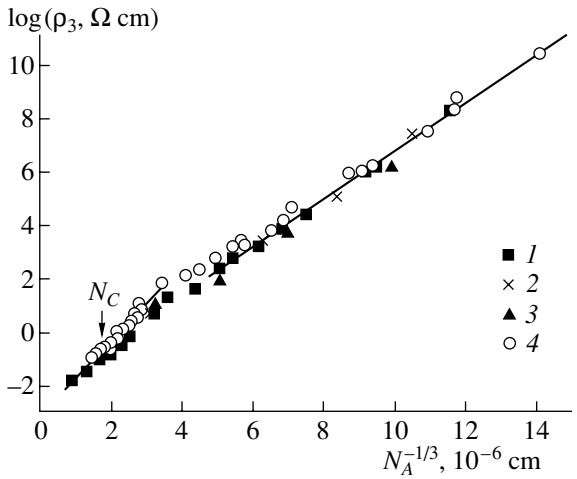

Fig. 1. The resistivity ρ_3 as a function of the gallium concentration N_A. (*1*) Experimental data from [5, 10] and (*2*, *3*, *4*) experimental data from [6, 7, 8], respectively. Solid lines represent the linear approximation.

mium (fast) neutrons; we rely on measurements of resistivity in the region of hopping conductivity.

2. EXPERIMENTAL

We studied samples of undoped germanium with an electron concentration of 3×10^{13} cm^{-3}. The samples were irradiated with various doses of reactor neutrons; the flux of fast neutrons with energies $E \geq 0.1$ MeV was in the range of 1×10^{17} cm^{-2} < Φ_f < 1×10^{19} cm^{-2}. In order to cut off the slow component of the reactor-neutron spectrum (E < 0.5 eV) and to attenuate the factors related to the nuclear-transmutation doping due to thermal neutrons, we irradiated the samples in cadmium containers with a wall thickness of 0.5 mm. During irradiation, the ratio between the doses of thermal (Φ_{th}) and fast neutrons was equal to about 10. The aforementioned values of the cadmium shield thickness and the Φ_{th}/Φ_f ratio are not infrequently used in experiments. The samples were annealed for 24 h at 450°C after irradiation. The resistivity of the samples was measured in the temperature range of 1.5 K < T < 4.2 K.

3. DISCUSSION

The method for determining the concentration of the majority impurity by studying the temperature dependences of hopping conductivity consists in the following. One determines the value of the resistivity ρ_3 by linearly approximating the low-temperature portions of the temperature dependence of the resistivity on the Arrhenius scale with subsequent extrapolation to $1/T = 0$. Previously [5–10], the mechanism of hopping conductivity with a constant activation energy ε_3 (1) was used in the analysis of resistivity extrapolated to $1/T = 0$. The majority-impurity concentration was then estimated from the concentration dependence $\rho_3 = f(N_A^{-1/3})$.

In Fig. 1, we show the concentration dependences $\rho_3 = f(N_A^{-1/3})$ for germanium doped with gallium using the nuclear-transmutation processes initiated by thermal neutrons. We used data published over a period of many years [5–8, 10]. It was previously assumed [1, 5] that $K = 0.4$ in germanium doped with gallium using nuclear transmutations initiated by thermal neutrons. Recent evolution of nuclear physics data led to the value of the degree of compensation in this material $K = 0.3$, which is confirmed by experimental data [11–14, 2]. When comparing the results obtained in different studies, we corrected experimental data [5–7, 10] with respect to concentration taking into account that $K = 0.3$.

At $N_A \leq 1 \times 10^{16}$ cm^{-3}, experimental data can be approximated by a straight line whose slope corresponds to $a_1 \approx 90$ Å. The value $a_1 \approx 90$ Å was also determined in the context of the effective-mass method for germanium doped with gallium [4]. It is noteworthy that, in the range of concentrations under consideration, experimental data are consistent with the theoretical dependence $\rho_3 = f(N_A^{-1/3})$ reported by Poklonskiĭ *et al.* [9]. At 1×10^{16} cm^{-3} < N_A < 3×10^{16} cm^{-3}, a deviation from the linear dependence is observed, which can be related to the processes of multielectron hops (see, for example, [15]). The range of concentrations from $N_A = 3 \times 10^{16}$ cm^{-3} to the concentration corresponding to the insulator–metal transition (and to higher concentrations) was studied in detail in [5, 8, 10]. We showed that, in the concentration range under consideration, the experimental data [5, 8, 10] can be approximated by a straight line whose slope corresponds to $a_2 \approx 57$ Å. A decrease in the Bohr radius for a hole in *p*-Ge with increasing impurity concentration was discussed previously [6, 8, 16] and was related to a change in the asymptotic behavior of the wave functions when the insulator–metal transition was approached. The critical concentration corresponding to the insulator–metal transition for uncompensated germanium doped with gallium is equal to $N_C = 1 \times 10^{17}$ cm^{-3} [17]. It follows from the Mott criterion $N_C^{1/3} a = 0.26 \pm 0.05$ [18] that $a = 56 \pm 11$ Å. Almost coinciding values of the Bohr radius were determined in different studies. The value $a_2 = 57$ Å determined by us from the hopping conductivity is in good agreement with the Bohr radius determined from the Mott criterion. The closeness of the Bohr radius determined from measurements of hopping conductivity in the region of intermediate concentrations to that determined from the Mott criterion was also noted by Zabrodskiĭ *et al.* [8].

Having analyzed the experimental results reported in many publications, we suggest using the concentra-

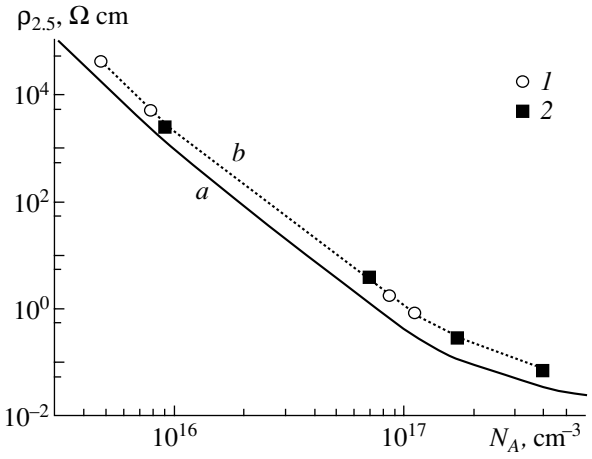

Fig. 2. The resistivity at $T = 2.5$ K as a function the gallium concentration N_A. (*a*) The data for germanium doped using nuclear transmutations initiated by thermal neutrons [17]; (*b*) the data for germanium doped using nuclear transmutations initiated by epicadmium neutrons: (*1*) the data of this study and (*2*) the data reported in [19].

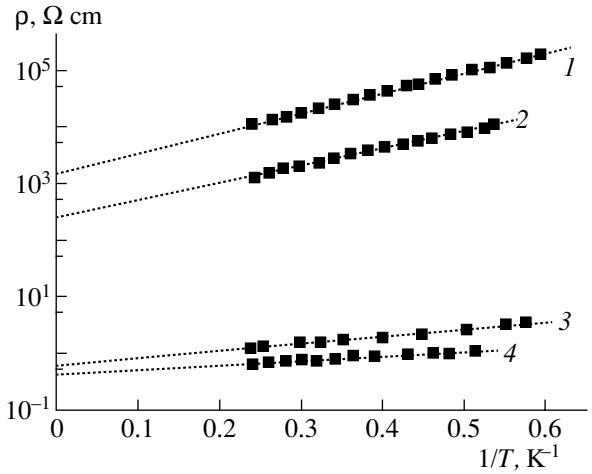

Fig. 3. Temperature dependences of resistivity in germanium doped using nuclear transmutations initiated by epicadmium neutrons. N_A = (*1*) 4.7×10^{15}, (*2*) 7.7×10^{15}, (*3*) 8.5×10^{16}, and (*4*) 1.1×10^{17} cm^{-3}.

tion dependence $\rho_3 = f(N_A^{-1/3})$ for determining the gallium concentration in germanium doped using nuclear transmutations initiated by thermal neutrons; this dependence includes two linear portions described by formula (2), where $a_1 = 90$ Å for $N_A \le 1 \times 10^{16}$ cm^{-3} and $a_2 = 57$ Å for $N_A \ge 3 \times 10^{16}$ cm^{-3} (up to the point of the insulator–metal transition).

It is possible to evaluate more easily the gallium concentration in germanium doped via nuclear transmutations initiated by thermal neutrons if the concentration dependence of resistivity measured at $T = 2.5$ K $\{\rho_{2.5} = f(N_A)\}$ is used. We have hopping conductivity at $T = 2.5$ K; as is well known, the hopping resistivity depends heavily on the concentration of the majority impurity via which the hopping conductivity proceeds. This method is less time consuming compared to the determination of the gallium concentration from the dependence $\rho_3 = f(N_A^{-1/3})$, since now it is not necessary to measure the temperature dependence of resistivity in a wide range. In order to determine the gallium concentration from the dependence $\rho_{2.5} = f(N_A)$, it is necessary to measure the resistivity at $T = 2.5$ K only. In Fig. 2 (curve *a*), we show the dependence $\rho_{2.5} = f(N_A)$ for germanium doped using nuclear transmutations initiated by thermal neutrons; this dependence is plotted in a wide range of concentrations (up to the point of the insulator–metal transition and beyond). The curve was corrected with respect to concentration taking into account that $K = 0.3$.

In practice, it is often necessary to determine the gallium concentration in germanium doped using nuclear transmutations initiated by epicadmium neutrons. In this case, one cannot use the dependence $\rho_{2.5} = f(N_A)$ for germanium doped via nuclear transmutations initiated by thermal neutrons. Consequently, it is necessary to obtain the dependence $\rho_{2.5} = f(N_A)$ for germanium doped using nuclear transmutations initiated by epicadmium neutrons.

Temperature dependences of resistivity in germanium doped using nuclear transmutations initiated by epicadmium neutrons are shown in Fig. 3; all samples feature hopping conductivity at $T < 4.2$ K. The hopping conductivity in this material was also studied previously [19, 20]. The samples were irradiated under similar conditions in our experiments and in [19]. The gallium concentration in the samples under investigation was determined from the obtained values of ρ_3 taking into account the Bohr radii $a_1 = 90$ Å (for $N_A \le 1 \times 10^{16}$ cm^{-3}) and $a_2 = 57$ Å (for $N_A \ge 3 \times 10^{16}$ cm^{-3}) and dependences (2).

In Fig. 2, curve *b* represents the dependence $\rho_{2.5} = f(N_A)$ for germanium doped with gallium using nuclear transmutations initiated by epicadmium neutrons. In order to determine the gallium concentration in the samples [19], the data on the hopping conductivity were analyzed using the above-described method.

As can be seen from Fig. 2, there is qualitative agreement between experimental data for germanium doped using transmutations initiated by thermal neutrons and those for germanium doped using epicadmium neutrons. A small quantitative difference is related to the fact that the degree of compensation in germanium doped using nuclear transmutations initiated by epicadmium neutrons ($K \approx 0.5$ [2]) exceeds that in germanium doped using nuclear transmutations initiated by thermal neutrons. According to expression (1), the resistivity depends on ρ_3 and ε_3. The values of $\alpha(K)$ in formula (2) are equal to 1.79 and 1.81 for $K = 0.3$ and 0.5, respectively [4]; as a result, there is a small quantitative difference between the values of ρ_3 in these two

cases for the same impurity concentration. The values of $F(K)$ in formula (3) are equal to 0.7 and 0.75 for $K = 0.3$ and 0.5, respectively [4]; consequently, the value of ε_3 is larger in germanium doped using nuclear transmutations initiated by epicadmium neutrons than in germanium irradiated with thermal neutrons (for identical impurity concentration). According to expression (1), this means that the plot of resistivity vs. impurity concentration for germanium doped using nuclear transmutations initiated by epicadmium neutrons runs above a similar plot for germanium irradiated with thermal neutrons (for the same impurity concentration). This conclusion is confirmed by experimental data shown in Fig. 2.

4. CONCLUSION

Thus, it is possible to evaluate the gallium concentration in germanium doped using nuclear transmutations initiated by neutrons on the basis of the value of ρ_3 determined from temperature dependences of the hopping conductivity using the concentration dependence $\rho_3 = f(N_A^{-1/3})$; the latter dependence consists of two linear portions described by formula (2) where $a_1 = 90$ Å at concentrations $N_A \le 1 \times 10^{16}$ cm^{-3} and $a_2 = 57$ Å at $N_A \ge 3 \times 10^{16}$ cm^{-3} (up to the point of the insulator–metal transition). It is simpler to evaluate the gallium concentration in germanium doped using nuclear transmutations initiated by neutrons on the basis of resistivity measured in the temperature region where the hopping conductivity is observed (for example, at $T = 2.5$ K). Dependences $\rho_{2.5} = f(N_A)$ for germanium doped using nuclear transmutations initiated by thermal and epicadmium neutrons make it possible to determine the gallium concentration using the value of resistivity measured at $T = 2.5$ K.

REFERENCES

1. K. Lark-Horovitz, in *Semi-Conducting Materials* (Butterworths, London, 1951; Inostrannaya Literatura, Moscow, 1954).
2. A. G. Zabrodskiĭ and M. V. Alekseenko, Fiz. Tekh. Poluprovodn. (St. Petersburg) **28**, 168 (1994) [Semiconductors **28**, 101 (1994)].
3. M. V. Alekseenko, A. G. Zabrodskiĭ, and L. M. Shterengas, Fiz. Tekh. Poluprovodn. (St. Petersburg) **32**, 811 (1998) [Semiconductors **32**, 720 (1998)].
4. B. I. Shklovskiĭ and A. L. Éfros, *Electronic Properties of Doped Semiconductors* (Nauka, Moscow, 1979; Springer, New York, 1984); Fiz. Tekh. Poluprovodn. (Leningrad) **14**, 825 (1980) [Sov. Phys. Semicond. **14**, 487 (1980)].
5. H. Fritzsche and M. Cuevas, Phys. Rev. **119**, 1238 (1960).
6. J. A. Ghroboczek, H. Fritzsche, and C. L. Jiang, Philos. Mag. B **44**, 685 (1981).
7. A. R. Gadzhiev and I. S. Shlimak, Fiz. Tekh. Poluprovodn. (Leningrad) **6**, 1582 (1972) [Sov. Phys. Semicond. **6**, 1364 (1972)].
8. A. G. Zabrodskiĭ, A. G. Andreev, and M. V. Alekseenko, Fiz. Tekh. Poluprovodn. (St. Petersburg) **26**, 431 (1992) [Sov. Phys. Semicond. **26**, 244 (1992)].
9. N. A. Poklonskiĭ, S. Yu. Lopatin, and A. G. Zabrodskiĭ, Fiz. Tverd. Tela (St. Petersburg) **42**, 432 (2000) [Phys. Solid State **42**, 441 (2000)].
10. N. Mott and W. Toose, Usp. Fiz. Nauk **79**, 691 (1963).
11. A. G. Zabrodskiĭ, Pis'ma Zh. Éksp. Teor. Fiz. **33**, 258 (1981) [JETP Lett. **33**, 243 (1981)].
12. A. G. Beda, V. V. Vaĭnberg, and F. M. Vorobkalo, Fiz. Tekh. Poluprovodn. (Leningrad) **15**, 1546 (1981) [Sov. Phys. Semicond. **15**, 896 (1981)].
13. Yu. A. Osip'yan, V. M. Prokopenko, and V. I. Tal'yanskiĭ, Zh. Éksp. Teor. Fiz. **87**, 269 (1984) [Sov. Phys. JETP **60**, 156 (1984)].
14. M. V. Alekseenko, A. G. Andreev, and A. G. Zabrodskiĭ, Pis'ma Zh. Tekh. Fiz. **13**, 1295 (1987) [Sov. Tech. Phys. Lett. **13**, 541 (1987)].
15. M. Pollak and M. L. Knotek, Solid State Commun. **21**, 183 (1977).
16. E. M. Gershenzon, I. N. Kurilenko, and L. B. Litvak-Gorskaya, Fiz. Tekh. Poluprovodn. (Leningrad) **8**, 1186 (1974) [Sov. Phys. Semicond. **8**, 768 (1974)].
17. H. Fritzsche, *The Metal–Nonmetal Transition in Disordered Systems*, Ed. by L. R. Friedman and D. P. Tunstall (Scotish Univ. Summer School, 1978), p. 193.
18. N. F. Mott and E. A. Davis, *Electronic Processes in Non-Crystalline Materials*, 2nd ed. (Clarendon Press, Oxford, 1979; Mir, Moscow, 1982).
19. M. L. Kozhukh and N. S. Lipkina, Fiz. Tekh. Poluprovodn. (Leningrad) **21**, 284 (1987) [Sov. Phys. Semicond. **21**, 172 (1987)].
20. O. P. Ermolaev, Fiz. Tekh. Poluprovodn. (St. Petersburg) **28**, 2021 (1994) [Semiconductors **28**, 1113 (1994)].

Translated by A. Spitsyn

Semiconductors, Vol. 38, No. 3, 2004, pp. 277–280. Translated from Fizika i Tekhnika Poluprovodnikov, Vol. 38, No. 3, 2004, pp. 289–292.

ELECTRONIC AND OPTICAL PROPERTIES OF SEMICONDUCTORS

Effect of Uniform Compression on Photoluminescence Spectra of GaAs Layers Heavily Doped with Beryllium

T. S. Shamirzaev*^, K. S. Zhuravlev*, J. Bak-Misiuk, A. Misiuk***, J. Z. Domagala**, and J. Adamczewska****

**Institute of Semiconductor Physics, Siberian Division, Russian Academy of Sciences, pr. Akademika Lavrent'eva 13, Novosibirsk, 630090 Russia*

^e-mail: timur@thermo.isp.nsc.ru

***Institute of Physics, Polish Academy of Sciences, Warsaw, 02-668 Poland*

****Institute of Electron Technology, Warsaw, 02-668 Poland*

Submitted May 21, 2003; accepted for publication June 18, 2003

Abstract—The effect of high-temperature annealing at high hydrostatic pressures on photoluminescence of heavily doped GaAs:Be layers grown by molecular-beam epitaxy on GaAs substrates was studied. A blue shift of the band-edge luminescence line and an increase in the relative intensity of the shoulder at the high-energy wing of this line were detected after annealing in the spectra of layers with a beryllium atom concentration higher than 5×10^{19} cm^{-3}. The same layers featured a concentration-related decrease in the GaAs lattice parameter, which does not conform to the Vegard law. These effects can be attributed to the formation of beryllium inclusions in heavily doped GaAs. Due to different compressibility and thermal expansion coefficients of Be inclusions and GaAs, high-temperature and high-pressure treatment gives rise to structural defects; hence, the probability of transitions that are indirect in the *k* space increases. © *2004 MAIK "Nauka/Interperiodica"*.

Heavily doped *p*-GaAs is widely used to produce ohmic contacts and active layers in device structures, such as tunnel diodes and bipolar transistors. One of the important parameters of heavily doped layers is the minority-carrier lifetime controlled by recombination via defect levels and Auger recombination. Such impurities as carbon and beryllium are widely used in growing heavily doped *p*-GaAs layers formed by molecular-beam epitaxy (MBE). It was shown recently that recombination of nonequilibrium electrons in GaAs layers heavily doped with carbon is mainly controlled by Auger processes, since carbon is fully incorporated into the GaAs lattice as a shallow substitutional acceptor and does not form defects with deep levels [1].

This study is devoted to the effect of high-temperature and high-pressure treatment on the luminescence properties of heavily doped GaAs:Be layers grown by MBE. The formation of structural defects acting as nonradiative-recombination centers was detected in GaAs:Be layers.

GaAs:Be layers 1.5 μm thick were grown using MBE on semi-insulating GaAs(100) substrates. The layers were separated from the substrate by a buffer GaAs layer 10 nm thick, at the center of which 20 $(AlAs)_5(GaAs)_5$ superlattice periods were grown. The GaAs:Be layers were covered with a layer of nominally undoped GaAs 10 nm thick. The layers were annealed for 1 h at a temperature of 870 K, equal to the layer growth temperature; the annealing was carried out either at atmospheric pressure or at a high hydrostatic pressure (12 kbar) [2].

Steady-state photoluminescence (PL) was measured at a temperature of 77 K, using a setup described in [3]. The steady-state PL was excited by an Ar^+ laser with a wavelength of 488 nm. To determine the relaxed lattice constant in initial and hydrostatically compressed GaAs layers, the Fewster method [4] and high-resolution X-ray diffractometry were used. The set of high-angle (006, 335, and 117) Bragg reflections was analyzed. The parameters of the relaxed lattice were calculated using the expression

$$a = \frac{a_\perp + 2Ca_\parallel}{1 + 2C}, \quad (1)$$

where $a_\perp$ and $a_\parallel$ are the lattice parameters in the directions perpendicular and parallel to the layer–substrate interface, respectively,

$$C = \frac{1 - \nu}{1 + \nu},$$

and ν is the Poisson ratio equal to 0.311 for GaAs.

The concentrations of beryllium atoms C_{Be} and holes N_p were determined using the secondary ion mass spectrometry (SIMS) and Van der Pauw methods, respectively. The SIMS and Hall measurement data for

Table 1. Concentrations of holes (N_p) and beryllium atoms (C_{Be}) in GaAs:Be layers

Sample	$N_p \pm 10\%$, 10^{19} cm^{-3}		$N_p \pm 10\%$, 10^{19} cm^{-3}		C_{Be}, 10^{19} cm^{-3}
	before annealing under pressure		after annealing under pressure		
	300 K	77 K	300 K	77 K	
A	0.5	0.5	0.5	0.5	0.5
B	2.6	2.7	2.5	2.0	5
C	8	7	5.0	2.4	18
D	9.2	5.8	4.2	1.8	21.5

the samples under investigation are listed in Table 1. Beryllium is mostly incorporated into the gallium sublattice and is a shallow acceptor (the hole binding energy at the acceptor is 28 meV). The hole concentration decrease as the measurement temperature decreases from 300 to 77 K for samples *C* and *D* is apparently caused by deep acceptors ionized at room temperature. Previously, we observed a similar effect in nominally undoped GaAs layers [5]; therefore, we assumed that the Hall hole concentration at 77 K was equal to the beryllium concentration Be_{Ga} in the gallium sublattice. The data listed in Table 1 show that the total concentration of beryllium atoms in layers determined using SIMS exceeds that of Be_{Ga} obtained from the Hall data. These additional atoms can fill interstices or aggregate as beryllium inclusions. We note that the concentration of Be_{Ga} in sample *D* is lower than in sample *C*; however, the beryllium concentration determined by SIMS was higher. This can mean that the concentration of beryllium inclusions and (or) interstitial atoms is not directly proportional to the beryllium atom concentration.

The low-temperature PL spectra of GaAs:Be layers with various doping levels are shown in Fig. 1. The edge-luminescence band caused by interband transitions with conservation of quasi-momenta of nonequilibrium carriers dominates in the spectra of all the initial layers, measured at 77 K. This band shifts to longer wavelengths with the hole concentration in proportion to $p^{1/5}$ due to the impurity-induced narrowing of the band gap [6]. Furthermore, the samples with a high doping level exhibit a shoulder in the short-wavelength wing of this band. This is caused by radiative recombination of electrons localized near the conduction-band bottom with holes having an energy corresponding to the Fermi energy in the valence band [7]. These transitions are indirect in the *k* space and result from quasi-momentum scattering at the potential of impurities and defects. We note that the optical properties of the samples are highly uniform over their area. For example, the PL spectra measured at five different points over the sample area are almost identical for each GaAs:Be film under investigation.

Annealing of the layers at a high hydrostatic pressure did not affect the PL spectra of the layers with hole concentrations $p \le 2.6 \times 10^{19}$ cm^{-3}. In the spectra of more heavily doped layers (see Fig. 2), an increase in the intensity of the short-wavelength shoulder (indicated by an arrow) was observed, as well as the blue shift of the edge PL band. The blue shift of the edge PL band peak is apparently caused by a decrease in the

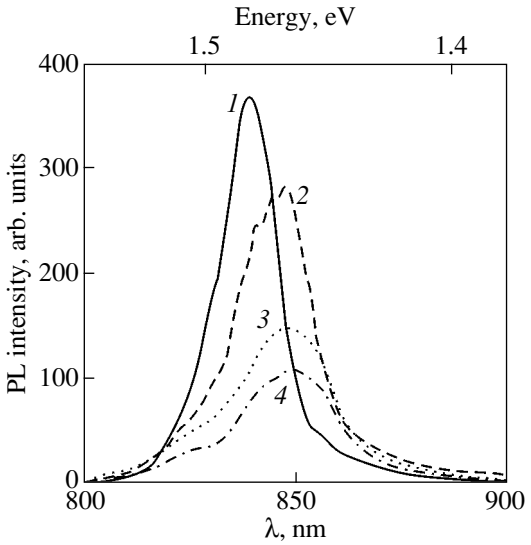

Fig. 1. Spectra of low-temperature (T = 77 K) photoluminescence of GaAs:Be layers with the beryllium atom concentration (determined by SIMS) C_{Be} = (*1*) 0.5, (*2*) 5, (*3*) 18, and (*4*) 21.5×10^{19} cm^{-3}.

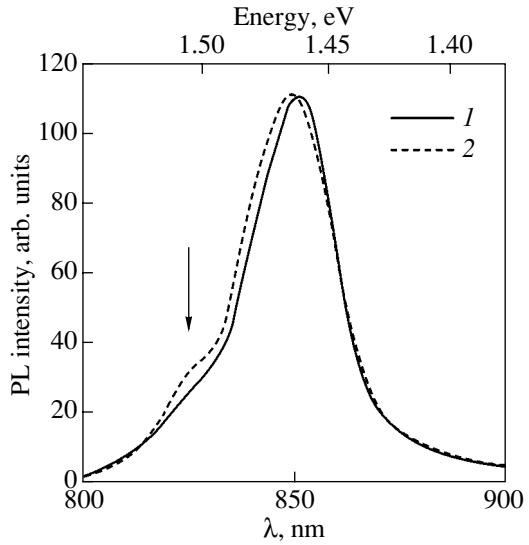

Fig. 2. Photoluminescence spectra of heavily doped GaAs:Be layers: (*1*) the initial one and (*2*) the layer after 870-K annealing at a pressure of 12 kbar. The arrow indicates the position of the shoulder caused by radiative transitions that are indirect in the *k* space.

concentration-related narrowing of the effective band gap, as evidenced by the decrease in the hole concentration after annealing under pressure (see Table 1).

The PL enhancement caused by transitions that are indirect in the *k* space suggests the formation of a high lattice defect density comparable to the beryllium atom concentration. This conclusion is also confirmed by the following data.

(i) The sixfold decrease in the PL intensity after annealing and hydrostatic compression.

(ii) The Hall measurement data (see Table 1) showing an approximately twofold decrease in the hole concentration after annealing under high pressure, which indicates the formation of compensating defects.

(iii) The X-ray diffraction data on the crystal structure of GaAs:Be layers.

The lattice constant $a_{\parallel}$ in the direction parallel to the substrate surface is equal to the GaAs lattice constant $a_{GaAs} = 5.65332$ Å for all the layers under investigation. However, a decrease in the lattice constant $a_{\perp}$ measured in the direction perpendicular to the layer–substrate interface was detected in all the heavily doped GaAs:Be layers; relaxation of the lattice parameters was also observed [8]. There are two known causes of the change in the lattice parameters of a material doped with electrically active impurity atoms: (i) the effect of the impurity atom size and (ii) the effect of free carriers. The relative changes in the lattice parameters of *p*-type semiconductors with the zinc-blende band structure, caused by the two aforementioned factors, are given by (see [9–11])

$$\Delta a/a = \beta_s N_a + \beta_p N_p, \quad (2)$$

where N_a is the beryllium atom concentration in the gallium sublattice (equal to the hole concentration in the samples at 77 K—see Table 1); N_p is the hole concentration in the valence band (at 300 K); and β_s and β_p are the parameters describing the size effect (corresponding to the Vegard rule) and the effect of holes,

$$\beta_s = \frac{4(R_d - R_s)}{\sqrt{3}aN_0} = 2.03 \times 10^{-24}, \quad (3)$$

$$\beta_p = \frac{D}{3B} = 0.4978 \times 10^{-24}. \quad (4)$$

Here, $N_0 = 2.21 \times 10^{22}$ cm^{-3} is the concentration of gallium atoms in undoped GaAs; R_d and R_s are the covalent radii of beryllium (1.11 Å) and gallium (1.22 Å), respectively; B is the GaAs bulk modulus, equal to 7.5×10^6 N/cm^2; and D is the deformation potential for the valence-band top, equal to 0.7 eV.

The changes in the relaxed lattice parameters of GaAs:Be layers are listed in Table 2. We can see that the experimentally detected decrease in the relaxed lattice parameters for samples *B–D* is smaller than those calculated using formula (2). This effect is apparently associated with beryllium inclusions that are formed as the layers grow. If such beryllium-containing inclusions are formed during the layer growth, annealing at a high hydrostatic pressure should affect the defect structure in GaAs:Be and cause an additional change in the lattice parameters. This change, i.e., the increase $\Delta a'$ in the lattice parameters after annealing, was indeed experimentally observed, as can be seen in Table 2. This change is caused by additional lattice defects introduced by annealing due to the difference between the compressibility and thermal expansion coefficients of the initial material and beryllium-containing inclusions. It is known that the stresses arising near the interfaces between precipitates and the host during annealing under a high hydrostatic pressure can reach a critical value when dislocation loops and other defects are introduced [12].

Table 2. Changes in the lattice parameters of the GaAs:Be layers ($\Delta a'$ is the change in Δa)

Sample	$\Delta a \pm 0.5 \times 10^{-4}$, Å Initial GaAs:Be layers		$\Delta a' \pm 0.5 \times 10^{-4}$, Å After annealing under pressure
	experiment	calculation	
A	–1	–0.5	<0.5
B	–3.7	–3.8	1
C	–8.6	–10.1	1.5
D	–6	–9.2	2

To validate the assumption on the effect of hydrostatic pressure on defect generation, reference annealing of initial samples was carried out at the same temperature and atmospheric pressure. We did not detect any changes in the shape and intensity of the PL spectra after annealing; the changes in the Hall concentration of holes were within the accuracy of measurements (±10%).

Thus, the structural defects associated with beryllium were detected in heavily doped GaAs:Be layers (the beryllium atom concentration was lower than 5×10^{19} cm^{-3}) annealed at a high hydrostatic pressure. These defects manifest themselves as nonradiative-recombination centers and increase the probability of radiative transitions without quasi-momentum conservation, which are associated with recombination of electrons near the conduction-band edge and holes at the Fermi level in the valence band.

REFERENCES

1. R. K. Ahrenkiel, R. Ellingson, W. Metzger, *et al.*, Appl. Phys. Lett. **78**, 1879 (2001).
2. A. Misiuk, Mater. Phys. Mech. **1**, 119 (2002).

3. K. S. Zhuravlev, V. A. Kolosanov, M. Holland, and I. I. Marokhovka, Fiz. Tekh. Poluprovodn. (St. Petersburg) **31**, 1436 (1997) [Semiconductors **31**, 1241 (1997)].
4. P. F. Fewster and N. L. Andrew, J. Appl. Crystallogr. **28**, 451 (1995).
5. K. S. Zhuravlev, A. V. Kalagin, N. T. Moshegov, *et al.*, Fiz. Tekh. Poluprovodn. (St. Petersburg) **30**, 1704 (1996) [Semiconductors **30**, 891 (1996)].
6. S. Kim, M.-S. Kim, K. S. Eom, and S.-K. Min, J. Appl. Phys. **73**, 4703 (1993).
7. D. Olego and M. Cardona, Phys. Rev. B **22**, 886 (1980).
8. J. Bak-Misiuk, A. Misiuk, K. S. Zhuravlev, *et al.*, Physica B (Amsterdam) **308–310**, 820 (2001).
9. T. Figielski, Phys. Status Solidi **1**, 306 (1961).
10. Wei Li and M. Pessa, Phys. Rev. B **57**, 14627 (1998).
11. M. Leszczynski, J. Bak-Misiuk, J. Domagala, *et al.*, Appl. Phys. Lett. **67**, 539 (1995).
12. J. Jung, Philos. Mag. A **30**, 257 (1984).

Translated by A. Kazantsev

Semiconductors, Vol. 38, No. 3, 2004, pp. 281–283. Translated from Fizika i Tekhnika Poluprovodnikov, Vol. 38, No. 3, 2004, pp. 293–295.

ELECTRONIC AND OPTICAL PROPERTIES OF SEMICONDUCTORS

Impedance of Solid Solutions Based on Gallium-Doped Lead Telluride

B. A. Akimov, V. V. Pryadun, L. I. Ryabova*, and D. R. Khokhlov

Moscow State University, Moscow, 119899 Russia

**e-mail: mila@mig.phys.msu.su*

Fax: (095) 932 8876

Submitted June 9, 2003; accepted for publication June 18, 2003

Abstract—The impedance of single-crystal PbTe:Ga and $Pb_{0.94}Ge_{0.06}Te$:Ga samples was studied in the frequency range from 10^2 to 10^6 Hz at temperatures of 4.2 to 300 K. It was shown that the effects associated with long-term relaxation processes do not result from a ferroelectric phase transition, because they are observed at much lower temperatures. The low-temperature features of the behavior of the capacitance in $Pb_{0.94}Ge_{0.06}Te$:Ga are regarded as a contribution from the impurity subsystem. © *2004 MAIK "Nauka/Interperiodica".*

Gallium has variable valence in lead telluride and a number of solid solutions based on this compound. This gives rise to a system of impurity levels and leads to stabilization of the Fermi level position and long-term relaxation processes at temperatures T below $T_C \approx 80$ K. In all of the known cases, the Fermi level is stabilized in solid solutions based on gallium-doped lead telluride within the energy gap, which leads to the formation of a semi-insulating state in crystals at low temperatures [1]. Taking into account the dramatic change in conductivity under illumination at $T = T_C$, the nonlinearity of the current–voltage characteristics, and the anomalous magnetic properties of PbTe:Ga at low temperatures, the possibility that a doping-induced phase transition may occur cannot be ruled out completely.

Direct experimental information about the occurrence of the phase transition and its possible influence on correlation processes in the system composed of a crystal lattice and impurity centers can be obtained by studying the full impedance. In addition to PbTe:Ga, single-crystal samples of $Pb_{0.94}Ge_{0.06}Te$:Ga (whose electrical and photoelectric characteristics have been previously studied in detail [2–5]) were chosen as objects of study.

The samples were rectangular plates with an area of $\sim 4 \times 4$ mm^2 and a thickness of ~1 mm. The plate surface was coated with an alloy containing 95% In, 4% Ag, and 1% Au. The measurements were performed in a chamber screening the samples from background illumination, with E7-12 and MIT 9216A ac bridges at frequencies f of 100 Hz to 1 MHz in the temperature range 4.2–300 K.

Figure 1 shows temperature dependences of the dc resistivity ρ of PbTe:Ga (curve *1*) and $Pb_{0.94}Ge_{0.06}Te$:Ga (curve *2*). The high-temperature portions of the curves (Fig. 1, inset) describe an activated temperature dependence of conductivity, with activation energies $E_a \approx$ 50 (*1*) and 75 meV (*2*), calculated using the relation $\rho \propto$

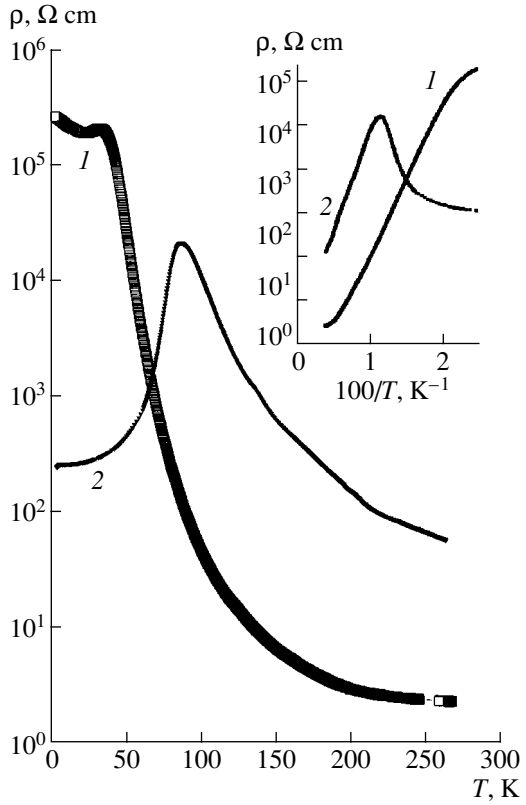

Fig. 1. Temperature dependences of the resistivity of (*1*) PbTe:Ga and (*2*) $Pb_{0.94}Ge_{0.06}Te$:Ga samples. Inset: the high-temperature portions of the same curves in relation to inverse temperature.

1063-7826/04/3803-0281$26.00 © 2004 MAIK "Nauka/Interperiodica"

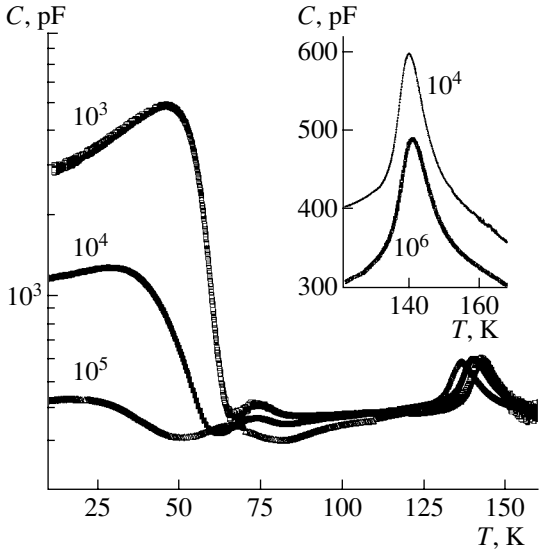

Fig. 2. Temperature dependences of capacitance for the $Pb_{0.94}Ge_{0.06}Te$:Ga sample. Numbers by the curves indicate the frequency in Hz. Geometric capacitance of the sample $C_0 = 0.18$ pF.

$\exp(E_a/kT)$. The $\rho(T)$ curve for the $Pb_{0.94}Ge_{0.06}Te$:Ga sample shows a peak at $T = T_M \simeq 90$ K. The real part of the impedance, Z', virtually coincides with ρ at frequencies lower than 10^5 Hz. With a frequency of 1 MHz, the value of Z' in the vicinity of the peak is approximately two times smaller than ρ.

As can be seen from Fig. 1, the crystals studied are not insulators; their conductivity, especially at elevated temperatures, is rather high. It was possible to obtain reliable impedance data only at temperatures below 80 K for lower-resistivity PbTe:Ga and below 170 K for $Pb_{0.94}Ge_{0.06}Te$:Ga. In processing the experimental data, the capacitance of the crystals was calculated from the real (Z') and imaginary (Z'') parts of the impedance in the approximation of an equivalent parallel RC circuit.

The temperature dependences of the capacitance of $Pb_{0.94}Ge_{0.06}Te$:Ga samples at different frequencies are shown in Fig. 2. It can be seen that the $C(T)$ curve exhibits a distinct peak at $T_F \simeq 140$ K, and the position of this peak shows no clearly pronounced frequency dependence (Fig. 2, inset). The temperature at which the peak lies is ~20 K lower than the temperature of the transition from the cubic phase to a rhombohedral phase for an undoped alloy of the same composition. A comparable decrease in the phase transition temperature has also been observed when $Pb_{1-x}Ge_xTe$ alloys are doped with indium [6].

At low temperatures ($T < 70$ K), the capacitance of $Pb_{0.94}Ge_{0.06}Te$:Ga exhibits a strong temperature dependence. At low frequencies $f \approx 10^3$ Hz, an abrupt, nearly stepwise rise in the capacitance C of almost an order of magnitude is observed. As f increases, the magnitude of this abrupt change decreases, so that the $C(T)$ curve becomes rather smooth at $f = 10^5$ Hz. For PbTe:Ga, the capacitance at $T < 70$ K is virtually independent of frequency f and temperature T. The value of C corresponds to a dielectric constant $\varepsilon \approx 1000$.

An additional contribution to the capacitance, observed for $Pb_{0.94}Ge_{0.06}Te$:Ga in the low-frequency range, cannot be attributed to polarization-induced processes or to resonance effects in the crystal lattice itself. Most probably, the increase in capacitance results from processes associated with the recharging of impurity centers. A similar effect was previously observed in the same frequency range in heterojunctions of germanium-silicon diodes and was interpreted as a contribution from the recharging of interfacial states to the capacitance of the *p–n* junction [7].

A possible factor determining the difference in behavior between the impurity subsystems in PbTe:Ga and $Pb_{0.94}Ge_{0.06}Te$:Ga samples is the absence of Fermi level stabilization in $Pb_{1-x}Ge_xTe$:Ga solid solutions. Specifically, this is indicated by the results of previous experimental studies concerned with the effect of irradiation with high-energy electrons on the electrical properties of $Pb_{1-x}Ge_xTe$:Ga samples [3, 5]. It is known that the range of gallium impurity concentrations at which the effect of Fermi level stabilization is observed in PbTe:Ga is rather narrow [1]. Since irradiation with high-energy electrons gives rise to defects of the donor type, the type of conduction in lightly doped *p*-PbTe:Ga crystals changes as the irradiation dose is raised, with the subsequent stabilization of the Fermi level position [8]. In $Pb_{1-x}Ge_xTe$:Ga samples, irradiation leads to a decrease in the resistance and a subsequent transition to metallic conduction. This may be associated with the presence of an excess amount of gallium in the samples studied. In the absence of stabilization of the Fermi level, the nonuniform distribution of the impurity throughout the crystal should affect the galvanomagnetic characteristics of the samples. This has been confirmed by the results of Hall measurements in $Pb_{1-x}Ge_xTe$:Ga [2].

It is important that the phase transition temperature T_F in $Pb_{0.94}Ge_{0.06}Te$:Ga was found to be considerably higher than the characteristic temperatures T_C (~80 K) at which persistent photoconductivity appears, temperatures T_M (~90 K) at which the peak in the $\rho(T)$ curve lies, and temperatures (~70 K) at which low-frequency anomalies appear in the temperature dependences of capacitance. Thus, the data obtained indicate that there is no direct relationship between the phase transition and long-term relaxation processes in the samples studied.

This study was supported in part by the Russian Foundation for Basic Research (project nos. 01-02-16356 and 02-02-17057) and INTAS (grant no. 2001-0184).

REFERENCES

1. B. A. Volkov, L. I. Ryabova, and D. R. Khokhlov, Usp. Fiz. Nauk **172**, 875 (2002) [Phys. Usp. **45**, 819 (2002)].
2. B. A. Akimov, A. V. Albul, I. I. Ivanchik, *et al.*, Fiz. Tekh. Poluprovodn. (St. Petersburg) **27**, 351 (1993) [Semiconductors **27**, 194 (1993)].
3. E. P. Skipetrov, E. A. Zvereva, L. A. Skipetrova, *et al.*, J. Cryst. Growth **210**, 292 (2000).
4. E. P. Skipetrov, E. A. Zvereva, V. V. Belousov, *et al.*, Phys. Status Solidi B **221**, 549 (2000).
5. E. P. Skipetrov, E. A. Zvereva, O. S. Volkova, *et al.*, Mater. Sci. Eng. B **91–92**, 416 (2002).
6. A. I. Lebedev and Kh. A. Abdullin, Fiz. Tekh. Poluprovodn. (Leningrad) **18**, 624 (1984) [Sov. Phys. Semicond. **18**, 388 (1984)].
7. J. P. Donnelly and A. G. Milnes, IEEE Trans. Electron Devices **14**, 63 (1967).
8. E. P. Skipetrov, A. N. Nekrasova, D. V. Pelekhov, *et al.*, Fiz. Tekh. Poluprovodn. (St. Petersburg) **28**, 1626 (1994) [Semiconductors **28**, 906 (1994)].

Translated by M. Tagirdzhanov

Semiconductors, Vol. 38, No. 3, 2004, pp. 284–287. Translated from Fizika i Tekhnika Poluprovodnikov, Vol. 38, No. 3, 2004, pp. 296–299.

ELECTRONIC AND OPTICAL PROPERTIES OF SEMICONDUCTORS

Role of Space Charge in the Resistance Formation in a Bipolar Semiconductor Sample

A. Konin

Semiconductor Physics Institute, Vilnius, 2600 Lithuania

Submitted July 2, 2003; accepted for publication July 4, 2003

Abstract—An expression for the current-independent resistance (Ohm's law) of a bipolar semiconductor is derived within the linear approximation for concentrations of nonequilibrium carriers. It is shown that the deviation of the resistance from the classical value is caused by a space charge arising in the sample. The semiconductor sample resistance can be higher and lower than the classical value, depending on the ratio of surface conductivities of electrons and holes. This effect is most pronounced in samples with low-rate surface recombination and a length shorter than the diffusion length. © *2004 MAIK "Nauka/Interperiodica".*

1. INTRODUCTION

In many physical problems associated with the formation of nonequilibrium electrons and holes (photoeffect, injection of carriers, Hall effect, etc.) in semiconductors, their recombination plays a fundamental role. Expressions for rates of bulk recombination were derived in [1] based on the Shockley–Read model [2] within the linear approximation for concentrations of nonequilibrium carriers. The recombination model proposed in [1] was used in [3] to calculate the resistance of a bipolar semiconductor sample. The boundary conditions (BCs) obtained in [4, 5] and used in [3] are sufficient to calculate the integration constants only under the assumption that the sample is quasi-neutral and are not correct for several reasons. In [3], it was assumed that the nonequilibrium concentration of electrons Δn and holes Δp are equal in the entire volume of the sample ($\Delta n = \Delta p$), which is the so-called quasi-neutrality condition. In this case, the charge (Debye charge) arising in the semiconductor near-junction region, whose thickness is on the order of the Debye length, is disregarded. Furthermore, the number of unknown parameters decreases; in fact, the nonequilibrium concentration of electron–hole pairs (EHPs) is the only unknown function. To determine the latter, it is quite sufficient to involve the known BCs [6] relating the EHP flux to the rate of their surface recombination. In this case, the BCs are formulated outside the region of the Debye surface charge [7] at a certain quasi-surface, rather than at the actual metal–semiconductor interface. Another consequence of the quasi-neutrality is the fact that the electric field in the sample is uniquely determined by the concentration gradient of nonequilibrium EHPs. In this case, a new contradiction arises: on the one hand, the electric field is a nonlinear function of the sample coordinate; on the other hand, this field is independent of the coordinate, judging by the Poisson equation. All these contradictions can be eliminated by solving exactly the set of continuity equations [1], taking into account the Poisson equation and using the BCs at an actual metal–semiconductor interface. In this case, the bulk diffusion and Debye surface charges, as well as the electrostatic potential induced by them, will be necessarily taken into account.

The aim of this study is to determine the resistance of a bipolar semiconductor sample, taking into account the BCs at the actual metal–semiconductor interface.

2. THEORY

Let us consider a semiconductor sample shaped as a parallelepiped ($-a \le x \le a$, $0 \le y \le b$, $0 \le z \le d$; $a \ll b, d$) with a direct electric current j_0 flowing along the x axis.

The distributions of the carrier concentrations and the electrostatic potential are defined by the continuity equations (see [1])

$$\frac{1}{e}\frac{dj_n}{dx} - \frac{\Delta n}{\tau_n} - \frac{\Delta p}{\tau_p} = 0, \quad (1)$$

$$\frac{1}{e}\frac{dj_p}{dx} + \frac{\Delta n}{\tau_n} + \frac{\Delta p}{\tau_p} = 0, \quad (2)$$

and the Poisson equation,

$$\frac{d^2\Delta\varphi}{dx^2} = \frac{e}{\varepsilon\varepsilon_0}(\Delta n - \Delta p), \quad (3)$$

where j_n and j_p are the electron- and hole-current densities, τ_n and τ_p are the semiconductor parameters in units of time (but they are not electron and hole lifetimes [1]), Δn and Δp are the nonequilibrium electron and hole concentrations, $\Delta\varphi$ is the nonequilibrium electrostatic potential, $(-e)$ is the elementary charge, ε is the semiconductor permittivity, and ε_0 is the permittivity of free space.

1063-7826/04/3803-0284$26.00 © 2004 MAIK "Nauka/Interperiodica"

Eqs. (1) and (2) satisfy the law of charge conservation

$$\frac{d}{dx}(j_n + j_p) = 0,$$

as they should, which suggests that

$$j_n + j_p = j_0 = \text{const}. \quad (4)$$

Let us formulate the BCs for Eqs. (1)–(3). In the most general case, the expressions for electron and hole currents in the linear approximation with respect to changes in the electric and chemical potentials are given by

$$j_n = \sigma_n\left[-\frac{d}{dx}\left(\Delta\varphi - \frac{1}{e}\Delta F_n\right)\right],$$

$$j_p = \sigma_p\left[-\frac{d}{dx}\left(\Delta\varphi + \frac{1}{e}\Delta F_p\right)\right], \quad (5)$$

where $\sigma_{n(p)}$ is the n-type (p-type) conductivity of the semiconductor and $\Delta F_{n(p)}$ is the change in the chemical potentials of electrons and holes, caused by a change in their concentrations.

To derive the BCs for the hole flux to the surface ($x = a$), we integrate Eq. (2) over x from $a - \delta$ to $a + \delta$ with δ tending to zero. We obtain

$$\frac{1}{e}\lim_{\delta\to 0}\int_{a-\delta}^{a+\delta}\frac{dj_p}{dx}dx + \lim_{\delta\to 0}\int_{a-\delta}^{a+\delta}\left(\frac{\Delta n}{\tau_n} + \frac{\Delta p}{\tau_p}\right)dx = 0. \quad (6)$$

Taking into account that $j_p(a + \delta) = 0$ (there are no holes in the metal), we finally obtain

$$\frac{1}{e}j_p\Big|_{x=a} = S_n^+\Delta n\Big|_{x=a} + S_p^+\Delta p\Big|_{x=a}, \quad (7)$$

where

$$S_{n,p}^+ = \lim_{\delta\to 0}\int_{a-\delta}^{a}\frac{dx}{\tau_{n,p}}$$

are the parameters characterizing the recombination properties of the surface but are not the surface recombination rates of electrons and holes in the strict sense. Similarly, for the surface $x = -a$, we derive

$$\frac{1}{e}j_p\Big|_{x=-a} = -S_n^-\Delta n\Big|_{x=-a} - S_p^-\Delta p\Big|_{x=-a}, \quad (8)$$

where

$$S_{n,p}^- = \lim_{\delta\to 0}\int_{0}^{\delta}\frac{dx}{\tau_{n,p}}.$$

Since condition (4) is valid in the entire semiconductor volume and at its interface with the metal, there is no need to introduce additional BCs for j_n.

When deriving BCs (11) and (12), we assumed that surface recombination centers are located in a thin surface layer much thinner than the Debye length (see the definition of $S_{n,p}^{\pm}$). Hence, in contrast to the BCs used previously [3–5], this model accounts for (in terms of $\Delta n|_{x=\pm a}$ and $\Delta p|_{x=\pm a}$) the influence of the Debye surface charge on the photovoltage induced at the actual metal–semiconductor interface.

We now use fundamental condition (4), being a consequence of the law of charge conservation, to derive the BCs for nonequilibrium electric and chemical potentials. To this end, we substitute expressions (5) into identity (4) and obtain

$$\frac{\sigma_n}{e}\frac{d\Delta F_n}{dx} - \frac{\sigma_p}{e}\frac{d\Delta F_p}{dx} - (\sigma_n + \sigma_p)\frac{d\Delta\varphi}{dx} = j_0. \quad (9)$$

Let us integrate Eq. (9) with respect to x from $a - \delta$ to $a + \delta$ with δ tending to zero,

$$\lim_{\delta\to 0}\int_{a-\delta}^{a+\delta}\frac{\sigma_n}{e}\frac{d\Delta F_n}{dx}dx - \lim_{\delta\to 0}\int_{a-\delta}^{a+\delta}\frac{\sigma_p}{e}\frac{d\Delta F_p}{dx}dx,$$
$$- \lim_{\delta\to 0}\int_{a-\delta}^{a+\delta}(\sigma_n + \sigma_p)\frac{d\Delta\varphi}{dx} - \lim_{\delta\to 0}\int_{a-\delta}^{a+\delta}j_0 dx = 0. \quad (10)$$

The last integral in Eq. (10) is equal to zero, since the integrand is finite. The next-to-last integral in Eq. (10) can be finite only in the case of the step $\Delta\varphi$ at the interface. We recall that $\Delta\varphi$ is the change in the potential, caused by the direct electric current j_0 in the sample. A physical cause, which can give rise to the step $\Delta\varphi$ is the voltage drop at the finite metal–semiconductor resistance,

$$\Delta\varphi|_{x=\mp a} - \Delta\varphi_M\big|_{x=\mp a} = \pm\frac{j_0}{\sigma_S^{\mp}}, \quad (11)$$

where $\Delta\varphi_M$ is the change in the electric potential of the metal contact and $\sigma_S^{\pm}$ is the sample surface conductivities (the $\sigma_S^{\pm}$ units are $1/\Omega\ \text{cm}^2$).

Taking into account the constant chemical potential of the metal contact, Eqs. (10) and (11) are written as

$$\frac{1}{e}\sigma_p^+\Delta F_p\Big|_{x=a} - \frac{1}{e}\sigma_n^+\Delta F_n\Big|_{x=a} - \frac{\sigma_n^+ + \sigma_p^+}{\sigma_S^+}j_0 = 0, \quad (12)$$

where $\sigma_{n,p}^+ = \lim_{x\to a-0}\sigma_{n,p}$ is the n- and p-type conductivities near the surface $x = a$ on the semiconductor side (surface conductivities). The units of the surface conductivities $\sigma_{n,p}^+$ are the same as those of the bulk ones, $1/\Omega\ \text{cm}$.

Similarly, for the surface $x = -a$, we obtain

$$\frac{1}{e}\sigma_p^-\Delta F_p\Big|_{x=-a} - \frac{1}{e}\sigma_n^-\Delta F_n\Big|_{x=-a} - \frac{\sigma_n^- + \sigma_p^-}{\sigma_S^-}j_0 = 0, \quad (13)$$

where $\sigma^{-}_{n,p} = \lim_{x \to -a+0} \sigma_{n,p}$.

If the surface conductivity at the metal–semiconductor contact is sufficiently high (the contact is ohmic), relation (11) can be written as

$$\Delta\varphi_M\big|_{x=\pm a} = \Delta\varphi\big|_{x=\pm a}. \quad (14)$$

Relation (14) is all the more valid at $j_0 = 0$. In this case, Eqs. (12) and (13) yield

$$\sigma^{\pm}_n \Delta F_n\big|_{x=\pm a} = \sigma^{\pm}_p \Delta F_p\big|_{x=\pm a}. \quad (15)$$

Hereinafter, we assume that BCs are symmetric: $S^{+}_{n(p)} = S^{-}_{n(p)} = S_{n(p)}$, $\sigma^{+}_{n(p)} = \sigma^{-}_{n(p)} = \sigma^{S}_{n(p)}$; the contacts are assumed to be ohmic. Solving Eqs. (1)–(3) with BCs (14) and (15) and supplementary condition (4), we obtain

$$\Delta n = j_0 \frac{eF_0}{kT}\left[\sinh\frac{x}{\lambda} + \frac{(\theta n_0/p_0 - 1)}{(1+\theta)}\frac{\sinh x/r_D}{\sinh a/r_D}\right], \quad (16)$$

$$\Delta p = j_0 \frac{eF_0}{kT}\left[\left(1 - \frac{(n_0 + p_0)(\mu_n - \mu_p)}{(n_0\mu_n + p_0\mu_p)}\frac{r_D^2}{\lambda^2}\right)\sinh\frac{x}{\lambda} - \frac{p_0}{n_0}\frac{(\theta n_0/p_0 - 1)}{(1+\theta)}\frac{\sinh x/r_D}{\sinh a/r_D}\right], \quad (17)$$

$$\Delta\varphi = j_0 F_0\left[\frac{(\theta n_0 - p_0)}{n_0 p_0 (1+\theta)}\frac{\sinh x/r_D}{\sinh a/r_D} + \frac{(\mu_n - \mu_p)}{(n_0\mu_n + p_0\mu_p)}\frac{\sinh x/\lambda}{\sinh a/\lambda}\right] - j_0 \frac{x}{e(n_0\mu_n + p_0\mu_p)}, \quad (18)$$

where

$$F_0 = \frac{\lambda}{D_S}\frac{p_0}{e\mu_n(n_0 + p_0)},$$

$$D_S = \coth\frac{a}{\lambda} + \frac{(n_0 + p_0)}{(1+\theta)}\left(\frac{\nu_n}{p_0}\theta + \frac{\nu_p}{n_0}\right), \quad (19)$$

$$\lambda = \sqrt{\frac{kT}{e}\frac{(n_0 + p_0)\mu_n\mu_p}{(n_0\mu_n + p_0\mu_p)}\tau}$$

is the diffusion length,

$$r_D = \sqrt{\frac{\varepsilon\varepsilon_0 kT}{e^2(n_0 + p_0)}}$$

is the Debye length, $\nu_{n,p} = S_{n,p}\tau/\lambda$, $\theta = \sigma^S_p/\sigma^S_n$, and $\tau = \tau_n\tau_p/(\tau_n + \tau_p)$ is the lifetime of nonequilibrium EHPs in the sample bulk.

A comparison of expressions (16) and (17) shows that a space charge indeed arises in the semiconductor, which causes the redistribution of the potential (the bracketed term in expression (18)).

It follows from expressions (14) and (18) that the voltage drop $U = \Delta\varphi_M(-a) - \Delta\varphi_M(a)$ in the sample is given by

$$U = j_0 \frac{2a}{e(n_0\mu_n + p_0\mu_p)}\left[1 - \frac{\lambda}{aD_S}\frac{(\theta n_0\mu_n - p_0\mu_p)}{n_0\mu_n(1+\theta)}\right]. \quad (20)$$

From Eq. (20), we find the sample resistance

$$R = R_0\left[1 - \frac{\lambda}{aD_S}\frac{(\theta n_0\mu_n - p_0\mu_p)}{n_0\mu_n(1+\theta)}\right], \quad (21)$$

where $R_0 = \dfrac{2a}{ebd(n_0\mu_n + p_0\mu_p)}$ is the classical resistance of the sample.

We note that, at $\sigma^S_{n(p)} = \sigma_{n(p)}$, the sample resistance is equal to the classical value irrespective of $S_{n,p}$ and the sample thickness. This result is obvious enough, since there is no physical metal–semiconductor interface in this case. At the same time, it confirms the validity of BCs (14) and (15). Such a situation can be experimentally realized using a "dumbbell-shaped" sample cut out from a semiconductor crystal. When deriving expressions (16)–(18), we assumed that the diffusion length greatly exceeds the Debye radius.

3. DISCUSSION

It follows from relation (13) that the resistance of the sample is equal to the classical value $R = R_0$ in the case of intense carrier recombination ($S_{n,p} \gg \lambda/\tau$) at surfaces $x = \pm a$, since there are no nonequilibrium carriers in the sample.

Let us consider the case of low-rate surface recombination of carriers, $S_{n,p} \ll \lambda/\tau$ in more detail. In this case, the sample resistance is given by

$$R = R_0\left[1 - \frac{(\theta n_0\mu_n - p_0\mu_p)}{(1+\theta)n_0\mu_n}\frac{\lambda}{a}\tanh\frac{a}{\lambda}\right]. \quad (22)$$

For short samples ($a \ll \lambda$), we use formula (22) to obtain

$$R = R_0\frac{(n_0\mu_n + p_0\mu_p)}{n_0\mu_n(1+\theta)}. \quad (23)$$

At $\theta \ll 1$ ($\sigma^S_p \ll \sigma^S_n$), it follows from formula (23) that

$$R = \frac{2a}{ebdn_0\mu_n}; \quad (24)$$

i.e., the resistance of the sample in this case is caused only by electrons and is the highest. At $\theta \gg 1$ ($\sigma^S_p \gg \sigma^S_n$), formula (23) is written as

$$R = \frac{2a}{ebdn_0\mu_n}\frac{\sigma^S_n}{\sigma^S_p}; \quad (25)$$

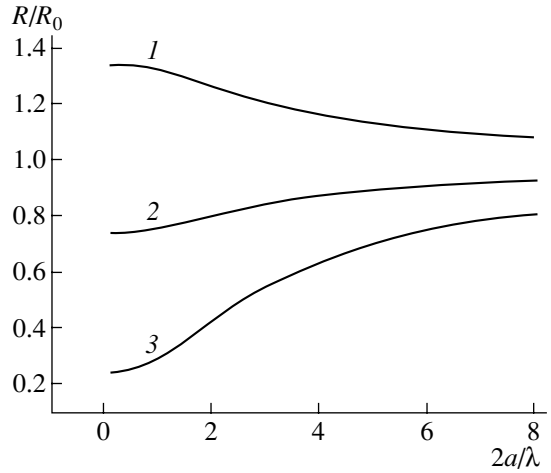

Dependence of the normalized resistance of a Ge sample on its length at θ = (*1*) 0.1, (*2*) 1, and (*3*) 5 and T = 310 K.

i.e., the resistance of the sample becomes much lower than the classical value.

Let us consider the causes of this extraordinary effect in detail. As follows from relations (16) and (17), nonequilibrium EHPs in the bulk of the sample (the terms $\propto \sinh x/\lambda$ are drifted by the current j_0 from the anode to the cathode; therefore, their concentration near the surface $x = a$ is positive. Using boundary condition (12) and taking into account the ohmic contacts, we obtain

$$\Delta n(a) = \frac{n_0}{p_0}\frac{\sigma_p^S}{\sigma_n^S}\Delta p(a).$$

Since $\sigma_p^S \gg \sigma_n^S$, we have $\Delta n(a) \gg \Delta p(a)$, and the concentrations of nonequilibrium carriers are positive. Hence, a negative surface charge is induced near the surface $x = a$ at a distance of the Debye length, and the electrostatic potential of the contact increases.

Relation (18) yields the distribution of the electrostatic potential in short samples at low-rate surface recombination,

$$\Delta\varphi = -\frac{j_0}{e\mu_n(n_0 + p_0)}\left[x - a\frac{(\theta - p_0/n_0)}{(1+\theta)}\frac{\sinh x/r_D}{\sinh a/r_D}\right]. \quad (26)$$

It follows from distribution (26) that φ is a steadily decreasing function of x at $\theta \ll 1$, and the electric field is positive at all the points of the sample. At $\theta \gg 1$, φ is a nonmonotonic function of x, having extrema at distances $r_D \ln a/r_D$ from the sample surfaces; as a result, the electric field becomes negative in surface regions.

The figure shows the dependence of the resistance of an intrinsic Ge sample (T = 310 K, λ = 0.1 cm, μ_n = 3800 cm^2/(V s), and μ_p = 1800 cm^2/(V s) on its length at various ratios of the surface conductivities θ in the case of $S_{n,p} \gg \lambda/\tau$. We can see that the resistance depends heavily on θ, especially in short samples.

4. CONCLUSION

It was shown that the deviation of the resistance from the classical value under symmetric boundary conditions is caused by a space charge arising in the semiconductor. The space charge is formed not only at the Debye length from the sample surface, but also at a diffusion length. Depending on the ratio of the surface *n*- and *p*-type conductivities, the resistance of the sample may become higher or lower than the classical value. This effect is most pronounced in samples whose rate of surface recombination is quite low and whose length is much shorter than the diffusion length.

REFERENCES

1. I. N. Volovichev and Yu. G. Gurevich, Fiz. Tekh. Poluprovodn. (St. Petersburg) **35**, 321 (2001) [Semiconductors **35**, 306 (2001)].
2. W. Shockley and W. T. Read, Phys. Rev. **87**, 835 (1952).
3. Yu. G. Gurevich, G. N. Logvinov, G. Espejo, *et al.*, Fiz. Tekh. Poluprovodn. (St. Petersburg) **34**, 783 (2000) [Semiconductors **34**, 755 (2000)].
4. Yu. G. Gurevich, J. Thermoelectr., No. 2, 5 (1997).
5. O. Yu. Titov, J. Giraldo, and Yu. G. Gurevich, Appl. Phys. Lett. **80**, 3108 (2002).
6. G. E. Pikus, Zh. Tekh. Fiz. **26**, 22 (1956).
7. G. P. Peka, *Physical Phenomena on Semiconductor Surfaces* (Vishcha Shkola, Kiev, 1984).

Translated by A. Kazantsev

Semiconductors, Vol. 38, No. 3, 2004, pp. 288–292. Translated from Fizika i Tekhnika Poluprovodnikov, Vol. 38, No. 3, 2004, pp. 300–304.

ELECTRONIC AND OPTICAL PROPERTIES OF SEMICONDUCTORS

Magnetic Investigations of $Cd_{1-x}Zn_xTe$ (x = 0.12, 0.21) Wide-Gap Semiconductors

Yu. V. Shaldin*^, I. Warchulska, M. Kh. Rabadanov*, and V. K. Komar'*****

**Shubnikov Institute of Crystallography, Russian Academy of Sciences, Leninskiĭ pr. 59, Moscow, 117333 Russia*

^e-mail: graimo@aha.ru

***International Laboratory of High Magnetic Fields and Low Temperatures, 53-421 Wroclaw, Poland*

****NTK Institute of Single Crystals, National Academy of Sciences of Ukraine, Khar'kov 61001, Ukraine*

Submitted June 25, 2003; accepted for publication July 9, 2003

Abstract—The results of measuring the magnetization M and magnetic susceptibility χ of $Cd_{1-x}Zn_xTe$ crystals are presented. The hysteresis of the $M(H)$ dependence, which is caused by the presence of arbitrarily oriented magnetic clusters, is observed in magnetic fields $H < 2$ kOe. Van Vlek paramagnetism, which is caused by electric fields of defects, makes a substantial contribution to the magnetic susceptibility. The anomalies in the $\chi(T)$ dependence in the temperature region $T < 50$ K are associated with variation in the charge state of interstitial Te for $x = 0.12$. For $x = 0.21$, these anomalies can be caused either by the paramagnetism of noninteracting defects or by antiferromagnetic ordering of the defect subsystem formed by Zn_{Cd} and Te_i. The effect of annealing on the magnetic state of a defect subsystem in the samples is ascertained.

1. INTRODUCTION

The development of a CdTe-based material with quite high resistivity is a rather complex problem of the materials science of semiconductors but is of great current interest. Such a material is necessary for the development of active elements of numerous devices, e.g., modulators and detectors. The starting point for the solution of this problem should be the modern conception of the actual structure of CdTe, which is determined by growth conditions.

It is evident a priori that wide-gap semiconductors with a band gap of $E_g > 1$ eV should possess low conductivity and be diamagnetic due to the known characteristic of a chemical bond formed by two bound electrons with opposite spins. However, all II–VI compounds are in fact nonstoichiometric, and intrinsic defects, namely, vacancies (V_A and V_B) and interstitials (A_i and B_i), cause deviation from the ideal structure. The emergence of defects during growth causes a substantial variation in physical properties. Therefore, the establishment of the correlation between growth conditions and physical properties is not only of practical interest. It is also necessary in order to refine our notion of the nature of physical properties of actual crystals.

At this stage, the state of research into the defects formed during growth in II–VI crystals has been analyzed in most detail in [1, 2]. Taguchi and Ray [1] paid special attention to the formation and stability of isolated and bound defects whose charge states may vary under external effects. Under specific conditions, for example, at low temperatures, donors and acceptors become paramagnetic [3], whereas the donor–acceptor pairs (DAPs), which are formed in the crystals, may cause the formation of specific magnetic clusters [4].

Kröger was the first to point out the potential of magnetic methods for studying defects [5]. Later on, the magnetic properties of CdTe doped with Ge [6, 7], In and Cl [8], Zn [9], and ZnO:Li [10] were investigated. The results of these investigations enabled researchers to reveal the substantial contributions of the Van Vlek paramagnetism, the precession Langevin diamagnetism, and the paramagnetism of mutually interacting DAPs to the total magnetic susceptibility. Moreover, the results of investigations for CdTe:Ge [11] and PbTe:In [12] crystals are indicative of a clearly pronounced hysteresis of magnetization in weak magnetic fields.

The investigation of the effect of isomorphic substitutions on the physical properties is undoubtedly also of interest. Komar *et al.* cast doubt on the current notion that the variation in the composition in the CdTe–ZnTe system is accompanied by variation in physical properties [13]. Their results indicate that the point-group macrosymmetry of the samples varies from $\bar{4}3m$ to $3m$. Consequently, at least an electret state is formed in the samples. This state is destroyed on heating above 450 K. The problem of studying the effect of heat treatment on the magnetic properties of $Cd_{1-x}Zn_xTe$ was not formulated.

In this study, we continue a series of papers on the results of measurements of the magnetization curves and magnetic susceptibility of actual II–VI crystals. Below, we will consider the magnetic properties of starting and thermally treated $Cd_{1-x}Zn_xTe$ (x = 0.12, 0.21) single crystals in magnetic fields as strong as H = 4.25 kOe in the temperature range T = 4.2–300 K.

1063-7826/04/3803-0288$26.00 © 2004 MAIK "Nauka/Interperiodica"

2. EXPERIMENTAL

Single crystals grown by the Bridgman–Stockbarger method from a melt under a high Ar pressure were studied [14]. During the entire crystal growth cycle, the pressure in the chamber was maintained at about 100 atm. Graphite crucibles with strengthening pyrolytic-carbon coating were used as the containers for charging. The charge consisted of preliminarily synthesized CdTe with the addition of crystalline ZnTe in an amount necessary to form a $Cd_{1-x}Zn_xTe$ ternary solid solution with a nominal Zn content $x = 0.12$ or $x = 0.21$ in most of the ingot. As multistage purification was applied to each of the main elements, all the components used before charging had a purity no lower than the 6*N* grade.

The Zn content in the solid solution was measured by electron-probe microanalysis (EPMA) using a JEOL JSM-820 scanning microscope with a LINK 10000 system for X-ray microanalysis. The concentration of the background impurities was measured by laser mass spectroscopy (LMS) using an EMAL-2 system. The integrated impurity level was no higher than 10^{-4} wt % for 75 elements. The degree of structural quality of the crystals was monitored by X-ray diffraction (XRD) using a double-crystal X-ray diffractometer based on a standard DRON-3 system. According to the data obtained, low-angle boundaries and twins were absent in the starting samples, whereas the average half-width of their rocking curves was equal to 16″–20″. Investigation of the current–voltage characteristics of the samples with nonrectifying contacts showed that even undoped samples had a high resistivity in the range from 10^{10} to 10^{11} Ω cm.

X-ray structural investigations (an Enraf-Nonius diffractometer, MoK_α radiation, $\sin\theta/\lambda < 1.14$ Å^{-1} at room temperature were performed for spherical samples of mixed CdTe–ZnTe crystals. When refining the atomic models of the structure, we assumed that the distribution of substitutional atoms in the samples is stochastic. In this case, according to the binomial distribution, the probability of formation of coordination tetrahedra of the [$TeCd_3Zn$] and [$TeCd_2Zn_2$] type, for example, for $x = 0.21$, is equal to 0.41 and 0.17, respectively. Since the local symmetry of such tetrahedra corresponds to the point-symmetry groups 3*m* and *mm*2, the packing of mesotetrahedra into the unit cell should satisfy the symmetry considerations and correspond to the minimum of the thermodynamic potential. The total dipole moment should be equal to zero. Processing the data of the precision X-ray diffraction experiment indicates with a high degree of confidence that the Zn site splits along the ⟨111⟩ crystallographic directions (Fig. 1). Calculations of single-particle atomic potentials for disordered models showed that a multivalley potential with energy barriers comparable to kT (k is the Boltzmann constant) emerges only for Zn atoms. This fact means that the clusters, which are grouped into domains, can emerge in the sample. The domain dimensions are apparently determined by the growth conditions of the samples. Thus, the results of processing the X-ray diffraction experiment do not contradict the fact that spontaneous polarization was found in CdTe–ZnTe crystals [13]. The local electric fields emerging in this case lead to a mixing of the energy levels of valence electrons and, as a result, to the emergence of at least the additional contribution of Van Vlek paramagnetism to the total magnetic susceptibility [8, 10, 11].

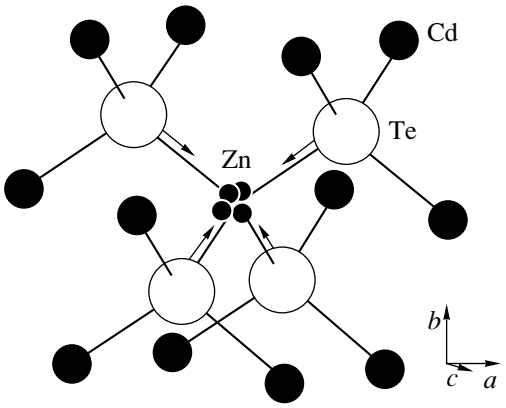

Fig. 1. Most probable variant of splitting the Zn atomic site in the CdTe lattice.

Starting samples shaped as plates oriented along the ⟨111⟩ direction were cut from ingots (boules). For magnetic measurements, the plates were cut into parallelepipeds $3.0 \times 3.0 \times 3.5$ mm^3 in size. The samples in a copper container were suspended on a Kevlar filament inside a flow-through He cryostat placed between the poles of a constant magnet with special heads. As a recording facility, a Cahn-1000 Electrobalance was used. All measurements of the magnetic susceptibility and magnetization curves were carried out under conditions of increasing temperature. The sensitivity of the setup was ~3×10^{-8} cm^3/g for a sample weight of ~0.3 g. Owing to the difficulty of exactly fixing the samples relative to the magnetic field direction, the results presented are averaged in the (111) plane. The magnetization of the samples was measured at T = 4.2, 77.5, and 293 K in a magnetic field from 0.05 to 4.25 kOe. The construction of the setup did not provide reversal of the magnetic field H. The samples measured were subsequently annealed in a muffle furnace at 450 K for 2 h and mounted inside the cryostat and cooled, after which the measurements were repeated.

3. RESULTS AND DISCUSSION

The results of measuring the magnetization M of CdTe–ZnTe samples at 4.2, 77.3, and 290 K, as well as the temperature dependences of magnetic susceptibility χ, are shown in Figs. 2 and 3. When analyzing the results presented, the following conditions should be established. (i) For all cases, when the total susceptibility is nega-

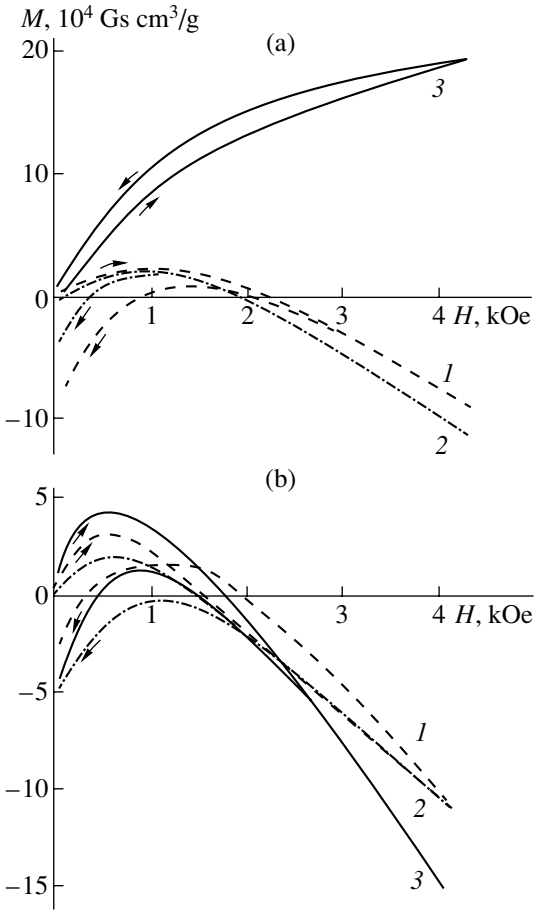

Fig. 2. Magnetization curves for the $Cd_{1-x}Zn_xTe$ single crystals. (a) $x = 0.12$ and (b) $x = 0.21$. $T =$ (*1*) 293, (*2*) 77.3, and (*3*) 4.2 K.

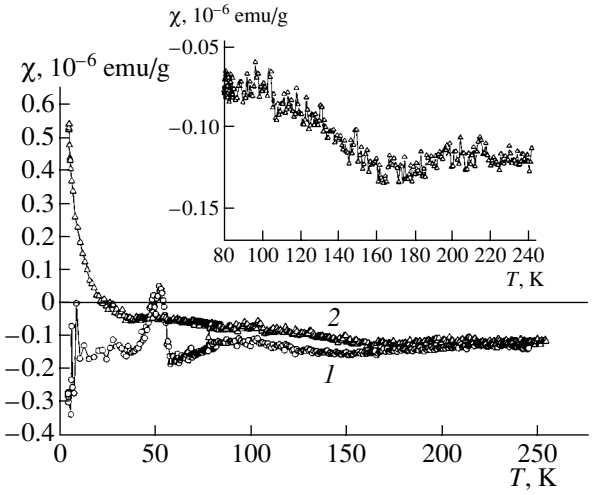

Fig. 3. Temperature dependences of the magnetic susceptibility for $Cd_{1-x}Zn_xTe$ single crystals. (*1*) $x = 0.12$ and (*2*) $x = 0.21$. $H = 3$ kOe. The portion of dependence *2* is in the inset.

tive, magnetic hysteresis is observed in the fields $H <$ 2 kOe. (ii) For $H > 2$ kOe, the samples tend to the equilibrium state with the minimum of the corresponding thermodynamic potential under the condition $\partial M/\partial H < 0$. (iii) The $M(H)$ dependence, which corresponds to the paramagnetic state of the sample with $x = 0.21$ (Fig. 2, curve *1*) with subsequent transition to the stable thermodynamic state in fields stronger than 4 kOe, is an exception. (iv) In the fields ~3 kOe, the magnetic susceptibility at $T > 100$ K is virtually independent of the concentration of Zn atoms. (v) The most significant distinction is observed only in the low-temperature range.

As was already noted above, the magnetic susceptibility of actual crystals is composed of the magnetic susceptibility of the nominally pure sample χ^d and the quantity $\Delta\chi^p$. The latter characterizes the contribution of intrinsic defects and their possible associations with impurities. The value of -3.5×10^{-7} cm^3/g given previously should be accepted for χ^d [5, 9]. As was shown by White, χ^d is practically independent of the external effects [4]. In this case, the difference $(\chi - \chi^d)$ will characterize the contribution of defects $\Delta\chi^p$ to the magnetic susceptibility of the samples under investigation.

We believe that the role of substitutional atoms and intrinsic lattice defects is twofold. On the one hand, their presence causes lattice strain and, consequently, is accompanied by local electric fields in the piezoelectric. On the other hand, the defects themselves and their associations may be the carriers of the magnetic moment in the electron subsystem of the crystals. In the crystals investigated, local electric fields of defects, namely, substitutional atoms and interstitial tellurium, cause the elimination of anisotropic (with allowance made for spin–orbit interaction) degeneracy of electron levels in the Brillouin zone. This degeneracy is linear in field [15]. It is our opinion that this is inevitably accompanied by partial mixing of the ground and excited states. This assumption enables us to explain the substantial distinction between the measured values of χ and estimates given in [5, 9] due to the contribution of Van Vlek paramagnetism, which is also practically independent of T. Therefore, we can further assume that the anomalies observed experimentally are the consequence of some magnetic interactions in the electronic subsystem of the samples. The direct manifestation of these interactions is the magnetic hysteresis in the fields $H < 2$ kOe, which emerges due to the existence of a large number of metastable states caused by the splitting of the Zn sites in the lattice. For semiconductors, magnetic hysteresis is caused by irreversible rotation of magnetization vectors of magnetic clusters formed by defects [4, 16]. When the external effects are varied, for example, the Zn concentration and temperature, the slow rotation is suppressed. Two suppressing factors should be taken into the consideration. One factor is the contribution of the Langevin paramagnetism of defects, which possess a magnetic moment and do not affect each other under the fixed parameters of interaction.

The other factor is the antiferromagnetic ordering of the defect subsystem formed by substitutional atoms and interstitial tellurium. This portion of the dependence is described by the Curie–Weiss law with the constant $C \approx 2 \times 10^{-6}$ cm^3/g. It seems impossible as yet to specify definitively the type of defects and their concentration.

An anomaly is clearly seen in the inset to Fig. 3; specifically, the magnetic susceptibility is partially saturated. The derivative $\partial\chi/\partial T$ is largest at $T \approx 130$ K. A similar saturation phenomenon is observed for CdTe crystals doped with other impurities [9]. All these facts enable us to state that the experimentally revealed anomaly is associated with the magnetic cluster formed by DAPs of the ($V_{Cd}X_{Cd}$) type. In this cluster, the Al atoms play the role of background impurity X. We estimated their contribution to the magnetic susceptibility to be equal to 4×10^{-8} cm^3/g at $T \longrightarrow 0$.

The situation for the samples with a lower Zn concentration is similar to that for Ge-doped CdTe [11]. Panchuk *et al.* considered the peak in the $\chi(T)$ dependence at $T \approx 50$ K as the result of variation in the charge state of interstitial Te from Te_i'' to Te_i' [8]. With a further decrease in temperature, the carriers are localized at acceptors and render them uncharged. The variation in the charge state of interstitial Te is accompanied by varying the strength of local electric fields. This process is naturally accompanied by a decrease in the contribution of Van Vlek paramagnetism. This leads to an increase in the magnitude of total magnetic susceptibility for the samples with a lower Zn content.

The effect of thermal treatment on the effective values of the magnetic susceptibility of starting CdTe–ZnTe samples is illustrated by the data shown in Fig. 4. Attention should be paid to the considerable variations in these dependences. The curves are virtually identical except for the range 50–100 K. This fact means that the incorporation of Zn atoms into the lattice is governed by certain mechanisms that lead to both electrical [13] and magnetic ordering of substitutional defects in starting samples. Therefore, it is not surprising that thermal treatment of the samples leads to a variation in the thermodynamic state of "quenched" samples, specifically, to the minimization of the thermodynamic potential. This process is apparently accompanied by variation in the charge state of the defect subsystem as a whole. This leads to a decrease in the local electric fields and, consequently, in the contribution of Van Vlek paramagnetism to the total magnetic susceptibility. The question of which centers are responsible for such electrical and magnetic interactions remains debatable.

We assume that anomalies of $\chi(T)$ in the range T = 20–50 K are associated with the magnetic ordering of the defect subsystem of the samples. Hence, we may conclude that the transition to the diamagnetic state of the sample as a whole is inevitably accompanied by

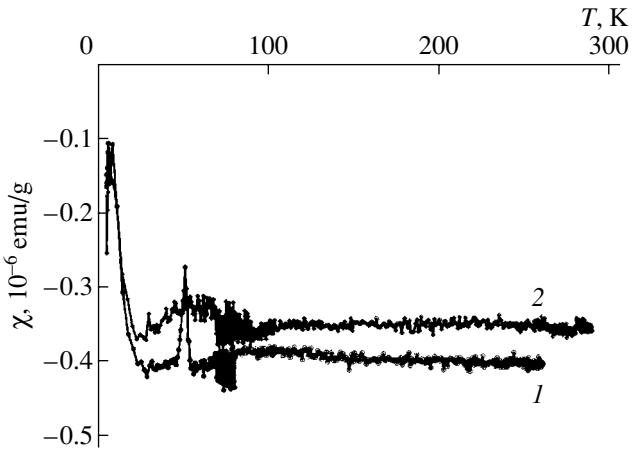

Fig. 4. Temperature dependences of the magnetic susceptibility for annealed $Cd_{1-x}Zn_xTe$ single crystals. (*1*) x = 0.12 and (*2*) x = 0.21. H = 3 kOe. The heating rate is 450 K/2h.

magnetic fluctuations of susceptibility, which are most noticeable after thermal treatment of the samples. It is difficult to fix the orientation of the samples in the Faraday method. Therefore, the difference between the experimental data for the starting and the thermally treated samples should be caused by the anisotropy of the physical processes occurring in the medium.

Thus, the lattice defects exert a substantial effect on the magnetic properties of the crystals investigated. Specifically, substitutional atoms and interstitial tellurium determine the magnitude of the Van Vlek paramagnetism. The existence of charged DAPs of the ($V_{Cd}X_{Cd}$) type makes an insignificant contribution to the total magnetic susceptibility. The role of substitutional atoms is clearly pronounced only in the low-temperature range and leads to an anomalous dependence of the contribution of defects to the total magnetic susceptibility of the crystals. Thermal treatment substantially affects the temperature dependences of the magnetic susceptibility of the samples. This leads to an increase in the magnitude of effective values of $\chi(T)$ due to an increase in the contribution of the Van Vlek paramagnetism caused by the electric fields of defects.

4. CONCLUSION

The existence of Van Vlek paramagnetism in CdTe–ZnTe mixed crystals can be used as the basis of a method for studying the actual structure of diamagnetic crystals. The potential of this method is considerably extended at temperatures below 4 K. Such methodological developments are necessary in order to understand the physical processes that determine the operational efficiency of practical devices, for example, detectors of hard radiation.

REFERENCES

1. T. Taguchi and B. Ray, Prog. Cryst. Growth Charact. **6**, 103 (1983).
2. *Physics of II–IV Compounds*, Ed. by A. N. Georgobiani and M. K. Sheĭnkman (Nauka, Moscow, 1986), Chap. 3, p. 72.
3. J. van Wieringen, Philips Tech. Rev. **19**, 301 (1957/1958).
4. R. M. White, *Quantum Theory of Magnetism*, 2nd ed. (Springer, Berlin, 1983; Mir, Moscow, 1985).
5. F. A. Kröger, *The Chemistry of Imperfect Crystals* (Wiley, New York, 1964; Mir, Moscow, 1969).
6. V. I. Ivanov-Omskii, B. T. Kolomiets, V. K. Ogorodnikov, *et al.*, Phys. Status Solidi A **13**, 61 (1972).
7. R. D. Ivanchuk, E. S. Nikonyuk, A. V. Savitskiĭ, and I. F. Snitsko, Fiz. Tekh. Poluprovodn. (Leningrad) **11**, 2046 (1977) [Sov. Phys. Semicond. **11**, 1202 (1977)].
8. O. Panchuk, A. Savitsky, P. Fochuk, *et al.*, J. Cryst. Growth **197**, 607 (1999).
9. Yu. V. Shaldin, Neorg. Mater. **37**, 671 (2001).
10. Yu. V. Shaldin, M. M. Musaev, and I. Varkhul'ska, in *Proceedings of V International Workshop on Magnetic Phase Transitions* (Makhachkala, 2002), p. 98.
11. Yu. V. Shaldin, I. Varkhul'ska, Yu. M. Ivanov, *et al.*, in *Proceedings of V International Workshop on Magnetic Phase Transitions* (Makhachkala, 2002), p. 65.
12. A. N. Vasil'ev, T. N. Voloshok, J. K. Warchulska, and H. Kageyama, J. Phys. Soc. Jpn. **70**, 22 (2001).
13. V. K. Komar', D. P. Nalivaĭko, A. S. Gerasimenko, *et al.*, Poverkhnost, No. 3, 94 (2002).
14. L. Benguigui, R. Weil, E. Muranevich, *et al.*, J. Appl. Phys. **74**, 513 (1993).
15. R. Parmenter, Phys. Rev. **100**, 573 (1955).
16. S. V. Vonsovskiĭ, *Magnetism* (Nauka, Moscow, 1971; Wiley, New York, 1974).

Translated by N. Korovin

Semiconductors, Vol. 38, No. 3, 2004, pp. 293–297. Translated from Fizika i Tekhnika Poluprovodnikov, Vol. 38, No. 3, 2004, pp. 305–309.

ELECTRONIC AND OPTICAL PROPERTIES OF SEMICONDUCTORS

Transport Phenomena in Coarse-Grain CdTe Polycrystals

S. A. Kolosov, Yu. V. Klevkov, and A. F. Plotnikov

Lebedev Institute of Physics, Russian Academy of Sciences, Leninskiĭ pr. 53, Moscow, 119991 Russia

Submitted March 31, 2003; accepted for publication July 15, 2003

Abstract—Transport properties of coarse-grain CdTe polycrystals are investigated. The results are interpreted on the basis of the assumption that a fairly large number of traps exist at the grain boundaries with trap energy levels being uniformly distributed within the band gap. It is shown that the exposure to white light affects appreciably the mobilities of majority carriers due to a variation in the height of intergrain energy barriers. © *2004 MAIK "Nauka/Interperiodica".*

1. INTRODUCTION

At present, polycrystalline semiconductors attract increased attention due to their potential use in microelectronics and in production of inexpensive solar cells [1, 2]. The progress in technologies of production of polycrystalline films already enabled researchers to suggest numerous new devices, namely, resistors, diodes, and bipolar and MOS transistors [3, 4]. Today, it is already clear that multilayered three-dimensional integrated structures based on polycrystalline films will be realized in the immediate future.

The potential usefulness of polycrystalline semiconductors depends on the crystalline quality of the grains and electronic properties of their boundaries. Despite the fact that the technological problems of preparing the polycrystalline materials have already been solved, the practical importance of intergrain boundaries as the dominant factor that affects the electrical properties of these materials is realized only now. Intergrain boundaries, in a general case, affect the electronic properties of the material in two ways.

First, the potential barriers induced by intergrain boundaries substantially reduce the mobilities of majority carriers, which leads to an increase in the effective resistivity of a semiconductor. This is undesirable for many practical applications because of both increased resistivity and difficulties in obtaining samples with reproducible resistivity.

Second, intergrain boundaries include dangling bonds, which may serve as carrier traps and attract impurities or intrinsic defects. These states reduce the mobilities and lifetimes of minority carriers.

A lot of models that more or less successfully interpret the experimental data have been suggested previously (see [5, 6]). However, none of these models explain the inconsistency between the results of crystallographic measurements and measurements of electronic characteristics of polycrystals. Perhaps only coarse-grained (>100 μm) polycrystals are an exception. However, in this case as well, the experimental methods that enable one to determine the energy distributions, i.e., the density of states of localized levels (traps) related to intergrain boundaries, are also based only on the measurements of majority-carrier transport characteristics [7]. Thus, de Graaf *et al.* measured the temperature dependences of conductivity of polycrystalline films using the doping method [8]. It was found that the density of electronic states within the band gap increases abruptly at the edges of the conduction (E_c) and valence (E_v) bands (Fig. 1).

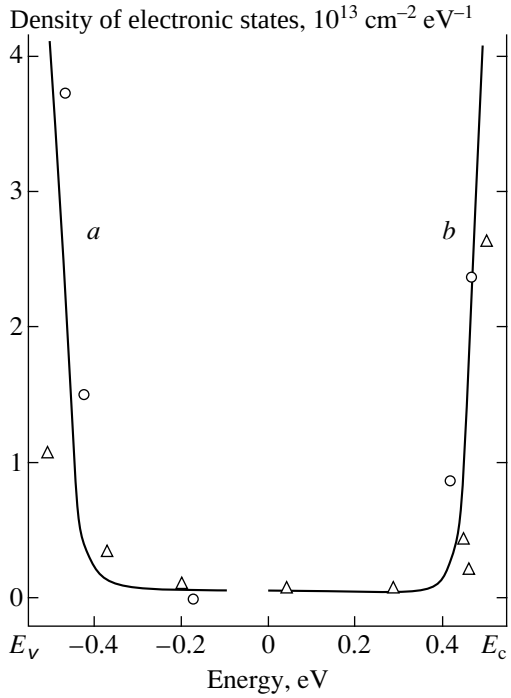

Fig. 1. Energy distribution of density of electronic states within the band gap at the grain boundaries in Si [8]: (*a*) acceptor traps and (*b*) donor traps.

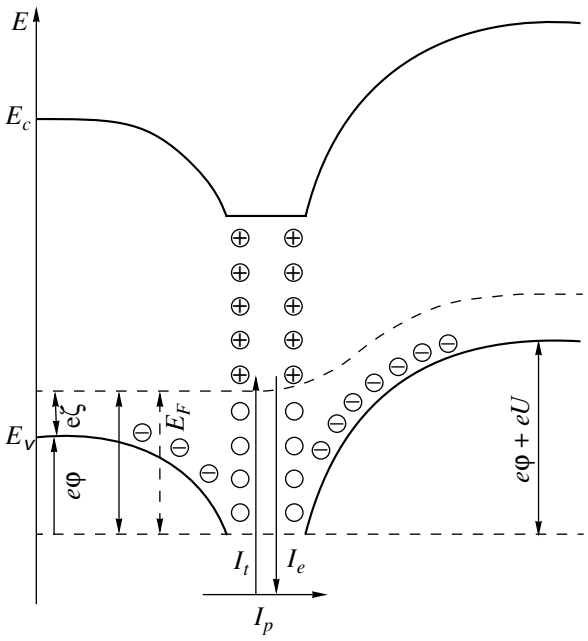

Fig. 2. Energy-band diagram of the intergrain boundary in *p*-conductivity polycrystals. I_p is the hole current through the barrier, I_t and I_e are the currents caused by the capture of holes at traps and by emission of holes from the traps, and *E* is the energy.

2. SCATTERING MECHANISMS AND TRANSPORT OF MAJORITY CARRIERS IN COARSE-GRAINED POLYCRYSTALS

In the ordinary sense, a polycrystal comprises the totality of grains (crystallites) separated by intergrain boundaries. The grain conductivity is determined by the concentration of dopants, by their activation energy, and by the mechanism of carrier scattering. As a rule, the current–voltage characteristic follows Ohm's law. The temperature dependences of grain conductivity under conditions of moderate doping enable one to determine the activation energies of dopants. However, the total current through the sample for polycrystals is determined both by the grain conductivity and by the mechanism of carrier transfer from one grain into another, i.e., by the mechanism of overcoming the intergrain barrier.

Fripp attempted to interpret the electrical properties of polycrystalline semiconductors on the basis of a so-called segregation model, according to which the impurity atoms are collected at intergrain boundaries, where they become electrically inactive [9]. However, it turned out that this model failed to account for either the temperature dependences of conductivity of polycrystals or the free-carrier mobilities.

The second model, suggested by Seto [10] and further improved by Baccarani and Ricco [11], implies the existence of a fairly large number of near-interface traps, which make free carriers immobile. On the basis of this model, the transport phenomena in polycrystals, which determine their main electrical properties, may be explained. In this case, it is assumed that the current of free carriers through the intergrain barriers follows the laws of thermionic emission and that these traps are occupied only partially when the depletion region does not exceed the crystallite size.

The schematic energy-band diagram of the intergrain boundary for *p*-type polycrystals is shown in Fig. 2. This model, which is already well developed now, was formulated for the first time by Petritz [12] and Mueller [13]. It is assumed, and this is already proven, that the holes are captured by the interface states, which are located above the Fermi level at the intergrain boundary E_F (Fig. 2). The negatively charged acceptors in the space charge region compensate the corresponding positive charge. This model predicts the existence of the total hole current I_p flowing from the left to the right,

$$I_p = A^*T^2 \exp\{-\beta(\zeta + \varphi)[1 - \exp(-\beta U)]\}. \quad (1)$$

Here, $\beta = e/kT$, e is the elementary charge, T is the temperature, k is the Boltzmann constant, A^* is the Richardson constant, and U is the voltage applied. The forward-biased (left) barrier is denoted as $e\varphi$, and $e\zeta$ is the Fermi level energy in crystalline grains, which depends on the dopant concentration and the degree of compensation. All energies are reckoned from the valence-band top.

According to this formula, the current I_p in a polycrystal of length L with the average grain size a is expressed by the formula

$$I_p = A^*T^2 \exp[-\beta(\zeta + \varphi)][1 - \exp(-\beta Ua/L)], \quad (2)$$

where Ua/L is the voltage drop per intergrain boundary. This quantity is usually small compared with kT/e, which enables us to determine the barrier conductivity σ using the expansion of the voltage-dependent term in formula (2) in a Taylor series:

$$\sigma = I_p/U = \sigma_\infty \exp(-E_a/kT), \quad (3)$$

where σ_∞ is a constant, and

$$E_a = E_F(T) + kT\ln(eA^*Ta/k\sigma_\infty). \quad (4)$$

It follows from (3) that, by measuring the temperature dependence of the barrier conductivity, it is possible to determine the activation energy E_a and, consequently, the barrier height

$$e\varphi = E_a - e\zeta. \quad (4a)$$

It was noted above that a polycrystal is the totality of grains and intergrain boundaries. Therefore, the temperature dependence of conductivity is determined by both the barrier and the grain conductivities. Both these constituents follow an exponential law, although with different activation energies. In the first case, this is the activation energy of the barrier conductivity, and in the second case, this is the activation energy of the doping impurity. Therefore, in order to reveal the role of barriers in the total conductivity of a polycrystal, polycrys-

tals with various doping levels of grains are investigated. As a rule, this method does not allow one to obtain unambiguous results since it is virtually impossible to grow polycrystals with grains that are identical in size and possess different doping levels. The second cause of ambiguity is related to the possible impurity segregation; as a result, certain number of impurity atoms remain electrically neutral, which is confirmed by experiments with ion doping of Si polycrystals by phosphorus [11].

Taking into account all these difficulties, we suggest a somewhat different method for investigation of polycrystals. Its essence is in the investigation of temperature dependences of conductivity of the samples exposed to optical radiation with a specified spectrum and a variable intensity. This enables us to generate a strictly controlled number of excess carriers.

Our results and their interpretation are given below.

3. EXPERIMENTAL

Electrical properties of high-purity textured *p*-CdTe polycrystals with resistivity at room temperature $\rho \sim 10^2$–10^5 Ω cm were investigated. The samples were cut from polycrystalline ingots grown at 600–620°C during the finish purification of CdTe [14]. The contacts were formed (after etching the samples in a bromine–methanol solution) by Au deposition from a solution of gold chloride. As a rule, these contacts were almost ohmic.

The temperature dependences of resistivity were measured in the temperature range from $T = 290$ to 65 K.

The samples were illuminated using a halogen lamp with a filament temperature of ~3000°C, which provided the white-light illumination of the samples with a photon-flux density of $\sim 10^{18}$ cm^{-2} s^{-1}.

4. RESULTS AND DISCUSSION

The temperature dependence of resistivity of the *p*-CdTe sample cut along the growth direction of the single-crystal grain is shown in Fig. 3 (curve *a*). The sample resistivity at 270 K was $\rho \sim 6 \times 10^2$ Ω cm, which corresponds to a free-hole concentration of $\sim 1.3 \times 10^{14}$ cm^{-3} and concentration of acceptor centers $N_A \approx 3 \times 10^{14}$ cm^{-3}.

Two slopes are pronounced in the temperature dependence of resistivity for this sample. The first slope is in a temperature range of 280–170 K, and the second slope is in the region of 160 K and below. The first slope corresponds to the activation energy (0.24 ± 0.02) eV and is apparently caused by local centers, which were observed by us previously [15, 16].

The second slope is more difficult to interpret. It cannot be attributed to the hole capture at shallower acceptors with a decrease in the temperature since the energy level of these acceptors calculated from the slope should be equal to 0.07 eV. However, it is known

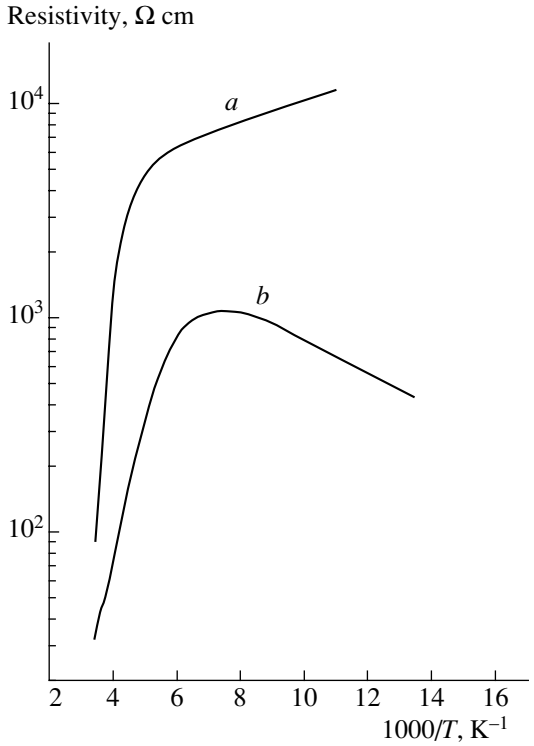

Fig. 3. Temperature dependences of resistivity for low-resistivity *p*-CdTe: (*a*) without illumination and (*b*) with irradiation by white light.

that the number of ionized acceptors at the temperature T is given by

$$N_{A^-} = N_A/[(2p/N_v)\exp(\Delta E/kT) + 1], \qquad (5)$$

where N_V is the density of states in the valence band and p is the free-hole concentration ($p \ll N_A$). In the temperature range under consideration, all acceptors with the energy $\Delta E = 0.07$ eV are ionized and, consequently, could not contribute to the variation in the free-carrier concentration.

Hence, it follows that this second slope is caused by a decrease in the hole mobility with decreasing temperature due to hole scattering at charged intergrain boundaries. The intensity of this scattering can be varied by decreasing or increasing the degree of charging of the intergrain boundary. This is confirmed by Fig. 3, which shows the temperature dependence for the same sample measured under the effect of white light (curve *b*).

When curves *a* and *b* in Fig. 3 are compared, three facts should be noted.

First, as should be expected, the illumination does not affect the energy position of the level of the local center, which captures the holes with decreasing temperature. The corresponding activation energy, as before, is equal to (0.24 ± 0.02) eV. Second, a rather large number of nonequilibrium carriers generated by radiation for some reason causes no substantial increase in conductivity in a temperature range of 280–

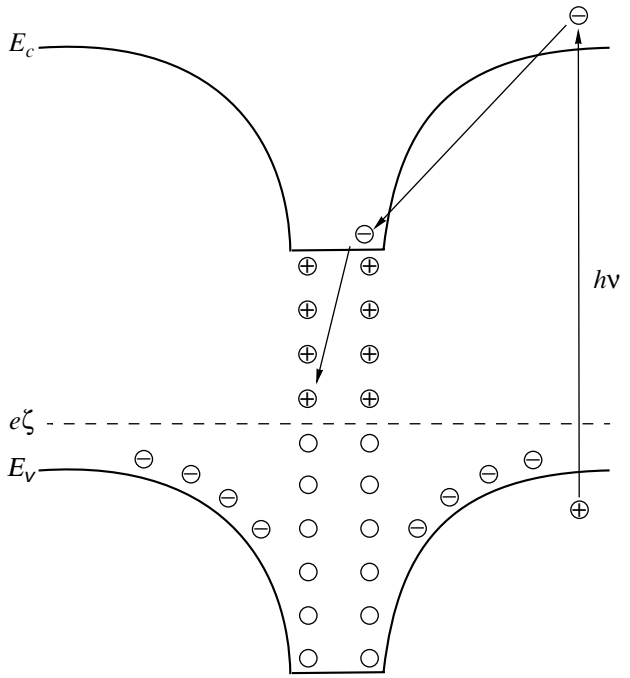

Fig. 4. A model of neutralization of the charge captured by the traps at the intergrain boundary with the generation of carriers by light with photon energy $h\nu$.

170 K. Third, most importantly, the hole mobility in the temperature region below 170 K decreases as $\mu \propto T^{-3/2}$, which is characteristic of carrier scattering by acoustic phonons.

The interpretation of the above results may cause doubts, especially with allowance made for the fact that these results are apparently obtained for CdTe polycrystals for the first time. However, the results are explainable based on the model of the barrier conductivity of polycrystals, and we are firmly sure of this fact.

It follows from the data presented in Fig. 3 that the barrier conductivity (see formula (3)) is controlled by the activation energy $E_a = (0.07 \pm 0.005)$ eV. Consequently, the potential barrier height at the grain boundaries can be calculated from formula (4a). The Fermi level in the grain $e\zeta = E_v - kT\ln(p/N_v)$ at ~200 K is located (0.20 ± 0.01) eV above the valence-band top. Correspondingly, the barrier height will be (0.13 ± 0.01) eV. The existence of this barrier is caused by the accumulation of a certain charge at a grain boundary. Unfortunately, the magnitude of this charge could not be calculated since the energy dependence of density of states at intergrain boundaries for CdTe polycrystals is known only qualitatively. However, this charge can be varied either by increasing or decreasing the Fermi level via doping or by illuminating the sample by radiation with a particular spectrum.

Absorption of light in the vicinity of the barrier causes the neutralization of localized charges, thus decreasing the barrier height and increasing the barrier conductivity. Petritz used the method of modulation of the barrier height for the first time in 1956 [17].

The model serving as the basis for our explanation of the results obtained is illustrated in Fig. 4. The radiation absorbed by the sample generates excess holes and electrons in the sample: $\Delta p = G\tau_p$ and $\Delta n = G\tau_n$, respectively. Here, G is the number of photons absorbed in 1 cm^3 of the sample per 1 s, and τ_p and τ_n are the hole and electron lifetimes. Note that $\tau_p < \tau_n$ for CdTe polycrystals. Therefore, the nonequilibrium concentration of electrons generated is substantially higher than the nonequilibrium hole concentration. However, this circumstance does not affect the conductivity type of the sample, since the initial slopes of *a* and *b* curves in Fig. 3 are identical. However, the character of conductivity at $T < 160$ K is appreciably affected. This is explained by the fact that the nonequilibrium electrons rapidly neutralize the holes captured by intergrain traps, which causes a substantial decrease in the barrier height.

The inequality between Δn and Δp also explains an insignificant variation in the sample conductivity at high temperatures. The holes excited by the light are captured by partially emptied intergrain traps and therefore do not contribute to conductivity.

It seems appropriate to make some comments related to the temperature range in which the barrier conductivity starts to play a substantial role. The electron emission current, which is determined by formula (1), accounts only for the presence of carrier energy sufficient to overcome the barrier. However, when passing from one grain into another one, the carrier should also possess a certain quasi-momentum to find an empty cell in the second grain. This quantum-mechanical selection rule causes a decrease in the rate of intergrain transitions. Therefore, the thermionic emission current should be decreased by a factor η, whose lowest value equals 0.8 at 300 K and 0.05 at 77 K [2]. This factor is mainly determined by misorientation of crystallographic axes of neighboring grains. Therefore, at high temperatures, when scattering by a large number of phonons efficiently "helps" the carrier to find its place in the **k** space of the corresponding grain, this factor is large. With decreasing temperature, when the number of phonons in the polycrystal becomes smaller and smaller, η decreases.

Figure 5 shows the temperature dependence of resistivity for a sample with a higher resistivity. However, the grain sizes in this sample are approximately the same as in the sample for which the results are shown in Fig. 3. The dependence has the same general form. The main contribution is as before made by defects with an ionization energy of (0.24 ± 0.02) eV, whereas the intergrain barrier height calculated from the second slope is equal to $\sim(0.07 \pm 0.01)$ eV. This is understandable, since the Fermi level in this sample is located substantially farther from the valence-band top and, consequently, corresponds to the region of substantially lower density of states (Fig. 1).

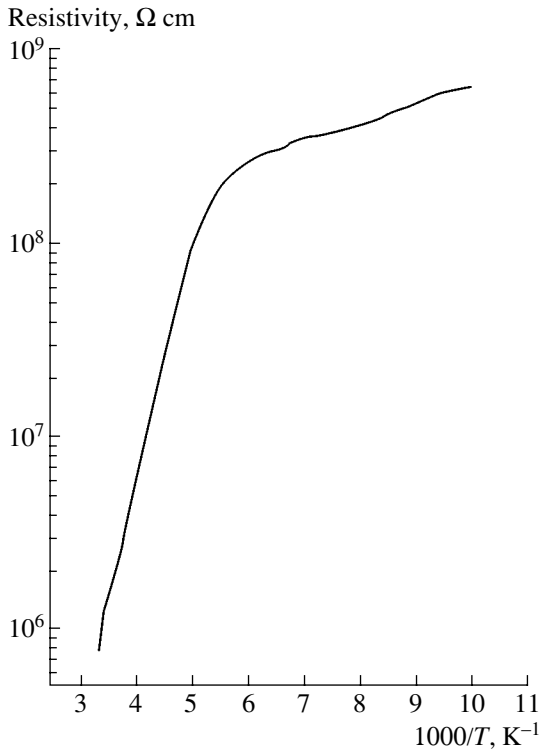

Fig. 5. Temperature dependence of resistivity for high-resistivity *p*-CdTe.

4. CONCLUSION

In this study, we used the model of formation of intergrain barriers due to the accumulation of localized charges at the interfaces and assumed that the current of free carriers through the barrier follows the laws of thermionic emission. On this basis, we attempted to explain the transport phenomena in coarse-grained CdTe polycrystals.

This model is debatable. Specifically, the transport phenomena in polycrystalline film were recently investigated by Meng and Cui [18]. They believe that the current through the barrier is the tunneling current. The barrier height calculated on the basis of this assumption is 0.55 eV. We cannot agree with this since the experimentally measured barrier heights in similar Si polycrystals do not exceed 0.03 eV.

We showed that it is possible to determine the barrier height without doping. Furthermore, the effect of white light substantially increases the majority-carrier mobility, which may facilitate the preparation of low-resistivity substrates from CdTe polycrystals.

ACKNOWLEDGMENTS

We thank Prof. V.S. Bagaev for his helpful suggestions.

This study was supported by the Russian Foundation for Basic Research, project nos. 02-02-17342 and 00-02-16500.

REFERENCES

1. H. J. Leamy, G. E. Pike, and C. H. Seager, *Crain Boundaries in Semiconductors* (North-Holland, New York, 1982).
2. E. S. Yang, Thin Solid Films **93**, 287 (1982).
3. R. R. Shah, D. C. Hollingsworth, G. A. Dejong, and D. L. Crosthwait, IEEE Electron Device Lett. **2**, 159 (1981).
4. T. I. Kamins, IEEE Electron Device Lett. **3**, 341 (1982).
5. I. Y. W. Seto, J. Appl. Phys. **46**, 5247 (1975).
6. N. C. C. Lu, L. Gertzberg, C. Y. Lu, and J. D. Meindl, IEEE Trans. Electron Devices **28**, 818 (1981).
7. *Polycrystalline Semiconductors: Physical Properties and Applications*, Ed. by G. Harbeke (Springer, Berlin, 1985; Mir, Moscow, 1989), Part 2.
8. H. C. de Graaff, M. Huybers, and J. G. de Groot, Solid-State Electron. **25**, 67 (1982).
9. A. L. Fripp, J. Appl. Phys. **46**, 1240 (1975).
10. I. Y. W. Seto, J. Electrochem. Soc. **122**, 701 (1975).
11. G. Baccarani and B. Ricco, J. Appl. Phys. **49**, 5565 (1978).
12. R. L. Petritz, Phys. Rev. **110**, 1254 (1958).
13. R. K. Mueller, J. Appl. Phys. **32**, 635 (1961).
14. S. A. Medvedev and Yu. V. Klevkov, RF Patent No. 243,014 (20 December 1999).
15. Yu. V. Klevkov, S. A. Kolosov, S. A. Medvedev, and A. F. Plotnikov, Fiz. Tekh. Poluprovodn. (St. Petersburg) **35**, 1192 (2001) [Semiconductors **35**, 1139 (2001)].
16. S. A. Medvedev, Yu. V. Klevkov, S. A. Kolosov, *et al.*, Fiz. Tekh. Poluprovodn. (St. Petersburg) **36**, 937 (2002) [Semiconductors **36**, 874 (2002)].
17. R. L. Petritz, Phys. Rev. **104**, 1508 (1956).
18. Fanying Meng and Rongqiang Cui, Jpn. J. Appl. Phys. **41**, 185 (2002).

Translated by N. Korovin

Semiconductors, Vol. 38, No. 3, 2004, pp. 298–303. Translated from Fizika i Tekhnika Poluprovodnikov, Vol. 38, No. 3, 2004, pp. 310–315.

ELECTRONIC AND OPTICAL PROPERTIES OF SEMICONDUCTORS

A Critical Analysis of Investigation of Deep Levels in High-Resistivity CdS Single Crystals by Photoelectric Transient Spectroscopy

A. P. Odrinskiĭ

Institute of Technical Acoustics, Belarussian Academy of Sciences, pr. Lyudnikova 13, Vitebsk, 210717 Belarus
e-mail: odra@mailru.com

Submitted June 26, 2003; accepted for publication August 26, 2003

Abstract—The investigation of high-resistivity CdS single crystals by photoelectric deep-level transient spectroscopy (PEDLTS) is discussed. Computer simulation of the experiment is carried out. This simulation enables us to compare the results obtained by the PEDLTS and thermally stimulated conductivity methods. The experimental potentials of these methods are compared. © *2004 MAIK "Nauka/Interperiodica".*

1. INTRODUCTION

In some fields of application of semi-insulating semiconductors, the effect of defects inducing deep levels in the band gap on the electrical properties of the material should be investigated. These fields are the development of semiconductor radiation detectors, various photoelectric converters, semiconductor lasers, and in-line control of substrates during the production of microcircuits.

At present, there are two main methods for investigation of deep levels in high-resistivity (as high as $10^{13}\ \Omega$ cm) semi-insulating semiconductors, which enable one to obtain "electrically measured" parameters of deep levels. These are the traditional method of thermally stimulated conductivity (TSC) and the PICTS method (photoinduced current transient spectroscopy), which was suggested relatively recently [1, 2] (see also [3]). Both methods may be applied not only to high-resistivity semiconductors. However, there are other numerous investigative methods applied to lower-resistivity materials. Therefore, it is of interest to apply these methods precisely to high-resistivity semiconductors.

In this study, the results of investigation of high-resistivity CdS crystals by the PICTS method are discussed. The currently existing theoretical model of the method is not without some contradictions [4, 5]. The bulk properties of crystals are considered in the model. However, the nonequilibrium carriers in the band are generated by radiation with $h\nu = E_g$, which is absorbed in a relatively thin surface layer. This calls for special care when the experiment and additional estimates are carried out, and the question always remains open as to which properties of the crystal, whether surface or bulk ones, are related to the phenomena observed. Another contradiction of the model is the question of experimental detectability of deep levels or occupancy of deep levels by nonequilibrium carriers in the temperature range where the PICTS signal should be detected. In this study, a computer simulation of the experiment by the PICTS method was carried out, which enabled us to refine the theoretical model.

2. EXPERIMENTAL

A number of CdS crystals grown by the Czochralski method under a controlled ratio of vapor pressures of starting components were investigated. The preliminary results of investigations have recently been reported [6], and a more detailed description is being prepared for publication. The setup was described in detail elsewhere [7]. The excitation by an Ar laser at the wavelength $\lambda = 4880$ Å was used in the experiment. Previously, Ag-doped CdS crystals were excited by an Ar laser with $\lambda = 4880$ Å and complicated spectra with overlapping peaks from several levels were observed [4]. Our investigations carried out using the same excitation for high-purity CdS crystals showed that this choice of excitation radiation is not quite appropriate. For some samples, the use of laser excitation provides well-structured spectra, whereas for other samples the spectra are "broadened" and structureless. This is apparently associated with the quality of the surface treatment. Optical radiation with wavelength $\lambda = 4880$ Å is absorbed in a thin surface layer, which may be completely located within the surface space charge region, where the analysis of recombination processes of nonequilibrium carriers is more complicated. Taking into account the requirement of uniformity of excitation over the entire sample bulk, I carried out the PICTS measurements with excitation by quasi-monochromatic light with $h\nu < E_g$ ($h\nu = 2.3$–2.5 eV). The radiation generated by a DKSSh-500 xenon lamp and passed through an MSD-1 monochromator with entrance and exit slits 5 mm in width, corresponding to the spectral

1063-7826/04/3803-0298$26.00

region of ~300 Å, was used. Corresponding optical filters eliminated overlapping with other orders of the grating. The inset in Fig. 1 shows the PICTS spectra obtained for a CdS single crystal grown with the ratio of partial vapor pressures $P(S)/P(Cd) = 4$ using laser excitation and excitation with $h\nu < E_g$. In [6], this sample was denoted as N_3. It can be noted that a decrease in the photon energy of excitation radiation for the N_3 single crystal does not affect the spectrum shape radically. The peak in a region of 80–120 K from deep levels with $E_t = 0.06$ eV and $S_{nt} = 10^{-19}$ cm^2 is dominant in the spectrum as before. However, some specific features can be revealed at higher temperatures. Figure 1 shows the spectra obtained for various energies of excitation radiation for a CdS single crystal grown at $P(S)/P(Cd) = 7.5$. In [6], this sample was denoted as N_4. For this crystal, the spectrum shape changes radically with decreasing photon energy of excitation radiation. The "broadened" structureless spectrum is transformed into a well-resolved spectrum, which is practically identical to the spectrum of the N_3 crystal with the same excitation. Thus, with decreasing photon energy of excitation radiation, the shape of PICTS spectra is improved. In this case, the signals from deep levels are detectable and are detected reliably.

An incandescent lamp with color filters cutting off some portions of the radiation spectrum was used as the source of excitation radiation. In this case, the presence or absence of some peaks attributed to various deep levels in the PICTS spectrum and the ratio of peak intensities depend on the spectrum of the excitation radiation. The temperature position of the peaks and parameters of deep levels, which are determined from these spectra, are virtually independent of the spectrum of the excitation radiation. Note that, in some studies [1, 4, 8–10], the excitation by light with $h\nu < E_g$ was also used in the PICTS experiments. This often made it possible to obtain signals from deep levels that were indistinguishable using the excitation with $h\nu \geq E_g$. In this case, it was implicitly assumed that the nonequilibrium filling of deep levels occurs due to captured carriers generated by the optical excitation from the band.

The possibility of detection of deep levels in PICTS measurements was evaluated on the basis of an estimate of the quasi-Fermi level shift under optical excitation [5]. The quasi-Fermi level shift for electrons under photoexcitation with $h\nu \approx E_g$, which was estimated from the photoconductivity, amounts to 0.03–0.08 eV. However, the deep levels with $E_t \approx 0.6$ eV are detectable. A crystal in the state of thermodynamic equilibrium was considered by Balland *et al.* [5]. The incident optical pulses periodically disturb the equilibrium state of the samples, and, during the dark period, the sample relaxes to the equilibrium state. For semi-insulating CdS crystals, even at 300 K, the characteristic relaxation times of impurity photoconductivity may be on the order of 10^2 s or longer. Consequently, during measurements with a characteristic periodicity of the optical excitation of no more than 0.1–1 s, the sample is always in a nonequilibrium state, and the model developed by Balland *et al.* [5] calls for refinement.

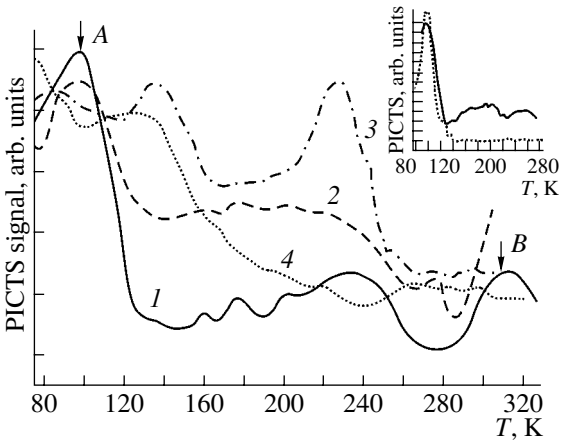

Fig. 1. PICTS spectra of the N_4 crystal (corresponding to a thermal emission rate of ~10^3 s^{-1}) with different photon energy of the excitation radiation $h\nu$: (*1*) 2.40, (*2*) 2.45, (*3*) 2.50, and (*4*) 2.54 eV. Excitation is performed using an Ar laser. Vertical arrows denote the peaks for which the computer simulation was carried out. The PICTS spectra for the N_3 crystal are given in the inset (the thermal emission rate ~10^3 s^{-1}). The excitation with $h\nu = 2.40$ eV is represented by a solid curve, and the laser excitation with $h\nu = 2.54$ eV is represented by a dashed line.

3. THEORETICAL MODEL OF THE PICTS METHOD

Let us consider a high-resistivity *n*-type semiconductor with a single level of capture of majority carriers. Let us introduce the following notation: E_t is the energy position of the electron capture center relative to the conduction band; N_t is the concentration of capture centers; e_{nt} is the rate of electron emission from the level (henceforth, when necessary for emphasis, the following notation is used: e_{nt}^{th} is the rate of thermal emission and e_{nt}^{op} is the rate of optical emission); C_{nt} is the capture coefficient of electrons from the conduction band; g_1 is the rate of electron generation under the photoexcitation; n_t is the electron concentration at the level; and n are the concentrations of free carriers in the band. Under the photoexcitation of the sample, the electron concentration in the conduction band and at deep levels can be written as [4]

$$\begin{cases} \dfrac{dn}{dt} = g_1 + e_{nt}n_t - C_{nt}n(N_t - n_t) - \dfrac{n}{\tau_n}, & (1) \\ \dfrac{dn_t}{dt} = C_{nt}n(N_t - n_t) - e_{nt}n_t, & (2) \end{cases}$$

where τ_n is the electron lifetime in the band. Henceforth, we disregard the thermal emission of electrons

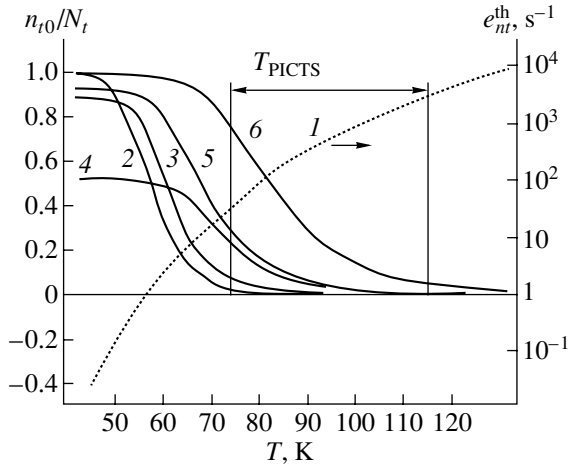

Fig. 2. Calculation of temperature dependences of the rate of thermal emission from deep levels (dotted curve *1*) and filled deep levels (solid curves): (*2*) for the "thermal" mechanism of filling the levels and (*3–6*) for the "optical" mechanism. The parameters of calculation: (*3*) $\alpha = 1$, $\beta_0 = 0.1$; (*4*) $\alpha = 0.1$, $\beta_0 = 1$; (*5*) $\alpha = 0.1$, $\beta_0 = 0.1$; and (*6*) $\alpha = 0.01$, $\beta_0 = 0$. The temperature range T_{PICTS}, where the PICTS signal from the deep level considered should be detected, is denoted by vertical lines.

from the E_t level (electron traps) as well as the dark carrier concentration in the high-resistivity material.

Solving kinetic equations (1) and (2) for time when the steady state with the photoexcitation is attained, the steady-state population of the level E_t may be represented as

$$n_{t0} = \frac{N_t}{(1+\beta)}, \tag{3}$$

where the parameter β, which determines the nonequilibrium filling of the level, is introduced. The physical meaning of the parameter β is the ratio of the rate of depletion of the level to the rate of its filling. The photocurrent relaxation after switching off the illumination is described by the set of Eqs. (1) and (2) for $g_1 = 0$.

Yoshie and Kamihara solved the set of Eqs. (1) and (2) analytically using some simplifying assumptions [4]. They showed that, at specific temperatures, a rapid decay caused by the recombination of nonequilibrium carriers from the band exists in the kinetics of relaxation of the photocurrent. This decay includes an exponential component with the characteristic time $\tau_x = 1/e_{nt}^{th}$, which is caused by the thermal emission of nonequilibrium carriers from deep levels. From the principle of detailed balance for the thermal emission rate, we have

$$e_{nt}^{th} = \frac{S_{nt} v_{th} N_c}{g \exp(E_t/kT)}, \tag{4}$$

where S_{nt} is the cross section of electron capture by a deep level, v_{th} is the thermal velocity of the electron, N_c is the effective density of states in the conduction band, and g is the degeneracy factor of the capture level. Using Eq. (4), it is possible to find S_{nt} and E_t from the experimental temperature dependence of τ_x obtained. To determine τ_x at various temperatures, the analysis of the form of kinetics of photocurrent relaxation is usually used. In this analysis, signal processing similar to that in the DLTS method (deep-level transient spectroscopy) is used [11].

4. ANALYSIS OF POPULATION OF DEEP LEVELS

In previous studies, it was assumed that the deep levels are filled due to the capture of nonequilibrium carriers from the band during the illumination of the sample. The rate of optical filling or depletion of deep levels was disregarded [1, 2, 4, 5]. Let us call this mechanism of filling of deep levels "thermal." In this case, the steady-state filling of deep levels under photoexcitation is described by formula (3), in which β has the form

$$\beta = \frac{e_{nt}}{g_1 \tau_n C_{nt}}. \tag{5}$$

Let us estimate filling of deep levels for $E_t = 0.06$ eV and $S_{nt} = 10^{-19}$ cm^2. We use the following values: $g_1 = 3 \times 10^{14}$ cm^{-3} s^{-1} and $\tau_n = 10^{-3}$ s. The parameters of deep levels are taken from the experiment (see peak *A* in Fig. 1). Figure 2 shows the temperature dependences of the thermal emission rate and population of deep levels (curves *1*, *2*) calculated from formulas (4) and (5). When the temperature dependence of population of deep levels is analyzed, three temperature ranges can be distinguished. In the low-temperature range, the thermal emission rate from the level is negligibly low and deep levels are not depleted during the dark period, being constantly in the filled state. At high temperatures, deep levels are in thermodynamic equilibrium with the band, are partially filled during the optical excitation of the sample, and are rapidly emptied ($\tau_x \ll \tau_n$) during the dark period. In this case, these levels do not introduce noticeable variations in the form of kinetics of the photocurrent relaxation. The temperature range marked by vertical lines in Fig. 2 and denoted T_{PICTS}, where the signal from the deep level under consideration can be detected, corresponds to the detected values $e_{nt} \approx 50$–5000 s^{-1}. A substantial variation in the population of deep levels occurs under the periodic optical excitation of the sample in the T_{PICTS} range. It is noticeable that the deep level is practically empty for the "thermal" mechanism of filling in the T_{PICTS} range. However, the signal from this deep level is dominant in the PICTS spectra for all crystals under investigation for both extrinsic and intrinsic optical excitation of the sample.

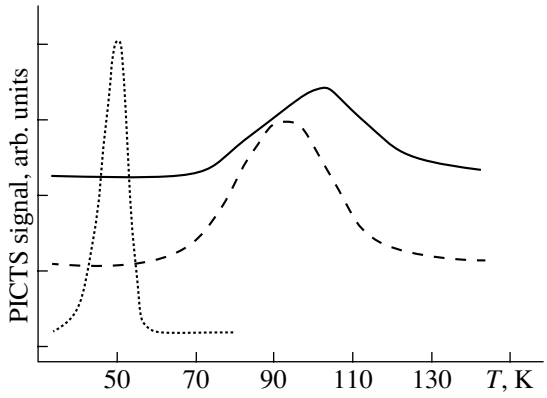

Fig. 3. Simulated PICTS spectra (the solid line corresponds to τ_x = 1/657 s and dashed line corresponds to τ_x = 1/1314 s) and simulated TSC spectrum represented by the dotted line.

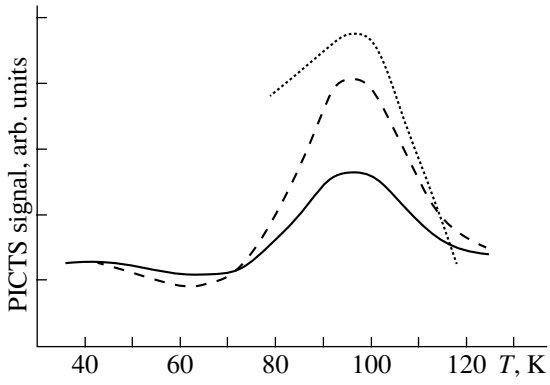

Fig. 4. PICTS spectra corresponding to the thermal emission rate ~1000 for α = 5 (solid line) and α = 1 (dashed line). The experimental curve (dotted line) is shown for comparison.

Let us consider another mechanism of filling the deep levels referred to as "optical." Under illumination, the level with energy E_t can be emptied due to direct optical transitions into the conduction band with the rate e_{nt}^{op}. This level may also be filled due to electron transition from the valence band to the level with the rate e_{pt}^{op}. Making allowance for both of these processes when solving Eqs. (1) and (2) for the steady-state photoexcitation, we will derive the expression

$$\beta = (e_{nt}^{th} + e_{nt}^{op})/(g_1\tau_n C_{nt} + e_{pt}^{op}). \quad (6)$$

Disregarding the recapture, i.e., considering $e_{pt}^{op} > g_1\tau_n C_{nt}$, the parameter β may be represented in the form

$$\beta = \beta_0 + \alpha e_{nt}^{th}, \quad (7)$$

where $\beta_0 = e_{nt}^{op}/e_{pt}^{op}$ determines the initial filling of deep levels at low temperatures when the thermal emission rate may be disregarded, and $\alpha = 1/e_{pt}^{op}$ is the normalizing coefficient. Disregarding the temperature dependence of the rates of optical filling and depletion of deep levels, we assume that β_0 and α are independent of temperature. The rates e_{nt}^{op} and e_{pt}^{op} are unknown to us. Zielinger and Tapiero noted that the Frank–Condon shift could not be too large [12]. Therefore, using the excitation with $h\nu = E_g$ or $h\nu < E_g$, but close to this value, it is reasonable to assume that $e_{nt}^{op} < e_{pt}^{op}$.

Figure 2 shows the temperature dependences of population of deep levels (curves *3–6*) calculated from formula (7) with the above parameters S_{nt}, τ_n, and E_t for various values of β_0 and α. It can be seen that, with the "optical" mechanism of filling in the T_{PICTS} range, the deep level is partially populated depending on α and weakly depending on β (see curves *4*, *5*). If the optical mechanism of filling the deep level under consideration dominates over the thermal one, $\alpha \le 10$ is required. It is difficult to estimate α experimentally since it is difficult to isolate the contribution of a specific transition to the total photocurrent signal. The estimate of the total rate of optical emission from the initial slope of the curve of the photocurrent rise [13] under extrinsic excitation showed that the emission rate of nonequilibrium carriers for the optical excitation level used was higher than or about 0.2 s^{-1}.

For a more detailed analysis, a computer simulation of the experiment with the optical mechanism of filling the deep levels was carried out using the above initial data. During the simulation, the kinetics of photocurrent relaxation upon switching off the illumination was calculated in the temperature range chosen for each temperature in this range with a step of 1 K using Eqs. (1) and (2), and the standard two-point processing of kinetics ("double boxcar"), i.e., obtainment of the PICTS signal, was carried out. In the temperature range chosen, two PICTS spectra corresponding to τ_x = 1/1314 and 1/657 s were plotted. To simplify the simulation, it was assumed that the electron lifetime is independent of temperature. The validity of this suggestion will be considered below. We assume that, during the entire thermal scanning procedure, the steady state of the photocurrent is attained. Thus, by the time that the illumination is switched off, the initial density of nonequilibrium electrons in the conduction band $n = g_1/\tau_n$, whereas the population of deep levels is determined by Eq. (7).

The spectra obtained by simulating the experiment with the optical mechanism of filling (see Fig. 3) feature a peak in the T_{PICTS} temperature range. Figure 4 shows the simulated PICTS spectra for α = 5 and α = 1. It can be seen that, with decreasing α, which causes an increase in the deep-level population, the signals detected increase. For comparison, the corresponding experimentally obtained PICTS spectrum is also shown in Fig. 4. The parameters of the deep level determined from processing of the spectra agree well with the values used in the simulation. It was found from the simulation that the signal from the deep level considered

could be observed experimentally with the optical mechanism of filling the deep level for $\alpha \le 10$ and could not be observed with the thermal mechanism of filling.

This level possesses a rather small capture cross section, which is indicative of a weak interaction with the conduction band. A deep level with $E_t = 0.56$ eV and $S_{nt} = 10^{-13}$ cm^2 was considered in a similar way (peak *B* in Fig. 1). The estimate of population of the deep level showed that, to reveal this deep level experimentally, its thermal filling by nonequilibrium carriers is sufficient.

With illumination of the samples by light with $h\nu < E_g$, the photon energy is insufficient for direct band-to-band transitions. The existence of nonequilibrium carriers in the conduction band is caused by optical electron excitation from filled acceptor deep levels. However, with the illumination of the sample, the donor deep levels are also filled with electrons, which are optically excited from the valence band. Both of these processes are equiprobable, and the prevalence of one of them is determined by the cross sections of photoionization and by the concentration of the centers forming the deep levels. Since the minority lifetime for CdS is very short, acceptor levels rapidly capture the nonequilibrium holes generated in the second case. Both processes of optical excitation lead to the accumulation of nonequilibrium holes in the lower half of the band gap at acceptor deep levels. This may cause a complex temperature dependence of the majority carrier lifetime. During the simulation, it was assumed for simplicity that the lifetime is temperature-independent. The mechanism of "optical" filling of deep levels suggested in the model is independent of τ_n. The temperature dependence of τ_n determines only the temperature dependence of the steady-state photocurrent and, correspondingly, the initial amplitude of the relaxation kinetics of the photocurrent. To exclude this dependence, the experimental PICTS signal is usually normalized to the magnitude of the steady-state photocurrent [4]. This allows one to assume that the initial values of the kinetics parameters are constant when analyzing the shape of relaxation kinetics of the photocurrent.

5. COMPARISON OF PICTS AND THERMALLY INDUCED PHOTOCONDUCTIVITY METHODS

To identify the level with $E_t = 0.06$ eV and $S_{nt} = 10^{-19}$ cm^2, a computer simulation of the experiment with thermally induced conductivity was carried out; the initial data in this simulation were identical to those in the simulation of the PICTS experiment. Figure 3 shows the calculated curve for a thermal scanning rate of 1 K/s. It turns out that the peak detected by the PICTS method in a range of 80–100 K corresponds to a deep level responsible for the TSC peak at 53 K. This result can be explained by analyzing the population of the deep level shown in Fig. 2. The conditions of sample excitation for both methods are different. However, the TSC peak is located in a temperature range of intense variation in the dark population of deep levels in the PICTS experiments. In this case, the thermal emission rates are lower than those detected in the PICTS method. By the TSC method, a deep level with $S_{nt} = 10^{-19}$ cm^2 and $E_t = 0.06$ eV was observed close to ~50 K for CdS in some studies [14, 15]. This deep level is usually interpreted as being related to interstitial Cd. A computer simulation of TSC experiments for the level responsible for the *B* peak in Fig. 1 was carried out in a similar way. In this case, the experimental PICTS parameters of the deep level are the following: $E_t = 0.58$ eV and $S_{nt} = 10^{-13}$ cm^2. It is found that this deep level corresponds to the TSC peak at ~263 K.

It is reasonable to carry out the analogy of PICTS measurements with the TSC method. In both methods, the sample is driven away from thermodynamic equilibrium during the experiment. To reveal the deep level, its filling with nonequilibrium carriers is necessary. During thermal scanning, the deep level "manifests itself" when the temperature at which the thermal emission rate from the deep level becomes insignificant is attained. In the TSC method, the variation in the free-carrier concentration is caused by thermal emission from deep levels filled by a single-shot prolonged illumination prior to the onset of thermal scanning. This variation serves as the signal that carries information on the parameters of the deep level. In this case, the higher the heating rate, the larger the signal magnitude. In the PICTS method, the cycles of filling–emptying of deep levels are repeated many times during heating. The scheme of carrying out the experiment enables us to use the principle of signal accumulation, where some variants of relaxation kinetics of photocurrent are summed. The requirements to the stability of thermal scanning are simplified in the PICTS method. Only one requirement is imposed on the thermal scanning conditions in this case. Specifically, the heating rate should be low enough to consider that *K* cycles of photoexcitation of the sample with subsequent relaxation are carried out at the same temperature. In this case, the signal-to-noise ratio during the detection of relaxation kinetics of the photocurrent is increased by a factor of $K^{1/2}$.

It should be noted that the set of relaxation kinetics of the photocurrent measured at various temperatures during thermal scanning in the PICTS method comprises the intermediate data, which are subjected to correlation processing. During this processing, if the component caused by the electron thermal emission from the deep level with the form $A_0\exp(-t/\tau_x)$ occurs in the relaxation kinetics of the photocurrent, the useful signal at its maximum takes the form A_0F_i/τ_x. Here, F_i is a numerical coefficient that depends on the specific form of the weighting functions used for processing. For example, for weighting functions of the form

$$W_i(t) = \begin{cases} 1, & \text{at } t_0 < t \le t_0 + \tau_i, \\ -1, & \text{at } t_0 + \tau_i < t \le t_0 + 2\tau_i, \\ 0, & \text{at } t < t_0 \text{ or } t > t_0 + 2\tau_i \end{cases}$$

which are often used in practice, the F_i magnitude is equal to 0.1–0.8. Thus, in the PICTS method, the intensity of the useful signal expressed in terms of the number of free electrons in the conduction band equals $n_{t0}\tau_n R$, where $R = F_i K^{1/2}$ is the coefficient accounting for statistical processing of the signal. Hence, it follows that the PICTS method is more sensitive for deep levels with lower concentrations than is the TSC method. Certain advantages of the PICTS method (more informative; one thermal scanning is sufficient during measurements) were noted by Yoshie and Kamihara [4]. Processing of the relaxation signal of the photocurrent is similar to that in the DLTS method. Namely, hardware- or software-realized correlators with different weighting functions [16] and regularization methods that enable one to extract the simultaneously emerging contributions to the signal from several deep levels [17] are used. This provides a considerably higher resolution in temperature in the PICTS method. Note that the temperature position of the signal from the same deep level in the TSC and PICTS methods is different, and a computer simulation of the experiment should be used to compare the data.

6. CONCLUSION

A computer simulation of the PICTS experiment made it possible to correlate the results obtained with the published data obtained by the TSC method. The relation is established between the TSC peaks at 53 K and the PICTS peaks in a range of 80–100 K as well as between the TSC peaks at 263 K and the PICTS peaks at 250–300 K. By example of the deep level with E_t = 0.06 eV and $S_{nt} = 10^{-19}$ cm^2, it is shown that the "optical" mechanism of filling the deep levels can be active in CdS in contrast to the "thermal" mechanism of filling the level, which was considered in the phenomenological model of the PICTS technique. The experimental potential of the TSC and PICTS methods is compared. It is found that the latter method is preferable for the investigation of semi-insulating materials.

REFERENCES

1. Ch. Hurter, M. Boulon, A. Mitonnear, and D. Bois, Appl. Phys. Lett. **32**, 821 (1978).
2. G. M. Martin and D. Boisin, J. Electrochem. Soc. **78**, 32 (1978).
3. É. M. Omel'yanovskiĭ, A. Ya. Polyakov, N. S. Rytov, and V. I. Raĭkhshteĭn, Fiz. Tekh. Poluprovodn. (Leningrad) **20**, 1428 (1986) [Sov. Phys. Semicond. **20**, 897 (1986)].
4. O. Yoshie and M. Kamihara, Jpn. J. Appl. Phys. **22**, 621 (1983).
5. J. C. Balland, J. P. Zielinger, C. Noguet, and M. Tapiero, J. Phys. D: Appl. Phys. **19**, 57 (1986).
6. O. F. Vyvenko, I. A. Davydov, A. P. Odrinskiĭ, and V. A. Teplitskiĭ, Fiz. Tekh. Poluprovodn. (St. Petersburg) **28**, 721 (1994) [Semiconductors **28**, 425 (1994)].
7. I. A. Davydov and A. P. Odrinskiĭ, Available from VINITI No. 6285-B90 (Moscow, 1990).
8. K. Ikeda and Y. Ishii, Jpn. J. Appl. Phys. **26**, 377 (1987).
9. A. Zerrai and G. Bremond, J. Appl. Phys. **84**, 5554 (1998).
10. A. Cavallini, B. Fraboni, W. Dusi, *et al.*, Appl. Phys. Lett. **77**, 3212 (2000).
11. D. V. Lang, J. Appl. Phys. **45**, 3023 (1974).
12. J. P. Zielinger and M. Tapiero, J. Phys. III **3**, 1332 (1993).
13. H. G. Grimmeiss, Annu. Rev. Mater. Sci. **7**, 341 (1977).
14. A. P. Zdebskiĭ, N. V. Mironyuk, S. S. Ostapenko, *et al.*, Fiz. Tekh. Poluprovodn. (Leningrad) **20**, 1861 (1986) [Sov. Phys. Semicond. **20**, 1167 (1986)].
15. N. E. Korsunskaya, I. V. Markevich, I. Yu. Shabliĭ, and M. K. Sheĭkman, Fiz. Tekh. Poluprovodn. (Leningrad) **15**, 279 (1981) [Sov. Phys. Semicond. **15**, 161 (1981)].
16. A. A. Istratov, O. F. Vyvenko, H. Hleslmair, and E. R. Weber, Meas. Sci. Technol. **9**, 477 (1998).
17. C. Eiche, D. Maier, M. Schneider, *et al.*, J. Phys.: Condens. Matter **4**, 6131 (1992).

Translated by N. Korovin

Semiconductors, Vol. 38, No. 3, 2004, pp. 304–309. Translated from Fizika i Tekhnika Poluprovodnikov, Vol. 38, No. 3, 2004, pp. 316–321.

ELECTRONIC AND OPTICAL PROPERTIES OF SEMICONDUCTORS

The Role of Alloying Effects in the Formation of Electronic Structure of Unordered Group III Nitride Solid Solutions

A. V. Voznyy* and V. G. Deibuk**

Chernovtsy National University, Chernovtsy, 58012 Ukraine

**e-mail: voznyy@elegance.cv.ua*

***e-mail: vdei@chnu.cv.ua*

Submitted August 26, 2003; accepted for publication August 28, 2003

Abstract—The effect of compositional and positional disorder on electronic properties of (Group III)-nitride solid solutions with the wurtzite structure was studied by the method of a model empirical pseudopotential using 32-atom supercells. The calculated values of the band-gap bowing parameter are found to be equal to 0.44, 2.72, and 4.16 for AlGaN, InGaN, InAlN, respectively. It is shown that the major contribution to the band-gap bowing parameter is made by the compositional disorder, whereas the bond-length relaxation reduces the effect of compositional disorder and the effects of the volume deformation. © *2004 MAIK "Nauka/Interperiodica".*

1. INTRODUCTION

Development of light-emitting diodes, laser diodes, and high-frequency transistors based on the Group III nitrides GaN, AlN, and InN [1] motivated intense theoretical studies of properties of these compounds. By varying the composition of ternary solid solutions, one can change the physical properties smoothly. So-called band engineering, in which case the band gap is controlled by the solid-solution composition, is a technologically important example.

Both the theoretical [2–4] and experimental [5–11] values of the composition-related band-gap bowing parameter for solid solutions of the III–N compounds feature an appreciable spread. The properties of the binary GaN, AlN, and InN compounds have been studied in detail using both the empirical-pseudopotential method [12–14] and the methods based on first principles [12, 15]. However, theoretical studies of properties of solid solutions under consideration are typically based on the virtual-crystal approximation or the coherent-potential approximation (CPA); these methods amount conceptually to the replacement of a certain microscopic configuration by an averaged effective medium and, thus, cannot account for experimentally observed compositional dependences of the band gap [2]. The recursion method [16] and calculations based on density-functional theory are the most promising for correct theoretical description of electronic properties of solid solutions; these methods make it possible to study any specific atomic configurations [3, 4, 17, 18].

In this paper, we report the results of studying the alloying effects on electronic properties of unordered AlGaN, InGaN, and InAlN ternary solid solutions; we use supercells containing 32 atoms in atomic configurations obtained on the basis of density-functional theory [19]. The calculations were performed by the density-functional method that had proven to be quite useful for describing the properties of quantum dots, superlattices, and solid solutions with spatial modulation of the composition [20–22].

2. THE CALCULATION PROCEDURE

The calculation procedure was described in detail elsewhere [5, 23]. We use the functional pseudopotential form which is continuous in reciprocal space and depends on the local strain ε that describes the charge redistribution and screening of the pseudopotential due to changes in the local environment [21, 22]; thus, we have

$$v(\mathbf{k}, \varepsilon) = a_0 \frac{(\mathbf{k}^2 - a_1)}{a_2 \exp(a_3 \mathbf{k}^2) - 1} [1 + a_4 \mathrm{Tr}(\varepsilon)]. \quad (1)$$

Initial parameters a_i were determined using the procedure for approximation of norm-preserving pseudopotentials obtained from first principles by Hamman [24] and screened by the Levine–Louie [25] dielectric function. We then modified the parameters so that experimental values of the energies of band-to-band transitions at the high-symmetry points of the Brillouin zone and optical properties of pure binary compounds could be reproduced [23, 26] (Table 1). In order to take correctly into account the effect of local strains, we included the values of the deformation potentials in the fitting procedure; i.e.,

$$a_g = V \frac{\partial E_g}{\partial V}. \quad (2)$$

The parameters a_4 were selected in such a way that they made it possible to obtain the recommended values of deformation potentials [27]: $a_g = -8.2$ eV for GaN, $a_g = -9$ eV for AlN, and $a_g = -4$ eV for InN. The final

Table 1. Energies of band-to-band transitions (T = 0 K)

	Transition	Energy, eV	
		this study	other calculations and experiments
GaN	Γ_{6V}–Γ_{1C} (E_g)	3.5	3.507[a], 3.5[b], 3.5[c]
	Γ_{3V}–Γ_{6V} (the width of the upper valence band)	7.3	6.8[b], 7.4 (8)[d]
	Γ_{1V}–Γ_{6V} (Δ_{cr})	0.02	0.019[a], 0.02[b], 0.038[c]
	$L_{2.4V}$–$L_{1.3C}$	7.76	7.57[b], 6.4 (8.2)[d]
	M_{4V}–M_{3C}	8.11	7.7[b], 7.6 (8.4)[d]
	H_{3V}–H_{3C}	8.47	9[b], 8.1 (9.9)[d]
AlN	Γ_{1V}–Γ_{1C} (E_g)	6.2	6.23[a], 6.24[c]
	Γ_{3V}–Γ_{1V} (the width of the upper valence band)	7	6.1 (6.9)[d]
	Γ_{1V}–Γ_{6V} (Δ_{cr})	–0.22	–0.164[a], –0.17[c]
	$L_{2.4V}$–$L_{1.3C}$	8.75	8.6[d]
	M_{4V}–M_{3C}	9.4	8.5[d]
	H_{3V}–H_{3C}	9.8	10.5[d]
InN	Γ_{6V}–Γ_{1C} (E_g)	0.7	0.7[e], 2.04[b]
	Γ_{3V}–Γ_{6V} (the width of the upper valence band)	6	5.77[b]
	Γ_{1V}–Γ_{6V} (Δ_{cr})	0.04	0.041[a], 0.017[b], 0.06[c]
	$L_{2.4V}$–$L_{1.3C}$	5.17	5.83[b]
	M_{4V}–M_{3C}	5.21	5.8[b]
	H_{3V}–H_{3C}	5.93	6.5[b]

Note: [a] The recommended values [27]. [b] Calculations by the empirical-pseudopotential method [13]. [c] Calculations based on first principles and an empirical pseudopotential [12]. [d] Calculations from first principles taking into account and disregarding the GW corrections [15]. [e] Experimental data for InN [7, 31].

values of the parameters a_i are listed in Table 2. The pseudopotentials obtained in this way are in good agreement with those calculated recently [13, 14].

In order to simulate electronic properties of AlGaN, InGaN, and InAlN solid-solution nitrides and take into account the compositional disorder in these nitrides, we used the 32-atom supercells $A_nB_{16-n}N$ (A = Al or In, B = Ga or Al) that corresponded to the doubled (along three directions) primitive unit cell in the wurtzite structure [3, 19]. For a given number of atoms A n = 0, …, 16, we can obtain various atomic configurations in contrast to the virtual-crystal approximation, according to which an unordered solid solution is replaced by a crystal with identical averaged "virtual" atoms in the cationic sublattice. We calculated the electronic structure only for configurations that had the lowest energy; the latter was calculated in the context of density-functional theory [19]. In Fig. 1, we show an example of such a structure for n = 4.

A nitrogen atom can have an environment of A_4B_{4-m} (where m = 0, 1, 2, 3, 4) in ternary solid solutions with the wurtzite structure. In order to take into account variations in the pseudopotential screening in relation to local atomic surroundings in the solid solution, we constructed the nitrogen pseudopotntial V_N as a linear combination of the nitrogen pseudopotentials in binary compounds AN and BN [21]; i.e.,

$$V_N(A_mB_{4-m}) = \frac{m}{4}V_N(AN) + \frac{4-m}{4}V_N(BN). \quad (3)$$

Such a linear combination of pseudopotentials in the anionic sublattice represents the essence of the virtual-crystal approximation; however, the description of an unordered solid solution is based on explicit consideration of each atom rather than on averaging over the entire crystal. At the same time, it should be noted that, for configurations with the lowest energy [19] in a supercell containing 32 atoms and with atomic content

Table 2. Parameters of screened atomic pseudopotentials in GaN, AlN, and InN (in atomic units)

Atom	a_0	a_1	a_2	a_3	a_4
Ga	1500	1.88	104.7	0.27	0.3
N in GaN	1224	4.76	83.3	0.419	0
Al	9.42	1.79	1.49	0.245	0.7
N in AlN	18	5.08	2.7	0.236	0
In	11	1.173	1.358	0.264	2.5
N in InN	45.85	5.1	4.875	0.421	0

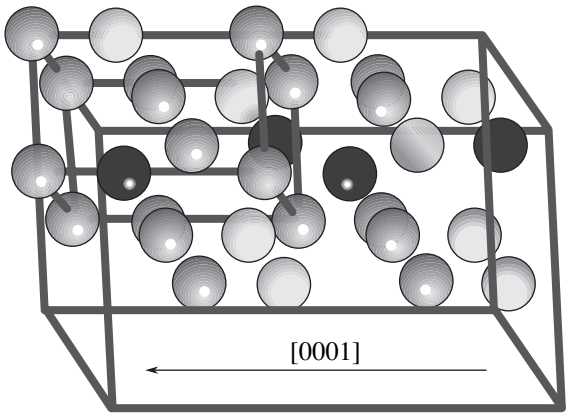

Fig. 1. An ordered structure of $Al_{1-x}B_xN$ with $x = 0.25$. The $2 \times 2 \times 2$ cell in the wurtzite structure contains 12 atoms of A (white spheres), 4 atoms of B (black spheres), and 16 atoms of N (gray spheres).

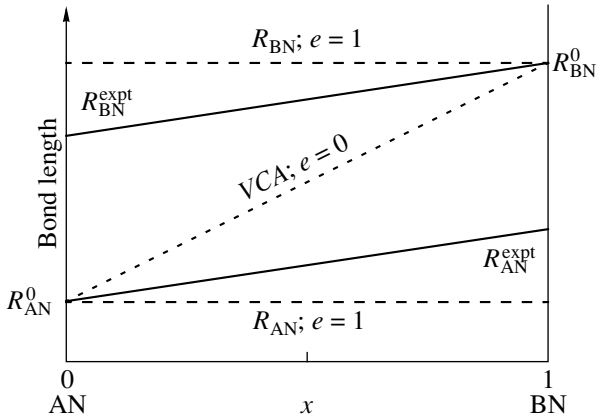

Fig. 2. Schematic representation of variations in the bonds lengths $R_{AN}(x)$ and $R_{BN}(x)$ in relation to the composition of the $Al_{1-x}B_xN$ solid solution. VCA stands for the virtual-crystal approximation.

of 25, 50, and 75% cations, all nitrogen atoms have the same local surroundings, which corresponds to the virtual-crystal approximation.

A deviation from the ideal lattice configuration is observed in solid solutions, in addition to compositional disorder. Atoms are displaced from their ideal sites specified by Vegard's rule, which is related to the difference between the bond lengths for compounds that form the solution (so-called positional disorder) (Fig. 2). Dependences of the bond lengths $R_{AN}(x)$ and $R_{BN}(x)$ on the composition in an $A_{1-x}B_xN$ solid solution can be characterized by the dimensionless parameter [28]

$$e = \frac{R_{BN}^{[AN:B]} - R_{AN}^0}{R_{BN}^0 - R_{AN}^0}, \quad (4)$$

where $R_{BN}^{[AN:B]}$ is the B–N bond length for the B impurity in an AN crystal and R_{BN}^0 and R_{AN}^0 are the bond lengths in pure binary compounds.

We used the method of the valence-force field (VFF) [28] to calculate the following expression for the dependence of the relaxation coefficient for the bond length e on characteristics of constituents of the solid solution:

$$e \approx \left[1 + \left(\frac{R_{BN}^0}{R_{AN}^0}\right)^3 \left(\frac{2}{3} - \frac{1}{2} f_i\right)\right]^{-1}. \quad (5)$$

Here, f_i is the ionicity according to Phillips. Using the values $f_i = 0.449$ for AlN, $f_i = 0.5$ for GaN, and $f_i = 0.578$ for InN [29], we obtained the values of the relaxation coefficient $e = 0.7$–0.8 for solid solutions of III–N compounds; these values are in good agreement with experimental data and the values obtained by calculations based on density-functional theory [30].

In order to take into account the structural relaxation, atoms in a 32-atom supercell were displaced from their ideal sites so that the lengths of all bonds corresponded to the values obtained from expression (5). We calculated the value of the local strain [22] for each cationic atom; this strain appears in formula (1) as a correction to the pseudopotential; i.e.,

$$\mathrm{Tr}(\varepsilon) = \frac{\Delta V}{V}, \quad (6)$$

where V is the volume of a tetrahedron with nearest cation neighbors at the vertices for a pure binary compound and ΔV is a change in the volume due to a variation in the crystal lattice of the solid solution and to the structural relaxation.

In the calculations, we used the basis of 2055 plane waves, which corresponded to the energy cutoff at 14 Ry.

3. DISCUSSION

Experimental compositional dependences of the band gap are described by the following quadratic equation with the bowing parameter b:

$$E_g(x) = E_{g1} + (E_{g2} - E_{g1})x - bx(1-x). \quad (7)$$

In order to analyze the effect of various factors on the bowing parameter, we decompose b into its components; i.e.,

$$b = b_{VD} + b_{CE} + b_{SR}, \quad (8)$$

where b_{VD} is the bowing caused by the effect of the volume deformation, b_{CE} is the bowing caused by the charge exchange between various bonds in an unordered solid solution, and b_{SR} is the bowing-parameter component related to the bond-length (structure) relaxation.

The results of our calculations are shown in Fig. 3 and are listed in Table 3. As can be seen, a deviation from the linear dependence $E_g(x)$ is observed even in calculations based on the virtual-crystal approximation; this deviation is caused by a difference in the lattice constants of compounds that form the solid solu-

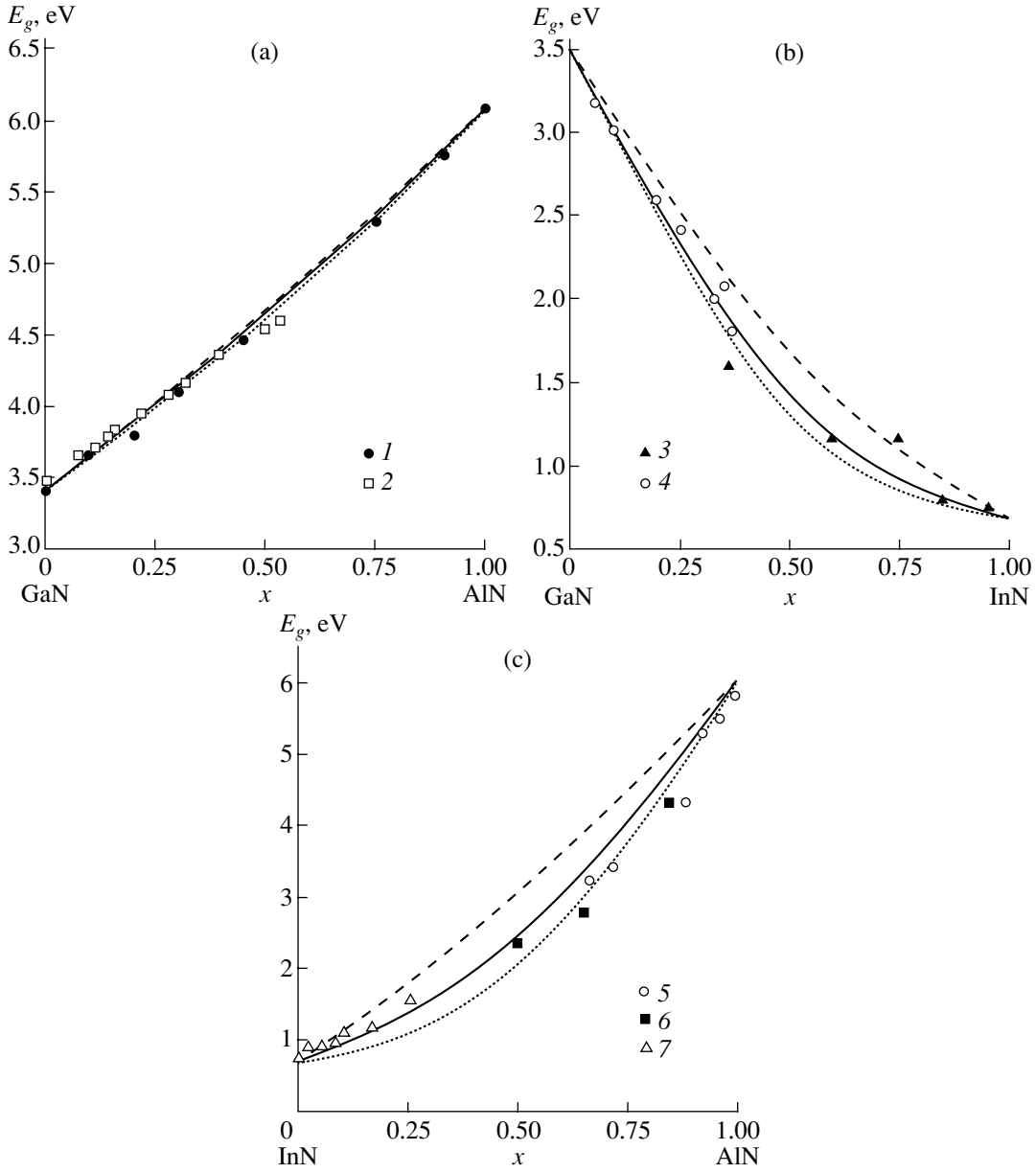

Fig. 3. The band gaps in relation to the composition of solid solutions of III–N compounds. Experimental data are represented by the symbols *1–7*. (a) Experimental data for AlGaN (T = 300 K) taken from (*1*) [15] and (*2*) [6]; data for InGaN (T = 77 K) taken from (*3*) [7] and (*4*) [9]; and (c) data for InAlN (T = 77 K) taken from (*5*) [10], (*6*) [11], and (*7*) [31]. Calculated dependences are represented by curves. Dashed lines correspond to the virtual-crystal approximation, dotted lines represent the results of calculations with compositional disorder taken into account, and solid lines correspond to calculations with both the compositional disorder and structural relaxation taken into account.

tion and, as a consequence, by deformation of the volume of the unit cell for constituent compounds when the solid solution is formed. In this case, the value of the bowing parameter is proportional to the difference between deformation potentials (2) for compounds that form the solid solution and to the relative variation in the lattice constant when the solid solution is formed:

$$b_{\mathrm{VD}} \propto \frac{\Delta a}{a}\Delta a_{\mathrm{g}}. \qquad (9)$$

The smallest value of the bowing parameter related to the volume deformation is observed in AlGaN, where the lattice-constant mismatch between GaN and AlN amounts to 2.5%, whereas the deformation potentials are almost the same. The largest bowing magnitude is observed in InAlN, where the lattice-constant mismatch is as large as 12% and the deformation potentials differ by a factor of 2. The volume deformation is the only effect that gives rise to bowing and can be taken into account in the virtual-crystal approximation.

Table 3. Experimental and theoretical values of the band-gap bowing parameter and its components

Solid solution	b_{VD}, eV	b_{CE}, eV	b_{SR}, eV	b, eV Our calculations	b, eV DFT [3]	b_{expt}, eV
AlGaN	0.37	0.28	–0.21	0.44	0.71	0.2–1 [5, 6]
InGaN	0.92	2.28	–0.48	2.72	1.7	2.5 [7]
InAlN	1.84	4.04	–1.72	4.16	4.09	3 [31]

Note: b_{expt} denotes the experimental data.

However, this effect by itself, as can be seen from Fig. 3 and Table 3, cannot ensure agreement between the results of calculations and experimental data.

The simulation of unordered solid solutions using specified atomic configurations in a 32-atom supercell makes it possible to calculate the value of additional band-gap bowing parameter b_{CE} related to the difference between atoms in the cationic sublattice. As our and other [18] calculations of the valence-electron charge density show, a redistribution of electrons between the AN and BN bonds is observed in the $A_xB_{1-x}N$ solid solution: the charge is transferred from the bond with a lower ionicity to that with a higher ionicity. Thus, the charge distribution in such a system differs from that obtained in the virtual-crystal approximation, which results in changes in the energy-band structure and in additional band-gap bowing parameter b_{CE}. The difference between ionicities of binary compounds forming the solid solution determines the magnitude of the charge redistribution and, correspondingly, the band-gap bowing parameter b_{CE}. It is impossible to take this effect into account in the virtual-crystal approximation since dissimilar atoms in the cationic sublattice are replaced in this approximation by "virtual" atoms that are identical at all lattice sites.

Taking into account the bond-length relaxation also leads to a variation in the compositional dependences of the band gap, which can be described using an additional component b_{SR} of the band-gap bowing parameter. As our calculations show (see also [18]), the bond-length relaxation results in a decrease in nonuniformity of the charge distribution; this nonuniformity is caused by the presence of dissimilar atoms in the cationic sublattice. Thus, the charge distribution becomes closer to that obtained in the virtual-crystal approximation. Structural relaxation also reduces the volume-deformation effect since the bond lengths in the solid solution become almost equal to the corresponding values in binary compounds. As a result, this effect leads to a decrease in the total band-gap bowing parameter, and b_{SR} is a negative quantity.

The results obtained are in good agreement with well-known experimental data (Table 3, Fig. 3). The calculation for AlGaN yields an almost linear dependence of the band gap on the solid-solution composition (b = 0.44 eV), which is attributed to a small difference between the lattice constants, deformation potentials, and ionicities in GaN and AlN. Anomalously large values of b are experimentally observed for InGaN and InAlN: 3.2 eV [8, 9] and 6.76 eV [10, 11], respectively. These experimental values of the band-gap bowing parameter were obtained under the assumption that the InN band gap was equal to 3 eV; in addition, the data were obtained for samples that had a low content of InN. However, it has been recently reported that the band gap of InN is equal to 0.7 eV [7, 31]. Correspondingly, it is necessary to use much smaller values of the band-gap bowing parameter for approximation of experimental data. In our calculations by the empirical-pseudopotential method, we assumed that E_g = 0.7 eV for InN (Table 1). In Figs. 3b and 3c, we show the curves $E_g(x)$ for InGaN and InAlN according to our calculations; the obtained values of the band-gap bowing parameter are equal to 2.72 and 4.16 eV for InGaN and InAlN, respectively, and are in good agreement with experimental data [10, 11, 31]. Large values of the band-gap bowing parameter for InGaN and InAlN are related to an appreciable lattice-constant mismatch (10 and 12%, respectively) and large differences in deformation potentials and ionicities for binary compounds that form these solid solutions.

Calculations show that compositional disorder and structural relaxation affect profoundly not only the band gap but also the energy-band structure as a whole. The presence of dissimilar atoms in the cationic sublattice and their displacement from ideal sites lead to a lowering of the crystal symmetry, which manifests itself in splitting of the energy bands along the main directions in the Brillouin zone. In addition, taking into account both compositional and positional disorder results in an appreciable variation in the widths of energy bands in the solid solutions with respect to the corresponding widths obtained in the virtual-crystal approximation; i.e., the valence band is widened and the asymmetric gap (the main parameter on the ionicity scale suggested by Wall *et al.* [32]) is narrowed. Our calculations of compositional dependences of the charge-asymmetry coefficient g_i suggested in [29] as a measure of ionicity showed the presence of bowing in these dependences; at the same time, the value of the charge-asymmetry coefficient for $In_xAl_{1-x}N$ with x = 0.5 was found to be smaller than for the binary AlN and InN compounds. Approximation of the results of calculations yields the following relations:

$$g_i(Al_xGa_{1-x}N) = 0.542 + (0.615 - 0.542)x, \quad (10)$$

$$g_i(In_xGa_{1-x}N) = 0.542 + (0.638 - 0.542)x - 0.019x(1-x), \quad (11)$$

$$g_i(In_xAl_{1-x}N) = 0.615 + (0.638 - 0.615)x - 0.145x(1-x). \quad (12)$$

4. CONCLUSION

We studied electronic properties of ternary solid solutions based on III–N compounds using the method of a model empirical pseudopotential and employing supercells. It is shown that, if the internal local strains in the solid solutions and both compositional and positional disorder are taken into consideration, a bowing in the compositional dependences of the band gap $E_g(x)$ is observed, which accounts satisfactorily for the available experimental data. The largest contribution to the band-gap bowing parameter is made by the compositional disorder. The bond-length relaxation reduces the effect of compositional disorder and the volume-deformation effects. The chosen model can satisfactorily account for electronic properties of ternary solid solutions and makes it possible to gain insight into the causes of appearance of bowing in the dependence $E_g(x)$.

REFERENCES

1. S. Nakamura, *Introduction to Nitride Semiconductor Blue Lasers and Light Emitting Diodes* (Taylor and Francis, London, 2000).
2. M. Goano, E. Bellotti, E. Ghillino, *et al.*, J. Appl. Phys. **88**, 6467 (2000).
3. Z. Dridi, B. Bouhafs, and P. Ruterana, Phys. Status Solidi C, No. 1, 315 (2002).
4. L. K. Teles, L. M. R. Scolfaro, J. Furthmuller, *et al.*, Phys. Status Solidi B **234**, 956 (2002).
5. V. G. Deĭbuk, A. V. Voznyĭ, and M. M. Sletov, Fiz. Tekh. Poluprovodn. (St. Petersburg) **34**, 35 (2000) [Semiconductors **34**, 35 (2000)].
6. M. Leroux, S. Dalmasso, F. Natali, *et al.*, Phys. Status Solidi B **234**, 887 (2002).
7. V. Davydov, A. Klochikhin, V. Emtsev, *et al.*, Phys. Status Solidi B **234**, 787 (2002).
8. S. Stepanov, W. N. Wang, B. Yavich, *et al.*, MRS Internet J. Nitride Semicond. Res. **6**, 6 (2001).
9. K. P. O'Donnel, J. F. W. Mosselmans, R. W. Martin, *et al.*, J. Phys.: Condens. Matter **13**, 6977 (2001).
10. M. J. Lukitsch, Y. V. Danylyuk, V. M. Naik, *et al.*, Appl. Phys. Lett. **79**, 632 (2001).
11. T. Peng, J. Piprek, G. Qiu, *et al.*, Appl. Phys. Lett. **71**, 2439 (1997).
12. S. Pugh, D. Dugdale, S. Brand, and R. Abram, Semicond. Sci. Technol. **14**, 23 (1999).
13. Y. Yeo, T. Chong, and M. Li, J. Appl. Phys. **83**, 1429 (1998).
14. M. Goano, E. Bellotti, E. Ghillino, *et al.*, J. Appl. Phys. **88**, 6476 (2000).
15. A. Rubio, J. L. Corkill, M. L. Cohen, *et al.*, Phys. Rev. B **48**, 11810 (1993).
16. R. Haydoc, W. Heine, and M. J. Kelly, J. Phys. C **15**, 2891 (1982).
17. A. Zaoui, J. Phys.: Condens. Matter **14**, 4025 (2002).
18. G. Srivastava, J. Martins, and A. Zunger, Phys. Rev. B **31**, 2561 (1985).
19. F. Grosse and J. Neugebauer, Phys. Rev. B **63**, 085207 (2001).
20. P. R. C. Kent, L. Bellaiche, and A. Zunger, Semicond. Sci. Technol. **17**, 851 (2002).
21. T. Matilla, L.-W. Wang, and A. Zunger, Phys. Rev. B **59**, 15270 (1999).
22. C. Pryor, J. Kim, L. W. Wang, *et al.*, J. Appl. Phys. **83**, 2548 (1998).
23. V. G. Deĭbuk, A. V. Voznyĭ, M. M. Sletov, and A. M. Sletov, Fiz. Tekh. Poluprovodn. (St. Petersburg) **36**, 398 (2002) [Semiconductors **36**, 398 (2002)].
24. D. R. Hamman, Phys. Rev. B **40**, 2980 (1989).
25. Z. H. Levine and S. G. Louie, Phys. Rev. B **25**, 6310 (1982).
26. W. R. L. Lambrecht and M. Prikhodko, Solid State Commun. **121**, 549 (2002).
27. I. Vurgaftman and J. Meyer, J. Appl. Phys. **89**, 5815 (2001).
28. J. L. Martins and A. Zunger, Phys. Rev. B **30**, 6217 (1984).
29. A. Garcia and M. L. Cohen, Phys. Rev. B **47**, 4215 (1993).
30. O. Ambacher, J. Majewski, C. Miskys, *et al.*, J. Phys.: Condens. Matter **14**, 3399 (2002).
31. J. Wu, W. Walukiewicz, K. M. Yu, *et al.*, Appl. Phys. Lett. **80**, 4741 (2002).
32. A. Wall, Y. Gao, A. Raisanen, *et al.*, Phys. Rev. B **43**, 4988 (1991).

Translated by A. Spitsyn

Semiconductors, Vol. 38, No. 3, 2004, pp. 310–312. Translated from Fizika i Tekhnika Poluprovodnikov, Vol. 38, No. 3, 2004, pp. 322–324.

ELECTRONIC AND OPTICAL PROPERTIES OF SEMICONDUCTORS

Optical Properties of Polycrystalline Zinc Selenide

A. N. Bryzgalov, V. V. Musatov, and V. V. Buz'ko

Chelyabinsk State Pedagogical University, Chelyabinsk, 454080 Russia

Submitted August 26, 2003; accepted for publication September 18, 2003

Abstract—Dependences of the exponent of radiation flux attenuation on the ZnSe grain size and the wavelength are experimentally determined. At a wavelength of 1.1 μm, the minimum and maximum attenuation is observed in crystals with the smallest and largest grain sizes, respectively. A reverse situation arises at a wavelength of 10 μm. It is concluded that the optical radiation at wavelengths of 1.1 and 10 μm is scattered at internal grain defects and mainly at grain boundaries, respectively. *© 2004 MAIK "Nauka/Interperiodica".*

1. INTRODUCTION

Zinc selenide is used in infrared (IR) optical devices with a transparency range of 0.5–13 μm, where the refractive index has a dispersion from 2.61 to 2.386 [1]. This property fully satisfies industrial requirements. However, it is practically impossible to produce ZnSe single crystals of large sizes and high structural quality. The production problems are associated with the fact that ZnSe crystals exist in two modifications [2], with hexagonal and cubic lattices in high- and low-temperature ranges, respectively. The latter modification is used in IR optical devices. The crystals are typically grown from melt, and crystallization is carried out in the high-temperature phase. Then, already in the solid state, the transition to the low-temperature phase takes place upon cooling. This process is often not completed; hence, twins, regions of elastic stresses, dislocations, and grains, at which the energy is dissipated, are formed in the crystal.

Recently, a growing number of applications have been found for polycrystalline materials produced using various methods: ceramics-based technology (CT), evaporative deposition (ED) from liquid phase, and chemical vapor deposition (CVD). The materials differ in grain size, the degree of crystal quality, and physical properties. Polycrystalline materials, in addition to above-mentioned defects, contain grain boundaries that scatter light [3]. This study is devoted to the optical properties of polycrystalline zinc selenide.

The studies were carried out at wavelengths of 1.1 and 10 μm. The data on the grain sizes, degree of imperfection, and optical properties were statistically processed. The samples were prepared as planar transparent disks 20 mm in diameter and 4–5 mm thick with polished surfaces. Hydrothermal etching [4] was used to reveal defects. The light transmittance was determined using a SPECORD JR-75 system with a relative error of 1%.

The grain boundary is an interlayer with a perturbed structure containing intergrain dislocations and impurities. The presence of the latter is explained by the fact that the growth of crystalline grains is accompanied by their self-purification with segregation of impurity atoms into the intercrystallite space. Therefore, the refractive index of the grain boundaries differs from that in grains $n = 2.403$ by Δn. The optical inhomogeneity $E = \Delta n/n$ characterizes the purity of polycrystalline materials. It was experimentally determined that $\Delta n = 10^{-3}$ for zinc selenide at a wavelength of 10 μm; hence, $E \approx 4 \times 10^{-4}$. Since E is small, the scattering of radiation related to refraction at the grain boundaries can be disregarded. Therefore, the basic mechanism of radiation-flux attenuation is reflection from grain boundaries when the grain size significantly exceeds the radiation wavelength. In the case of grain sizes comparable to or shorter than the wavelength of light, the diffraction effect should also be taken into account.

Under the assumption of chaotic grain orientations, one of the basic characteristics of optical systems is the light transmission in the operating range of the spectrum with the coefficient μ of radiation-flux attenuation

$$\mu = d^{-1}\bar{R},$$

where $\bar{R}$ is the reflectance averaged over angles of incidence and d is the average grain size. Taking into account multiple reflection from grain boundaries, the optical transmittance is theoretically defined as

$$T = \frac{(1-R^2)e^{-\mu L}}{1-R^2e^{-2\mu L}},$$

1063-7826/04/3803-0310$26.00 © 2004 MAIK "Nauka/Interperiodica"

Table 1

Material type	Average density of grains, mm^2	Transmittance at a wavelength of 1.1 μm T, %	Attenuation coefficient $\mu_{1.1}$
CVD	7.89×10^{-5}	63	0.261
ED	5.02×10^{-3}	54	0.265
CT	5.20×10^{-1}	42	0.474
Single crystals	–	53–56	–

Table 2

Sample no. and material type		Average cross-sectional area of grains, mm^2	Linear density of twins, cm^{-1}	Average dislocation density, cm^{-2}	Attenuation coefficient at a wavelength of 10 μm
1	(Single crystals)	–	–	3.2×10^7	0.183
2	(CT)	6.88	1.77	2.0×10^6	0.049
3	(CT)	5.12	3.27	5.0×10^5	0.053
4	(CT)	4.16	6.32	1.5×10^6	0.043
5	(CT)	4.12	5.65	8.0×10^5	0.044
6	(CT)	3.54	5.53	3.8×10^6	0.036
7	(CT)	3.19	4.64	2.4×10^6	0.036
8	(CT)	2.90	5.07	5.0×10^6	0.049
9	(CT)	1.72	5.29	1.3×10^6	0.057
10	(CT)	1.28	7.75	3.0×10^6	0.097
11	(CT)	0.98	9.79	5.0×10^6	0.077
12–1	(ED)	3.8×10^{-1}	12.42	2.5×10^6	0.176
12–2	(ED)	2.4×10^{-2}	14.46	2.5×10^6	0.176
13–1	(ED)	2.0×10^{-1}	5.19	1.7×10^6	0.254
13–2	(ED)	3.8×10^{-1}	5.37	1.7×10^6	0.254
14–1	(CVD)	2.2×10^{-2}	16.7	1.6×10^6	0.243
14–2	(CVD)	6.4×10^{-4}	16.7	1.6×10^6	0.243
15–1	(CVD)	2.0×10^{-2}	2.16	2.3×10^6	0.336
15–2	(CVD)	4.6×10^{-4}	2.16	2.3×10^6	0.336

where $R = (n-1)^2/(n+1)^2$ is the reflectance. As a result, we obtain the formula for calculating the attenuation coefficient [5] at the wavelength λ,

$$\mu_\lambda = -L^{-1}\log\frac{n_\lambda^2+1}{2n_\lambda}T_\lambda,$$

where L is the sample thickness.

2. RESULTS

Previously, we have established that the size distribution of grains in the materials under investigation is exponential [6].

Optical transmission spectra in the visible and near-IR regions show that the transmittance increases with the wavelength of light and attains a maximum at 1.1 μm (see Table 1). CVD-type crystals have the smallest average grain size, almost perfect structure, and the smallest attenuation coefficient. The transmittance of ED-type crystals is virtually identical to that of single crystals.

Table 2 lists the results of studies at a wavelength of 10 μm. For comparison, the data on single crystals are also listed.

These data show that the material produced using the CT is characterized by the largest grain sizes. The average cross-sectional area of grains in the ED- and CVD-type materials is smaller than that of the CT-type material by one and two to four orders of magnitude, respectively. The difference in the linear density of twin boundaries and dislocations is insignificant for all the crystals. Coarse- (CT) and fine- (CVD) grained materials feature the lowest and highest attenuation coefficients, respectively. The attenuation coefficient of the ED-type material differs slightly from that of single crystals.

We note that the smallest attenuation coefficient (0.036) is characteristic of CT-type materials with a grain cross-sectional area of 3–4 mm^2. The average grain size of the CT-type material is 10^3 μm, which exceeds the wavelength of 10 μm by two orders of magnitude; therefore, the light attenuation is mainly controlled by reflection from grain boundaries. The grain diameter in the ED-type material is of the same order of magnitude as the radiation wavelength. The grain diameter of the CVD-type polycrystalline material is an order of magnitude smaller than the wavelength; therefore, in addition to reflection from grain boundaries, the attenuation is also affected by the diffraction effect.

3. CONCLUSIONS

(i) The optical properties of a polycrystalline material are controlled not only by the grain size but also by the grains' structural quality.

(ii) The material structural quality and grain size are controlled by the growth method; the smallest and largest grain sizes are characteristic of ED- and CT-type materials, respectively.

(iii) At the wavelength of 1.1 μm, the smallest and largest attenuation coefficients are characteristic of CVD- and CT-type samples, respectively. As for the studies at 10 μm, a reverse situation arises. The ED-type material has an attenuation coefficient close to that of single crystals.

(iv) At the wavelength of 10 μm, light is mainly scattered by grain boundaries of a polycrystalline material containing grain-confined dislocations and impurity atoms. At 1.1 μm, scattering is mostly associated with grain defects, i.e., twin boundaries and dislocations.

The studies showed that the optical properties of polycrystalline zinc selenide are no worse than those of single crystals and, in some cases, are superior.

REFERENCES

1. I. P. Kulakov and A. V. Fadeev, Izv. Akad. Nauk SSSR, Neorg. Mater. **16** (1), 159 (1980).
2. *Acoustic Crystals* (Nauka, Moscow, 1976).
3. B. M. Slepchenko, V. V. Musatov, and A. N. Bryzgalov, Fiz. Tverd. Tela (Leningrad) **32**, 638 (1990) [Sov. Phys. Solid State **32**, 375 (1990)].
4. A. N. Bryzgalov, Doctoral Dissertation (Ufa, 1998).
5. A. N. Bryzgalov, B. M. Slepchenko, and V. V. Musatov, Izv. Akad. Nauk SSSR, Neorg. Mater. **25**, 1430 (1989).
6. A. A. Yaksenovskikh, A. N. Bryzgalov, V. V. Musatov, *et al.*, Izv. Akad. Nauk SSSR, Neorg. Mater. **27**, 1176 (1991).

Translated by A. Kazantsev

Semiconductors, Vol. 38, No. 3, 2004, pp. 313–318. Translated from Fizika i Tekhnika Poluprovodnikov, Vol. 38, No. 3, 2004, pp. 325–330.

SEMICONDUCTOR STRUCTURES, INTERFACES, AND SURFACES

Low-Temperature Relaxation of Elastic Stresses in SiGe/Si Heterostructures Irradiated with Ge^+ Ions

V. S. Avrutin*, Yu. A. Agafonov*, A. F. Vyatkin*^, V. I. Zinenko*, N. F. Izyumskaya*, D. V. Irzhak*, D. V. Roshchupkin*, É. A. Steinman, V. I. Vdovin***, and T. G. Yugova******

**Institute of Microelectronic Technology, Russian Academy of Sciences, Chernogolovka, Moscow oblast, 142432 Russia*

^e-mail: vyatkin@ipmt-hpm.ac.ru

***Institute of Solid-State Physics, Russian Academy of Sciences, Chernogolovka, Moscow oblast, 142432 Russia*

****Institute for Chemical Problems in Microelectronics, Moscow, 117571 Russia*

*****State Research Institute for the Rare-Metals Industry, Moscow, 119017 Russia*

Submitted June 18, 2003; accepted for publication July 1, 2003

Abstract—Pseudomorphic $Si_{0.76}Ge_{0.24}$/Si heterostructures grown by molecular-beam epitaxy were irradiated with 350-keV Ge^+ ions at a temperature of 400°C so that the peak of the ions' energy losses was located within the silicon substrate (deeper than the SiGe–Si interface). The effect of ion implantation on the relaxation of elastic stresses and the defect structure formed as a result of postimplantation annealing is studied. It is found that annealing at a temperature even as low as 600°C makes it possible to ensure a very high degree of relaxation of elastic stresses in the heterostructure and a comparatively low density of threading dislocations in the SiGe layer ($<10^5$ cm^{-2}). The results obtained make it possible to suggest a method for the formation of thin SiGe/Si layers that feature a high degree of relaxation, low density of threading dislocations, and a good surface morphology.

1. INTRODUCTION

The active interest in epitaxial growth of $Si_{1-x}Ge_x$ layers on Si substrates is related primarily to the fact that new electronic and optoelectronic devices can be fabricated on the basis of SiGe/Si heterostructures. As is well known, SiGe films obtained as a result of pseudomorphic growth on Si substrates are found to be elastically stressed owing to the large mismatch between the lattice parameters of Si and Ge (4.12%). At the same time, SiGe layers with a high degree of relaxation are required to fabricate certain types of devices based on SiGe/Si structures (field-effect transistors, photodetectors, and solar cells) [1]. In addition, the use of relaxed SiGe buffer layers presents additional opportunities for controlling the energy-band structure and for integrating devices based on III–V compounds into conventional silicon technology. It is well known that the relaxation of elastic stresses in heterostructures occurs if the critical thickness of an epitaxial layer is exceeded by introducing misfit dislocations into the vicinity of the interphase boundary. It is important that tilted segments of the dislocations introduced thread through the epitaxial layer [2]. The presence of threading dislocations in the film significantly impairs its characteristics and makes it virtually impossible to use such structures in electronic and optical devices [3]. Therefore, reducing the threading-dislocation density is the most important problem in the development of electronic devices based on SiGe/Si heterostructures.

At present, epitaxial growth of $Si_{1-x}Ge_x$ buffer layers with a gradient of Ge concentration is the most highly developed method for fabricating SiGe films with a high degree of relaxation and a comparatively low density of threading dislocations (10^5–10^6 cm^{-2}) [4, 5]. However, in order to obtain films with a low density of threading dislocations, one has to ensure that gradients of Ge concentration are very low (typically, 5–10% per micrometer). This circumstance necessitates a large thickness of the buffer layer (several micrometers); as a result, growth times are long and a large amount of material is consumed. This significantly increases the production cost of devices and makes it more difficult to integrate them into Si integrated circuits. Another serious drawback of the method described above is the large-amplitude surface roughness of the buffer layers with a gradient of Ge concentration [6]. Introducing nonequilibrium point defects into the heterostructures is an alternative approach to solving the above-formulated problem. It has been recently shown that nonequilibrium point defects introduced into the heterostructures promote the relaxation of stresses and, at the same time, can reduce the density of threading dislocations to a great extent [7–15]. Point defects can be introduced by lowering the growth temperature, which leads to a saturation of the growing layers with nonequilibrium point defects of the vacancy type [7–12], and also by irradiating the layers with low-energy ions in the course [11–13]

or after completion [14–21] of epitaxial growth. It is generally believed that promoted relaxation of stresses is caused by the formation of clusters of point defects that act as origination sites for misfit dislocations. However, the specific mechanism of promotion of elastic-stress relaxation in SiGe/Si heterostructures oversaturated with point defects has not yet been ascertained and requires further investigation.

In our previous publications [19–21], we reported the results of studying the effects of the ion type and the temperature and dose of ion implantation on relaxation of elastic stresses in pseudomorphic SiGe/Si heterostructures. We found that irradiation of heterostructures with Ge^+ heavy ions at elevated temperatures increased the rate of the relaxation process appreciably. In this study, we concentrate on studying the effect of irradiation of $Si_{0.76}Ge_{0.24}$/Si heterostructures with Ge^+ ions on the dislocation structure formed as a result of relaxation of elastic stresses in the course of postimplantation annealing. We then discuss the causes of the increase in the relaxation rate.

2. EXPERIMENTAL

An undoped pseudomorphic $Si_{0.76}Ge_{0.24}$ 135-nm-thick layer was grown on the Si(100) substrate using molecular-beam epitaxy at a substrate temperature of 550°C. The layer thickness was chosen so that the stress relaxation was suppressed in the course of growth. The film composition was determined from the analysis of X-ray diffraction. The spread of Ge concentration over the wafer did not exceed 2%. The wafer was cut into the samples with an area of about 1.5×1.0 cm^2. The samples were irradiated with 350-keV Ge^+ ions at a temperature of 400°C; the doses were 10^{13}, 2.5×10^{13}, and 5×10^{13} cm^{-2}. On the basis of calculations carried out using the SUSPRE software package, the energy of implanted ions was chosen so that the peak of the ion energy losses was beyond the $Si_{0.76}Ge_{0.24}$/Si interface (i.e., in silicon, at a depth of about 200 nm from the outer surface of the heterostructure). The doses were chosen so that, on the one hand, the amorphization of the layer was avoided and, on the other hand, a high concentration of nonequilibrium point defects was formed. Samples irradiated with ions and unirradiated (reference) samples were annealed in a vacuum furnace (at a pressure of ~10^{-6} Torr) for 15 min at temperatures of 500, 550, and 600°C. The temperature was maintained constant to within ±2°C. The relaxation of elastic stresses in the samples was studied by transmission electron microscopy (TEM) using a JEM 200CX microscope with an accelerating voltage of 200 kV, by double-crystal X-ray diffraction (using a Rigaku RU-200 diffractometer and Cu K_α radiation or Mo K_α radiation), and by analyzing the spectra of low-temperature photoluminescence (PL). The degree of elastic-stress relaxation was determined from the X-ray diffraction data using the following formula:

$$R = \frac{a_\perp^{\text{pseud}} - a_\perp^{\text{rel}}}{a_\perp^{\text{pseud}} - a_c} \times 100\%.$$

Here, $a_\perp^{\text{pseud}}$ and $a_\perp^{\text{rel}}$ are the lattice parameters of the pseudomorphic and relaxed SiGe layers in the direction perpendicular to the growth plane, and a_c is the lattice parameter of bulk SiGe. The PL was excited at a temperature of 4.2 K using radiation from an Ar laser (514.5 nm). The PL signal was detected using a cooled germanium photoresistor and an MDR-2 wide-aperture monochromator. In order to determine the contribution of different regions in the structure under investigation to the PL signal, we used layer-by-layer chemical etching of the sample. The PL spectrum was measured after each specific layer was etched off. The density of threading dislocations in the layer was evaluated from the density of etching pits after the treatment of the sample in an HF : Cr_2O_3 : H_2O (4 : 1 : 1.5) solution using a Nomarski optical microscope. The roughness of the sample surfaces was evaluated using a Dimension 3100 NanoScope III*a* System (Digital Systems) atomic-force microscope (AFM).

3. RESULTS

According to the X-ray diffraction and PL data, the degree of relaxation of elastic stresses in the as-grown $Si_{0.76}Ge_{0.24}$/Si structures is equal to zero. The curves of X-ray reflection diffraction for all the samples measured before and after ion implantation have a similar shape. In order to reveal the effect of ion implantation on the relaxation process, we annealed first the sample irradiated with the highest dose of ions (5×10^{13} cm^{-2}) and then the reference (unirradiated) sample each for 15 min at a temperature of 500°C. However, the curves of reflection diffraction of both samples were unaffected by this annealing. Therefore, these samples were subjected to an additional annealing for 15 min at a temperature of 600°C. In Fig. 1, we show the curves of reflection diffraction for the reference sample (curve *1*) and the sample irradiated with a dose of 5×10^{13} cm^{-2} (curve *2*). Both samples were subjected to the two-stage annealing: first, for 15 min at 500°C and then for 15 min at 600°C. It can be seen that the second annealing resulted in an appreciable relaxation of stresses in the irradiated sample: the degree of relaxation in this sample R is about 80% (curve *2*), whereas R is on the order of 1% for the reference sample (curve *1*).

In Fig. 2, we show the TEM images of cross sections of the aforementioned samples. It can be seen that, in agreement with the X-ray diffraction data, the networks of misfit dislocations in these samples differ widely. A planar network is observed in the reference sample (Fig. 2a); the dislocation density and, accordingly, the degree of relaxation are low in this sample. In contrast,

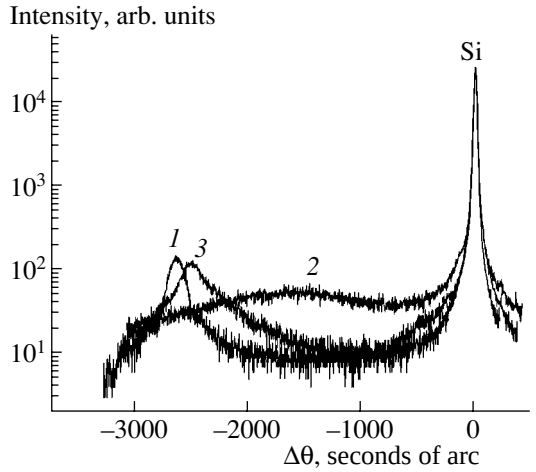

Fig. 1. Curves of reflection diffraction 004 (Cu K_α radiation) for (*1*) a reference (unirradiated) sample annealed first for 15 min at 500°C and then for 15 min at 600°C and (*2*, *3*) two samples irradiated with Ge^+ ions at 400°C with a dose of 5×10^{13} cm^{-2} and then annealed (*2*) first for 15 min at 500°C and then for 15 min at 600°C and (*3*) annealed for 15 min at 550°C.

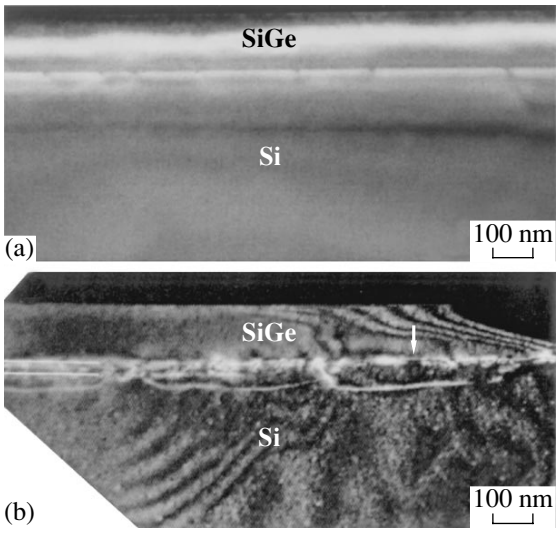

Fig. 2. A TEM image of cross sections ($g = \langle 220 \rangle$) of the samples subjected to two-stage annealing, first for 15 min at 500°C and then for 15 min at 600°C: (a) the reference sample (the bright field) and (b) the sample irradiated with a dose of 5×10^{13} cm^{-2} of Ge^+ ions (the dark field). The upper boundary of the misfit-dislocation network in the irradiated sample coincides with the SiGe–Si interface (indicated by the arrow).

the network of misfit dislocations is three-dimensional and very dense in the implanted sample (Fig. 2b); the upper boundary of this network coincides with the SiGe–Si interface (indicated by an arrow). The thickness of the region containing the network of misfit dislocations is 30–50 nm (indicated by two parallel lines

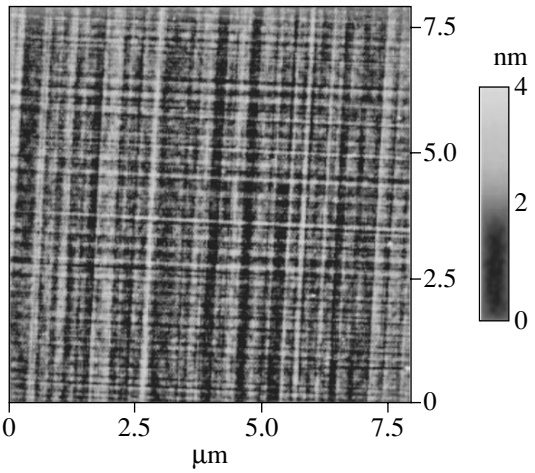

Fig. 3. An AFM image of the surface of a sample irradiated with 5×10^{13} cm^{-2} dose of Ge^+ ions with subsequent annealing first for 15 min at 500°C and then for 15 min at 600°C.

in Fig. 2b), which is smaller than the corresponding values observed typically at high degrees of relaxation. It is worth noting that the depth to which the dislocation half-loops propagate into the substrate is comparatively small, and the number of these loops is not large considering the high degree of relaxation observed. We also note that a significant deterioration of the sample's surface morphology is not observed in the TEM image of the sample with a high degree of relaxation (Fig. 2b) (a corrugated surface is typically observed in the case of a high degree of relaxation). According to the AFM data, the rms amplitude of the surface roughness for this sample is equal to a mere 0.4 nm for the scanned area of 8×8 μm^2 (Fig. 3). The dislocation lines observed by TEM for planar films and by AFM and Nomarski optical microscopy are straight and long. According to an estimation based on the TEM data, the density of threading dislocations in the SiGe layer is lower than 10^6 cm^{-2}. It follows from the density of etching pits observed at the sample surface and measured using Nomarski optical microscopy that the density of threading dislocations is lower than 10^5 cm^{-2}.

In Fig. 4, we show a PL spectrum measured immediately after the structures were grown; the spectrum includes the SiGe TO (transverse optical phonon), SiGe ZP (zero phonon), and Si TO lines (curve *1*). The PL spectra of two samples subjected to two-stage annealing first for 15 min at 500°C and then for 15 min at 600°C—for the reference sample (curve *2*) and for a sample irradiated with 5×10^{13} cm^{-2} of Ge+ ions (curve *3*)—are also shown in Fig. 4 (the TEM images of cross sections of these samples are shown in Fig. 2). It can be seen from comparison of spectra *2* and *3* that the relaxation proceeds in the samples under consideration differently: the spectrum of the reference sample features

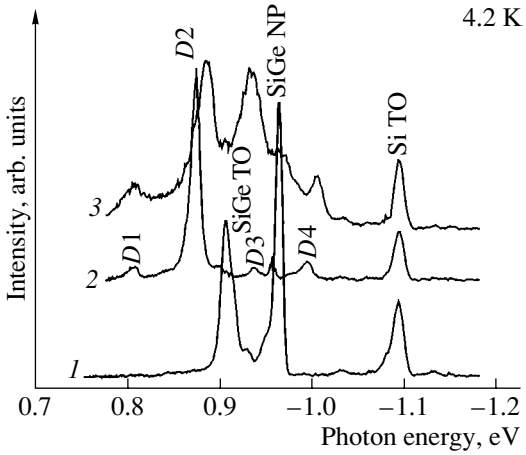

Fig. 4. PL spectra of (*1*) an as-grown $Si_{0.76}Ge_{0.24}$/Si structure and (*2*, *3*) two samples subjected to the two-stage annealing first for 15 min at 500°C and then for 15 min at 600°C: (*2*) the reference sample and (*3*) the sample irradiated with a dose of 5×10^{13} cm^{-2} of Ge^+ ions. The spectra are shifted along the vertical axis to make it easier to trace the spectra. $T = 4.2$ K.

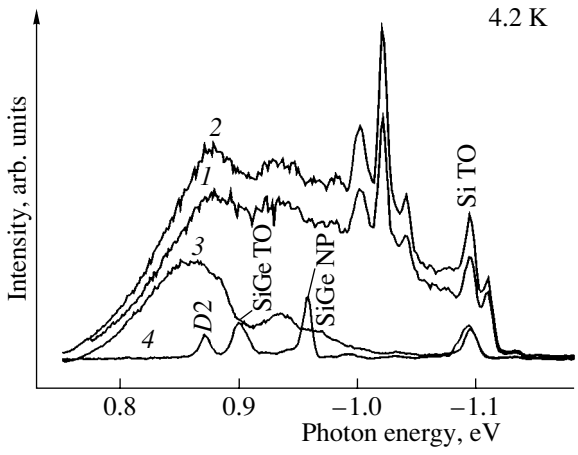

Fig. 5. PL spectra of a sample irradiated with Ge^+ ions at 400°C with a dose of 5×10^{13} cm^{-2}; the spectra were measured (*1*) immediately after irradiation, (*2*) after chemical etching, and (*3*) after postirradiation annealing for 15 min at 550°C. Curve *4* represents the PL spectrum of the reference (unirradiated) sample annealed under the same conditions. All spectra were measured at 4.2 K.

the well-known dislocation-related spectral lines *D*1 (0.81 eV), *D*2 (0.87 eV), *D*3 (0.93 eV), and *D*4 (1.0 eV), whereas the spectrum of implanted samples features lines peaked at 0.89, 0.93, 0.97, and 1.005 eV, as well as the line *D*1 and a shoulder at 0.87 eV that corresponds to the line *D*2. So far, we have failed to attribute these lines to specific recombination centers; we have also failed to find any published data on these lines. The layer-by-layer etching of the samples in combination with PL measurements showed that the recombination centers responsible for the appearance of the lines under consideration were located at a depth that exceeded the thickness of the SiGe layer (the PL intensity increased as more of the SiGe sublayers were etched off). It may be assumed that these lines are related to a specific dislocation structure formed in the irradiation-damaged region of the silicon substrate.

In order to gain insight into the initial stage of the stress relaxation, we annealed the samples, which were irradiated with different doses of ions, for 15 min at 550°C. In Fig. 1 (curve *3*), we show the curve of reflection diffraction for a sample irradiated with a dose of 5×10^{13} cm^{-2} and then annealed for 15 min at 550°C. It can be seen that the SiGe peak broadens and shifts closer to the Si peak as a result of annealing, which is indicative of relaxation of stresses in the structure. The degree of stress relaxation in the structure under consideration amounts to about 1%. At the same time, the curves of reflection diffraction for the samples irradiated with lower doses (the same as the curve for the reference sample) virtually did not change as a result of annealing at a temperature of 550°C.

In Fig. 5, we show the PL spectra measured immediately after ion implantation (curve *1*), after chemical etching (curve *2*), and after postimplantation annealing for 15 min at a temperature of 550°C (curve *3*). The PL spectrum of the reference sample annealed under the same conditions is also shown (curve *4*) for the sake of comparison. The PL spectrum measured after ion implantation features a line peaked at 1.018 eV and related to the recombination of electron–hole pairs at multivacancies [22]; the corresponding phonon replicas are also observed (Fig. 5, curve *1*). Excitonic lines related to the SiGe layer are not observed, since the radiation defects apparently give rise to a more efficient recombination channel. The PL intensity increases after a 160-nm-thick layer is chemically etched off (Fig. 5, curve *2*). This means that the PL signal originates at a depth of >160 nm, i.e., in the Si substrate (the SiGe layer thickness is 135 nm). This fact is consistent with the TEM data and with calculations of the depth corresponding to the peak of energy losses of ions according to the SUSPRE software package (~200 nm). As a result of annealing, the 1.018-eV line and its phonon replicas disappear and broad bands peaked at 0.86–0.89 and 0.94 eV come into existence (Fig. 5, curve *3*). Similar PL bands were previously observed by Schmidt *et al.* [23]; however, the origin of these bands remains unknown. It is of interest that the spectrum of the reference sample includes the well-known dislocation-related line *D*2 peaked at 0.87 eV in addition to two lines related to the stressed SiGe layer (the SiGe-TO line at 0.90 eV and the SiGe-ZP line at 0.96 eV) (see Fig. 5, curve *4*). The presence of the *D*2 line in the PL spectrum indicates that relaxation of elastic stresses sets in as a result of annealing for 15 min at 550°C,

although, according to the X-ray diffraction data, the degree of relaxation in this sample is equal to zero. This discrepancy is attributed to the fact that PL is a method that is more sensitive to initial stages of relaxation than X-ray diffraction.

4. DISCUSSION

On the basis of the above results, we may assume that irradiation of SiGe/Si heterostructures with Ge^+ ions at elevated temperature gives rise to point-defect complexes that are conducive to subsequent relaxation of elastic stresses by providing the generation sites for dislocations. As was mentioned above, the TEM study of a cross section of a sample that is implanted and then annealed revealed a very dense network of misfit dislocations below the SiGe–Si interface (Fig. 2b), which indicates that the dislocation loops were generated in a rather thin layer beneath this interface. These loops expanded in the course of annealing, reached the SiGe–Si interface, and formed a network of misfit dislocations. Furthermore, a high generation rate of dislocation loops should give rise to a uniform distribution of these loops and, as a result, to a uniform distribution of threading segments of dislocations, which in turn is conducive to mutual annihilation of these segments. This circumstance may account for the low density of threading dislocations in the SiGe layer.

Thus, we obtained thin and highly relaxed SiGe films with a comparatively low density of threading dislocations as a result of annealing at a moderately high temperature (600°C). This method appears to be very useful for fabricating thin SiGe layers with a high degree of relaxation and a good surface morphology. It should be noted that the thickness of the layers we obtained is appreciably smaller (for the same degree of relaxation) than the thickness of buffer layers with a gradient of Ge concentration [5] and that of SiGe films formed on buffer Si layers grown at comparatively low temperatures [4]. Previously, Hollander *et al.* [14, 15] successfully used the implantation of H^+ ions with a dose of 3×10^{16} cm^{-2} to obtain SiGe layers with a high degree of stress relaxation and a low density of defects. However, in the conditions of our experiments, both the annealing temperature and the implantation dose required for appreciable promotion of relaxation were much lower than in the case of hydrogen implantation. This fact can be explained in the following way: heavy Ge^+ ions that give rise to dense collision cascades and a fairly high temperature of implantation (400°C) and ensure a high diffusive mobility of point defects introduced by implantation are conducive to the formation of defect complexes; the latter then act as sites for the origination of dislocation loops. The above assumption is also confirmed by the results of our previous studies [19, 20], in which we did not observe any significant promotion of stress relaxation in structures irradiated with lighter Ar^+ ions (with a dose of 10^{14} cm^{-2}) at 400°C or in structures irradiated with Ge^+ ions at a lower temperature of 230°C (the dose was 5×10^{13} cm^{-2}).

5. CONCLUSION

Irradiation of $Si_{0.76}Ge_{0.24}$/Si heterostructures with Ge^+ ions at a temperature of 400°C leads to an appreciable promotion of elastic-stress relaxation in the course of postimplantation annealing. In contrast to unirradiated samples, the relaxation of stresses in irradiated structures proceeds at a significant rate at such comparatively low temperatures as 550–600°C. The results obtained suggest a method for obtaining thin SiGe layers on Si with a high degree of stress relaxation, a comparatively low density of misfit dislocations ($<10^5$ cm^{-2}), and a low surface roughness. The main advantages of the method under consideration are low implantation doses ($\sim 10^{13}$ cm^{-2}) and the low temperature of the postimplantation annealing. Data from TEM, X-ray diffraction, and PL make it possible to conclude that complexes of point defects formed as a result of implantation of Ge^+ ions are responsible for the promoted relaxation of stresses in the heterostructures under consideration.

ACKNOWLEDGMENTS

We thank T. Hackbarth (Daimler Chrysler AG) for fabricating the SiGe/Si epitaxial structures.

This study was supported by the Russian Foundation for Basic Research, project nos. 00-02-18039 and 02-02-16692.

REFERENCES

1. D. J. Pau, Adv. Mater. **11**, 191 (1999).
2. A. N. Larsen, Solid State Phenom. **69–70**, 43 (1999).
3. U. Kenig and J. Hersener, Solid State Phenom. **47–48**, 17 (1996).
4. Y.-H. Xie, E. A. Fitzgerald, D. Monroe, *et al.*, J. Appl. Phys. **73**, 8364 (1993).
5. C. W. Leitz, M. T. Currie, A. Y. Kim, *et al.*, J. Appl. Phys. **90**, 2730 (2001).
6. S. Yu. Shiryaev, F. Jensen, and J. W. Petersen, Appl. Phys. Lett. **64**, 3305 (1994).
7. K. K. Lindner, F. C. Zhang, J.-S. Rieh, *et al.*, Appl. Phys. Lett. **70**, 3224 (1997).
8. I. H. Li, C. S. Peng, Y. Wu, *et al.*, Appl. Phys. Lett. **71**, 3132 (1997).
9. C. S. Peng, Z. Y. Zhao, H. Chen, *et al.*, Appl. Phys. Lett. **72**, 3160 (1998).
10. C. S. Peng, H. Chen, Z. Y. Zhao, *et al.*, J. Cryst. Growth **201–202**, 530 (1999).
11. E. Kasper, K. Lyutovich, M. Bauer, and M. Oehme, Thin Solid Films **336**, 319 (1998).
12. K. Lyutovich, F. Ernst, E. Kasper, *et al.*, Solid State Phenom. **69–70**, 179 (1999).
13. M. Bauer, M. Oehme, K. Lyutovich, and E. Kasper, Thin Solid Films **336**, 104 (1998).
14. S. Mantl, B. Hollander, R. Liedtke, *et al.*, Nucl. Instrum. Methods Phys. Res. B **147**, 29 (1999).

15. B. Hollander, S. Mantl, R. Liedtke, *et al.*, Nucl. Instrum. Methods Phys. Res. B **148**, 200 (1999).
16. R. Hull, E. A. Stach, R. Tromp, *et al.*, Phys. Status Solidi A **171**, 133 (1999).
17. E. A. Stach, R. Hull, J. C. Bean, *et al.*, Microsc. Microanal. **4**, 294 (1998).
18. H. Trindaus, B. Hollander, S. Rongen, *et al.*, Appl. Phys. Lett. **76**, 3552 (2000).
19. A. F. Vyatkin, V. S. Avrutin, N. F. Izyumskaya, *et al.*, in *Proceedings of XIII International Conference on Ion Implantation Technology (IIT-2000), Alphach, Austria*, Ed. by H. Ryssel *et al.* (IEEE, Piscataway, N.J., 2000), p. 70.
20. A. F. Vyatkin, V. S. Avrutin, N. F. Izyumskaya, *et al.*, in *Proceedings of 7th Russian–Japanese International Symposium on Interaction of Fast Charged Particles with Solids* (Nizhni Novgorod, 2000), p. 22.
21. V. S. Avrutin, N. F. Izyumskaya, A. F. Vyatkin, *et al.*, Mater. Sci. Eng. B **89**, 350 (2002).
22. N. Burger, E. Irion, A. Teschner, *et al.*, Phys. Rev. B **35**, 3804 (1987).
23. D. C. Schmidt, B. G. Svensson, M. Seibt, *et al.*, J. Appl. Phys. **88**, 2309 (2000).

Translated by A. Spitsyn

Semiconductors, Vol. 38, No. 3, 2004, pp. 319–321. Translated from Fizika i Tekhnika Poluprovodnikov, Vol. 38, No. 3, 2004, pp. 331–334.

SEMICONDUCTOR STRUCTURES, INTERFACES, AND SURFACES

Native Disorder Potential at the Surface of a Heavily Doped Semiconductor

V. B. Bondarenko, V. V. Korablev, and Yu. I. Ravich

St. Petersburg State Technical University, ul. Politekhnicheskaya 29, St. Petersburg, 195251 Russia

Submitted April 28, 2003; accepted for publication July 9, 2003

Abstract—The dependence of native potential inhomogeneities on spatial dispersion of the dielectric response of the two-dimensional electron gas at the surface of a heavily doped semiconductor is discussed. The amplitude and scale of the disorder potential in the case of a strongly degenerate surface electron gas are determined. It is shown that the inhomogeneities considered depend on the surface and bulk parameters. © *2004 MAIK "Nauka/Interperiodica".*

The previous analysis of inhomogeneities of the electric potential at the surface of extrinsic semiconductors [1, 2] produced by the discrete character of the distribution of the bulk charge has shown that, in the presence of a high density of surface delocalized electronic states, the average value of the random potential is on the order of several meV. For most surface processes at room and higher temperatures, the changes in the electron potential energy are small compared to the thermal energy and, as a rule, can be disregarded. However, these estimations can fail, at least for heavily doped structures (with concentrations of about 10^{18} cm^{-3} or higher), for which the probability of localization of a charged defect directly at the surface is increased. First of all, for these systems it is necessary to take into account that potential perturbations created by point charges, specifically, by electrically active defects in surface depletion layers, are nonlinearly screened by the two-dimensional electron gas [3]. Obviously, the dependence of the surface dielectric response on the degree of inhomogeneity of the initial potential must result in a change in the average magnitude of the random potential. It should also be noted that the dependence of the response on the surface density of states obtained in [2] produces appreciable estimation errors for densities exceeding about 10^{12} cm^{-2} eV^{-1}. In this case, the surface-potential inhomogeneities obtained for a heavily doped semiconductor increase in the presence of a delocalized electron gas. The reason for this unsatisfactory result consists in the limitations of the use of the standard imaging method when calculating the electric field and potential at the surface for finite densities of electronic states. To obtain the best approximation, one must evaluate the permittivity of the medium using a wider range of wave vectors for the initial perturbation; i.e., one must take into account the spatial dispersion of the permittivity. The aim of this study is to find the dependence of the amplitude of the random potential at the surface of a heavily doped semiconductor on the dispersion properties of a two-dimensional electron gas.

In order to evaluate the effect of spatial dispersion on the native-potential inhomogeneities, we consider the case of a strongly degenerate two-dimensional electron gas. Let the Fermi energy for surface electrons E_F be much greater than the thermal energy kT. We write the potential energy of an electron in the field of the ith Coulomb center (singly charged donor) in the surface plane outside of dielectric medium as

$$V_i(\rho) = -\frac{e^2}{\sqrt{\rho^2 + d_i^2/4}}. \quad (1)$$

Here, ρ is the radial coordinate in the plane of electron localization and d_i is the doubled distance of the ith Coulomb center to this plane. The Fourier transform of the potential (1) is well known,

$$V_i(q) = -\frac{e^2 \exp(-qd_i/2)}{q}, \quad (2)$$

where q is the magnitude of the wave vector in the surface plane. The screened potential, which is generated by the ith Coulomb center at the surface, is determined in the usual way,

$$U_i(\rho) = \int_0^\infty U_i(q) J_0(\rho q) q dq, \quad (3)$$

where $J_0(s)$ is the Bessel function of order zero, $U_i(q) = V_i(q)/\kappa(q)$ is the Fourier transform of the screened potential, and $\kappa(q)$ is the dielectric response function of

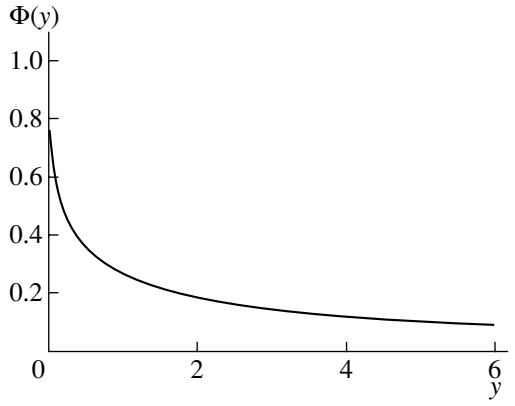

Fig. 1. Function $\Phi(y)$, Eq. (13).

the medium. In this case, in the presence of a free semiconductor surface, the function $\kappa(q)$ has the form [3]

$$\kappa(q) = \begin{cases} \dfrac{\varepsilon+1}{2}\left(1+\dfrac{q_s}{q}\right), & q \le 2k_F, \\ \dfrac{\varepsilon+1}{2}\left[1+(1-\sqrt{1-4k_F^2/q^2})\dfrac{q_s}{q}\right], & q > 2k_F, \end{cases} \quad (4)$$

where ε is the static permittivity of the semiconductor, k_F is the wave vector of a surface electron at the Fermi level, $q_s = 4\pi e^2 D_0/(\varepsilon+1)$, and D_0 is the surface density of states. Under conditions of strong degeneracy of the two-dimensional electron gas, we should set $\kappa(q)$ for $q \le 2k_F$. For a small inhomogeneity of the perturbation, i.e., for $q \ll q_s$, the dielectric response function is given by

$$\kappa(q) = \frac{(\varepsilon+1)q_s}{2q}. \quad (5)$$

Using transform (3) and expression (5), we obtain the screened potential

$$U_i(\rho) = -\frac{d_i}{4\pi D_0(\rho^2 + d_i^2/4)^{3/2}}; \quad (6)$$

this potential can also be obtained using the Thomas–Fermi approximation. Averaging the potential (6) and assuming that the positions of charged impurities at the surface are independent, we find the dependence of native potential inhomogeneities δU on the parameters of the system [2],

$$\delta U = \frac{1}{D_0 L_0}\sqrt{\frac{N_s}{\pi}}. \quad (7)$$

Here, $L_0 = \sqrt{\varepsilon U_0/2\pi e^2 N_0}$ is the width of the depletion layer, U_0 is the magnitude of the band bending, N_0 is the doping level, and $N_s = N_0 L_0$ is the surface charge density. The result (7) is valid in the presence of a delocalized high-density electron gas at the surface. For complete localization of the surface charge, the potential of the ith center at the surface can also be calculated using the formalism of the dielectric response function. This situation corresponds to the other limiting case for the perturbation wave vectors, $q \gg q_s$. It follows from formula (4) that, in this range of wave vectors q, the permittivity is equal to the arithmetic mean of permittivities of the neighboring media. Since in this case κ is a constant, we directly obtain the screened potential in the form

$$U_i(\rho) = \frac{2}{\varepsilon+1}V_i(\rho). \quad (8)$$

For a Poisson ensemble of discrete impurity charges in the depletion layer, the expression for the characteristic amplitude of potential inhomogeneities at the surface with localized states was obtained in [2]. Averaging expression (8) and then finding the maximum of the functional, we obtain the following result:

$$\delta U = \frac{4e^2\sqrt{\pi N_s}}{\varepsilon+1}. \quad (9)$$

Generally, when analyzing native inhomogeneities at the semiconductor surface, it is necessary to find the screened potential taking into account the corresponding dielectric response function (4). As before, we assume that the electron gas at the semiconductor surface is strongly degenerate. Using expression (3) and changing the integration order in the expression for the average value of the surface potential inhomogeneity $\delta U(R)$ over an area of radius R, we obtain

$$\delta U(R) = \frac{4e^2\sqrt{\pi N_s}}{(\varepsilon+1)L_0}\int_0^\infty \frac{1-\exp(-qL_0)}{q(q+q_s)}J_1(qR)dq, \quad (10)$$

where $J_1(s)$ is the first-order Bessel function. Subsequent calculations show that the maximum of $\delta U(R)$ is attained at some value of the radius $R = R_0$, which is approximately estimated as

$$R_0 \approx \sqrt{\frac{L_0}{q_s}}; \quad (11)$$

the radius R_0 gives an order-of-magnitude estimate of the scale of potential inhomogeneities at the semiconductor surface. The value δU can be estimated by directly substituting formula (11) into expression (10),

$$\delta U = \frac{4e^2\sqrt{\pi N_s}}{\varepsilon+1}\Phi(q_s L_0), \quad (12)$$

where a new function $\Phi(y)$ introduced here is given by

$$\Phi(y) = \int_0^\infty \frac{1-\exp(-x)}{x(x+y)}J_1(x/\sqrt{y})dx. \quad (13)$$

The function $\Phi(y)$ is plotted in Fig. 1. It follows from the definition of this function [4] that $\Phi(0) = 1$ and that its asymptotic behavior is described by $\Phi(y) \propto 1/y$ as $y \gg 1$.

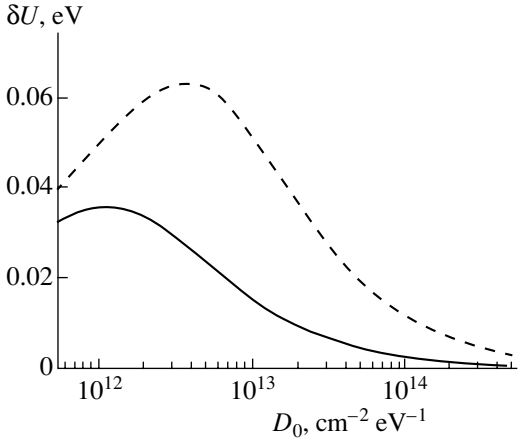

Fig. 2. Amplitude of the native potential inhomogeneity at the surface of heavily doped Si (ε = 12, E_g = 1.1 eV) as a function of the surface density of states for the impurity concentrations of 10^{18} cm^{-3} (solid curve) and 10^{19} cm^{-3} (dashed curve).

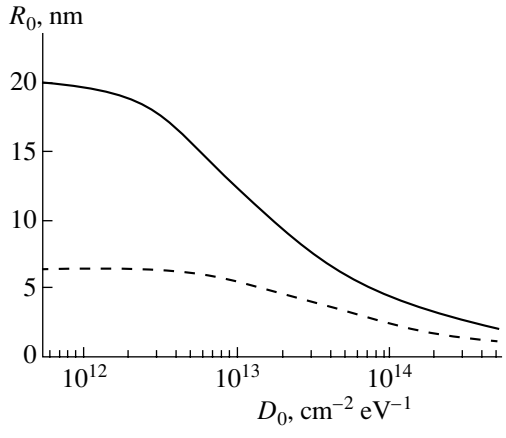

Fig. 3. The scale of the native potential inhomogeneity at the surface of heavily doped Si (ε = 12, E_g = 1.1 eV) as a function of the surface density of states for impurity concentrations 10^{18} cm^{-3} (solid curve) and 10^{19} cm^{-3} (dashed curve).

Formula (12) is not yet the final form of the expression for the average potential inhomogeneity. The magnitude of the band bending U_0 in this formula a priori depends on the density and the spectrum of the surface states. In the case of a strongly degenerate electron gas at the surface of a semiconductor with a high density of electronic states, the Fermi level is pinned in the middle of the surface state band, whose width is many times larger than the energy *kT*. Using general theoretical reasoning [5], we can assume that the surface band is symmetric with respect to the midgap. Thus, for heavily doped semiconductors, disregarding the Fermi energy in the semiconductor bulk, we find that the surface band bending is given by

$$U_0 \approx \frac{E_g}{2} - \Delta U, \tag{14}$$

where E_g is the band gap and ΔU is the variation of band bending due to the finite surface-state density. Using the electrical neutrality condition for the entire system, we find that the magnitude of the surface charge must be equal to the charge of the depletion layer,

$$D_0 \Delta U = N_0 L_0. \tag{15}$$

Taking into account the explicit dependence of ΔU and L_0 on U_0, we use expression (15) to derive the equation, whose solution is written as

$$U_0 = \frac{E_g}{2} + \frac{\varepsilon N_0}{4\pi e^2 D_0^2}\left(1 - \sqrt{1 + \frac{4\pi e^2 D_0^2 E_g}{\varepsilon N_0}}\right). \tag{16}$$

By using formula (16) to evaluate the parameters in expression (12), we can determine the amplitude of the potential inhomogeneity at the semiconductor surface, related to the discreteness of the charge distribution in the depletion layer. A typical dependence of the amplitude of the potential inhomogeneity on the surface density of states is shown in Fig. 2 for two doping levels. The scale of potential inhomogeneities (Fig. 3) is determined by expression (11), in which the width of the depletion layer depends on the surface density of states.

Now let us sum up. It follows from the above analysis that, in the presence of a strongly degenerate electron gas at the semiconductor surface, the amplitude of potential inhomogeneities considered is limited. If spatial dispersion of the permittivity of the system is taken into account, a nonmonotonic variation of optimum fluctuations of the surface potential is obtained, with the largest value exceeding the thermal energy at room temperature. The characteristic inhomogeneity scale grows with decreasing surface density of states; this variation exhibits a saturation as the largest values of potential inhomogeneities are attained (Fig. 3). The calculations show that the limiting values of the scale R_0 are on the order of the average distance between the impurity atoms $N_0^{-1/3}$.

REFERENCES

1. V. B. Bondarenko, Yu. A. Kudinov, S. G. Ershov, and V. V. Korablev, Fiz. Tekh. Poluprovodn. (St. Petersburg) **30**, 2068 (1996) [Semiconductors **30**, 1078 (1996)].
2. V. B. Bondarenko, M. V. Kuz'min, and V. V. Korablev, Fiz. Tekh. Poluprovodn. (St. Petersburg) **35**, 964 (2001) [Semiconductors **35**, 927 (2001)].
3. T. Ando, A. B. Fowler, and F. Stern, *Electronic Properties of Two-Dimensional Systems* (Am. Phys. Soc., New York, 1982; Mir, Moscow, 1985).
4. I. S. Gradshteyn and I. M. Ryzhik, *Table of Integrals, Series, and Products*, 5th ed. (Nauka, Moscow, 1971; Academic, New York, 1980).
5. *Solid State Surface Science*, Ed. by M. Green (Marcel Dekker, New York, 1969; Mir, Moscow, 1972).

Translated by I. Zvyagin

Semiconductors, Vol. 38, No. 3, 2004, pp. 322–328. Translated from Fizika i Tekhnika Poluprovodnikov, Vol. 38, No. 3, 2004, pp. 335–341.

LOW-DIMENSIONAL SYSTEMS

Spectral Line Broadening in Quantum Wells due to the Coulomb Interaction of Carriers

A. A. Afonenko

Belarussian State University, pr. Fr. Scorini 4, Minsk, 220050 Belarus

e-mail: afonenko@bsu.by

Submitted June 10, 2003; accepted for publication July 1, 2003

Abstract—Theoretical analysis of the emission-line broadening in the case of the Coulomb interaction of carriers has been performed. An approximate analytical expression for the contour of spectral lines with exponential fall-offs was derived using the perturbation theory for a nondegenerate many-body electron–hole system. A qualitative explanation of the known experimental data, including the contour asymmetry and the change in the contour width with varying temperature and excitation level, is given. *© 2004 MAIK "Nauka/Interperiodica".*

1. INTRODUCTION

An adequate theoretical description of the spectral characteristics of semiconductor structures requires taking into account the effects of emission-line broadening. Analysis of the emission processes in terms of the density-matrix formalism with introduction of an empirical time of interband-polarization decay, as well as the description of many-body processes in the first order of perturbation theory with an energy-independent carrier-relaxation time, leads to the Lorentzian profile of a homogeneously broadened emission line [1]. The investigation of laser structures of high crystallographic perfection, in which the effect of spatial inhomogeneities on the spectral broadening was negligible, showed that the form factor of homogeneous broadening has exponential edges [2].

The non-Lorentzian shape of emission lines was theoretically justified in [3, 4] with regard to non-Markovian processes. However, since the calculations are rather complex, the emission processes can be investigated only numerically in the proposed models, which hinders any analysis of the influence of the excitation conditions and the parameters of semiconductor materials on the spectral profile.

In this study, we performed a theoretical analysis of the emission-line broadening in quantum wells in the case of Coulomb interaction between carriers in the approximation of two-dimensional electron–hole system. The main concept of the proposed method lies in the use of many-body perturbation theory for determining the functional dependence of the wings of the emission-line profile with subsequent extrapolation of the central part of the profile with regard to the normalization condition. On the basis of the analytical expression for a homogeneously broadened spectral line obtained in the parabolic-band approximation, the effect of different factors on the transition-line shape was analyzed.

2. PROBABILITY OF OPTICAL TRANSITIONS WITH REGARD TO THE COULOMB INTERACTION

Let us consider spontaneous optical transitions due to which a state with n electron–hole pairs changes to a state with $(n-1)$ electron–hole pairs. We will choose single-particle wave functions in the form of Bloch functions with different wave vectors. Different second-quantization operators will be used for the states in the conduction and valence bands. The electromagnetic-interaction operator, which describes radiative transitions with conservation of the wave vector, can be written in the form

$$\hat{V}_{ph} \propto \sum_{\mathbf{q}} \hat{b}_{-\mathbf{q}} \hat{a}_{\mathbf{q}}, \tag{1}$$

where $\hat{a}_{\mathbf{q}}$ and $\hat{b}_{-\mathbf{q}}$ are the annihilation operators for a conduction electron with the wave vector $\mathbf{q}$ and a valence hole with the wave vector $-\mathbf{q}$, respectively.

We will introduce the interaction between conduction electrons, between valence holes, and between electrons and holes into the Coulomb interaction operator, disregarding the spin and exchange interaction between electrons and holes:

$$\hat{V} = \sum_{i,\,j,\,i',\,j'} V_{\mathbf{k}_i - \mathbf{k}_{i'}} \delta_{\mathbf{k}_{i'} + \mathbf{k}_{j'},\,\mathbf{k}_j + \mathbf{k}_i} \times \left(\frac{1}{2} \hat{a}_{i'}^{+} \hat{a}_{j'}^{+} \hat{a}_j \hat{a}_i + \frac{1}{2} \hat{b}_{i'}^{+} \hat{b}_{j'}^{+} \hat{b}_j \hat{b}_i - \hat{a}_{i'}^{+} \hat{b}_{j'}^{+} \hat{b}_j \hat{a}_i \right). \tag{2}$$

Here, $\hat{a}^{+}$ and $\hat{b}^{+}$ are the creation operators for a conduction electron and a valence hole, respectively, with a certain wave vector and $V_{\mathbf{k}_i - \mathbf{k}_{i'}}$ is the matrix element of the Coulomb interaction.

1063-7826/04/3803-0322$26.00 © 2004 MAIK "Nauka/Interperiodica"

The operator adding the first-order perturbation-theory corrections to the initial many-body states can be written formally as

$$\hat{\Psi}_{cv} = \left\{1 + \sum_{i,j,i',j'} V_{\mathbf{k}_i - \mathbf{k}_{i'}} \delta_{\mathbf{k}_{i'} + \mathbf{k}_{j'}, \mathbf{k}_j + \mathbf{k}_i} \times \left[\frac{\hat{a}_{i'}^+ \hat{a}_{j'}^+ \hat{a}_j \hat{a}_i}{2(E_{c\mathbf{k}_i} + E_{c\mathbf{k}_j} - E_{c\mathbf{k}_{j'}} - E_{c\mathbf{k}_{i'}})} + \frac{\hat{b}_{i'}^+ \hat{b}_{j'}^+ \hat{b}_j \hat{b}_i}{2(E_{v\mathbf{k}_i} + E_{v\mathbf{k}_j} - E_{v\mathbf{k}_{j'}} - E_{v\mathbf{k}_{i'}})} - \frac{\hat{a}_{i'}^+ \hat{b}_{j'}^+ \hat{b}_j \hat{a}_i}{(E_{c\mathbf{k}_i} + E_{v\mathbf{k}_j} - E_{v\mathbf{k}_{j'}} - E_{c\mathbf{k}_{i'}})} \right] \right\}, \quad (3)$$

where $E_{c\mathbf{k}}$ and $E_{v\mathbf{k}}$ are the energies of one-particle states of the conduction and valence bands counted from the energies of the ground one-particle states with $\mathbf{k} = 0$. The uncertainty in the expansion coefficients before terms with similar energies of initial and mixed states will be taken into account separately in a further analysis.

Expression (3) is used to find the first-order Coulomb corrections to the radiative transitions. For the conduction band, we can write

$$\hat{M}_{cc} = \sum_{\mathbf{q}} \hat{b}_{-\mathbf{q}} \sum_{i,j,j'} V_{\mathbf{k}_i - \mathbf{q}} \delta_{\mathbf{q} + \mathbf{k}_{j'}, \mathbf{k}_j + \mathbf{k}_i} \times \frac{\hat{a}_{j'}^+ \hat{a}_j \hat{a}_i}{(E_{c\mathbf{k}_i} + E_{c\mathbf{k}_j} - E_{c\mathbf{k}_{j'}} - E_{c\mathbf{q}})}. \quad (4)$$

A similar expression is valid for the valence band. The matrix elements of the first-order corrections for the Coulomb interaction between carriers in different bands to the radiative transitions have the form

$$\hat{M}_{cv} = -\sum_{\mathbf{q}} \sum_{i,j,i';\, \mathbf{k}_{i'} \neq \mathbf{q}} V_{\mathbf{k}_i - \mathbf{k}_{i'}} \delta_{\mathbf{k}_{i'} - \mathbf{q}, \mathbf{k}_j + \mathbf{k}_i} \times \frac{\hat{a}_{\mathbf{q}} \hat{a}_{i'}^+ \hat{b}_j \hat{a}_i}{(E_{c\mathbf{k}_i} + E_{v\mathbf{k}_j} - (E_v)_{-\mathbf{q}} - E_{c\mathbf{k}_{j'}})} - \sum_{\mathbf{q}} \sum_{i,j,j';\, \mathbf{k}_{j'} \neq \mathbf{q}} V_{\mathbf{k}_i - \mathbf{q}} \delta_{\mathbf{q} + \mathbf{k}_{j'}, \mathbf{k}_j + \mathbf{k}_i} \times \frac{\hat{b}_{-\mathbf{q}} \hat{b}_{j'}^+ \hat{b}_j \hat{a}_i}{(E_{c\mathbf{k}_i} + E_{v\mathbf{k}_j} - E_{v\mathbf{k}_{j'}} - E_{c\mathbf{q}})} - \sum_{\mathbf{q}} \sum_{i} V_{\mathbf{k}_i - \mathbf{q}} \frac{\hat{b}_{-\mathbf{k}_i} \hat{a}_{\mathbf{k}_i} (1 - n_{c\mathbf{q}} - (n_v)_{-\mathbf{q}})}{(E_{c\mathbf{k}_i} + (E_v)_{-\mathbf{k}_i} - (E_v)_{-\mathbf{q}} - E_{c\mathbf{q}})}. \quad (5)$$

Matrix element (4) and the first term in (5) describe the recombination of an electron and a hole with a transfer of excess momentum to another electron. The third term in (5) describes the variation in the recombination probability for an electron–hole pair with a zero quasi-momentum. One of the methods of theoretical analysis of the latter effect was reported in [5].

With regard to matrix elements (4) and (5), the normalized probability of a radiative transition with energy $\hbar\omega$, which describes spontaneous transitions from the nth electronic state (this state, among others, includes the one-particle states of the conduction band with the wave vectors $\mathbf{k}_1$ and $\mathbf{k}_2$ and the one-particle state of the valence band with the wave vector $\mathbf{k}_3$) to the $(n-1)$th electronic state (which, instead of the aforementioned set of one-particle states, includes only the one-electron state of the conduction band with the wave vector $\mathbf{k}_4$), has the form

$$\omega_c = \left\{ \frac{(V_{\mathbf{k}_1 + \mathbf{k}_3} - V_{\mathbf{k}_1 + \mathbf{k}_2})}{(E_{c\mathbf{k}_1} + E_{c\mathbf{k}_2} - E_{c\mathbf{k}_4} - (E_c)_{-\mathbf{k}_3})} - \frac{V_{\mathbf{k}_1 + \mathbf{k}_3}}{(E_{c\mathbf{k}_2} + E_{v\mathbf{k}_3} - (E_v)_{-\mathbf{k}_1} - E_{c\mathbf{k}_4})} + \frac{V_{\mathbf{k}_2 + \mathbf{k}_3}}{(E_{c\mathbf{k}_1} + E_{v\mathbf{k}_3} - (E_v)_{-\mathbf{k}_2} - E_{c\mathbf{k}_4})} \right\}^2 \times \delta(E_{c\mathbf{k}_1} + E_{c\mathbf{k}_2} + E_{v\mathbf{k}_3} - E_{c\mathbf{k}_4} - \Delta\hbar\omega), \quad (6)$$

where $\Delta\hbar\omega = \hbar\omega - E_g$, E_g is the effective band gap in a quantum well. Here, we used the energies of the initial and final many-electron states, with the Coulomb interaction being disregarded. Accounting for the Coulomb interaction even in the first-order of perturbation theory leads to the dependence of ω_c on all the one-electron components of the many-particle state, which significantly complicates further analysis. We can conclude qualitatively that a change in the energy of an ensemble of particles due to their interaction should shift the argument of the delta function to lower energies (the effect of narrowing of the band gap) and broaden the delta function itself upon averaging over the set of many-electron states. The latter circumstance also leads to the broadening of emission lines. The effect of this mechanism requires separate investigation and is beyond the scope of this study.

When the argument of the delta function is taken into account, one can see that, for specified different values of $\mathbf{k}_1$, $\mathbf{k}_2$, and $\mathbf{k}_3$, the value of ω_c, depending on the energy of emitted photons, has three resonance peaks near the energies of the direct transitions with the corresponding wave vectors. This phenomenon is due to the fact that perturbation theory was used; it would be absent if an exact basis expansion of many-electron states was used instead of approximate expression (3). Far from the resonances, only the basis components of expansion (3) with small coefficients are present in the transition probability (6), which justifies the application of perturbation theory in these spectral regions.

Let us distinguish the terms with poles with respect to each variable ($\mathbf{k}_1$, $\mathbf{k}_2$, and $\mathbf{k}_3$) individually in expression (6):

$$\omega_c = \omega_{c1}(\Delta\hbar\omega - E_{r\mathbf{k}_1}) + \omega_{c2}(\Delta\hbar\omega - E_{r\mathbf{k}_2}) + \omega_{c3}(\Delta\hbar\omega - (E_r)_{-\mathbf{k}_3}), \quad (7)$$

where

$$\omega_{c3}(\Delta\hbar\omega - (E_r)_{-\mathbf{k}_3}) = \left\{\frac{V_{\mathbf{k}_1+\mathbf{k}_3}(V_{\mathbf{k}_1+\mathbf{k}_3} - V_{\mathbf{k}_2+\mathbf{k}_3})((E_r)_{-\mathbf{k}_3} - E_{r\mathbf{k}_1})^2}{(\Delta\hbar\omega - (E_r)_{-\mathbf{k}_3})^2 + (\Delta\hbar\omega - E_{r\mathbf{k}_1})^2}\right.$$
$$\left. + \frac{V_{\mathbf{k}_2+\mathbf{k}_3}(V_{\mathbf{k}_2+\mathbf{k}_3} - V_{\mathbf{k}_1+\mathbf{k}_3})((E_r)_{-\mathbf{k}_3} - E_{r\mathbf{k}_2})^2}{(\Delta\hbar\omega - (E_r)_{-\mathbf{k}_3})^2 + (\Delta\hbar\omega - E_{r\mathbf{k}_2})^2}\right\} \quad (8)$$
$$\times \frac{\delta(E_{c\mathbf{k}_1} + E_{c\mathbf{k}_2} + E_{v\mathbf{k}_3} - E_{c\mathbf{k}_4} - \Delta\hbar\omega)}{(\Delta\hbar\omega - (E_r)_{-\mathbf{k}_3})^2},$$

$$\omega_{c1}(\Delta\hbar\omega - (E_r)_{-\mathbf{k}_1}) = \left\{\frac{V_{\mathbf{k}_1+\mathbf{k}_3}(V_{\mathbf{k}_1+\mathbf{k}_3} - V_{\mathbf{k}_2+\mathbf{k}_3})(E_{r-\mathbf{k}_3} - E_{r\mathbf{k}_1})^2}{(\Delta\hbar\omega - (E_r)_{-\mathbf{k}_3})^2 + (\Delta\hbar\omega - E_{r\mathbf{k}_1})^2}\right.$$
$$\left. + \frac{V_{\mathbf{k}_1+\mathbf{k}_3}V_{\mathbf{k}_2+\mathbf{k}_3}(E_{r\mathbf{k}_1} - E_{r\mathbf{k}_2})^2}{(\Delta\hbar\omega - E_{r\mathbf{k}_1})^2 + (\Delta\hbar\omega - E_{r\mathbf{k}_2})^2}\right\} \quad (9)$$
$$\times \frac{\delta(E_{c\mathbf{k}_1} + E_{c\mathbf{k}_2} + E_{v\mathbf{k}_3} - E_{c\mathbf{k}_4} - \Delta\hbar\omega)}{(\Delta\hbar\omega - E_{r\mathbf{k}_1})^2},$$

where $E_{r\mathbf{k}} = E_{c\mathbf{k}} + (E_v)_{-\mathbf{k}}$. The quantity $\omega_{c2}(\Delta\hbar\omega - E_{r\mathbf{k}_2})$ is derived from expression (9) for $\omega_{c1}(\Delta\hbar\omega - E_{r\mathbf{k}_1})$ by the interchange $\mathbf{k}_1 \longleftrightarrow \mathbf{k}_2$.

3. STATISTICAL AVERAGING OF THE PROBABILITY OF OPTICAL TRANSITIONS

The quantum-mechanical probability (6) with the specified values of $\mathbf{k}_1$, $\mathbf{k}_2$, $\mathbf{k}_3$, and $\mathbf{k}_4$ can be applied to the entire ensemble of many-particle states. In order to calculate the resulting contribution to the rate of spontaneous transitions, it is necessary to sum expression (6) over all the initial many-particle states containing the noted one-particle state, with regard to their occupation numbers. Summation over the final states is left out in accordance with the quasi-momentum conservation law and the existence of only one final state with $\mathbf{k}_4 = \mathbf{k}_1 + \mathbf{k}_2 + \mathbf{k}_3$. The calculation will be performed disregarding the Coulomb interaction, as for the delta function in expression (6). Using the occupation numbers n_{c1}, n_{c2}, n_{v3}, and n_{c4}, we will find the statistical factor for the states with the corresponding set of wave vectors:

$$p_{\mathbf{k}_1, \mathbf{k}_2, \mathbf{k}_3} = n_{c1}n_{c2}n_{v3}(1 - n_{c4}). \quad (10)$$

In the approximation of a nondegenerate electron gas for $n_{c\mathbf{k}} = \exp[(F_e - E_g - E_{c\mathbf{k}})/kT]$ and $n_{v\mathbf{k}} = \exp[(-E_{v\mathbf{k}} - F_h)/kT]$ and with regard to the electroneutrality of the quantum-well layer, we obtain

$$p_{\mathbf{k}_1, \mathbf{k}_2, \mathbf{k}_3} = \sqrt{\frac{N_v}{N_c}}\exp\left[\frac{3(\Delta F - E_g)}{2kT} - \frac{(E_{c\mathbf{k}_1} + E_{c\mathbf{k}_2} + E_{v\mathbf{k}_3})}{kT}\right], \quad (11)$$

where N_c and N_v are the effective densities of states of electrons and holes and $\Delta F = F_e - F_h$ is the difference between the quasi-Fermi levels for electrons (F_e) and holes (F_h).

In order to obtain contributions to the spectral broadening of individual components of the probability of optical transitions, one has to fix the wave vector $\mathbf{k}_i$ (i = 1, 2, 3) responsible for a pole and integrate (with regard to the statistical factor) ω_{ci} over the phase space of the remaining wave vectors. Finally, denoting the argument of the obtained functions by the same variable $\mathbf{k}$ and summing these functions, we will find the line shape for the direct transition with the indicated wave vector, which is valid for the entire spectral range (except for the region $\Delta\hbar\omega - E_{r\mathbf{k}} \approx 0$). The values of the broadening function in this region can be estimated by way of its limitation and normalization to the probability of optical transitions, disregarding Coulomb interaction.

4. CALCULATION OF THE EMISSION-LINE PROFILE

In order to calculate the emission-line profile, it is necessary to specify the dependence of the energies of one-electron states on the wave vector. In the parabolic-band approximation, we have

$$E_{c\mathbf{k}} = \frac{\hbar^2\mathbf{k}^2}{2m_c}, \quad E_{v\mathbf{k}} = \frac{\hbar^2\mathbf{k}^2}{2m_v}, \quad (12)$$

where m_c and m_v are the electron and hole effective masses, respectively. We will use the matrix element of the Coulomb interaction in a two-dimensional system in the simplest form

$$V_{\Delta\mathbf{k}} = \frac{e^2}{2\varepsilon\varepsilon_0|\Delta\mathbf{k}|S}, \quad (13)$$

where ε is the permittivity of a semiconductor material (see, for example, [6]) and S is the area of the quantum-well layer.

Let us consider the component of the probability of optical transitions (8) that has a pole when the energy of light photons coincides with the energy of direct transitions involving the states of the valence band with

the wave vector $\mathbf{k}_3$: $\Delta\hbar\omega = (E_r)_{-\mathbf{k}_3}$. To obtain the spectral-line profile, we will integrate the product of (8) and (11) over the phase space of the wave vectors $\mathbf{k}_1$ and $\mathbf{k}_2$:

$$L_{c3}(\Delta\hbar\omega) = \frac{1}{2}\iint p_{\mathbf{k}_1,\mathbf{k}_2,\mathbf{k}_3}\omega_{c3}(\Delta\hbar\omega - (E_r)_{-\mathbf{k}_3})\frac{Sd\mathbf{k}_1}{(2\pi)^2}\frac{Sd\mathbf{k}_2}{(2\pi)^2}. \quad (14)$$

Here, the factor 1/2 accounts for the indistinguishability of many-electron states to interchanges between $\mathbf{k}_1$ and $\mathbf{k}_2$.

Integral (14) cannot be calculated analytically, but it can be estimated for the limiting cases $|\Delta\hbar\omega'| \gg kT$ and $|\Delta\hbar\omega'| \gg (E_r)_{-\mathbf{k}_3}$, where $\Delta\hbar\omega' = \Delta\hbar\omega - E_r$. With this purpose in mind, it is convenient to perform a linear transformation of the integration variables, which reduces the quadratic form of the components of the wave vectors in the delta function to the diagonal form. For the long-wavelength wing of the spectral line ($\Delta\hbar\omega' < 0$), we can find

$$L_{c3}(\Delta\hbar\omega') = \frac{A}{2}\frac{m_c^2(m_c^2 - 4m_cm_r - 24m_r^2)}{(m_c^2 + 4m_cm_r + 8m_r^2)^2}\frac{(kT)^2}{(\Delta\hbar\omega')^4} \times \exp\left[-\frac{E_r}{kT}\left(1 + \frac{m_r}{m_c}\right) + \frac{\Delta\hbar\omega'}{kT}\right] I_0\left[\sqrt{-8\frac{m_r}{m_c}\frac{\Delta\hbar\omega' E_r}{(kT)^2}}\right], \quad (15)$$

where I_0 is the modified Bessel function of the first kind, $m_r^{-1} = m_c^{-1} + m_v^{-1}$, and

$$A = \left(\frac{e^2}{2\varepsilon\varepsilon_0}\right)^2\frac{\sqrt{m_v m_c}}{8\pi^2\hbar^2}\exp\left[\frac{3(\Delta F - E_g)}{2kT}\right] = \mathrm{Ry}\frac{\sqrt{m_c m_v}}{m_e\varepsilon^2}\exp\left[\frac{3(\Delta F - E_g)}{2kT}\right].$$

Here, Ry ≈ 13.6 eV.

For the short-wavelength wing of the spectral line ($\Delta\hbar\omega' > 0$), we have

$$L_{c3}^{+}(\Delta\hbar\omega') = \frac{A}{2}\frac{m_c^2(m_c^2 + 4m_cm_r - 24m_r^2)}{(m_c^2 - 4m_cm_r + 8m_r^2)^2}\frac{(kT)^2}{(\Delta\hbar\omega')^4} \times \exp\left[-\frac{E_r}{kT} - \frac{\Delta\hbar\omega'}{kT}\right]. \quad (16)$$

Expressions (15) and (16) are not positive at arbitrary ratios of the effective masses. Since the probability of spontaneous transitions (6) cannot be negative, in the resulting rate of spontaneous transitions at an arbitrary frequency, the negative contribution of expressions (15) and (16) obtained for small values of $(E_r)_{-\mathbf{k}_3}$ should be compensated by the contribution at large values of $(E_r)_{-\mathbf{k}_3}$ and by the other component of the transition probability (9).

By analogy with the previous case for the component of the spectral-line profile corresponding to the probability of optical transitions (9), we have the following estimates for the spectral-line wings:

$$L_{c1}^{-}(\Delta\hbar\omega') = -\frac{A}{10}\frac{m_c(m_c^3 + 4m_c^2m_v - 2m_cm_v^3 + 2m_v^3)}{(m_c^4 + 2m_c^2m_v^2 + 2m_v^4)} \times \frac{kT}{(\Delta\hbar\omega')^3}\exp\left[-\frac{E_r}{kT}\left(1 + \frac{m_rm_c}{m_v^2}\right) + \frac{m_c}{m_v}\frac{\Delta\hbar\omega'}{kT}\right] \times I_0\left[\sqrt{-4\frac{m_c^2}{m_v^2}\frac{\Delta\hbar\omega' E_r}{(kT)^2}}\right], \quad (17)$$

for the long-wavelength wing ($\Delta\hbar\omega' < 0$) and

$$L_{c1}^{+}(\Delta\hbar\omega') = \frac{A}{2}\frac{kT}{(\Delta\hbar\omega')^3}\exp\left[-\frac{E_r}{kT} - \frac{\Delta\hbar\omega'}{kT}\right] \quad (18)$$

for the short-wavelength wing ($\Delta\hbar\omega' > 0$).

Expressions (17) and (18) are positively defined at any ratios of the effective masses and, in comparison with expressions (15) and (16), show slower decay, which provides positive values for the wings of the resulting profile.

As the numerical calculations show (see Fig. 1), the approximate expressions for the components of the spectral profile yield a sufficiently good approximation even at detunings $|\Delta\hbar\omega'| > kT$. For radiative transitions with $E_r < kT$, the recombination of an electron–hole pair with a transfer of excess momentum (upon electron–hole Coulomb interaction) to an electron makes the main contribution to the long-wavelength ($\Delta\hbar\omega' < 0$) broadening: $L_{c1}(\Delta\hbar\omega')$. At the same time, the recombination with a transfer of excess momentum either to an electron or to a hole contributes predominantly to the short-wavelength broadening: $L_{c1}(\Delta\hbar\omega')$ and $L_{v1}(\Delta\hbar\omega')$, respectively.

5. EXTRAPOLATION OF THE EMISSION-LINE PROFILE NEAR THE RESONANCE

Exponential and power factors are clearly pronounced in expressions (15)–(18); these factors originate from the statistical and quantum-mechanical properties of a many-body system. The exponent of the exponential factor, which is due to the statistical factor (11), includes the minimum sum of the energies of interacting carriers at which the difference between the energies of the initial and final many-particle states (with regard to the quasi-momentum conservation) corresponds to the specified energy detuning from the center of the emission line, $\Delta\hbar\omega'$. In the other factor, the part of the exponent equal to 2 is due to the use of per-

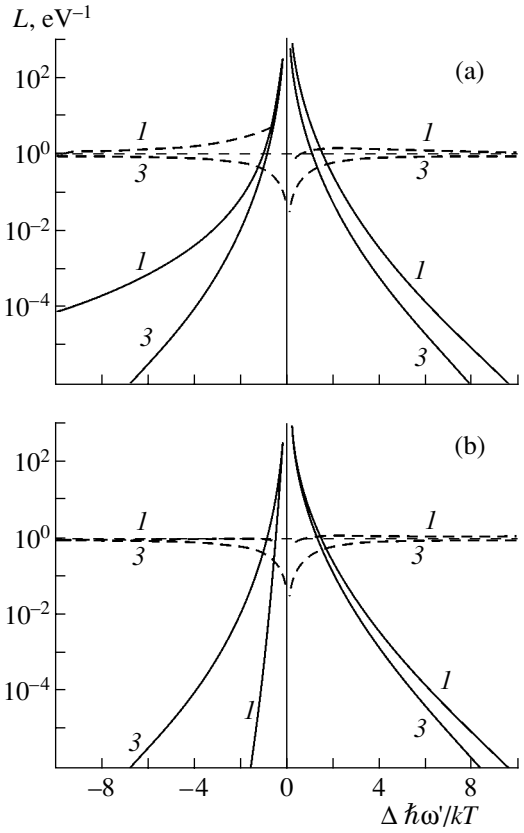

Fig. 1. Components of the broadening profile related to the recombination of an electron–hole pair with a transfer of excess momentum to (a) an electron and (b) a hole. The components of the broadening due to the Coulomb interaction with a transfer of excess momentum to a hole are derived from expressions (15)–(18) by the replacement $m_c \longleftrightarrow m_v$. The dashed line shows the ratio of the values obtained by numerical integration to the approximate functions. Curves *1* refer to the processes of interband Coulomb interaction and their interference with the processes of intraband Coulomb interaction, and curves *3* refer to the processes of intraband Coulomb interaction and their interference with the processes of interband Coulomb interaction. For the profile L_{c3}, absolute values are given. The parameters are as follows: $T = 286$ K, $m_c = 0.055m_e$, $m_v = 0.49m_e$, $E_r = 0$, and $\Delta F - E_g = 0$.

turbation theory, while the remaining part is related to the form of the matrix element of the Coulomb interaction (13). Thus, the spectral-line wings calculated by the above method would formally coincide with the Lorentzian shape if the constant matrix element were used in the analysis and the quasi-momentum conservation law were disregarded.

Therefore, we will perform limiting of the spectral line in the region of small detunings by analogy with the Lorentzian shape and matching of the exponential factors for positive and negative detunings as in [2]. Assuming that the total intensity of the emission line is the same as in the one-electron approximation for direct radiative transitions, we will write the form factor of homogeneous broadening as follows:

$$L(\Delta\hbar\omega') \approx \frac{\mathrm{Ry}\dfrac{\sqrt{m_c m_v}}{m_e\varepsilon^2}\exp\left[\dfrac{\Delta F - E_g}{2kT}\right]}{\dfrac{5m_v}{m_c}\exp\left[-\dfrac{m_c}{m_v}\dfrac{\Delta\hbar\omega'}{kT}\right] + \dfrac{1}{2}\exp\left[\dfrac{\Delta\hbar\omega'}{kT}\right]} \times \frac{kT}{(\gamma^2 + (\Delta\hbar\omega')^2)^{3/2}}. \quad (19)$$

Here, we assumed that $m_v \gg m_c$ and excluded the exponential and Bessel factors, which only weakly depend on the energy of the states, from the long-wavelength part on the profile. The parameter γ is found from the normalization condition in which integral (19) over all energies of emitted photons is equal to unity.

At low excitation levels, when the decay of the profile near the resonance is mainly due to the power factor, the parameter γ can be expressed analytically:

$$\gamma^2 = \mathrm{Ry}\frac{\sqrt{m_c m_v}}{m_e\varepsilon^2}\frac{4m_c kT}{10m_v + m_c}\exp\left[\frac{\Delta F - E_g}{2kT}\right]. \quad (20)$$

The decay of the spectral line near the resonance at $\gamma < kT$ is mainly due to the quantum-mechanical factor. At $\gamma > kT$, the statistical factor plays the dominant role. For the energies of photons $|\Delta\hbar\omega'| < \gamma$, when the effect of artificial normalization is significant, the main reason for the emission-line broadening due to Coulomb interaction is the splitting of the energy levels of many-particle states.

6. RESULTS AND DISCUSSION

The results of calculations of the form factor of homogeneous broadening using expression (19) are shown in Fig. 2. Although the above calculations are valid for a nondegenerate electron–hole system, Fig. 2 also contains curves corresponding to the case of a degenerate system, which can be used to interpret the known experimental data. We may conclude the following.

(i) The emission-line profile has asymmetric exponentially decaying wings. The long-wavelength wing decays slower than the short-wavelength one. The asymmetric exponential behavior of the decay is related to the statistical energy distribution of charge carriers and the fact that the laws of conservation of energy and momentum are satisfied upon interaction. Such behavior is not related to the form of the interaction matrix element. Therefore, a similar exponential factor will be present in the spectral-line profiles obtained for quantum wires and semiconductors with bulk properties.

(ii) The emission line broadens as the excitation level increases. Mathematically, the broadening of an emission line is expressed by the fact that the integrated-emission intensity increases proportionally to

exp[$\Delta F/kT$], while the emission intensity in the line wings is $\propto$exp[$3\Delta F/2kT$]. Taking into account the fact that an increase in the excitation level leads to an increase in the number of particles in the bands, the line broadening is explained as follows: the increase in the rate of the three-particle processes (which is proportional to the third power of the number of particles, n^3) is ahead of the increase in the rate of direct radiative transitions involving two particles (which is proportional to n^2).

(iii) The dependence of the emission-line width on the excitation level is more pronounced at high temperatures. At low temperatures, the range of splitting of the levels of many-particle states becomes equal to the thermal energy kT at lower relative excitation levels $(\Delta F - E_g)/kT$ (see expression (20)), after which the spectral-line profile turns out to be close to the asymptotic curve determined by a statistical factor independent of the excitation level (see Fig. 2a). For the same reason, the degree of asymmetry of the profile wings is higher at lower temperatures.

The aforementioned qualitative features of the emission-line profile are in agreement with the experimental results [2]. A quantitative comparison with experiment requires a more detailed account of the features of the band structure of the emitting quantum-well layers (instead of the use of the parabolic-band approximation), estimation of the degeneracy effect and the spins of interacting particles, and analysis of the conditions of inhomogeneous excitation of samples, which hardly seems possible in the scope of one study. As can be seen from Fig. 2, the width of spectral profiles is comparable with the experimental data [2] for temperatures of 286 and 77 K and is underestimated for 4.2 K. However, one should take into account that, at equal injection currents, the quantity $(\Delta F - E_g)/kT$ increases as temperature decreases, and the spectral-line profile approaches the asymptotic curve. Apparently, for this reason, the experimental value of the decay decrement for the long-wavelength edge of the spontaneous-emission spectrum, $\varepsilon_1 = 3.2$ meV at 4.2 K, coincides quantitatively with the asymptotic decay decrement in expression (19): $\varepsilon_1 = kTm_v/m_c$. The short-wavelength edge of the emission line decays slower than formula (19) predicts. This circumstance may be caused by the splitting of the levels of many-particle states (more significant at low temperatures), which was not taken into account in this study. Concerning the effect of the electron–phonon interaction on the spectral broadening, according to our estimation, this interaction should lead to the appearance of phonon replicas in the emission spectrum. Apparently, their absence in the experimental spectra indicates the dominance of the Coulomb mechanism at sufficiently high excitation levels.

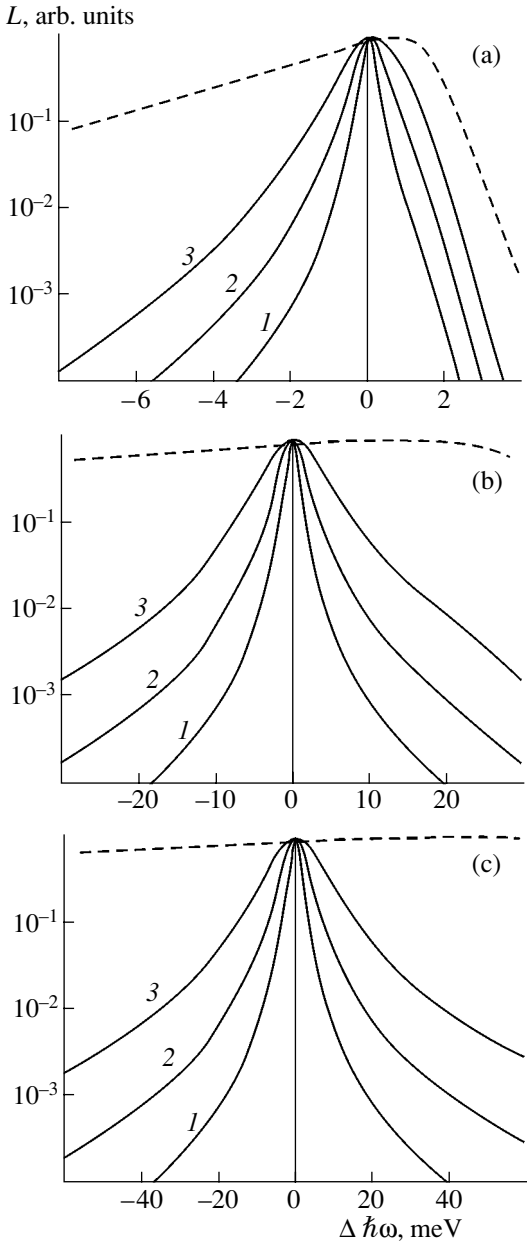

Fig. 2. Emission-line profiles, normalized to the maximum, at T = (a) 4.2, (b) 77, and (c) 286 K at relative excitation levels $\Delta F - E_g$ = (*1*) $-5kT$, (*2*) 0, and (*3*) $5kT$. The dashed line shows the asymptotic emission-line profile in the limit $\Delta F \longrightarrow \infty$.

7. CONCLUSION

The theoretical analysis of the emission-line broadening due to the Coulomb interaction between charge carriers shows that the exponential fall-offs in the line profiles are related to the statistical energy distribution of carriers. The asymmetry of the line profile is the consequence of the laws of conservation of energy and momentum of an electron–hole system upon Coulomb interaction. The emission-line broadening with an

increase in the excitation level is explained by the fact that the increase in the rate of three-particle recombination, which determines the intensity of the line wings, is ahead of the rate of direct radiative two-particle transitions, which determine the intensity of the central part of the spectral line.

ACKNOWLEDGMENTS

I am grateful to Prof. V.K. Kononenko for an introduction to the problems of spectral broadening and D.V. Ushakov for helpful remarks on the presentation of the results.

REFERENCES

1. M. Asada, IEEE J. Quantum Electron. **25**, 2019 (1989).
2. P. G. Eliseev and I. V. Akimova, Fiz. Tekh. Poluprovodn. (St. Petersburg) **32**, 472 (1998) [Semiconductors **32**, 423 (1998)].
3. T. Ohtoshi and M. Yamanishi, IEEE J. Quantum Electron. **27**, 46 (1991).
4. D. Ahn, IEEE J. Sel. Top. Quantum Electron. **1**, 301 (1995).
5. H. Haug and S. W. Koch, Phys. Rev. A **39**, 1887 (1989).
6. A. I. Kucharska and D. Robbins, IEEE J. Quantum Electron. **26**, 443 (1990).

Translated by Yu. Sin'kov

Semiconductors, Vol. 38, No. 3, 2004, pp. 329–334. Translated from Fizika i Tekhnika Poluprovodnikov, Vol. 38, No. 3, 2004, pp. 342–348.

LOW-DIMENSIONAL SYSTEMS

Dependence of Structural and Optical Properties of QD Arrays in an InAs/GaAs System on Surface Temperature and Growth Rate

V. G. Dubrovskiĭ*^, Yu. G. Musikhin*, G. É. Cirlin, V. A. Egorov**, N. K. Polyakov**, Yu. B. Samsonenko**, A. A. Tonkikh**, N. V. Kryzhanovskaya*, N. A. Bert*, and V. M. Ustinov***

**Ioffe Physicotechnical Institute, Russian Academy of Sciences, St. Petersburg, 194021 Russia*

^e-mail: v_dubr@mail.ru

***Institute for Analytical Instrumentation, Russian Academy of Sciences, St. Petersburg, 190083 Russia*

Submitted July 7, 2003; accepted for publication July 9, 2003

Abstract—Properties of InAs QD arrays on a <100> GaAs surface in relation to the surface temperature and InAs growth rate are studied experimentally and theoretically. A kinetic model of QD formation in heteroepitaxial growth is developed, which allows the calculation of the mean lateral size and surface density of islands as functions of the growth conditions and duration. Experimental study of optical and structural properties is performed for QDs with an effective thickness of 2 ML, grown at different substrate temperatures and growth rates. The calculated results correlate well with the experimental data. The raising of the surface temperature and slowing of the growth rate result in a considerable increase in the QD mean lateral size and a decrease in their surface density. *© 2004 MAIK "Nauka/Interperiodica".*

1. INTRODUCTION

The direct formation of coherent nanosize islands in heteroepitaxial growth is the main technological procedure for fabricating QD arrays [1]. The unique optical and electrical properties of semiconductor heterostructures with QDs, which are related to the atomic-like spectrum of QD energy states, make these structures rather promising for application in modern opto- and microelectronics [2]. One of the main problems in the technology of QD growth is the fabrication of QD arrays with prescribed optical and structural properties [1]. The solution of this problem demands theoretical and experimental studies of the dependence of QD properties on technologically controllable parameters of their growth. In the case of MBE growth of InAs on singular (100)GaAs substrates, the basic growth parameters to be controlled are the following: the surface temperature, T; the amount of InAs deposited, H_0 (the effective thickness after the termination of growth of the island layer); the ratio between the fluxes of Group III and Group V elements; the growth rate of InAs, V; and the time of exposure, Δt_{exp}, to the As flow after the termination of growth before the overgrowth of the sample. Evidently, the experimentally observed dependence of structural characteristics of QD arrays on the last two parameters [3] cannot in principle be described in terms of equilibrium theoretical models [4, 5], so a kinetic approach must be developed [6–8].

In this study, we apply a kinetic model of coherent island formation in MBE [7, 8] to theoretical study of the dependences of structural properties of QD arrays on the growth rate and temperature. Growth experiments in an InAs/GaAs system were performed at different growth rates of InAs and surface temperatures and with zero exposure and fixed $H_0 = 2$ monolayers (ML). Studies of QD photoluminescence (PL) spectra that were begun in [7] were continued. Structural properties of QD arrays were studied by transmission electron microscopy (TEM). A comparison was made between the predictions of the theoretical model and the experimental data obtained. Good agreement was observed, which made it possible to obtain dependences of the average size of islands, their surface density, and the spectral position of the PL peak from a 2-ML InAs QD array on a (100)GaAs surface on the InAs growth rate and surface temperature. The data obtained indicate that QDs are formed at the growth stage under study in the kinetic mode.

2. THEORY

As shown in [7], the process of QD growth by the Stranski–Krastanow mechanism at the kinetic stage can be discussed in terms of the classical theory of nucleation in a materially open system [9]. If the principal mechanism of island growth is the consumption of material from the wetting layer (WL), which results from the difference between elastic energies within the island and in the WL, the role of the metastable condensable phase is played by WL with average thickness $h > h_{eq}$, the coherent islands act as nuclei of a new phase, and the quantity $\zeta = h/h_{eq} - 1$ is the metastability parameter of the system [7]. The equilibrium thickness of the WL, h_{eq}, is determined by the balance between elastic and wetting forces, in accordance with the Müller–Kern criterion [10]. The islands are formed via fluctuation-assisted overcoming of the activation bar-

rier by nuclei of the new phase. The island nucleation intensity I strongly depends on the metastability parameter and temperature: $I \propto \exp[-F(T, \zeta)]$. The activation barrier for nucleation, F, can be represented in $k_B T$ units as

$$F(T, \zeta) = \frac{T_e}{T\zeta^2}. \quad (1)$$

The equilibrium temperature, T_e, determines the island nucleation intensity at a given surface temperature T and wetting layer thickness h. With small variations of the surface temperature, T_e can be considered as independent of T. For pyramidal islands with a square base, the expression for T_e has the form [8]

$$T_e = \frac{4}{27}\frac{[\sigma(\theta)/\cos\theta - \sigma(0)]^3(6\cot\theta)^2}{k_B[(1-z(\theta))\lambda\varepsilon_0^2]^2 \ln^2[\Psi_0/h_0(1-z(\theta))\lambda\varepsilon_0^2]}, \quad (2)$$

where $\sigma(0)$ and $\sigma(\theta)$ are specific surface energies in planes of the substrate surface and side faces of the pyramid, taking into account the renormalization necessitated by lattice mismatch [1]; θ, the contact angle of the pyramid; $z(\theta)$, the θ-dependent coefficient of elastic energy relaxation in an island [11]; λ, the elastic modulus of the deposit; ε_0, the lattice mismatch; Ψ_0, the density of the wetting energy on the substrate surface [10]; and h_0, the ML thickness. Equation (2) shows that T_e sharply decreases as the lattice mismatch increases: $T_e \propto 1/\varepsilon_0^4$; i.e., all other factors being the same, the activation barrier for nucleation is lower in systems with a larger mismatch. The equilibrium temperature increases with increasing contact angle θ, because the relaxation of elastic strain in high islands is stronger than in flat ones.

The characteristics of the island formation process for a supercritical effective thickness of deposition at the kinetic stage are defined by the kinetic parameter Q [7], which is of the same order of magnitude as the ratio between the time needed to grow an equilibrium WL and the time it takes atoms from the WL to reach the growing islands. Evidently, Q is very large: $Q > 10^3$ for typical MBE conditions. The dependence of Q on the surface temperature and growth rate is given by

$$Q = Q_0 \frac{V_0 T_0}{VT} \exp\left(\frac{T_D}{T_0} - \frac{T_D}{T}\right), \quad (3)$$

where T_D is the diffusion temperature, which defines the temperature dependence of the coefficient of diffusion of atoms from the WL to islands (caused by elastic stress), and $Q_0 = Q(V_0, T_0)$, the value of Q at the growth rate V_0 and temperature T_0. The strong inequality $F_c = (5/2)\ln Q \gg 1$, where F_c is the activation barrier for nucleation at the maximum thickness of the WL, ensures that the classical nucleation theory can be applied to the description of the QD formation process [6, 7, 9]. The maximum WL thickness h_c, at which island nucleation occurs at the highest rate, is ensured by the balance between the delivery of atoms from the molecular beam into the WL and their consumption from the WL by the growing islands. Reaching the maximum metastability of the system at some point is a characteristic feature of the nucleation process in materially open systems [9] (in the case of MBE, the atomic beam incident onto the substrate surface plays the role of the external source). As shown in [7, 8], owing to the very sharp dependence of the nucleation intensity on the WL thickness, the process of island nucleation occurs at virtually constant effective thickness $H \approx h_c$. Thus, the maximum WL thickness nearly equals the critical effective thickness of deposition, which corresponds to the appearance of a 3D reflection in the reflection high-energy electron diffraction (RHEED) patterns [1]. The expression for critical thickness obtained in [7] can be represented as

$$h_c = h_{eq}\left[1 + \left(\frac{2}{5}\frac{T_e}{T\ln Q}\right)^{1/2}\right]. \quad (4)$$

Expression (4) shows that, despite the kinetic nature of the critical thickness, h_c only weakly depends on the growth rate, and it is mainly defined by the energetics of the heteroepitaxial system. This conclusion correlates with the results obtained using equilibrium models of QD formation [5]. If the desorption in the time scale of interest is negligible, the time dependence of the efficient thickness is $H = Vt$ at $t < t_0$ and $H = H_0 + Vt_0$ at $t > t_0$, where the instant of time $t = 0$ corresponds to the onset of the growth process and $t = t_0$, to the termination of growth of the island layer (in an InAs/GaAs system with the In flow shut off). The growth time of a WL with equilibrium thickness is $t_{eq} = h_{eq}/V$, and the growth time for a WL of critical thickness is $t_c = h_c/V$. The time of WL growth from equilibrium to critical thickness is $t_c - t_{eq}$.

In our model, the hierarchy of times of different stages of island formation is $\Delta t \ll t_R \ll t_c - t_{eq}$, where Δt is the duration of the islands' nucleation stage, and t_R, the characteristic time of their size relaxation. Therefore, the nucleation time of islands is much less than the time of their size relaxation, which, in turn, is much less than the time of formation of the WL with critical thickness. The stage of Ostwald ripening is a later stage of the process; it cannot occur in the kinetic stage, which corresponds to times $0 < t < t_c + 3t_R$ [12]. The desorption of atoms from the surface is negligible at such small times. Other effects that could change the growth mechanisms of the islands, e.g., a decrease in the growth rate due to an additional potential barrier for the delivery of atoms from the WL to islands, which is induced by elastic stress [13], or dipole–dipole elastic interaction of islands [1], are also insignificant at the kinetic stage. The relations obtained in [7] for the dura-

tion of the nucleation stage and the characteristic time of size relaxation of the islands

$$\Delta t = \frac{0.57}{\ln Q}(t_c - t_{eq}), \quad (5)$$

$$t_R = \frac{0.47}{\ln^{1/3} Q}(t_c - t_{eq}) \quad (6)$$

demonstrate the existence of the above hierarchy of times with sufficiently large Q.

In the case $H_0 > h_c + \Delta H/2$, where $\Delta H = V\Delta t$ is the range of effective thicknesses corresponding to the nucleation stage, the growth is terminated after the end of island nucleation. The surface density of islands reaches a constant value given by the relation [7]

$$N = \frac{4}{l_0^2} h_{eq} \frac{T}{T_e} \left(\frac{\ln Q}{Q}\right)^{3/2}, \quad (7)$$

where l_0 is the average interatomic distance on the surface. This value remains virtually unchanged at the stage of size relaxation of the islands. The size distribution of islands is nearly Gaussian at $H_0 > h_c + \Delta H$ [8]. The time dependence of the lateral size of islands, L, which corresponds to the peak of the size distribution ("average size"), at the relaxation stage ($t_c < t < 3t_R$) is found in the form of an inverse dependence $t(L)$ [7]:

$$\frac{t - t_c}{t_R} = \ln\left[\frac{(1 + l + l^2)^{1/2}}{1 - l}\right] - \sqrt{3}\arctan\left(\frac{2l + 1}{\sqrt{3}}\right) + \frac{\pi}{2\sqrt{3}} \equiv U(l), \quad (8)$$

where $l = L/L_R$. It is usually assumed here that zero-size islands nucleate, because the critical size in the classical nucleation theory is much less than L_R [6–9]. The average lateral size of islands, L_R, upon termination of the size relaxation stage is given by

$$L_R = \alpha l_0 \left(\frac{h_c - h_{eq}}{l_0^2 N}\right)^{1/3}, \quad (9)$$

where $a = (6h_0 \cot\theta / l_0)^{1/3}$ is a geometric factor. Equation (9) shows that an increase in the surface density always leads to a decrease in the lateral size and vice versa, since at the end of the size relaxation stage the WL thickness equals its equilibrium value h_{eq}, and all the additional amount of deposited material is distributed among the islands. The function $U(l)$ on the right side of (8) contains no parameters of the model, and, therefore, the dependence of l on $(t - t_c)/t_R$ has the universal form shown in Fig. 1. This dependence makes it possible to find, for a given effective thickness H_0, the evolution of the average size with the time t or the time of exposure to As flow by using an apparent relation $t - t_c = t_0 - t_c + \Delta t_{exp}$. Zero exposure, which corresponds to the overgrowth of structures immediately after the shutoff of In flow, corresponds to the instant of time $t = t_0$ and size $L(t_0)$.

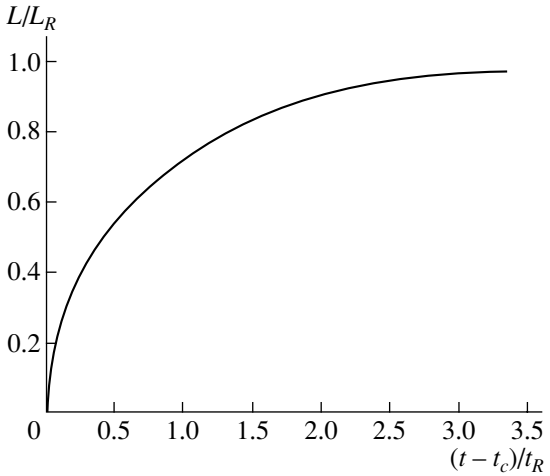

Fig. 1. Universal dependence of the reduced average island size L/L_R on the reduced time $(t - t_c)/t_R$ at the stage of size relaxation of the islands; obtained by inversion of Eq. (8).

The given analytical expressions solve the problem of quantitative description of island formation at the kinetic stage. Equation (2) makes it possible to calculate the equilibrium temperature T_e for the known energetics of a heteroepitaxial system and island configuration. Equation (4) allows one to calculate the unknown constant Q_0 in Eq. (3) at known h_{eq} and h_c for the growth rate V_0 and temperature T_0. Critical thickness at different temperatures and growth rates can be calculated from (4) by setting the value of T_D. The characteristic times of the nucleation and size relaxation stages are calculated from Eqs. (5) and (6). The average size and surface density of islands as functions of four control parameters of the growth process, T, V, H_0, and Δt_{exp}, can be determined using Eqs. (7)–(9) and the universal dependence shown in Fig. 1. Thus, the principal parameters of the model are the equilibrium thickness of the WL, h_{eq}; equilibrium temperature, T_e; and diffusion temperature, T_D. Finding h_{eq} and T_e requires that the energy parameters of the system be determined precisely, taking into account renormalizations related to lattice mismatch, together with the contact angle θ. Finding T_D demands a detailed study of the atomic diffusion from the WL into the island, induced by elastic stress. The principal qualitative conclusion made from Eqs. (3), (7), and (9) is that the island size increases as the growth rate decreases and temperature rises, which is followed by a corresponding decrease in island density. This conclusion is supported by the experimental data obtained for two systems, InAs/GaAs(100) [7] and Ge/Si(100) [14].

In the calculation, the following parameters of the model were used: $h_0 = 0.303$ nm, $l_0 = 0.429$ nm, $\alpha = 1.82 \approx$ const, $Q_0 = 600$ at $T_0 = 440$°C and $V_0 = 0.1$ ML s^{-1}, $T_D = 4700$ K, $h_0 = 2$ ML, and $\Delta t_{exp} = 0$; h_{eq} and T_e values

Characteristics of the process of formation of island arrays and their structural properties at different surface temperatures and growth rates

V, ML s^{-1}	T, °C	h_{eq}, ML	T_e, K	h_c, ML	Q	F_c	ΔH, ML	Δt, s	t_R, s	t_c–t_{eq}, s	N, 10^{10} cm^{-2}	$L(t_0)$, nm	L_R, nm
0.01	440	1.12	4630	1.70	6000	21.7	0.039	3.9	13.2	58	2.8	16.3	18.5
0.03	440	1.0	7630	1.75	2000	19.0	0.056	1.9	6.0	25	4.8	12.7	15.9
0.05	440	0.94	9900	1.77	1200	17.7	0.066	1.3	4.1	16.6	6.7	11.0	14.7
0.1	440	0.9	11400	1.80	600	16.0	0.080	0.8	2.3	9	13	8.8	12.1
0.01	485	1.12	4590	1.68	16200	24.2	0.033	3.3	12.3	56	0.62	23.1	27.0
0.03	485	1.02	8110	1.74	5400	21.5	0.048	1.6	5.5	24	1.3	18.9	23.9
0.05	485	0.95	11300	1.77	3240	20.2	0.058	1.2	3.8	16.4	1.7	17.1	20.2
0.1	485	0.9	13700	1.79	1620	18.5	0.069	0.7	2.2	8.9	3.3	12.7	17.6

were varied taking into account that $h_{eq} \approx 1$ ML and $h_c \approx$ 1.7–1.8 ML. The growth rate was varied in the range 0.01–0.1 ML s^{-1} for two temperatures, T = 440 and 485°C. The numerical characteristics of the process of formation of island arrays and their structural properties for given values of the parameters modeling the InAs/GaAs(100) heteroepitaxial system are listed in the table. The numerical data show a strong dependence of the average size and surface density of islands on the growth rate and substrate temperature. The hierarchy of times for the stages of nucleation and size relaxation of islands and the formation of a WL with critical thickness exists for all the studied range of temperatures and growth rates. In all cases, islands have no time to reach their maximum size L_R at zero exposure, so that the observed size $L(t_0) < L_R$.

3. EXPERIMENT

Growth experiments were performed in an EP1203 MBE setup, with semi-insulating singular (100)GaAs substrates. After removal of the oxide layer at 630°C and growth of the GaAs buffer, an active region consisting of an InAs QD layer with an effective thickness of 2 ML was grown. The active region was confined between $Al_{0.3}Ga_{0.7}As$/GaAs short-period superlattices (25 Å/25 Å, 10 pairs) to prevent the transport of nonequilibrium carriers to the surface region and into the substrate in the course of optical studies. On top, the structure was covered with a 50-Å-thick capping layer immediately after the shutoff of the In flow, at the same substrate temperature. The substrate temperature was then raised, and the remaining part of the structure was grown at 600°C. To study the dependence on substrate temperature in the growth of an InAs/GaAs QD system, two sets of samples were grown at active region growth temperatures T = 440 and 485°C. The rate of InAs growth was varied from 0.01 to 0.1 ML s^{-1} in both sets. In all the experiments, the residual pressure of As_4 vapor in the growth chamber was 1.8×10^{-6} Pa.

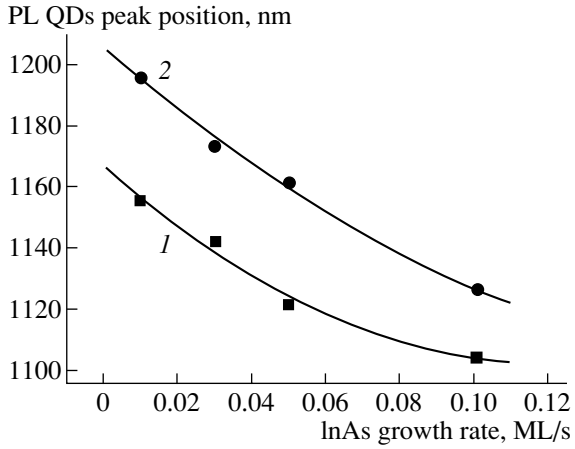

Fig. 2. Position of the peak of PL from InAs QDs as a function of the InAs deposition rate for two surface temperatures T_{sub}: (*1*) 440 and (*2*) 485°C.

The deposition of InAs QDs was monitored by recording and analyzing RHEED patterns. The observed dynamics of the variation in the RHEED pattern revealed a sharp transition from a striped diffraction pattern, which corresponds to planar growth, to a pointlike pattern corresponding to 3D growth. This transition, which is characteristic of the Stranski–Krastanow growth mechanism, was observed after the deposition of a 1.7–1.8-ML-thick InAs layer in all the range of temperatures and growth rates under study.

The PL was excited using an argon-ion laser (λ = 514.5 nm, excitation density ~100 W/cm^2). The light emitted was detected with a cooled Ge photodiode. The spectra obtained show that, with the deposition rate decreasing from 0.1 to 0.01 ML s^{-1}, the PL peak related to the recombination via QDs shifts steadily to longer wavelengths from 1126 to 1196 nm for T = 485°C and from 1104 to 1155 nm for T = 440°C. Figure 2 shows the dependence of the PL peak position on the growth rate for two temperatures. The red shift of the PL peak is associated with the increase of the lateral size of InAs QDs, which occurs upon deposition over a longer time at a lower growth rate. A similar red shift of the PL peak is clearly pronounced when submonolayer migration-

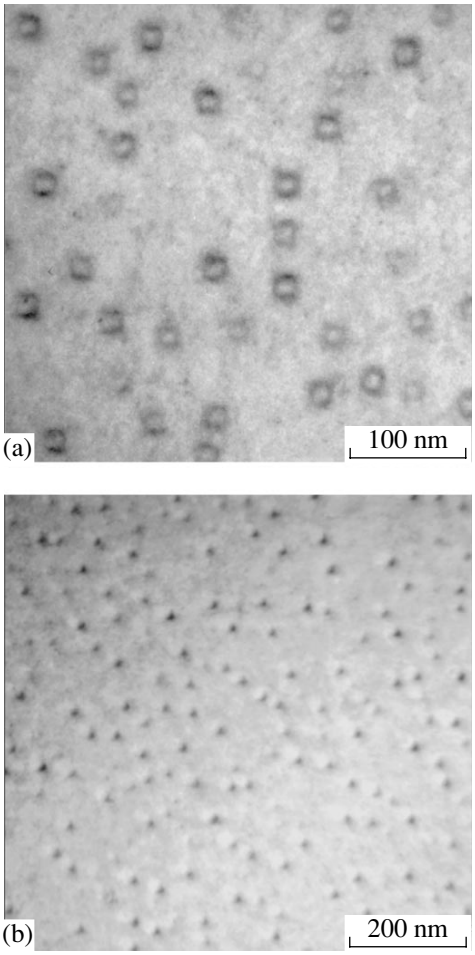

Fig. 3. TEM images of 2-ML InAs QDs produced at T = 485°C and V = 0.03 ML s^{-1}. (a) Multibeam mode, beam incidence parallel to [001] direction; (b) BF(g = 220) mode.

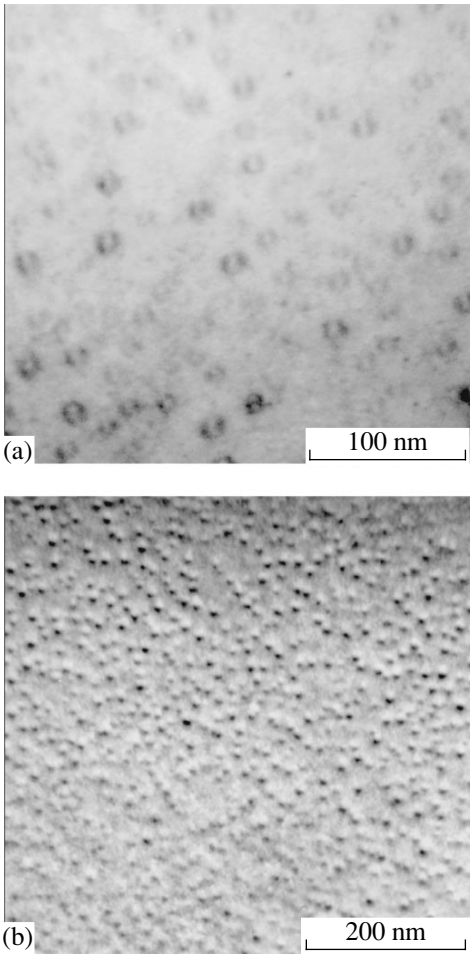

Fig. 4. TEM images of 2-ML InAs QDs produced at T = 440°C, V = 0.05 ML s^{-1}. (a) Multibeam mode, beam incidence parallel to [001] direction; (b) BF(g = 220) mode.

enhanced epitaxy [15] is used, in which the growing structure is kept for a certain time in an arsenic flow, with the flow of metal atoms interrupted, in order to enhance the surface migration of adatoms and thereby raise the lateral size of nanoislands. Thus, the red shift of the emission wavelength agrees qualitatively with the trends following from the theoretical model.

To obtain quantitative data on the dependences of structural properties of InAs QD arrays on the surface temperature and growth rate, TEM studies of the grown samples were performed. The morphology of QD arrays was studied using a Philips EM420 transmission electron microscope operating at an acceleration voltage of 100 kV. The array density and lateral size of QDs were determined from the analysis of planar TEM images. Samples for study were prepared by mechanical grinding and polishing in a Gatan 603 Dimple Grinder setup, with subsequent chemical etching in a $H_2SO_4 : H_2O_2 : H_2O$ (5 : 1 : 1) solution. The density of QD array was determined from the analysis of bright-field (BF) TEM images obtained under double-beam conditions, with active diffraction vector g = 220 (Figs. 3a, 4a). The lateral size was estimated from TEM images obtained under multibeam conditions with normal incidence of the electron beam onto the growth surface (Figs. 3b, 4b).

The TEM data showed a strong dependence of the morphology of QD arrays on the growth temperature and on the rate of InAs deposition. As the deposition rate increases from 0.01 to 0.1 ML s^{-1}, the density of the QD array in a single-layer structure increases from 3.5×10^{10} to 1.2×10^{11} cm^{-2}, for a substrate temperature of 440°C, and from 7×10^9 to 3×10^{10} cm^{-2} for 485°C (Fig. 5). In this case, the average lateral size of QDs decreases from 12 to 10 nm, for a substrate temperature of 440°C, and from 21 to 13 nm for 485°C (Fig. 6). Figures 3a and 3b show TEM images of a 2-ML QD array grown with an InAs growth rate of 0.03 ML s^{-1} at 485°C, obtained in multibeam and BF(220) modes, respectively. Similar images of a structure grown at a substrate temperature of 440°C and InAs growth rate of 0.05 ML s^{-1} are shown in Figs. 4a and 4b. It is worth

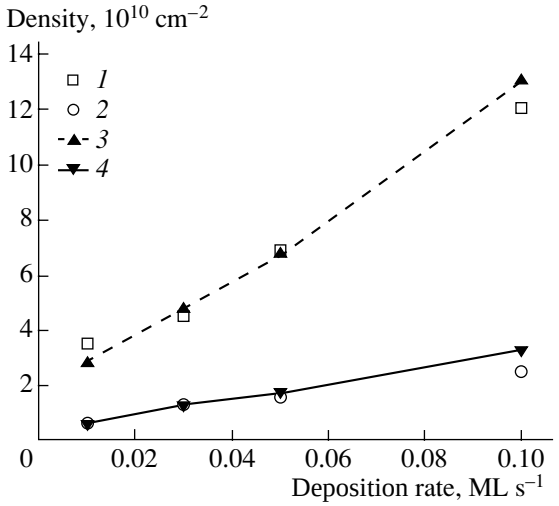

Fig. 5. Theoretical and experimental dependences of the surface density of InAs QDs on the InAs growth rate for two surface temperatures T_{sub}: (*1*, *3*) 440 and (*2*, *4*) 485°C; (*3*, *4*) calculated.

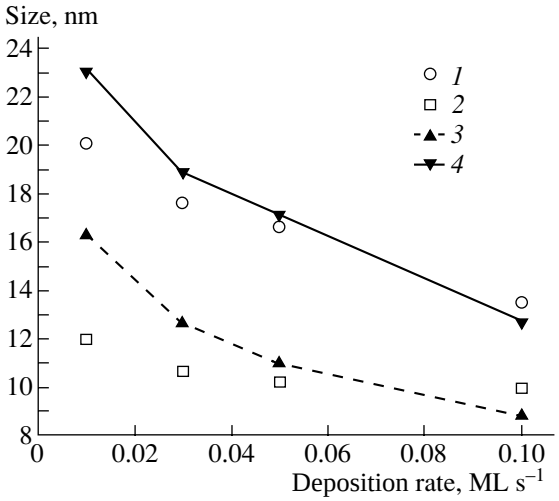

Fig. 6. Theoretical and experimental dependences of the average size of InAs QDs on the InAs growth rate for two surface temperatures T_{sub}: (*1*, *3*) 440 and (*2*, *4*) 485°C; (*3*, *4*) calculated.

noting the good agreement of the experimental data with the theoretical calculations in Section 2 (Figs. 5, 6).

Thus, we performed theoretical and experimental studies of the dependences of structural and optical properties of QD arrays in an InAs/GaAs system on the rate of InAs growth and surface temperature. The derived kinetic model of coherent island formation via the Stranski–Krastanow mechanism allows one to calculate the average size and surface density of islands as functions of time for different temperatures and growth rates. Optical and structural properties of 2-ML InAs/GaAs QDs grown at different rates and different surface temperatures were studied, and the experimental data were compared with the predictions of the theoretical model. The results obtained show that, with the InAs growth rate increasing from 0.01 to 0.1 ML s^{-1}, the average size of a QD decreases from ~21 to ~13 nm at a temperature of 485°C and from ~12 to ~10 nm for 440°C. In this situation, the surface density increases, respectively, from $\sim 7 \times 10^9$ to $\sim 3 \times 10^{10}$ cm^{-2} and from $\sim 3.5 \times 10^{10}$ to $\sim 1.2 \times 10^{11}$ cm^{-2}. The array of QDs with maximum density and minimum size is formed at elevated growth rates and low surface temperatures. The theoretical and experimental results obtained make it possible to control the properties of QD arrays at the kinetic stage of their formation.

ACKNOWLEDGMENTS

This study was financially supported in part by scientific programs of the Ministry of Industry, Science, and Technology of the Russian Federation.

G.E.C. acknowledges the support of the Alexander von Humboldt Foundation.

REFERENCES

1. D. Bimberg, M. Grundmann, and N. N. Ledentsov, *Quantum Dot Heterostructures* (Wiley, Chichester, 1999).
2. Zh. I. Alferov, Fiz. Tekh. Poluprovodn. (St. Petersburg) **32**, 3 (1998) [Semiconductors **32**, 1 (1998)].
3. P. M. Petroff and G. Medeiros-Riberio, MRS Bull. **21**, 50 (1996).
4. V. A. Shchukin, N. N. Ledentsov, P. S. Kop'ev, and D. Bimberg, Phys. Rev. Lett. **75**, 2968 (1995).
5. I. Daruka and A.-L. Barabasi, Phys. Rev. Lett. **79**, 3708 (1997).
6. A. V. Osipov, F. Schmitt, S. A. Kukushkin, and P. Hess, Appl. Surf. Sci. **188**, 156 (2002).
7. V. G. Dubrovskiĭ, V. A. Egorov, G. É. Tsyrlin, *et al.*, Fiz. Tekh. Poluprovodn. (St. Petersburg) **37**, 883 (2003) [Semiconductors **37**, 855 (2003)].
8. V. G. Dubrovskii, G. E. Cirlin, and V. M. Ustinov, Phys. Rev. B **68**, 075409 (2003).
9. F. M. Kuni, Preprint No. 84-178E (Inst. of Theoretical Physics, Kiev, 1984).
10. P. Müller and R. Kern, Appl. Surf. Sci. **102**, 6 (1996).
11. C. Ratsch and A. Zangwill, Surf. Sci. **293**, 123 (1993).
12. S. A. Kukushkin and V. V. Slezov, *Disperse Systems on the Surface of Solids: Formation Mechanisms of Thin Films (the Evolution Approach)* (Nauka, St. Petersburg, 1996).
13. A. V. Osipov, S. A. Kukushkin, F. Schmitt, and P. Hess, Phys. Rev. B **64**, 205421 (2001).
14. A. A. Tonkikh, V. G. Dubrovskii, G. E. Cirlin, *et al.*, Phys. Status Solidi B **236**, R1 (2003).
15. G. É. Tsyrlin, A. O. Golubok, S. Ya. Tipisev, *et al.*, Fiz. Tekh. Poluprovodn. (St. Petersburg) **29**, 1697 (1995) [Semiconductors **29**, 884 (1995)].

Translated by D. Mashovets

Semiconductors, Vol. 38, No. 3, 2004, pp. 335–339. Translated from Fizika i Tekhnika Poluprovodnikov, Vol. 38, No. 3, 2004, pp. 349–353.

LOW-DIMENSIONAL SYSTEMS

Quantum Confined Stark Effect and Electroabsorption in Semiconductor Spherical Layers

V. A. Arutyunyan*, K. S. Aramyan, and G. Sh. Petrosyan****

**The Gyumri Educational Complex of the Armenian State Engineering University, Gyumri, 377503 Armenia*

***Artsakhi State University, Armenia*

Submitted July 16, 2003; accepted for publication August 26, 2003

Abstract—The effect of a uniform external electric field on quantum confined charge-carrier states in a spherical layer is considered. The dependence of the energy shift on the external field and on the size of the sample is obtained. The electro-optical absorption coefficient is calculated for interband dipole transitions. *© 2004 MAIK "Nauka/Interperiodica".*

1. INTRODUCTION

Nowadays optical and electro-optical properties of various quasi-zero-dimensional structures with spherical symmetry such as quantum dots (see, e.g., the review [1]) and multilayered spherical nanoheterostructures [2–6] are being intensively studied. These studies are stimulated by the fact that such heterophase systems are very promising materials for fabricating new devices of modern optoelectronics. Clearly, a necessary stage in the studies of these structures is the examination of physical properties of "individual" nanocrystalline spherical layers. Such nanocrystals are interesting from both purely physical and applied points of view. First of all, they combine the properties of quantum films and spherical quantum dots and therefore can be used both in a "pure" form and as a component for the fabrication of multilayered spherical nanoheterostructures with desired characteristics. In this respect, the study of the effect of an external electric field on charge-carrier states in such layers is of certain interest. Numerous experimental and theoretical studies deal with the Stark level splitting and electro-optical effects in quantum films (e.g., see the review [7]). In some studies, the quantum confined Stark effect in spherical quantum dots was also considered [8–10]. For example, the dependence of the Stark energy-level shift caused by quantum confinement of electrons and holes on the sample size was experimentally observed in [8, 9]. In [10], the theory of the Stark effect in quantum dots was developed under conditions where, in addition to the quantum confinement of each type of carrier, the electron–hole pairs can be bound to form a bulk exciton. A new electro-optical method was suggested that makes it possible to determine the "critical" size of the sphere such that for spheres of greater size a three-dimensional exciton can be formed.

The aim of this study is to theoretically analyze the modification of the energy spectrum of charge carriers confined in a spherical layer in a uniform electric field and the corresponding effect of the external field on the shape of the band of interband optical absorption.

2. ELECTRONIC STATES IN A LAYER

We will consider a case in which the layer is quite thin and the so-called strong quantum-confinement conditions are satisfied; i.e., the layer thickness L is much smaller than the Bohr radius a_{ex} of a three-dimensional exciton in the layer. At the same time, from the technical point of view, the most realistic case corresponds to layers of "large" radius such that the thickness L of the layer itself is much smaller than the radii R_1 of the core and R_2 of the surrounding medium:

$$L^2 \ll R_{1,2}^2, \quad R_{1,2} \approx a_{ex}. \tag{1}$$

In this case, an adequate physical model of the layer is the model of a "potential well folded into a sphere" (e.g., see [11]):

$$U(r) = \begin{cases} 0, & \text{for } R_1 \le r < R_2, \\ \infty, & \text{for } r \ge R_2, \quad r \le R_1. \end{cases} \tag{2}$$

This model approach is justified if the band gap of the layer is narrow compared to that of the material of the core and the medium, and if the band offsets at the interface (for overlapping band gaps of the contacting materials) are much greater than the charge-carrier confinement energy in the layer. In this respect, the composition CdS/HgS/CdS is typical (see Appendix). Using this model and the approximation of the isotropic effective mass μ, we obtain the following expressions for the energies and the envelope wave functions of unperturbed one-electron states in the layer:

$$E_{n,l}^{(0)} = \frac{\pi^2\hbar^2 n^2}{2\mu L^2} + \frac{\hbar^2 l(l+1)}{2\mu R_0^2} \equiv E_{1,0}^{(0)} n^2 + U_l(R_0) \equiv E_{conf} + E_{rot}, \tag{3}$$

$$\psi^{(0)}_{n,l,m}(r,\vartheta,\varphi) = \Phi^{(0)}_n(r)Y_{l,m}(\vartheta,\varphi) \equiv \sqrt{\frac{2}{L}}\frac{1}{r}Y_{l,m}(\vartheta,\varphi)\sin\frac{\pi n}{L}(r-R_1), \quad (4)$$

where n, l, and m are the radial, orbital, and azimuthal quantum numbers, respectively; $Y_{l,m}(\vartheta,\varphi)$ are the normalized spherical functions; r, ϑ, and φ are the spatial spherical coordinates; and the effective "rotational" radius R_0 is defined by the condition

$$U_l(R_0) = \frac{1}{2}[U_l(R_1) + U_l(R_2)]. \quad (5)$$

Let us assume that the external uniform field $\mathbf{F}$ is directed along the Z axis, so that $\mathbf{F} = \mathbf{F}(0, 0, F)$. Generally, if the permittivities of the "core" (ε_1), the layer (ε_2), and the environment (ε_3) are different, we obtain the following expression for the electrostatic potential $\varphi(\mathbf{r})$ inside the layer [12]:

$$\varphi(\mathbf{r}) = \left(Br + \frac{C}{r^2}\right)F\cos\vartheta, \quad (6)$$

where

$$B = \frac{C}{R_1^3}\frac{\varepsilon_3 + 2\varepsilon_2}{\varepsilon_2 - \varepsilon_1},$$

$$C = \frac{3\varepsilon_1(\varepsilon_2 - \varepsilon_1)R_1^3R_2^3}{(\varepsilon_2 + 2\varepsilon_1)(\varepsilon_3 + 2\varepsilon_2)R_2^3 + 2(\varepsilon_1 - \varepsilon_2)(\varepsilon_2 - \varepsilon_3)R_1^3}.$$

From general considerations, it is clear that for this case the external field can be considered as a perturbation if the energy $\Delta E(F)$ transferred from the field to a particle is much smaller than the confinement energy $E^{(0)}_{n,l}$,

$$\Delta E(F) \ll E^{(0)}_{n,l}. \quad (7)$$

The corresponding perturbation operator is given by

$$\hat{V} = qF\left(Br + \frac{C}{r^2}\right)\cos\vartheta, \quad (8)$$

where q is the particle charge.

It can then easily be seen that there is no linear Stark effect in the system.

We obtain the following general expression for the second-order correction $\Delta E^{(2)}_{n,l}$ to the energy of arbitrary state $|n, l, m\rangle$:

$$\Delta E^{(2)}_{n,l} = |V_{l,l-1}|^2\sum_{n\neq n'}\frac{|V_{n,n'}|^2}{E^{(0)}_{n,l} - E^{(0)}_{n',l-1}} + |V_{l,l+1}|^2\sum_{n\neq n'}\frac{|V_{n,n'}|^2}{E^{(0)}_{n,l} - E^{(0)}_{n',l+1}} + |V_{n,n}|^2\left(\frac{|V_{l,l-1}|^2}{E^{(0)}_{n,l} - E^{(0)}_{n,l-1}} + \frac{|V_{l,l+1}|^2}{E^{(0)}_{n,l} - E^{(0)}_{n,l+1}}\right), \quad (9)$$

where $V_{n,n'}$ is the matrix element of operator (8) constructed from the radial wave functions $\Phi^{(0)}_n(r)$ appearing in Eq. (4),

$$V_{n,n'} = qFL\frac{8nn'}{\pi^2(n^2 - n'^2)^2}\left[-B + C\frac{R_1^3 + R_2^3}{R_1^3R_2^3}\right] \equiv V(R_1, R_2)\frac{nn'}{(n^2 - n'^2)^2}qFL \quad \text{for } n \neq n', \quad (10)$$

$$V_{n,n} = \frac{qFC}{R_1^3}\left\{1 + \varepsilon + \left(\frac{\varepsilon}{2} - 1\right)\frac{L}{R_1} + \frac{L^2}{R_1^2}\right\} \equiv qFd \quad \text{for } n = n',$$

where

$$\varepsilon = \frac{\varepsilon_3 + 2\varepsilon_2}{\varepsilon_2 - \varepsilon_1}.$$

For $V_{l,l\pm1}$, we have

$$V_{l,l\pm1} = \begin{cases} i\sqrt{\dfrac{(l+m)(l-m)}{(2l+1)(2l-1)}} \\ \text{for } l \longrightarrow l-1 \quad (l = 1, 2, \ldots), \\ -i\sqrt{\dfrac{(l+m+1)(l-m+1)}{(2l+3)(2l+1)}} \\ \text{for } l \longrightarrow l+1 \quad (l = 0, 1, 2, \ldots). \end{cases} \quad (11)$$

Substituting expressions (10) and (11) into formula (9) and performing summation over n' [13], we obtain the expression for the correction $\Delta E^{(2)}_{n,l}$,

$$\Delta E^{(2)}_{n,l} = \frac{(qFL)^2}{48n^2E^{(0)}_{n,0}}|V(R_1, R_2)|^2(f_{n,l} + g_{n,l}) + \frac{(qFd)^2}{2U_l(R_0)}t_l \equiv \Delta E^{(2)}_{n,l}(FL) + \Delta E^{(2)}_l(Fd), \quad (12)$$

where $f_{n,l}$, $g_{n,l}$, and t_l are given by

$$f_{n,l} = \left(1 - \frac{15}{\pi^2n^2}\right)(|V_{l,l-1}|^2 + |V_{l,l+1}|^2), \quad (13)$$

$$g_{n,l} = \left(\frac{1}{5} + \frac{1}{2\pi^2n^2} - \frac{21}{\pi^4n^4}\right)\left(\frac{L}{R_0}\right)^2 \times [(l+1)|V_{l,l+1}|^2 - l|V_{l,l-1}|^2], \quad (14)$$

$$t_l = (l+1)|V_{l,l-1}|^2 - l|V_{l,l+1}|^2.$$

The general expression for the perturbation part of the wave function $\psi^{(1)}_{n,l,m}(r, \vartheta, \varphi)$ is

$$\psi^{(1)}_{n,l,m}(r, \vartheta, \varphi) \simeq Y_{l,m}(\vartheta, \varphi)\cos\vartheta \times \frac{1}{E^{(0)}_{1,0}} \sum_{n \neq n'} \frac{V_{n,n'}\Phi^{(0)}_{n'}(r)}{n^2 - n'^2} + \frac{V_{n,n}\Phi^{(0)}_{n}(r)}{2U_l(R_0)} \times [(l+1)V_{l,l-1}Y_{l-1,m}(\vartheta, \varphi) - lV_{l,l+1}Y_{l+1,m}(\vartheta, \varphi)]. \quad (15)$$

3. INTERBAND TRANSITIONS IN THE PRESENCE OF A UNIFORM ELECTRIC FIELD

To be specific, we assume that the incident wave with frequency ω is linearly polarized and the polarization vector **e** is directed along the Z axis, so that **e** = $e(0, 0, 1)$. Then, in the dipole approximation, the perturbation $\hat{A}$ related to the light wave can be written in the form

$$\hat{A} = -i\hbar\frac{|e|A_0}{m_0 c}\left(\cos\vartheta\frac{\partial}{\partial r} - \frac{\sin\vartheta}{r}\frac{\partial}{\partial\vartheta}\right), \quad (16)$$

where A_0 is the wave amplitude, m_0 is the free-electron mass, e is the elementary charge, and c is the speed of light in free space. The matrix element of interband transitions $v \longrightarrow c$ can be generally expressed as

$$M_{c,v} = A_{c,v}\int[\psi^{(0)}_c(\mathbf{r}) + \psi^{(1)}_c(\mathbf{r})]^*[\psi^{(0)}_v(\mathbf{r}) + \psi^{(1)}_v(\mathbf{r})]d\mathbf{r}, \quad (17)$$

where $A_{c,v}$ is the matrix element of operator (16) constructed from the Bloch amplitudes for the valence (v) and conduction (c) bands. Substituting expressions (4) and (15) into Eq. (17) and retaining the first-order terms, we obtain for $M_{c,v}$

$$M_{c,v} \simeq A_{c,v}\delta_{|m_c|,|m_v|}(M^{(0)} + M^{(1)}_1 + M^{(1)}_2), \quad (18)$$

where

$$M^{(0)} = \delta_{n_c,n_v}\delta_{l_c,l_v}, \quad (19)$$

$$M^{(1)}_1 = \frac{qFd}{2\hbar^2}(\mu_c + \mu_v)R_0^2\frac{V_{l_c,l_v\pm1}}{l_v + \frac{1}{2} \pm \frac{1}{2}}\delta_{n_c,n_v}\delta_{l_c,l_v\pm1}, \quad (20)$$

$$M^{(1)}_2 = \left(l + \frac{1}{2} \pm \frac{1}{2}\right)V_{l_c,l_v\pm1}V(R_1, R_2)(qFL) \times \left[\frac{S_{n_c}}{E^{(0)}_{n_c,0}} + \frac{S_{n_v}}{E^{(0)}_{n_v,0}}\right]\delta_{l_c,l_v\pm1}, \quad (21)$$

$$S_{n_{c,v}} = \psi'(-z_{c,v}) - \psi'(z_{c,v}) + \frac{z_{c,v}}{2}[\psi''(-z_{c,v}) + \psi''(z_{c,v})],$$

$z_{c,v} = n_{c,v} - \frac{1}{2}$; $\psi'(z)$ and $\psi''(z)$ are the first and second derivatives of the logarithmic derivative of Euler's Γ function $\psi(z) = \Gamma'(z)/\Gamma(z)$, respectively; and $\delta_{i,k}$ is the Kronecker delta. The upper sign in Eqs. (20) and (21) corresponds to $l \longrightarrow l+1$ transitions and the lower sign, to $l \longrightarrow l-1$ transitions.

Let us find out which region of the interband absorption spectrum corresponds to transitions with matrix elements (18)–(21). Due to the difference in selection rules (except for the selection rule $\Delta m = 0$, which is common to all transitions), for transitions (19)–(21) there is no "interference" between the matrix elements $M^{(0)}$, $M^{(1)}_1$, and $M^{(1)}_2$ in the calculation of the absorption coefficient. Accordingly, the interband absorption band is a set of series with the following threshold frequencies:

(1) transitions $n_c = n_v$, $l_c = l_v$:

$$\hbar\omega = E_g^L + \frac{\pi^2\hbar^2n^2}{2\mu_{c,v}L^2} + \frac{\hbar^2l(l+1)}{2\mu_{c,v}R_0^2} + \frac{(\mu_c + \mu_v)R_0^2}{\hbar^2l(l+1)} \times [(l+1)|V_{l,l-1}|^2 - l|V_{l,l+1}|^2](qFd)^2; \quad (22)$$

(2) transitions $n_c = n_v$, $l_c = l_v \pm 1$:

(2a) $n_c = n_v$, $l_c = l_v - 1$:

$$\hbar\omega = E_g^L + \frac{\pi^2\hbar^2n^2}{2\mu_{c,v}L^2} + \frac{\hbar^2l}{2R_0^2}\left(\frac{l+1}{\mu_c} + \frac{l-1}{\mu_v}\right) + \left[\mu_v\left(\frac{|V_{l,l-1}|^2}{l} - \frac{|V_{l,l+1}|^2}{l+1}\right) + \mu_c\left(\frac{|V_{l-1,l-2}|^2}{l-1} - \frac{|V_{l,l-1}|^2}{l}\right)\frac{(qFd)^2R_0^2}{2\hbar^2}, \quad (23)$$

(2b) $n_c = n_v$, $l_c = l_v + 1$:

$$\hbar\omega = E_g^L + \frac{\pi^2\hbar^2n^2}{2\mu_{c,v}L^2} + \frac{\hbar^2l(l+1)}{2R_0^2}\left(\frac{l+2}{\mu_c} + \frac{l}{\mu_v}\right) + \left[\mu_v\left(\frac{|V_{l,l-1}|^2}{l} - \frac{|V_{l,l+1}|^2}{l+1}\right) + \mu_c\left(\frac{|V_{l,l+1}|^2}{l+1} - \frac{|V_{l+1,l+2}|^2}{l}\right)\frac{(qFd)^2R_0^2}{2\hbar^2}; \quad (24)$$

(3) transitions $n_c \neq n_v$, $l_c = l_v \pm 1$:

(3a) $n_c \neq n_v$, $l_c = l_v - 1$:

$$\hbar\omega = E_g^L + \frac{\pi^2\hbar^2}{2L^2}\left(\frac{n_c^2}{\mu_c} + \frac{n_v^2}{\mu_v}\right) + \frac{\hbar^2 l}{2R_0^2}\left(\frac{l-1}{\mu_c} + \frac{l+1}{\mu_v}\right) + \Delta E^{(2)}_{n_v, l}(FL) + \Delta E^{(2)}_{n_c, l-1}(FL), \quad (25)$$

(3b) $n_c \neq n_v$, $l_c = l_v + 1$:

$$\hbar\omega = E_g^L + \frac{\pi^2\hbar^2}{2L^2}\left(\frac{n_c^2}{\mu_c} + \frac{n_v^2}{\mu_v}\right) + \frac{\hbar^2 l(l+1)}{2R_0^2}\left(\frac{l+2}{\mu_c} + \frac{l}{\mu_v}\right) + \Delta E^{(2)}_{n_v, l}(FL) + \Delta E^{(2)}_{n_c, l+1}(FL). \quad (26)$$

Here, E_g^L is the band gap of the bulk semiconductor formed from the layer material, $\mu_{c,v}^{-1} = \mu_c^{-1} + \mu_v^{-1}$, and μ_c and μ_v are the electron and hole effective masses.

4. DISCUSSION AND CONCLUSIONS

The results obtained in this paper in the framework of the suggested model can be summarized as follows.

(i) Since the energy shift explicitly depends on m, the external field partially removes the degeneracy in the azimuthal number. In the presence of the field, the energy levels are found to be doubly degenerate, except for the states with $m = 0$, which are nondegenerate.

(ii) Under the above approximations, the orbital motion and radial motion can be "separated" for the unperturbed system, and the Stark shift to a large degree depends on the configuration and the dimensions of the sample. On the one hand, the energy shift is determined by the quantity

$$\Delta E_l^{(2)}(Fd) = \frac{(qFd)^2}{2U_l(R_0)}[(l+1)|V_{l,l-1}|^2 - l|V_{l,l+1}|^2]. \quad (27)$$

This quantity is characteristic of the rotation motion that occurs over the sphere and is perturbed by a uniform field. In particular, using expression (27) with $\varepsilon_1 = \varepsilon_3$ and $\varepsilon_2 = 2\varepsilon_1$, we obtain the well-known result for the correction to the ground state energy with $l = 0$ (e.g., see [14]),

$$\Delta E_0(Fd) \simeq \frac{(qFR_1)^2\mu R_0^2}{3\hbar^2}. \quad (28)$$

On the other hand, the correction to the energy of radial motion $\Delta E^{(2)}_{n,l}(FL)$ also contributes to the Stark shift. It is readily seen in expressions (12) and (13) that this contribution to the field-induced shift is determined by the degree of the layer "sphericity" as compared to a plane-parallel film. This degree is defined in our case by the relation $\lambda = L/R_0$. Taking the ground-state level as an example, we can easily see that, in the limiting case $\lambda \longrightarrow 0$, the expression for the correction $\Delta E^{(2)}_{n,l}(FL)$ in expression (12) assumes a form similar to the result for the Stark effect in a "conventional" quantized film [7],

$$\Delta E^{(2)}_{1,0} \simeq \frac{1}{3}\left(\frac{qFL}{\varepsilon}\right)^2 \frac{1}{48E^{(0)}_{1,0}}\left(1 - \frac{15}{\pi^2}\right).$$

(iii) The band of interband optical absorption consists of two series: the "fundamental" one (expressions (19) and (22)), for which only the transitions diagonal in all three quantum numbers (n, l, m) are possible, and the "field satellites" (expressions (20), (21), and (23)–(26)), where the selection rules in "angular" quantum numbers $\Delta m = 0$ and $\Delta l = \pm 1$ are valid. These series do not overlap, and for each series its own selection rules hold and determine the corresponding threshold frequencies. The absorption (20), (21) is due exclusively to the presence of the external field and is modulated in each of the series by the field factors $(Fd)^2$ and $(FL)^2$, respectively.

(iv) The presence of the field also results in an explicit dependence on the effective charge-carrier masses; this can be used for experimental determination of the optical effective masses of the charge carrier.

(v) It can be seen from the patterns of effective variation in the band gap

$$\Delta_g^{c,v} = \hbar\omega - E_g^L,$$

which are determined for each case by formulas (22)–(26), that, by varying the field and the dimensions of the sample, we can produce the desirable controllable changes in some parameters of the sample. This can be used for fabricating both single layers and compositional multilayered nanoheterostructures with specified (and controllable) characteristics.

APPENDIX

We consider the model approach developed for the composition CdS/HgS/CdS. In the table, we list the corresponding physical parameters for β-CdS and β-HgS semiconductor crystals (the data are taken from [2–4, 15, 16]).

In the table, we use the following notation: μ_c and μ_v are the charge-carrier effective masses, a is the lattice constant, E_g is the band gap of the bulk sample, U^c is the conduction band minimum measured from the vacuum level, U^v is the valence band maximum, ΔU^c and ΔU^v are the offsets for the corresponding bands, a_{ex} is the Bohr radius of a three-dimensional exciton in the material under consideration, and ε_0 is the static permittivity.

I. APPLICABILITY OF THE PROPOSED MODEL

If we assume that the HgS layer has the thickness $L \approx 5$–10 nm, then $L^2/a_{ex}^2 \approx 0.01$–$0.04$ and Coulomb interaction can be disregarded. The condition for strong confinement is satisfied for charge carriers in the layer. If we take the values in the range $R_1 \approx 15$–30 nm for the

Table

Material	a, nm	ε_0	E_g, eV	μ_c/m_0	μ_v/m_0	U^c, eV	U^v, eV	ΔU^c, eV	ΔU^v, eV	a_{ex}, nm
CdS	0.5818	9.1	2.5	0.2	0.7	–3.8	–6.3	–	–	~3
HgS	0.5851	18.2	0.5	0.036	0.044	–5	–5.5	1.2	–0.8	~50

core radius, then, on the one hand, there is no carrier confinement in the core (and in the surrounding shell). On the other hand, conditions (1) are satisfied, since $L^2/R_1^2 \approx 0.1$, and the separation of the particle motion into its radial and rotational components is also justified. For the specified system dimensions, the estimation yields the following values of E_{conf} and E_{rot} for electrons (c) and holes (v):

(a) $L = 5$ nm, $R_1 = 15$ nm, $R_2 = 20$ nm,

$$E^c_{conf} \approx 42.4 \times 10^{-3} \text{ eV}, \quad E^v_{conf} \approx 34.7 \times 10^{-3} \text{ eV}, \quad E^c_{rot} \approx 3.7 \times 10^{-3} \text{ eV}, \quad E^v_{rot} \approx 3 \times 10^{-3} \text{ eV}; \tag{A.I.1}$$

(b) $L = 10$ nm, $R_1 = 30$ nm, $R_2 = 40$ nm,

$$E^c_{conf} \approx 10.6 \times 10^{-3} \text{ eV}, \quad E^v_{conf} \approx 8.7 \times 10^{-3} \text{ eV}, \quad E^c_{rot} \approx 10^{-3} \text{ eV}, \quad E^v_{rot} \approx 0.82 \times 10^{-3} \text{ eV}. \tag{A.I.2}$$

Comparison of the carrier confinement energies $E^{c,v}_{conf}$ in (A.I.1) and (A.I.2) with the band offsets $\Delta U^{c,v}$ in the table clearly shows that, for low excited states, the model of the quantum well (2) is also valid with satisfactory accuracy for the composition considered.

II. EXTERNAL FIELD AS A PERTURBATION

For the structure under consideration, condition (7) assumes the form

$$(qFR_1)^2 \frac{\mu R_0^2}{3\hbar^2} + \frac{(qFL)^2}{18E^{(0)}_{1,0}\pi^4}\left(1 + \frac{4L}{2R_1}\right) \ll E^{(0)}_{1,0}. \tag{A.II.1}$$

In order to find the upper limit of the values of the field considered as a perturbation using condition (A.II.1), it is convenient to derive the following fairly accurate formula:

$$F \ll \frac{6 \times 10^{-18}}{LR_1^2}. \tag{A.II.2}$$

It follows that for

$$L \approx 5\text{–}10 \text{ nm}, \quad R_1 \approx 15\text{–}30 \text{ nm},$$

the electric field can be treated as a perturbation if the electric-field strength is lower than

$$F \approx 10^3\text{–}10^2 \text{ V/cm}.$$

Accordingly, the Stark shift of the ground-state level is given by

$$\Delta E^{(2)}_{1,0} \approx 6 \times 10^{-4} \text{ eV}$$

for $L = 5$ nm, $R_1 = 15$ nm, $F = 2 \times 10^3$ V/cm;

$$\Delta E^{(2)}_{1,0} \approx 1.2 \times 10^{-4} \text{ eV}$$

for $L = 10$ nm, $R_1 = 30$ nm, $F = 2 \times 10^2$ V/cm.

REFERENCES

1. S. V. Gaponenko, Fiz. Tekh. Poluprovodn. (St. Petersburg) **30**, 577 (1996) [Semiconductors **30**, 315 (1996)].
2. J. W. Haus, H. S. Zhou, I. Honma, and H. Komiyama, Phys. Rev. B **47**, 1359 (1993).
3. D. Schooss, A. Mews, A. Eychmuller, and H. Weller, Phys. Rev. B **49**, 17072 (1994).
4. A. Mews, A. V. Kadavanich, U. Banin, and A. P. Alivasatos, Phys. Rev. B **53**, 13242 (1996).
5. N. V. Tkach, Fiz. Tverd. Tela (St. Petersburg) **39**, 1109 (1997) [Phys. Solid State **39**, 995 (1997)].
6. N. V. Tkach, V. A. Golovatskiĭ, and O. N. Voĭtsekhovskaya, Fiz. Tekh. Poluprovodn. (St. Petersburg) **34**, 602 (2000) [Semiconductors **34**, 583 (2000)].
7. S. Schmitt-Rink, D. S. Chemia, and D. A. Miller, Adv. Phys. **38**, 89 (1989).
8. A. I. Ekimov, P. A. Skvortsov, and T. V. Shubina, Zh. Tekh. Fiz. **59**, 202 (1989) [Sov. Phys. Tech. Phys. **34**, 371 (1989)].
9. S. Nomura and T. Kobayashi, Solid State Commun. **74**, 1153 (1990).
10. S. I. Pokutniĭ, Fiz. Tekh. Poluprovodn. (St. Petersburg) **34**, 1120 (2000) [Semiconductors **34**, 1079 (2000)].
11. V. V. Rotkin and R. A. Suris, Fiz. Tverd. Tela (St. Petersburg) **36**, 3569 (1994) [Phys. Solid State **36**, 1899 (1994)].
12. W. R. Smythe, *Static and Dynamic Electricity*, 2nd ed. (McGraw-Hill, New York, 1950; Inostrannaya Literatura, Moscow, 1954).
13. A. P. Prudnikov, Yu. A. Brychkov, and O. I. Marichev, *Integrals and Series* (Nauka, Moscow, 1981; Gordon and Breach, New York, 1986).
14. V. M. Galitskiĭ, B. M. Karnakov, and V. I. Kogan, *Problems in Quantum Mechanics* (Nauka, Moscow, 1981).
15. N. V. Tkach, A. M. Makhanets, and G. G. Zegrya, Fiz. Tekh. Poluprovodn. (St. Petersburg) **36**, 543 (2002) [Semiconductors **36**, 511 (2002)].
16. *Tables of Physical Data: Reference Book*, Ed. by I. K. Kikoin (Atomizdat, Moscow, 1976).

Translated by I. Zvyagin

Semiconductors, Vol. 38, No. 3, 2004, pp. 340–343. Translated from Fizika i Tekhnika Poluprovodnikov, Vol. 38, No. 3, 2004, pp. 354–357.

LOW-DIMENSIONAL SYSTEMS

Structural and Optical Properties of Heterostructures with InAs Quantum Dots in an InGaAsN Quantum Well Grown by Molecular-Beam Epitaxy

I. P. Soshnikov*, N. V. Kryzhanovskaya*, N. N. Ledentsov*, A. Yu. Egorov*, V. V. Mamutin*, V. A. Odnoblyudov*, V. M. Ustinov*, O. M. Gorbenko, H. Kirmse***, W. Neumann***, and D. Bimberg******

**Ioffe Physicotechnical Institute, Russian Academy of Sciences, St. Petersburg, 194021 Russia*

***Institute for Analytical Instrumentation, Russian Academy of Sciences, St. Petersburg, 198103 Russia*

****Humboldt University of Berlin, D-12489 Berlin, Germany*

*****Technical University of Berlin, D-10623 Berlin, Germany*

Submitted August 26, 2003; accepted for publication September 9, 2003

Abstract—Results obtained in a study of the structural and optical properties of GaAs-based heterostructures with InAs quantum dot layers overgrown with InGaAsN quantum wells are presented. Transmission electron microscopy has been applied to analyze how the thickness of the InGaAsN layer and the content and distribution of nitrogen in this layer affect the size of nanoinclusions and the nature and density of structural defects. It is shown that the size of InAs nanodomains and the magnitude of the lattice mismatch in structures containing nitrogen exceed those in nitrogen-free structures. A correlation between the luminescence wavelength and the size and composition of nanodomains is demonstrated. Furthermore, a correlation between the emission intensity and defect density in the structure is revealed. © *2004 MAIK "Nauka/Interperiodica".*

1. INTRODUCTION

One way to extend the spectral range of GaAs-based light-emitting devices is to use structures in which quantum dots (QDs) are overgrown with a layer with an InGaAs quantum well (QW) [1–7]. Specifically, heterostructures of this type provide lasing in InAs/InGaAs/GaAs structures at 1.3 μm [3–7]. Attempts to shift the emission band further to wavelengths of 1.5 μm or more encounter difficulties, which may possibly be resolved by using InGaAsN solid solutions [1, 2, 7–9]. Therefore, studying the formation and optical properties of GaAs-based heterostructures with InAs QDs overgrown with InGaAsN layers is an important task of current interest.

2. EXPERIMENTAL

The samples studied were grown on an EP1203 machine equipped with an EPI Unibulb RF Plasma Source of chemically active nitrogen. Standard epiready (001)-oriented GaAs wafers doped with silicon to 5×10^{18} cm^{-3} served as the substrates. The samples had a structure typical of lasers, with a waveguide that contains the active region. To fabricate the active region, InAs QD nanodomains with an effective thickness of 3 monolayers were deposited and then overgrown with $In_{0.18}Ga_{0.82}As/In_{0.18}Ga_{0.82}(As_aN_b)$ layers. The thicknesses (x/y) of the InGaAs/InGaAsN overgrowth layers are listed in the table. The nitrogen content in the overgrowth layer was chosen so that the average content of nitrogen was the same for all the samples ($b \approx 0.01$).

The characterization of the structure was carried out by means of transmission electron microscopy (TEM) on a Hitachi H8000 (Japan) microscope. High-resolution electron micrographs were analyzed with an original software package [10].

The photoluminescence (PL) was studied on a special-purpose setup with a closed-cycle optical helium cryostat and cooled germanium diode. The PL was excited with an argon laser (wavelength 514 nm, power density ~100 W/cm^2).

3. RESULTS AND DISCUSSION

The structural studies revealed the formation of InAs-enriched nanodomains with a characteristic size of about 4 nm in the growth direction and 11 ± 3 nm in the lateral direction. An electron micrograph of the active region is shown as an example in Fig. 1. An analysis of high-resolution electron micrographs (Fig. 2) demonstrated that the content of InAs in these nanodomains is 60% or more. It is noteworthy that there exists a size distribution of the nanodomains. In addition, layers in the interdomain regions are characterized by a lattice mismatch of about 1.5–2% in the growth direction, which corresponds to an InAs content of about 12–18% in the case of an InGaAs QW. It should

1063-7826/04/3803-0340$26.00

PL (position and intensity of the emission band) and TEM (lattice mismatch, characteristic height and lateral size of the nanoinclusions, the density of extended and point defects) data

Structure of overgrowth layer	PL	TEM
x = 1 nm, y = 4 nm	λ = 1490 nm, I/I_0 = 1.35%	$(\Delta a/a_0)_{max}$ = 7.5% h = 4.5 nm, l = 11 nm, $\rho_{ext} \approx 5 \times 10^4$ cm^{-3}, $\rho_{pnt} \approx 10^{15}$ cm^{-3}
x = 2 nm, y = 3 nm	λ = 1451 nm, I/I_0 = 3.5%	$(\Delta a/a_0)_{max}$ = 6.5% h = 4 nm, l = 10 nm, $\rho_{ext} \approx 2 \times 10^4$ cm^{-3}, $\rho_{pnt} \approx 3 \times 10^{14}$ cm^{-3}
(InAs–3ML, x = 1 nm, y = 4 nm) × 3	λ = 1470 nm, I/I_0 = 2.3%	$(\Delta a/a_0)_{max}$ = 7.2% h = 4 nm, l = 10 nm, $\rho_{ext} \approx 10^5$ cm^{-3}, $\rho_{pnt} \approx 10^{16}$ cm^{-3}
x = 5 nm, y = 0 nm	λ = 1289 nm, I/I_0 = 100%	$(\Delta a/a_0)_{max}$ = 6% h = 4.5 nm, l = 13 nm, $\rho_{ext} \approx 3 \times 10^3$ cm^{-3}, $\rho_{pnt} \approx 2 \times 10^{10}$ cm^{-3}

Note: x and y are the thicknesses of the nitrogen-containing and nitrogen-free layers, respectively; λ is the PL wavelength; I and I_0, the relative PL intensities of a sample under study and the reference sample, respectively (a structure containing no nitrogen was used as the reference); h and l, the characteristic sizes of nanodomains in the vertical and lateral directions, respectively; and $(\Delta a/a_0)_{max}$, the relative lattice mismatch in InAs/InGaAsN nanodomains and the embedding GaAs matrix.

also be noted that a region with zero lattice mismatch is observed directly over a QD. This may mean that either the QW is only formed in the interdomain region or the lattice mismatch is compensated for by an increased concentration of nitrogen. In addition, comparing the results obtained for structures with and without nitrogen in the QW shows that the addition of N leads to a decrease in the average size of the nanodomains. It is noteworthy that, in the case of a multilayer structure (table, third row), the density of nanodomains decreases as one passes from the bottom to the top layer, with the characteristic dimensions remaining unchanged.

The structures obtained contain defects of both the extended and the point type. An example of an electron micrograph that reflects the content of defects in the structure is given in Fig. 1c. The densities of the extended (ρ_{ext}) and point-type (ρ_{pnt}) defects in the structures studied are evaluated in the table. Comparison of the estimated defect densities shows that reducing the thickness of the nitrogen-containing layer from 4 to 3 nm leads to a decrease in defect density by approximately a factor of 2–4. At the same time, the defect density in a multilayer (stacked) structure, on the contrary, increases. It is noteworthy that some of the defects penetrate the upper layers from the lower layers. In addition, the strain produced when part of the defect-free nanodomains are overgrown promotes the formation of defects in the upper layers.

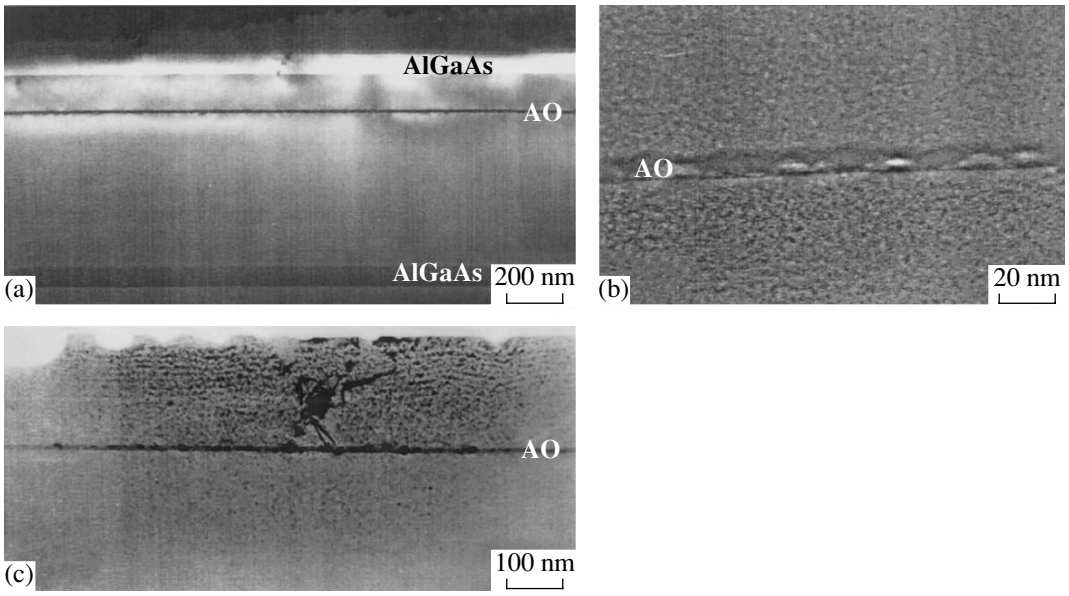

Fig. 1. (a, b) (002) and (c) (022) dark-field (110) cross-sectional electron micrographs of a GaAs-based heterostructure with InAs QDs overgrown with a ⟨1 nm InGaAs⟩/⟨4 nm InGaAsN⟩ layer.

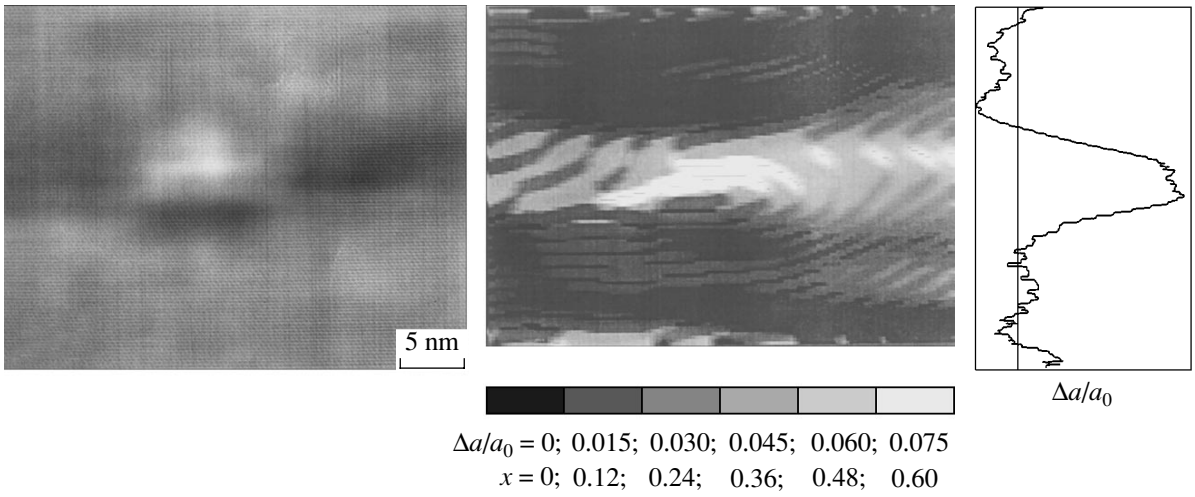

Fig. 2. High-resolution (110) cross-sectional electron micrographs of a GaAs-based heterostructure with InAs QDs overgrown with a ⟨1 nm InGaAs⟩/⟨4 nm InGaAsN⟩ layer and a map of the lattice mismatch distribution in InAs/InGaAsN nanodomains in the direction (002); a_0 is the lattice constant of the embedding GaAs matrix.

The PL spectra of the heterostructures studied are shown in Fig. 3. It can be seen that the introduction of nitrogen into the overgrowth matrix shifts the emission band from around 1.3 μm for a structure containing no nitrogen to the region of 1.54 μm for a structure containing 1.5% N. The intensity of PL from nitrogen-containing structures is lower by a factor of 10–100, depending on the content and distribution of nitrogen. If the distribution of nitrogen is modified in such a way that the integral content of nitrogen remains the same but the thickness ratio of the separating and nitrogen-containing layers, $x : y$, changes from 1 : 4 to 2 : 3, the PL intensity increases by approximately a factor of 4.

The structure with stacked QD layers (Fig. 3, curve *3*) demonstrates an increase in the PL band intensity by a factor of 2–3 compared to a "single-layer" structure, with a minor short-wavelength shift.

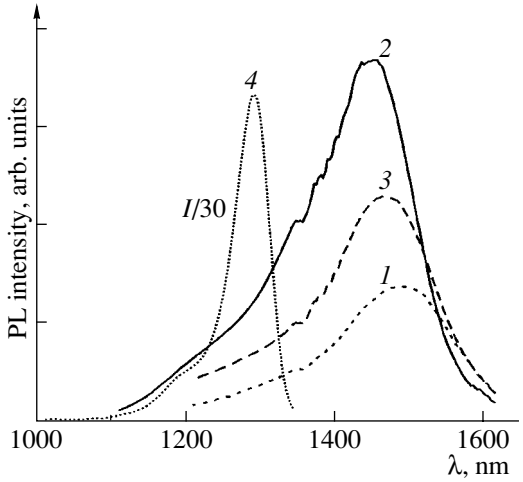

Fig. 3. PL spectra of heterostructures with InAs QDs overgrown with the following layers: (*1*) ⟨1 nm InGaAs⟩/⟨4 nm InGaAsN⟩, (*2*) ⟨2 nm InGaAs⟩/⟨3 nm InGaAsN⟩, (*3*)(⟨1 nm InGaAs⟩/⟨4 nm InGaAsN⟩) × 3, and (*4*) 5-nm InGaAs.

Analysis of the data obtained in structural and optical studies of single-layer heterostructures shows a satisfactory correlation between the density of extended defects and the PL band intensity. At the same time, correlation analysis of the nanodomain size and the position of the emission band reveals an opposite dependence; i.e., a shift to longer wavelengths occurs as the QD size decreases, which can be accounted for by the incorporation of nitrogen into the nanodomains.

Comparison with the structural data for InGaAsN/GaAs heterostructures [1] shows that the growth scheme employed in the present study leads to a decrease in the QD size and defect density, which, in turn, leads to a significant rise in the PL intensity.

4. CONCLUSION

Thus, the structural and optical properties of GaAs-based heterostructures in which InAs QDs are overgrown with an InGaAsN layer with varied nitrogen distribution were studied. It was shown that the size of the InAs nanodomains and the magnitude of the lattice mismatch were smaller in structures containing nitrogen compared to structures that do not contain nitrogen. A correlation between the wavelength of the PL band and the size and composition of nanodomains was demonstrated. Furthermore, a correlation between the emission intensity and the defect density in the structure was revealed.

ACKNOWLEDGMENTS

This study was supported by the Russian Foundation for Basic Research and the BMBF (Bundesministerium für Bildung und Forschung) program NanoOp.

REFERENCES

1. N. N. Ledentsov, *Growth Processes and Surface Phase Equilibria in Molecular Beam Epitaxy* (Springer, Berlin, 1999), Springer Tracts Mod. Phys., Vol. 156.
2. D. Gollub, M. Fischer, and A. Forchel, Electron. Lett. **38**, 1183 (2002).
3. D. G. Deppe, D. L. Huffaker, Z. Zou, *et al.*, IEEE J. Quantum Electron. **35**, 1238 (1999).
4. N. N. Ledentsov, IEEE J. Sel. Top. Quantum Electron. **8**, 1015 (2002).
5. V. M. Ustinov, A. E. Zhukov, A. Yu. Egorov, *et al.*, Electron. Lett. **34**, 670 (1998).
6. A. E. Zhukov, A. R. Kovsh, S. S. Mikhrin, *et al.*, Fiz. Tekh. Poluprovodn. (St. Petersburg) **37**, 1143 (2003) [Semiconductors **37**, 1119 (2003)].
7. H. A. Wonill, V. Gambin, B. Sank, *et al.*, in *Abstracts of International Conference on Molecular Beam Epitaxy* (2002), Vol. 61, p. 89.
8. I. P. Soshnikov, N. V. Kryzhanovskaya, O. M. Gorbenko, *et al.*, Semicond. Sci. Technol. (in press).
9. L. H. Li, V. Sallet, G. Patriarche, *et al.*, Electron. Lett. **39**, 519 (2003).
10. I. P. Soshnikov, O. M. Gorbenko, A. O. Golubok, and N. N. Ledentsov, Fiz. Tekh. Poluprovodn. (St. Petersburg) **35**, 361 (2001) [Semiconductors **35**, 347 (2001)].
11. I. P. Soshnikov, N. N. Ledentsov, B. V. Volovik, *et al.*, in *Proceedings of 9th International Symposium on Nanostructures: Physics and Technology* (2001), Vol. 1, p. 82.

Translated by M. Tagirdzhanov

Semiconductors, Vol. 38, No. 3, 2004, pp. 344–346. From Fizika i Tekhnika Poluprovodnikov, Vol. 38, No. 3, 2004, pp. 358–360.

AMORPHOUS, VITREOUS, AND POROUS SEMICONDUCTORS

Diffusion of Chromium in Thin Hydrogenated Amorphous Silicon Films[1]

S. K. Persheyev*, P. R. Drapacz, M. J. Rose, and A. G. Fitzgerald

Carnegie Laboratory of Physics, Electronic Engineering and Physics Division, University of Dundee, Dundee, DD1 4HN, Scotland, UK

**e-mail: s.persheyev@dundee.ac.uk*

Submitted July 17, 2003; accepted for publication July 18, 2003

Abstract—The diffusion of a chromium bottom contact has been studied through thin 10-nm amorphous silicon film. The concentration of the diffused impurity has been analyzed by an X-ray photon spectroscopy technique and the diffusion coefficient was estimated. Diffusion annealing was carried out in vacuum (10^{-6} mTorr), the temperature was kept at 400°C, and the annealing time was varied from 0 to 300 min. The authors propose that diffusion of chromium in thin hydrogenated amorphous film is limited by silicide formation at the metal–silicon interface. © *2004 MAIK "Nauka/Interperiodica".*

1. INTRODUCTION

While production of microelectronic devices is moving into the nanoscale region, chromium diffusion in amorphous silicon (*a*-Si:H) is a significant area of study for a number of reasons. Good electrical contacts to semiconductors are crucial for the proper functioning of circuits because signals enter and leave devices through them. One requirement for contacts is chemical stability. Furthermore, it is essential that a contact does not introduce unwanted electrical characteristics such as signal rectification or high resistance into the circuit. Since *a*-Si:H consists of a random network of atoms, distorted considerably from the minimum energy sites of its crystalline counterpart, it can easily interact with other materials. Interaction at a metal/*a*-Si:H contact can cause irreversible interfacial degradation; however, it may also be used to some advantage.

Memory devices based on *a*-Si:H [1] that act as two-state digital devices or analog devices with a continuum of states depending on the nature of their metal contacts (e.g. chromium or vanadium) are finding applications as nonvolatile switching materials. The nature of the top metal interaction is of crucial importance to the switching characteristics.

Amorphous silicides formed in hydrogenated amorphous silicon are not well understood despite the fact that silicides are widely used in contacting technologies for the thin film transistors needed in active matrix liquid crystal displays. The most widely studied metal is chromium, and it has been shown that silicide layers at most a few nanometers thick are formed after sputtering chromium onto hydrogenated amorphous silicon even with no subsequent annealing treatment. Recent work [2] suggests that using an ultrathin metal-like chromium silicide in an entirely amorphous structure naturally forms a hot electron device with a high electron barrier emitter and low electron barrier collector. The aim of this work is a further understanding of the chromium diffusion mechanism and metal/*a*-Si:H interface reactions mediated by thermal annealing.

2. EXPERIMENTAL

Hydrogenated amorphous silicon layers were deposited onto Corning 7059 glass preliminarily coated with sputtered chromium as shown in Fig. 1. Films were deposited using plasma-enhanced chemical vapor deposition (PECVD) from silane at a substrate temperature of 300°C, applied RF power of 6.5 W, and a silane flow rate of 40 sccm, giving a growth rate of ~0.9 Å/s. Typical layers had a thickness of 10 nm for Cr diffusion experiments and 600-nm films on silicon wafers for Fourier transform infrared spectroscopy (FTIR).

Chromium was sputtered on glass substrates to a thickness of 30 nm and immediately amorphous silicon was grown to avoid Cr surface oxidation. Films for thickness measurements were patterned using an inter-

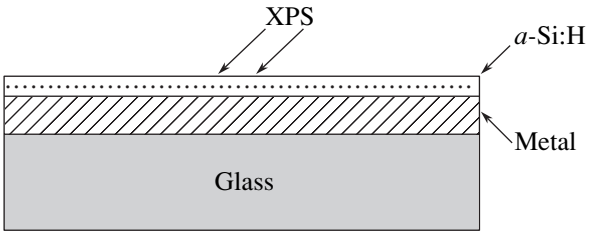

Fig. 1. Schematic representation of layers for diffusion study.

[1]This article was submitted by the authors in English.

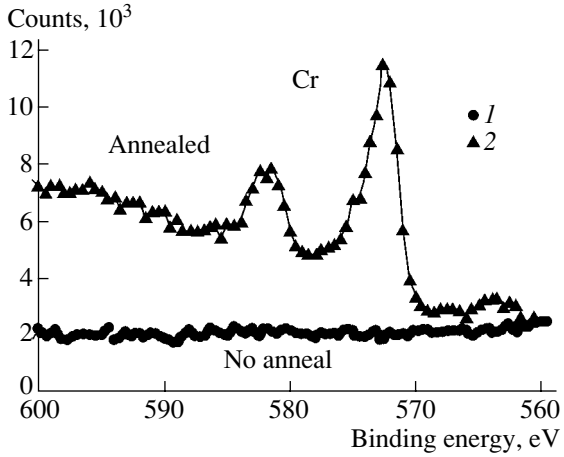

Fig. 2. XPS signal from amorphous Si: (*1*) before and (*2*) after annealing at 400°C, 5 h.

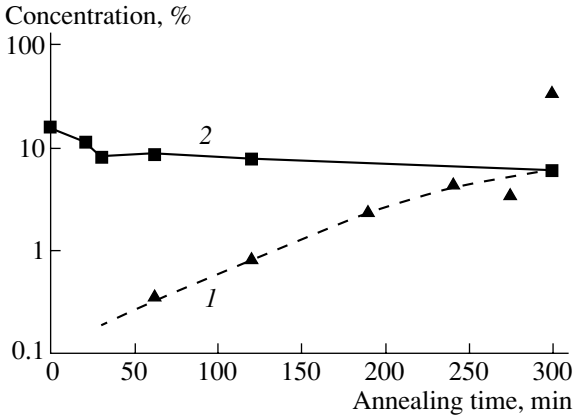

Fig. 3. Concentration of chromium (*1*) and hydrogen (*2*) after annealing in vacuum. Dashed lines are our theoretical calculations for diffused chromium.

digital photomask, and after removing the photoresist film, the surface was profiled using a thickness profiling technique. To study the thermal diffusion of chromium, samples on glass were annealed at 400°C in vacuum (10^{-6} mTorr) and then the samples were analyzed for presence of chromium in an X-ray photon spectroscopy (XPS) system. The spectra are shown in Fig. 2.

All the XPS measurements that we performed were for the chromium diffusion studies using Mg-K-alpha radiation. The apparatus (a VG HB 100 adapted to incorporate XPS) was operated in a constant analyzer energy mode with the X-ray gun itself running at 130 W. The pass energies were 50 eV for survey scans and 20 eV for region scans. Spectra were collected using VGX900 software and the system was kept calibrated using the procedures outlined in ISO/DIS 15472.

3. DISCUSSION

The diffusion at the contact metals in PECVD amorphous hydrogenated films shows unusual behavior of the diffusing materials and is quite different than that found in crystalline silicon [3]. The diffusion coefficient of the impurity in amorphous silicon depends only weakly on the impurity itself, and the diffusion coefficient and its activation energy are nearly equal to those of hydrogen. It was found that boron diffuses quite fast with a diffusion coefficient of about 10^{-13} cm^2/s, and the antimony diffusion coefficient was found to be 10^{-14} cm^2/s at 400°C. Activation energies are the same for both and are about 1.5 eV.

A. Polman *et al.* [4] studied the diffusion of copper in annealed and unannealed *a*-Si:H in the temperature range 150–270°C. The diffusion rate in annealed amorphous silicon is a factor of 2–5 higher than in unannealed *a*-Si:H. The diffusion activation energy E_a = 1.39 eV in annealed *a*-Si:H is not significantly different than in unannealed *a*-Si:H, where it is measured to be E_a = 1.25 eV.

The diffusion of silver has been studied in a previous work [5] and those authors conclude that silver diffuses in undoped amorphous silicon interstitially and through hydrogen vacancies with activation energies of 1.3 eV and 1.7 eV, respectively. Interstitial diffusion is described as $D_i = 4.4 \times 10^{-3}\exp(-1.3/kT)$ cm^2/s and diffusion through vacancies as $D_v = 70\exp(-1.7/kT)$ cm^2/s.

In our experiments, an annealing temperature of 400°C has been chosen for two reasons: it is known that diffusion of metals in *a*-Si:H at temperatures lower than 400°C is small and requires very long diffusion annealing times, and, second, hydrogen effusion occurs at temperatures higher than 400°C and changes the amorphous structure and its network. The experimental results are shown in Fig. 3. As we can see from the graph, the hydrogen concentration decreases from 15 to 8.3 at % mainly at the beginning of the anneal, where the initial drop in the first 30 min is obviously due to hydrogen effusion from the film. At longer times, the change in the hydrogen content is relatively small, and after 5 h of annealing, the remaining hydrogen is about 6 at %. The change in hydrogen content in the beginning can also be explained due to relaxation processes in the amorphous matrix. With the release of some hydrogen, we create additional "hydrogen vacancies," enabling diffusion of chromium impurities. The XPS surface analysis technique allowed detection of Cr atoms that diffused through the very thin 10-nm *a*-Si:H layer. The time dependence of the Cr concentration is also plotted in Fig. 3. For purpose of theoretical calculations, a thick layer of Cr (30 nm) can be considered as an unlimited source, and diffusion through a thin film can be described as diffusion in a body with one impermeable border [6]. The impurity concentration at the first boundary of a body ($x = 0$) has a constant value C_0 which does not change with time. The second boundary is regarded as impermeable, with $dC/dx = 0$ at $x = l$. For

such a body, the impurity concentration as a function of coordinate x and time t is given by

$$C(x,t) = C_0\left\{1 - \frac{4}{\pi}\sum_{k=0}^{\infty}\frac{(-1)^k}{(2k+1)} \times \exp\left[-(2k+1)^2\frac{\pi^2}{4}\frac{Dt}{l^2}\right]\sin(2k+1)\frac{\pi}{2}\frac{x}{l}\right\}. \quad (1)$$

At the boundary $x = l$, the concentration changes with time,

$$C(l,t) = C_0\left\{1 - \frac{4}{\pi}\sum_{k=0}^{\infty}\frac{(-1)^k}{(2k+1)}\exp\left[-(2k+1)^2\frac{\pi^2}{4}\frac{Dt}{l^2}\right]\right\}. \quad (2)$$

After a transient period of time, the terms with large k will decay away and only the first term (with $k = 0$) will have to be considered,

$$C(l,t) = C_0\left[1 - \frac{4}{\pi}\exp\left(-\frac{\pi^2}{4}\frac{Dt}{l^2}\right)\right]. \quad (3)$$

The calculation (dashed line in Fig. 3) gives a good match with the experimental results except for the last point.

Simulation results allowed us to estimate Cr diffusion in thin *a*-Si:H films with a diffusion coefficient of 4×10^{-17} cm^2/s, which is quite slow compared to impurities such as Cu, Sb, B, and Ag. The reason is likely the processes at the silicon and metal interface. Initially, during even short deposition of *a*-Si:H on metal, Cr forms a silicide layer, which creates a barrier for the diffusion and subsequently prevents penetration of Cr atoms into the bulk. The diffusion process is followed apparently by the growth of a silicide layer, which gives a fast increase in Cr concentration at the end of the annealing ($t = 300$ min).

The same experiments were carried out using vanadium metal as the diffusion source, but even after a 5-h annealing in vacuum, vanadium was not found to diffuse through 10-nm-thick amorphous silicon.

4. CONCLUSIONS

We have studied diffusion (at 400°C) of chromium in 10-nm *a*-Si:H films by means of XPS and found that it includes two processes. First of all, there is silicide formation and growth during annealing at the metal–silicon interface and, secondly, silicide limits diffusion of Cr atoms through the thin amorphous silicon film. We propose a new XPS-based method of diffusion analysis of contact materials on thin films.

ACKNOWLEDGMENTS

We acknowledge R-Sh. Malkovich for helpful discussions. This work was partially supported by a Royal Society NATO Advanced Fellowship.

REFERENCES

1. J. Hu, J. Hajto, A. J. Snell, *et al.*, Philos. Mag. A **74**, 37 (1996).
2. A. Kovsarian, J. M. Shannon, and F. Cristiano, J. Non-Cryst. Solids **276**, 40 (2000).
3. H. Matsumura, M. Maeda, and S. Furukava, J. Non-Cryst. Solids **59–60**, 517 (1983).
4. A. Polman, D. C. Jacobson, S. Coffa, and A. Poate, Appl. Phys. Lett. **57**, 1230 (1990).
5. M. S. Ablova, G. S. Kulikov, S. K. Persheyev, and K. K. Khodzhaev, Sov. Phys. Semicond. **24**, 1208 (1990).
6. J. Crank, *The Mathematics of Diffusion* (Clarendon Press, Oxford, 1956), p. 58.

Semiconductors, Vol. 38, No. 3, 2004, pp. 347–351. Translated from Fizika i Tekhnika Poluprovodnikov, Vol. 38, No. 3, 2004, pp. 361–365.

PHYSICS OF SEMICONDUCTOR DEVICES

Temperature Dependence of Electroluminescence of Er Ions in Tunnel Diodes Based on (111)Si:(Er, O)

A. M. Emel'yanov and N. A. Sobolev

Ioffe Physicotechnical Institute, Russian Academy of Sciences, Politekhnicheskaya ul. 26, St. Petersburg, 194021 Russia

Submitted May 13, 2003; accepted for publication June 18, 2003

Abstract—Electroluminescence and current–voltage characteristics of tunnel diodes obtained by implantation of Er, O, and B ions into *n*-Si(111) with the subsequent heat treatment are investigated in a temperature range of 80–300 K in the breakdown mode. The observed increase in electroluminescence intensity with temperature for Er ions is caused by thermal emptying of the traps that captured the holes in the *n*-region of the diode at low temperatures. This emptying leads to a variation in the breakdown characteristics. It is shown that some of the traps at low temperatures retain the charge captured even after the voltage applied to the diode is switched off. This circumstance gives rise to the peculiar memory effect in the structures investigated. © *2004 MAIK "Nauka/Interperiodica".*

1. INTRODUCTION

Investigations of semiconductor structures doped with rare earth elements are aimed at developing electroluminescence emitters and radiation detectors for optoelectronics and fiber-optic communications. Electroluminescence (EL) at the wavelength $\lambda \approx 1.54$ μm in diodes based on Si:(Er, O) is related to Er^{3+} ions. The EL intensity is typically highest in the breakdown mode of the *p–n* junction at room temperature. Both for tunnel [1] and for avalanche [2, 3] breakdown of the (100)Si:(Er, O) diodes, a decrease in the intensity of the Er^{3+}-related EL band is observed as temperature increases from 77 to 295 K. This behavior is usually associated with an increase in a fraction of the nonradiative transitions between the levels of Er^{3+} ions of the first excited state $^4I_{13/2}$ to the ground state $^4I_{15/2}$, as well as with the broadening of the EL lines corresponding to these transitions. In the (111)Si:(Er, O)-based diodes, which exhibit avalanche breakdown at room temperature, the temperature dependences of intensity of Er^{3+}-induced EL contain portions of increase in EL in the temperature range mentioned above [3–5]. This effect was described for the first time in detail and explained by us [4]. It was shown that the temperature range of Er^{3+}-induced EL corresponds to the portion of sharp rise in temperature in the diode voltage with a fixed current in the breakdown mode. From the sign reversal of the derivative of the temperature dependence of this voltage, it was concluded that the portion of the increase in EL intensity with temperature corresponds to the transition from tunnel breakdown (at lower temperatures) to avalanche breakdown. The variation in the breakdown mechanism was attributed to the hole capture by the traps in the depletion *n*-type layer of the *p–n* junction at sufficiently low temperatures. As the temperature varied from 300 to 80 K, an anomalous decrease in the EL intensity associated with the phenomena described, as well as a decrease in the efficiency of excitation of Er^{3+} ions, was also observed.

The existence of the portion of increase in EL intensity in the temperature dependence of intensity of Er^{3+}-induced EL was also recently observed in (111)Si:(Er, O) diodes with tunnel breakdown at room temperature [6]. This study is devoted to a more detailed investigation of this effect. We measured for the first time the parameters that characterize the kinetics of filling the hole traps in such structures and ascertained that the traps that retain a captured positive charge after the voltage applied to the diode is switched off are involved in the effect of the temperature-related increase in the EL intensity.

2. EXPERIMENTAL

The main difference between the tunnel (111)Si:(Er, O)-based light-emitting diodes (LEDs) investigated in this study and the avalanche (111)Si:(Er, O) diodes investigated earlier in detail [4] is the higher (by a factor of 3) doses of implanted Er and O ions. The implantation of Er ions (energies of 2.0 and 1.6 MeV and doses 3×10^{14} cm^{-2}) and O ions (0.28 and 0.22 MeV, 3×10^{15} cm^{-2}) into the polished Czochralski-grown *n*-Si(100) wafers with a resistivity of 5 Ω cm was accompanied by the amorphization of the surface layer. The B ions (40 keV, 5×10^{15} cm^{-2}) and P ions (80 keV, 10^{15} cm^{-2}) were implanted into the front and rear sides of the wafer, respectively, to produce heavily doped p^+- and n^+-type layers. Sequential thermal treatments at 620°C for 1 h and at 900°C for 0.5 h caused the recrystallization of the amorphous layer and formation of Er-containing optically and electrically active centers. According to the secondary-ion mass spectrometry (SIMS) data, the Er-doped Si layer was formed as a result of implantation and thermal treatments. This

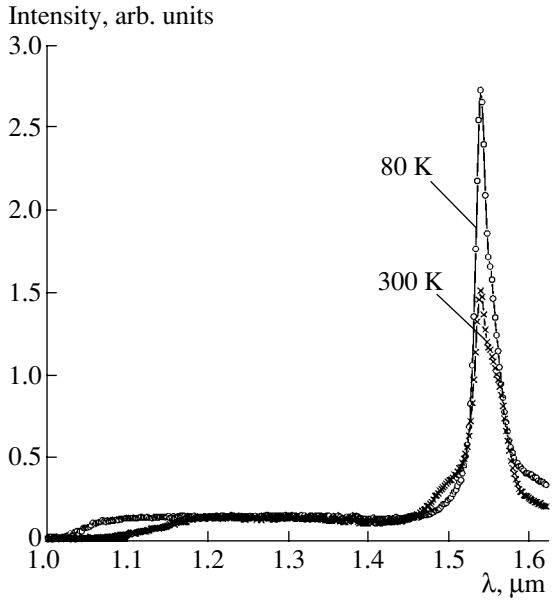

Fig. 1. Electroluminescence spectra of light-emitting diodes at 80 and 300 K with a current of 300 mA.

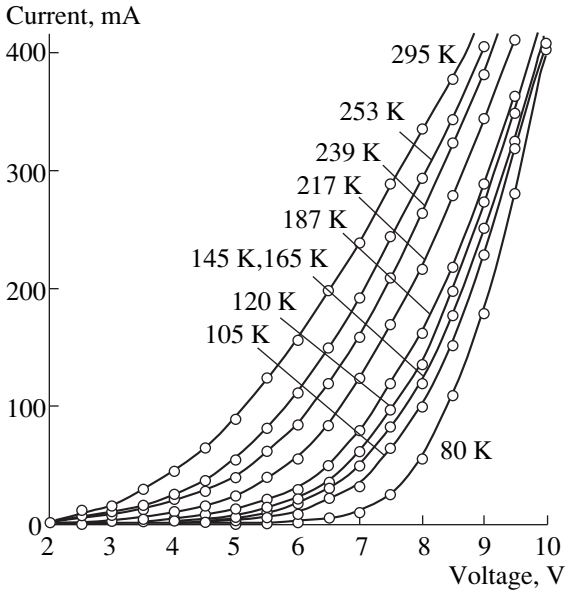

Fig. 2. Reverse portion of the current–voltage characteristics of a light-emitting diode measured at various temperatures.

layer had a virtually constant Er concentration of ~10^{19} cm^{-3} at a distance of 0.5–0.8 μm from the semiconductor surface. The concentration of electrically active centers determined from the capacitance–voltage characteristics was ~10^{18} cm^{-3}. According to the SIMS data, the peak concentration of B atoms was ~3×10^{20} cm^{-3}. Mesa diodes were fabricated with an active area of $S = 2.3$ mm^2. The current–voltage (I–V) characteristics of diodes were measured at a frequency of 32 Hz with a pulse width of 0.5 ms. EL was excited by rectangular current pulses with widths of 2–5 ms and a pulse-repetition period of 30 ms. The samples under investigation were mounted on a massive copper cylinder. The temperature of the samples was measured using a thermocouple also mounted on this cylinder. When measuring the EL spectra, the emission of diode structures was focused by a lens system onto the entrance slit of an MDR-23 monochromator and was detected on its exit using an uncooled InGaAs diode with a resolution of 7 nm in the range $\lambda = 1.0$–1.65 μm.

3. RESULTS AND DISCUSSION

The EL spectra for a reverse-biased diode with a current of 300 mA at 300 and 80 K are shown in Fig. 1. The peaks at $\lambda = 1.538$ μm, which are caused by radiative electron transitions between the levels $^4I_{13/2}$ and $^4I_{15/2}$ of Er^{3+} ions split in the crystal field, are observed in the spectra. In addition to these peaks, a relatively weak and almost λ-independent emission, which is caused by transitions of "hot" electrons within the conduction band of Si, so-called "hot" EL [7], is observed in the spectra. The dependence of intensity of Er^{3+}-induced EL on the current density at 300 and 80 K for the diodes investigated in this study was reported in [6]. Unlike avalanche (111)Si:(Er, O) diodes [4], the intensity of Er^{3+}-induced EL in these diodes is higher at 80 K than at 300 K. This relationship is retained in a wide current range until the virtual leveling off of dependences of the EL intensity on the current density is attained. It should also be noted that the virtual leveling off of the EL dependences at 80 and 300 K is attained at almost the same current densities, unlike the (111)Si:(Er, O) diodes, whose breakdown at 300 K followed the avalanche mechanism [4].

The reverse portion of the I–V characteristic of the diode structure at various temperatures is shown in Fig. 2. The dependences shown were obtained with increasing sample temperature after keeping the sample under a reverse pulse current of 100 mA for several minutes at 80 K. An increase in the breakdown voltage with decreasing temperature is characteristic of tunnel diodes. However, the breakdown voltage V_{th}, i.e., the voltage obtained by the linear extrapolation of dependences in Fig. 2 for large currents to a zero current, varies nonmonotonically in the temperature range from 80 to 300 K (see curve *1*, Fig. 3). As the temperature increases from 120 to 165 K, a slight increase in the breakdown voltage is observed. The temperature dependence of Er^{3+}-induced EL at a wavelength of $\lambda = 1.538$ μm, which was measured simultaneously with the measurements of the I–V characteristic for a current of 100 mA, is represented by curve *2* in Fig. 3. From comparison of curves *1* and *2* in Fig. 3, it can be seen that the portion of increasing breakdown voltage with increasing temperature corresponds to the portion of the temperature-related increase in the EL intensity. In this respect, the diodes investigated by us are similar to

the (111)Si:(Er, O) LEDs investigated previously, which follow the avalanche breakdown mechanism at room temperature [4]. The most substantial qualitative difference is that the LEDs investigated in this study have the temperature dependence of the breakdown voltage characteristic of the tunnel breakdown mechanism; i.e., the breakdown voltage increases with decreasing temperature. Such is the case both for the temperatures below the portion of the temperature-related increase in the EL intensity and for higher temperatures. The experimental results reported here suggest that, as in [4], the temperature-related increase in the intensity of Er^{3+}-induced EL is caused by the thermal emptying of hole traps occupied at low temperatures. The emptying affects breakdown characteristics, such as the width of the space charge region, as well as the spatial and energy distribution of hot carriers. The variation in the breakdown characteristics, in turn, affects the EL intensity.

All the investigations of temperature dependences of Er^{3+}-induced EL in reverse-biased (111)Si:(Er, O) diodes were carried out under conditions in which a pulse voltage was applied to the diodes. Thus, in the time intervals between the current pulses inducing EL, the voltage was not applied to the diode. Therefore, two possible mechanisms of hole-trap filling may be suggested:

(i) Traps are rapidly filled with holes during each current pulse passage and are emptied in the absence of voltage.

(ii) It is possible that the traps are filled with holes during a certain number of pulses rather than during a single current pulse and remain filled in the absence of the external voltage for a long time.

The first situation may occur, for example, if the traps are arranged in the part of the space charge region of the *p–n* junction that becomes electrically neutral after the external voltage is switched off. The second situation can occur, for example, if the traps are arranged in the part of the space charge region of the *p–n* junction whose depletion of majority carriers (electrons) is also retained after the external voltage is switched off. The results of the experiments described below showed that both these mechanisms occur in the diodes investigated by us. For the first of them, the filling of hole traps in the *n* layer of the *p–n* junction should cause an increase in the current after applying each rectangular voltage pulse to the diode. The reason is that filling the traps causes a decrease in the breakdown voltage and shifts the *I–V* characteristic to lower voltages. If the time in which the current increases substantially exceeds the time in which the voltage across the diode increases, this effect can be easily detected experimentally. In our experiments, the rise time of the dc voltage pulses was ~1 μs. During measurements of curve *2* in Fig. 3 at 170–300 K, the shape of current pulses with an amplitude of 100 mA for times >1 μs virtually repeated the shape of the voltage pulses (see Fig. 4a). At temperatures that corresponded to an increase in EL intensity and at lower temperatures, a substantial increase in the current was actually observed for several milliseconds, which is shown in Fig. 4b for 80 K and a current amplitude of 100 mA.

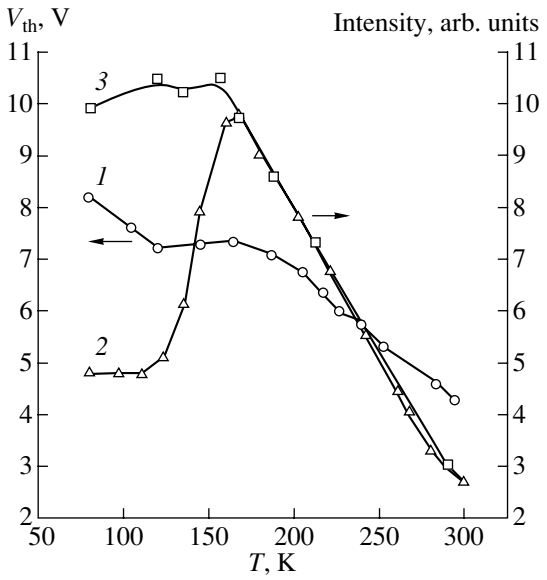

Fig. 3. (*1*) Temperature dependence of the breakdown voltage (V_{th}) of diodes; (*2*, *3*) temperature dependences of intensity of electroluminescence of Er^{3+} ions at a wavelength of λ = 1.538 μm with a reverse current of 100 mA; (*2*) after keeping the sample before measurements for several minutes at 80 K and 100 mA; (*3*) 2 s after switching on the current.

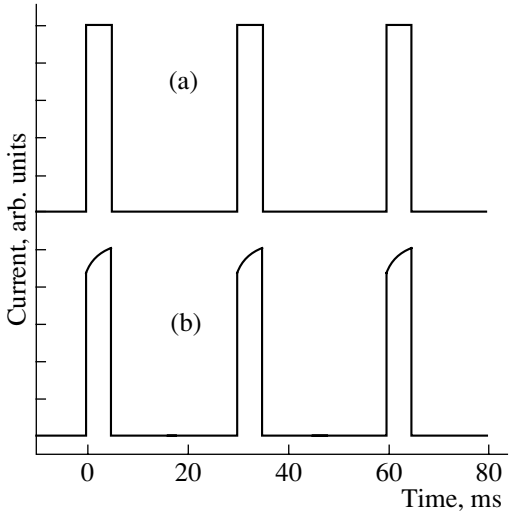

Fig. 4. Shape of reverse current pulses when rectangular voltage pulses are applied to the diode: (a) at 170–300 K and (b) at 80 K. The amplitude of the current pulses is 100 mA. The time constant of the voltage rise and decay is ~1 μs.

We note once more that the experiments on measuring EL at low temperatures described above were car-

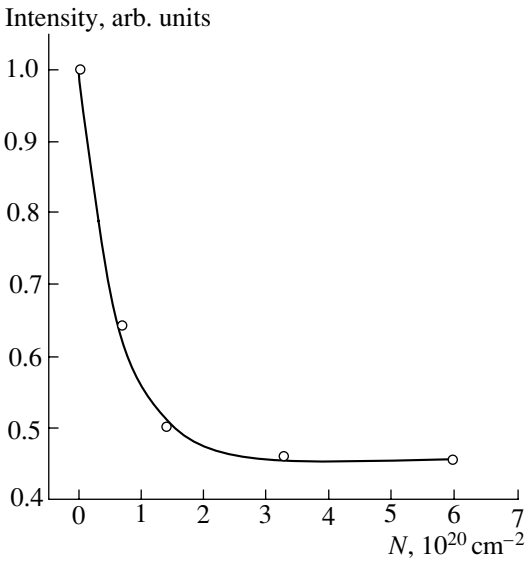

Fig. 5. Dependence of Er^{3+}-induced electroluminescence at a wavelength of $\lambda = 1.538$ μm on the density of carriers passing through the *p–n* junction with a reverse current of 100 mA at 80 K. The origin of the time coordinates for the carrier density corresponds to the time of passing of the reverse current with a pulse amplitude of 100 mA and duration of 5 ms, which is equal to 2 s.

ried out after keeping the sample at 80 K under a reverse pulsed current of 100 mA for several minutes. If the sample is cooled without applying the voltage and the EL measurements are taken ~2 s after applying the pulse voltage, the temperature dependence of the EL intensity for the same current is described by curve *3* rather than curve *2* in Fig. 3. Curve *3* differs from curve *2* only in the temperature range that corresponds to an increase in the EL intensity and at even lower temperatures. No pronounced increase in the EL intensity with temperature is observed in dependence *3*. Thus, the experimental results show that the hole traps exist in the structures investigated, whose filling time at 80 K and for a current of 100 mA considerably exceeds the longest pulse duration used by us (5 ms). These traps are practically not emptied during the absence of voltage in the pulse-to-pulse intervals. It is these traps that mainly determine the increase in EL intensity with increasing temperature.

For a reverse current of 100 mA, a current pulse duration of 5 ms, and a repetition period of 30 ms, the decay of the EL intensity at 80 K was completed in about several tens of seconds (less that 1 min). The dependence of intensity of Er^{3+}-induced EL on the density N of carriers passing through the *p–n* junction at 80 K and a reverse pulse current of 100 mA is shown in Fig. 5. The origin of the time coordinates corresponds to the time the structure was kept under the pulse current $t \approx 2$ s ($N \approx 9 \times 10^{18}$ cm^{-2}), which is short compared to the time required for equilibrium EL intensity to be established. The latter, as can be seen from Fig. 5, was virtually attained at $N \approx 3 \times 10^{20}$ cm^{-2}. The EL intensity decreases by more than a factor of 2 compared with that for $t = 2$ s. The data obtained show that the diode structures under investigation feature a peculiar memory effect at low temperatures. Specifically, after passing the current and voltage switch-off, these structures retain information on the current effect. To erase this information, it is sufficient to heat the structure to a temperature higher than the region of the temperature-related increase in the EL intensity. It is possible that the trap formation is associated with the formation of SiO_2-like precipitates in Si [8].

Thus, the breakdown voltage of the *p–n* junction decreases due to the hole capture by traps in the absence of rapid trap emptying after the voltage is switched off. These notions may provide the basis for an alternative explanation to the one suggested by Andreev *et al.* [9] of so-called "delayed" Er^{3+}-induced EL. Delayed EL is observed in the reverse current mode for Si diodes selectively doped by molecular beam epitaxy. In fact, let us assume that the hole traps with the aforementioned properties were filled during the passage of forward current through the structures investigated in [9]. In this case, with polarity reversal of the voltage applied to the diode from forward to reverse, considerable reverse currents and intensities of Er^{3+}-induced EL can be observed for reverse voltages lower than the breakdown voltage in equilibrium conditions before the hole traps are filled. This situation takes place until the hole traps are emptied and the breakdown voltage of the *p–n* junction is increased accordingly. As can be understood from the description presented in [9], it is this effect that is observed in this study. Andreev *et al.* [9] attributed the observed effect to the capture of electrons by the traps during the passage of the forward current and to excitation of Er^{3+}-induced EL by electrons from the traps emptied in the reverse voltage mode [9]. It should be noted that the SiO_2-like precipitates probably exist in the structures investigated in [9]. This indirectly confirms the above hypothesis that hole trap formation may be associated with the formation of such defects.

4. CONCLUSION

The experimental results presented confirm the earlier assumption that the temperature-related increase in the intensity of Er^{3+}-induced EL in (111)Si:(Er, O)-based LEDs in the tunneling mode is caused by the thermal emptying of the traps in the *n*-type layer, which capture holes at a low temperature. This emptying affects the breakdown characteristics. It is shown for the first time that the hole traps that retain the positive charge captured after the voltage applied to the diode was switched off are formed in such structures. It is these traps that mainly determine the temperature-related increase in the EL intensity and the peculiar memory effect in the structures investigated at low temperatures. Based on the results obtained, an alternative

explanation to that given by Andreev *et al.* [9] is suggested for so-called "delayed" Er^{3+}-induced EL in selectively Er-doped Si diodes.

ACKNOWLEDGMENTS

This study was partly supported by the Russian Foundation for Basic Research, project no. 02-02-16374; INTAS, grant no. 2001-0194; and the Section of Physical Sciences, Russian Academy of Sciences, within the framework of the "New Materials and Structures" program.

REFERENCES

1. G. Franzo, F. Priolo, S. Coffa, and A. Carnera, Appl. Phys. Lett. **64**, 2235 (1994).
2. N. A. Sobolev, A. M. Emel'yanov, and K. F. Shtel'makh, Appl. Phys. Lett. **71**, 1930 (1997).
3. N. A. Sobolev, A. M. Emel'yanov, Yu. A. Nikolaev, and V. I. Vdovin, Fiz. Tekh. Poluprovodn. (St. Petersburg) **33**, 660 (1999) [Semiconductors **33**, 613 (1999)].
4. A. M. Emel'yanov, N. A. Sobolev, and A. N. Yakimenko, Appl. Phys. Lett. **72**, 1223 (1998).
5. N. A. Sobolev, A. M. Emel'yanov, Yu. A. Nikolaev, *et al.*, Izv. Ross. Akad. Nauk, Ser. Fiz. **64**, 348 (2000).
6. N. A. Sobolev, A. M. Emel'yanov, and Yu. A. Nikolaev, Fiz. Tekh. Poluprovodn. (St. Petersburg) **34**, 1069 (2000) [Semiconductors **34**, 1027 (2000)].
7. J. Bude, N. Sano, and A. Yoshii, Phys. Rev. B **45**, 5848 (1992).
8. W. Jantsch, S. Lanzerstorfer, L. Palmetshofer, *et al.*, J. Lumin. **80**, 9 (1999).
9. B. A. Andreev, Z. F. Krasil'nik, D. I. Kryzhkov, *et al.*, in *Proceedings of Workshop on Nanophotonics* (Nizhni Novgorod, 2003), p. 330.

Translated by N. Korovin

Semiconductors, Vol. 38, No. 3, 2004, pp. 352–354. Translated from Fizika i Tekhnika Poluprovodnikov, Vol. 38, No. 3, 2004, pp. 366–368.

PHYSICS OF SEMICONDUCTOR DEVICES

Blue–Green Radiation in GaAs-Based Quantum-Well Lasers

N. V. Baĭdus'*, A. A. Biryukov*, B. N. Zvonkov*^, S. M. Nekorkin*, and V. Ya. Aleshkin**

**Nizhni Novgorod Research Physicotechnical Institute, Nizhni Novgorod State University, pr. Gagarina 23/5, Nizhni Novgorod, 603600 Russia*

^e-mail: zvonkov@nifti.unn.ru

***Institute of Physics of Microstructures, Russian Academy of Sciences, Nizhni Novgorod, 603600 Russia*

e-mail: Aleshkin@ipm.sci-nnov.ru

Submitted June 30, 2003; accepted for publication July 9, 2003

Abstract—Second-harmonic generation in InGaAs/GaAs/InGaP quantum-well lasers is studied. It is shown that second-order lattice nonlinearity of permittivity leads to the generation of the fundamental TM mode of the dielectric waveguide at a doubled lasing frequency. Additional lasing lines near the second-harmonic peak are observed. © *2004 MAIK "Nauka/Interperiodica".*

1. INTRODUCTION

The potential wide application of blue–green radiation in the optical recording of data, the design of monitors, high-resolution lithography, spectroscopy, and medical diagnostics has stimulated research aimed at developing lasers that operate in this spectral range. The research is being conducted in several areas: infrared (850–890 nm) frequency doubling in solid-state crystal $LiTaO_3$ due to nonlinear interaction [1] and the employment of II–VI (ZnSeS/CdZnSe) [2] or III–V (GaN/InGaN) [3] semiconductor materials. One more possibility for obtaining blue–green radiation with the help of III–V materials is to make use of the nonlinear properties of GaAs diode lasers. Indeed, the electric field of the electromagnetic wave in the laser cavity is high (~10^4 V/cm), and the nonlinear permittivity of GaAs is six times that of $LiNbO_3$. The observation of second harmonic generation (SHG) in vertical-cavity lasers was reported in [4–6]. There are also data on SHG in stripe-type diode lasers based on a (In, Ga)As/GaAs heterostructure with two quantum wells (QWs) and radiation extraction through an aperture in the upper electrode [7]. In this study, we observed the second harmonic generated in InGaAs/GaAs/InGaP structures from the chips that served as mirrors for fundamental wave lasing.

2. HETEROSTRUCTURES AND FABRICATION OF THE LASERS

Laser heterostructures of InGaAs/GaAs/InGaP were grown by MOVPE (metal-organic vapor-phase epitaxy) at atmospheric pressure and consisted of the following layers: an n^+-GaAs substrate, a 0.7-μm-thick lower confining layer of *n*-InGaP, a 0.8-μm-thick *i*-GaAs waveguide layer with an active region of InGaAs with two 9-nm-wide QWs, an upper confining layer of *p*-InGaP, and a contact layer of p^+-GaAs. The structures were fabricated based on technology described in [8]. The resulting lasers operated at a wavelength of λ = 0.94–0.99 μm. All of them had a stripe width of w = 100 μm and a cavity length of L = 1 mm. The diodes were mounted on a copper heat sink with their stripe contact down. A multilayer reflective coating and an antireflection coating were deposited onto the rear and the front laser faces, respectively.

3. RESULTS AND DISCUSSION

Direct-current driving of lasers was used during the experiments. Spectral characteristics were measured using an MDR-23 grating monochromator at 300 K. Along with the spectral characteristics, we also studied the angular dependences of the radiation intensities in the planes parallel and perpendicular to the *p–n* junction at fixed wavelengths (the intensity patterns).

Figure 1 shows the spectra of SHG (curve *1*) and the first-harmonic generation (curve *2*) detected at a driving current of 1.5 A (which corresponds to 1.1 W power of the fundamental lasing wave). The peak half-width was measured as 1 and 3.5 nm for the second harmonic and the fundamental waves, respectively.

In order to establish the origin of the SHG, we measured the SHG power as a function of the fundamental-wave power (Fig. 2). It can be seen that the dependence is quadratic and, therefore, the SHG stems from the second-order nonlinearity. To find out the origin of this nonlinearity, we carried out a polarization study of the laser radiation.

According to the results of our polarization measurements, the electric-field vector of the second harmonic is perpendicular to the QW plane (TM-mode). Note that, in materials with a zinc blende structure, the second-order susceptibility tensor $\varepsilon_{ijk}^{(2)}$ corresponding to the lattice nonlinearity has nonzero components only

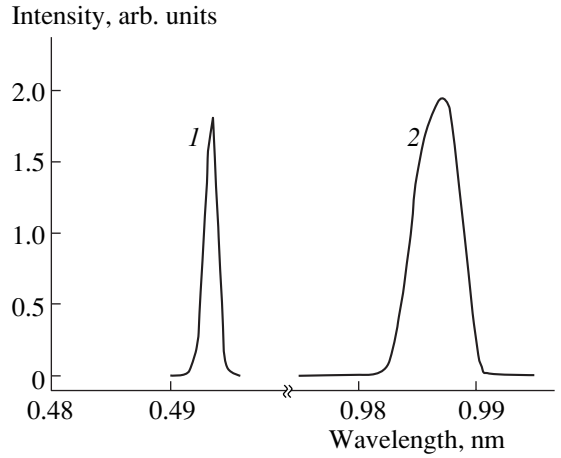

Fig. 1. Spectra of InGaAs/GaAs/InGaP diode lasing: (*1*) the second harmonic and (*2*) the fundamental wave.

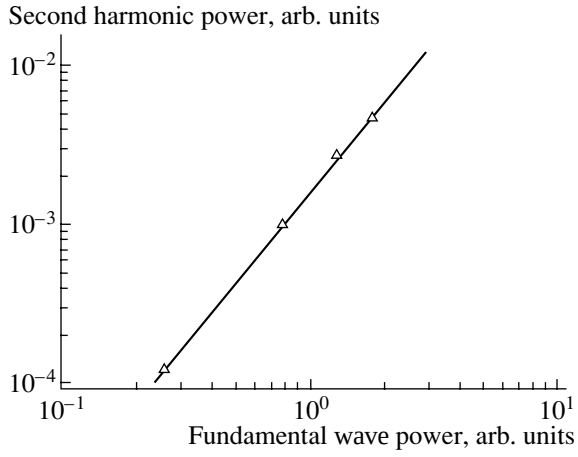

Fig. 2. Second harmonic power vs. fundamental wave power.

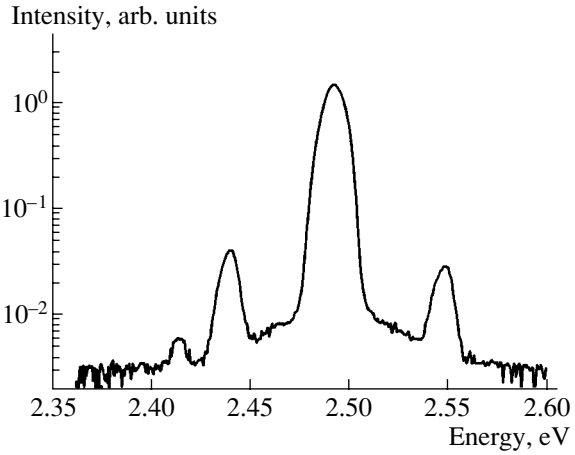

Fig. 3. Second harmonic spectrum observed at certain chips of the diode lasers.

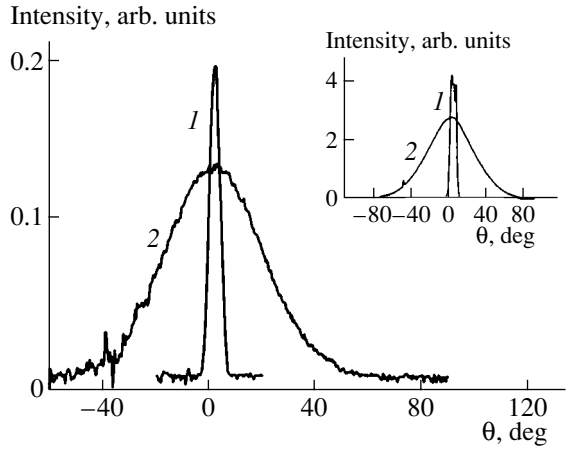

Fig. 4. Second harmonic intensity patterns (*1*) in the plane of the *p–n* junction and (*2*) in the plane perpendicular to the *p–n* junction; the inset shows the fundamental intensity patterns for the same laser.

at $i \neq j \neq k$ (the coordinate axes *x*, *y*, and *z* are chosen along the [100], [010], and [001] directions, respectively; the direction of growth is [001]). Since the fundamental lasing mode is the TE waveguide mode and propagates along the [110] direction, its electric-field vector lies in the *x–y* plane. Therefore, the electric field of the second harmonic generated due to the lattice nonlinearity should be directed along the *z* axis ([001] direction), which is exactly what is observed experimentally. This circumstance suggests that the lattice nonlinearity is the source of the SHG. The estimations of the SHG power suggest that its ratio to the fundamental harmonic power does not exceed 10^{-6}.

In the vicinity of the double-frequency radiation peak, we observed satellite peaks whose intensities varied from sample to sample. Figure 3 shows the observed SHG spectrum on which three satellite peaks can be clearly seen. The two highest of them are equally spaced ~50 meV from the short- and long-wavelength sides of the main peak. Note that the ratio of the intensity of the long-wavelength satellite (Stokes line) to the intensities of the second harmonic and the short-wavelength satellite (anti-Stokes line) is approximately 1 to 30 and 2 to 1, respectively. One more low-intensity satellite is observed near the Stokes line. It is well known that the optical-phonon energies do not exceed 37 meV in GaAs [9] and are about 43 meV (InP-like phonon) and 47 meV (GaP-like phonon) in InGaP. It is conceivable that the satellites appear as a result of the Raman scattering of the second harmonic in InGaP. The small difference between the intensities of the Stokes and anti-Stokes lines, as well as the high intensity of the lines themselves, indicates the presence of a large number of nonequilibrium optical phonons in the active region. No satellites were detected in the vicinity of the fundamental lasing line.

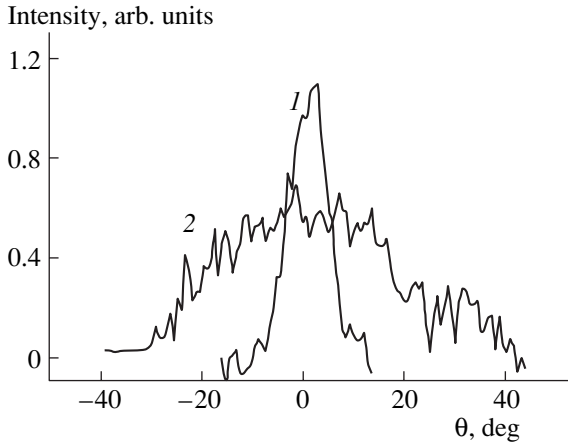

Fig. 5. Long-wavelength satellite (Stokes line) intensity patterns (*1*) in the plane of the *p–n* junction and (*2*) in the plane perpendicular to the *p–n* junction.

Figure 4 shows the intensities of the second harmonic and the fundamental-wave radiation versus the angle θ in the planes parallel and perpendicular to the *p–n* junction. The intensity pattern for the second harmonic is similar to that for the main laser mode and corresponds to the fundamental TM mode of the dielectric waveguide. This fact indicates that the second-order lattice nonlinearity of permittivity gives rise to the fundamental TM mode of the dielectric waveguide at a doubled frequency. Note that the angular intensity pattern of the Stokes line (see Fig. 5) also corresponds to the fundamental mode of the dielectric waveguide.

Thus, we observed generation of the fundamental TM mode at double the frequency of the main lasing wave in a QW laser. It was established that the SHG takes its origin from the lattice nonlinearity of GaAs permittivity.

ACKNOWLEDGMENTS

This study was supported by the Russian Foundation for Basic Research, project no. 01-02-16441; the Russian Foundation for Basic Research–Belarusian Republican Foundation for Fundamental Research, project no. 02-02-81036; NATO program SfP-973799 "Semiconductors"; and the International Science and Technology Center (ISTC), grant no. 2293.

REFERENCES

1. K. Yamamoto, K. Mizuuchi, Y. Kitaoka, and M. Kato, Appl. Phys. Lett. **62**, 2599 (1993).
2. T. Yokogawa, S. Yoshii, A. Tsujimura, *et al.*, Jpn. J. Appl. Phys. **34**, L751 (1995).
3. S. Nakamura, M. Senoh, S. Nagahama, *et al.*, Jpn. J. Appl. Phys. **35**, L74 (1996).
4. D. Vakhshoori, R. J. Fischer, M. Hong, *et al.*, Appl. Phys. Lett. **59**, 896 (1991).
5. N. Yamada, Y. Kaneko, S. Nakagawa, *et al.*, Appl. Phys. Lett. **68**, 1895 (1996).
6. Y. Kaneko, S. Nakagawa, Y. Ichimura, and N. Yamada, J. Appl. Phys. **87**, 1597 (2000).
7. P. A. Ramos and E. Towe, Appl. Phys. Lett. **69**, 3321 (1996).
8. I. A. Avrutskiĭ, L. M. Batukova, E. M. Dianov, *et al.*, Kvantovaya Élektron. (Moscow) **21**, 921 (1994).
9. J. S. Blakemore, J. Appl. Phys. **53**, 123 (1982).

Translated by A. Sidorova

Semiconductors, Vol. 38, No. 3, 2004, pp. 355–359. Translated from Fizika i Tekhnika Poluprovodnikov, Vol. 38, No. 3, 2004, pp. 369–373.

PHYSICS OF SEMICONDUCTOR DEVICES

GaAs/Ge Heterostructure Photovoltaic Cells Fabricated by a Combination of MOCVD and Zinc Diffusion Techniques

V. M. Andreev, V. P. Khvostikov*, N. A. Kalyuzhnyĭ, S. S. Titkov, O. A. Khvostikova, and M. Z. Shvarts

Ioffe Physicotechnical Institute, Russian Academy of Sciences, St. Petersburg, 194021 Russia

**e-mail: vlkhv@scell.ioffe.ru*

Submitted July 7, 2003; accepted for publication July 9, 2003

Abstract—Ge photovoltaic cells based on GaAs/Ge heterostructures have been produced by a combination of metal-organic chemical-vapor deposition and Zn diffusion from the gas phase. The cells are characterized by increased photocurrent and open-circuit voltage. The calculated efficiency of a Ge solar cell under concentrated sunlight exceeds 5.5%. The photocurrent achieved in a Ge photovoltaic cell is close to that obtained in GaAs solar cells under similar conditions of illumination with air-mass-zero (*AM*0) sunlight, which enables one to design high-efficiency concentrator-type cascade solar cells with a GaAs top cell and a Ge bottom cell. © *2004 MAIK "Nauka/Interperiodica".*

1. INTRODUCTION

Recently, there has been a considerable growth in interest in the crystallization of GaAs on Ge substrates using metal-organic chemical-vapor deposition (MOCVD) in order to produce cascade solar cells.

In a GaAs/Ge-based cascade solar cell, the short-wavelength portion of the solar spectrum with a photon energy of $h\nu > E_g$(GaAs) is absorbed in the top cell. The unabsorbed light with $h\nu < E_g$(GaAs) passes to the bottom cell and at $h\nu > E_g$(Ge) is absorbed near the second (bottom) *p*–*n* junction in Ge. Thus, owing to utilization of the IR spectral range, a tandem cell makes it possible to raise the efficiency of solar energy conversion compared to a single-junction GaAs cell. It is especially important that the photocurrent achieved in the Ge cell of this monolithic cascade cell is not lower than that in the GaAs cell, since these cells are connected in series.

Structure polarities of two types are possible for GaAs/Ge heterostructure solar cells grown on an *n*- or *p*-type substrate. In this case, Ge can be "active" or "passive." In the latter case, no *p*–*n* junction is formed in Ge, and Ge does not contribute to the efficiency of the cell. This approach was used in several studies [1, 2].

More important is the situation with "active" Ge used as a bottom cell in tandem. In the 1990s, a monolithic GaAs/Ge tandem cell was presented [3, 4] in which the junction in Ge was produced by Ga diffusion into an *n*-Ge substrate during MOCVD epitaxial growth. The "contribution" made by the Ge cell to the conversion efficiency was $\eta = 1.5$–1.7%, with the open-circuit voltage $U_{oc} = 0.16$ V and the short-circuit current $J_{sc} = 21.9$ mA/cm^2 in the wavelength range 800–1800 nm under *AM*0 illumination. Later, fabrication of tandem (GaAs/Ge) and triple-junction (GaInP/GaAs/Ge) solar cells on *n*-Ge was reported [5–8]. Despite significant improvements in cascade solar cells as a whole and its bottom Ge element in particular ($U_{oc} = 0.22$–0.24 V, $\eta = 2.5$–3%, $J_{sc} = 23.6$ mA/cm^2), the potentiality of Ge has not yet been completely realized. First of all, this is related to difficulties in the stabilization of parameters of the *p*–*n* junction formed in Ge by the diffusion of Ga and As from the gas phase in the MOCVD process. For example, the open-circuit voltage and the depth at which the *p*–*n* junction lies are strongly dependent on the initial growth temperature. Thus, intentional diffusion of acceptors, e.g., Zn atoms, into a *n*-Ge substrate seems to be a more reliable method of forming *p*–*n* junctions. This type of diffusion provides a fairly deep *p*–*n* junction in Ge and suppresses the parasitic junction formed by Ga diffusion.

In this study, the diffusion of Zn into Ge from the gas phase was performed either prior to epitaxial growth of GaAs or after it, across the MOCVD-grown GaAs layer.

2. MOCVD GROWTH OF GaAs LAYERS ON Ge

The close lattice constants of Ge and GaAs create prerequisites for the fabrication of epitaxial layers with low dislocation density. However, the growth of a polar crystal (GaAs) on a nonpolar one (Ge) can give rise to the formation of out-of-phase dislocations. Since the zinc-blende symmetry of GaAs is lower than the symmetry of the diamond structure of Ge, growing GaAs on a (100) Ge substrate yields two orientations, (100*A*) and (100*B*), in which the lattices of the epitaxial layer and substrate are parallel. This may lead to domain-type growth of GaAs on Ge, with out-of-phase boundaries (involving Ga–Ga and As–As bonds), which are centers of nonradiative recombination and channels of current

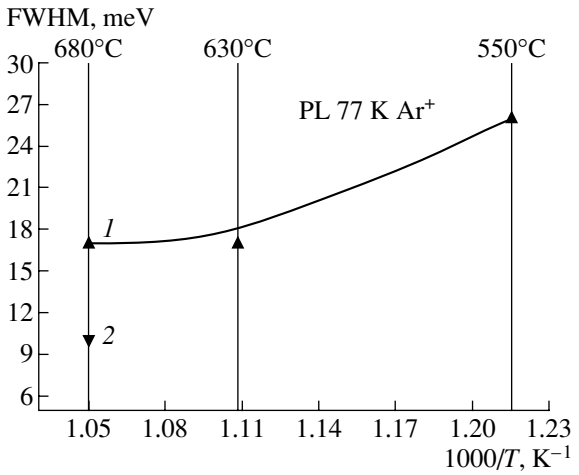

Fig. 1. Half-widths of PL spectra of (*1*) GaAs layers grown on Ge by MOCVD at different temperatures and (2) GaAs layers grown on GaAs at 680°C.

leakage in *p–n* junctions. Thus, one of the requirements for MOCVD growth of GaAs on Ge is to create conditions for single-domain growth or growth with the formation of domains whose size is much greater than that of the device. The conditions of MOCVD that provide single-domain growth of a polar crystal on a nonpolar one were analyzed in [9]. It was found that the density of out-of-phase domains decreases with increasing pressure and growth temperature in the reaction chamber, as well as with decreasing growth rate. Furthermore, it was noticed that the density of out-of-phase domains decreases with decreasing width of atomic steps formed on the (100) surface of the Ge substrate owing to its slight misorientation in the (110) direction; in other words, the probability of single-phase growth increased as the substrate misorientation angle increased. On this basis, we chose growth parameters that ensured a decrease in the density of out-of-phase domains: Ge substrates misoriented by 6° from (100) were used, and the pressure in the growth chamber was 760 Torr.

As mentioned above, another important issue in the growth of GaAs on Ge is the doping of Ge with As and Ga atoms from the growing GaAs layer. According to published data [10], the depth of As diffusion into Ge is several micrometers, and that of Ga into Ge is several tenths of a micrometer. Since the diffusion rate of As and Ga decreases as the growth temperature increases, the temperature of GaAs growth in this study was lowered in steps from 680 to 550°C, which reduced the coefficient of diffusion from the growing layer by nearly two orders of magnitude [11].

3. EXPERIMENTAL RESULTS

The wide-gap GaAs layer for a GaAs/Ge heterostructure was grown by MOCVD in an installation with a horizontal reactor under atmospheric pressure. *n*-Ge doped with As served as substrates. The Ga and As precursors were, respectively, trimethylgallium (TMG) and arsine (AsH_4). In the temperature range used (680–550°C), the growth rate is determined by the diffusion of the Group III element (Ga) in the gas phase to the growth surface, and it is temperature-independent [12].

Figure 1 shows the temperature dependence of the half-width of the photoluminescence (PL) peaks for GaAs layers grown on Ge substrates at different temperatures and on a GaAs substrate at a growth temperature of T_{gr} = 680°C and growth rate of ~1μm/h. As can be seen in this dependence, the half-widths of PL peaks for GaAs layers grown on Ge substrates at 680 and 630°C virtually coincide, although they are nearly twice the half-width of PL peaks for similar layers on GaAs substrates. As the growth temperature decreased from 680 to 550°C, the PL intensity decreased by nearly two orders of magnitude, but the surface morphology of the structure changed only slightly; i.e., the lowering of the growth temperature of GaAs layers on Ge should not lead to any significant increase in the recombination rate at the heterointerface nor to a decrease in the coefficient of the minority carrier collection in a photocell. The key factor is that GaAs is not the photosensitive layer in the GaAs/Ge photocell structure, its function being to lower the recombination rate on the GaAs/Ge heterointerface.

In order to obtain photovoltaic cells on *n*-Ge substrates, we studied the following technologies for the fabrication of photosensitive structures (see table).

*N*1. Planar diffusion of Zn from the gas phase into a Ge substrate with subsequent growth of a wide-gap window layer (GaAs), additional Zn diffusion for the doping of this layer, and deposition of a dielectric coating to reduce current leakage.

*N*2. Deposition of a Si_3N_4 dielectric coating, opening of windows in the insulator in the areas meant for the conversion of light, selective diffusion of Zn, selective crystallization of a GaAs layer, and additional Zn diffusion for the doping of this layer.

*N*3. Growth of a planar GaAs layer on the surface of a Ge substrate, deposition of Si_3N_4 dielectric coating, opening of windows in the insulator, and selective diffusion of Zn.

*N*4. Deposition of dielectric coating, opening of windows in the insulator in the areas meant for the conversion of light, selective growing of a GaAs layer, and selective diffusion of Zn in the same areas.

The first method can be used in the fabrication of a cascade solar cell in a single technological process. In this case, the diffusion of Zn into Ge can be performed in a MOCVD reactor with subsequent overgrowth with the second wide-gap GaAs cell for a multijunction solar cell. In other methods, the dielectric coating prevents the diffusion *p–n* junction from extending to the lateral surface of a photovoltaic cell. A similar approach was applied in the fabrication of GaSb-based thermophotovoltaic cells [13].

Technological procedures for fabrication of *p*-GaAs/*p*-Ge/*n*-Ge structures

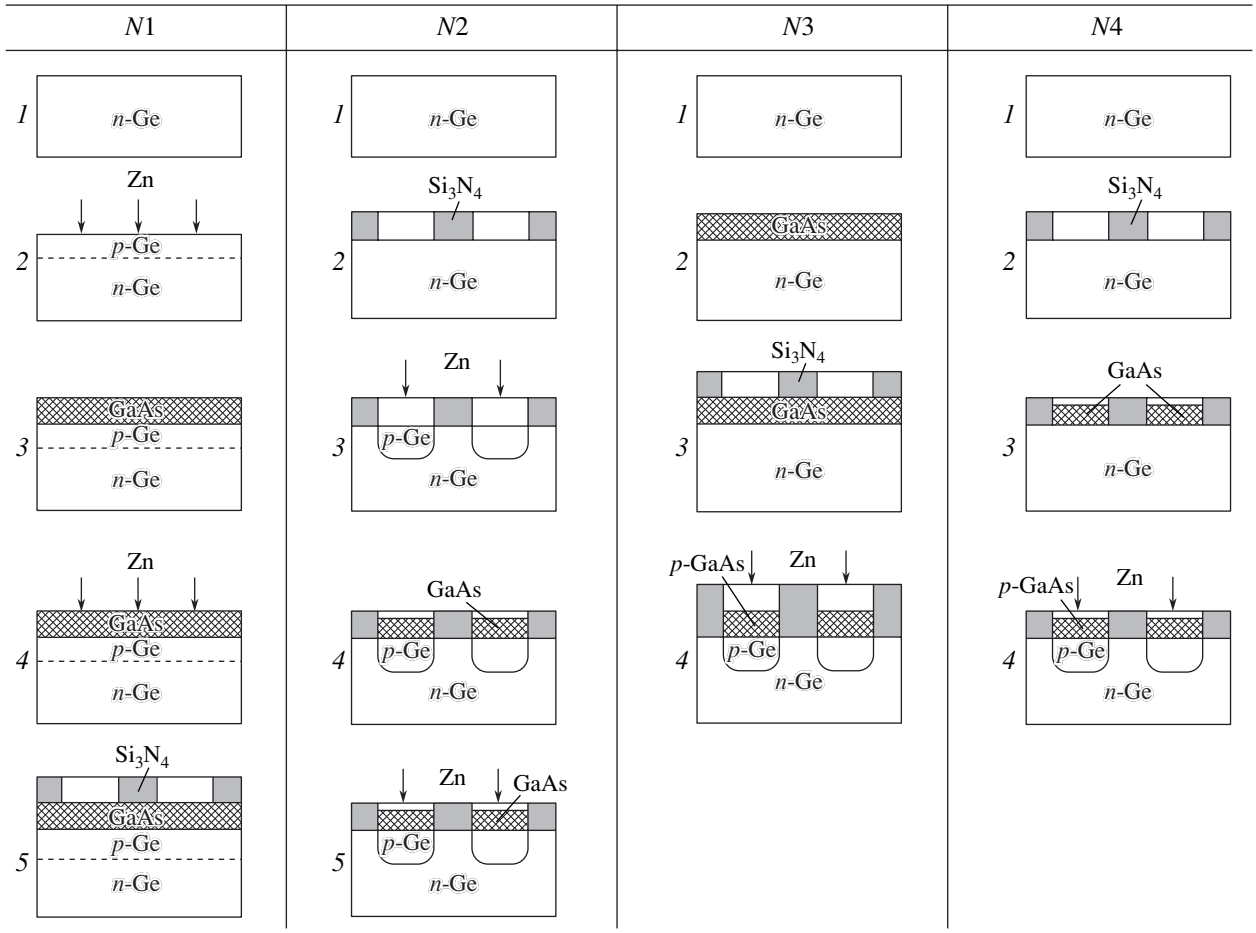

Preepitaxial gas diffusion of Zn into Ge was performed at 670–680°C [14]. At higher temperatures, deposition of Zn onto the Ge surface was observed. In the case of diffusion into Ge across a thin (0.1 μm) GaAs layer, the diffusion temperature was lowered to 620°C, and in the case of additional Zn diffusion to obtain heavy doping of the surface GaAs layer, the diffusion temperature was 550°C. The diffusion of Zn was performed in saturated Zn vapor in an atmosphere of hydrogen purified with a Pd filter, in a graphite boat placed in a quartz reactor.

Figure 2 shows spectra of a GaAs/Ge heterostructure solar cell fabricated by scheme *N*1, with the GaAs layer crystallized at a temperature of 590°C. The rather high internal quantum yield (0.8–0.9) in the wavelength range 900–1500 nm indicates the high quality of the GaAs/Ge heterointerface and the optimal doping profile in the *p*-emitter of the cell based on this heterostructure. The maximum photocurrent density of 28.9 mA/cm^2 (at T_{gr} of GaAs equal to 550, 590°C), calculated from the spectral dependence of the internal quantum yield for the extra-atmospheric sunlight spectrum *AM*0 in the wavelength range 900–1820 nm, is comparable with the photocurrent density obtained in GaAs photocells (λ = 400–900 nm), measured under the same conditions. An obvious advantage of this method is that it can be used in the growing of a GaAs/Ge structure in a single MOCVD process, because it does not include an intermediate stage of deposition of dielectric coating.

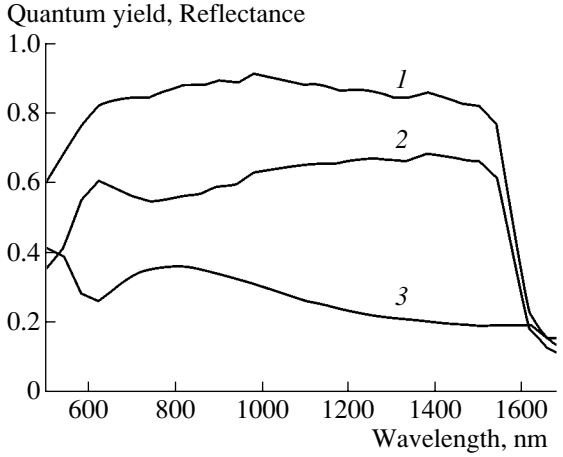

Fig. 2. Spectra of (*1*) internal and (*2*) external quantum yield and (*3*) reflectance of a photovoltaic cell based on a *p*-GaAs/*p*-Ge/*n*-Ge heterostructure.

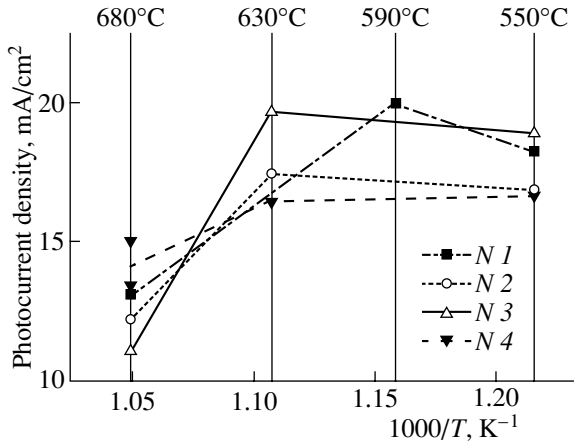

Fig. 3. Photocurrent density in the range 900–1820 nm under *AM*0 sunlight illumination vs. GaAs growth temperature for *p*-GaAs/*p*-Ge/*n*-Ge heterostructure cells without antireflection coating, fabricated using technological procedures listed in the table.

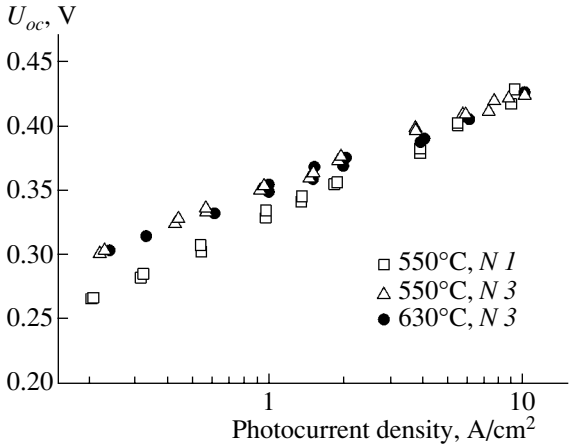

Fig. 4. Open-circuit voltage vs. photocurrent density for GaAs/Ge photocells grown by MOCVD at temperatures of 630 and 550°C.

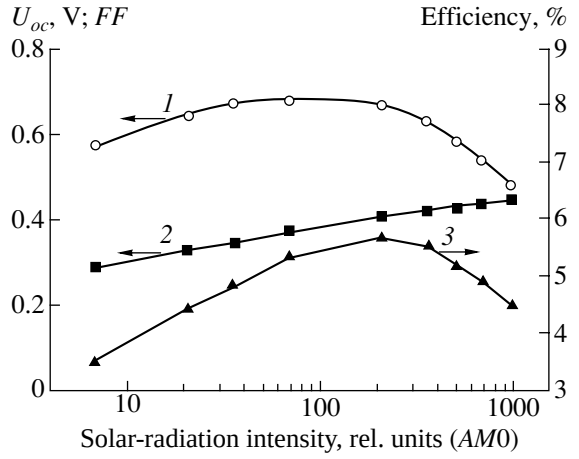

Fig. 5. (*1*) Fill factor of the current–voltage characteristic, (*2*) open-circuit voltage, and (*3*) calculated efficiency of concentrator solar cells vs. the sun concentration (illumination through a GaAs filter, *AM*0 sunlight spectrum).

Based on the measured spectral characteristics of the photocells, we calculated photocurrent density (Fig. 3) for all the four technological procedures, with the growth temperature of the wide-gap GaAs window varying from 680 to 550°C. It can be seen from these dependences that, when the optical losses are taken into account, the photocurrent density in the cells changes from 12–15 to 17–20 mA/cm^2 as the growth temperature is decreased from 680 to 590°C. The maximum open-circuit voltage U_{oc} = 0.26 V at these photocurrent densities was obtained in the cells fabricated using scheme *N*3 at growth temperatures of 630 and 550°C.

One should note that photocells with a high photocurrent density (J_{max} = 28.9 mA/cm^2, calculated from the internal quantum yield) were also grown using technological scheme *N*3 (at T_{gr} of GaAs equal to 630, 550°C). Thus, this approach is also promising for the fabrication of high-efficiency photovoltaic cells. The advantages of the *N*3 method—comparatively high photocurrent density and open-circuit voltage—can be explained by the planar growth of the wide-gap GaAs window with the most uniform morphology of the growing layer and by the selective diffusion of Zn, as a result of which the *p*–*n* junction does not extend to the surface of the photovoltaic cell.

Figure 4 shows the open-circuit voltage as a function of photocurrent density for concentrator solar cells fabricated on the basis of GaAs/Ge heterostructure by schemes *N*1 and *N*3 at different temperatures. As can be seen in the figure, the open-circuit voltage U_{oc} increases linearly with increasing photocurrent density to become 0.42–0.43 V at a photocurrent density of 10 A/cm^2. As far as we know, this is the maximum open-circuit voltage for a GaAs/Ge heterostructure measured under the conditions of this kind.

Figure 5 shows how the fill factor *FF* of the current–voltage characteristic, U_{oc}, and the cell efficiency behave as the sunlight concentration increases. The efficiency calculated for a photocurrent density of 28.9 mA/cm^2 reaches its maximum of 5.5–5.7% at a 200-fold sunlight concentration.

Thus, our study showed that the combination of MOCVD with the diffusion of Zn from the gas phase makes it possible to fabricate Ge photocells based on a GaAs/Ge heterostructure that are characterized by increased photocurrent and open-circuit voltage. The calculated efficiency of a Ge cell exceeds 5.5%, which is nearly twice the value reported earlier for concentrator Ge cells under solar irradiation in space. The photocurrents obtained in a Ge cell are close to those obtained in GaAs solar cells under the same *AM*0 conditions, which enables one to fabricate high-efficiency cascade solar cells with a top GaAs and a bottom Ge cell.

ACKNOWLEDGMENTS

GaAs layers were grown by MOCVD at the Center of Nanoheterostructure Physics, Ioffe Physicotechnical Institute, Russian Academy of Sciences.

The authors are grateful to B.V. Pushnyĭ and V.M. Lantratov for assistance in the experiment and valuable discussions, N.Kh. Timoshina and P.A. Blazhnov for the spectral measurements, and Zh.I. Alferov for support and attention.

This study was supported by the Russian Foundation for Basic Research.

REFERENCES

1. K. Takahashi, S. Yamada, T. Unno, and S. Kuma, in *Technical Digest of 9th International Photovolt Scientific and Engineering Conference* (Japan, 1996), p. 531.
2. C. Hardingham, S. J. Taylor, S. P. Wood, *et al.*, in *Proceedings of 2nd World Conference on Photovoltaic Science and Engineering* (Vienna, 1998), p. 3765.
3. S. J. Wojtczuk, S. P. Tobin, C. J. Keavney, *et al.*, IEEE Trans. Electron Devices **37**, 455 (1990).
4. S. J. Wojtczuk, S. P. Tobin, M. M. Sanfacon, *et al.*, in *Proceedings of 22nd IEEE Photovoltaic Special Conference* (Las Vegas, 1991), p. 73.
5. N. H. Karam, R. P. King, B. T. Cavicchi, *et al.*, IEEE Trans. Electron Devices **46**, 2116 (1999).
6. H. L. Cotal, D. R. Lilington, J. H. Ermer, *et al.*, in *Proceedings of 28th IEEE Photovoltaic Special Conference* (Alaska, 2000), p. 955.
7. D. J. Friedman, J. M. Olson, J. S. Ward, *et al.*, in *Proceedings of 28th IEEE Photovoltaic Special Conference* (Alaska, 2000), p. 965.
8. D. J. Friedman and J. M. Olson, Prog. Photovolt.: Res. Appl. **9**, 179 (2001).
9. Y. Li, M. G. Bongers, L. J. Giling, *et al.*, J. Cryst. Growth **163**, 195 (1996).
10. S. P. Tobin, S. M. Vernon, C. Bajgar, *et al.*, IEEE Electron Device Lett. **9**, 405 (1988).
11. B. E. Samorukov, *Properties of Semiconductors* (S.-Peterb. Gos. Tekh. Univ., St. Petersburg, 1992).
12. M. Razegi, *The MOCVD Challenge*, Ed. by A. Hilger (Inst. of Physics, Bristol, 1989), Vol. 2, p. 179.
13. V. M. Andreev, V. P. Khvostikov, O. A. Khvostikova, *et al.*, in *Proceedings of 17th European Photovoltaic Solar Energy Conference* (Munich, 2001), p. 219.
14. V. P. Khvostikov, V. D. Rumyantsev, O. A. Khvostikova, *et al.*, in *Proceedings of 5th ISTC SAC Seminar: Nanotechnologies in the Area of Physics, Chemistry, and Biotechnology* (St. Petersburg, 2002), p. 387.

Translated by D. Mashovets

Semiconductors, Vol. 38, No. 3, 2004, pp. 360–367. Translated from Fizika i Tekhnika Poluprovodnikov, Vol. 38, No. 3, 2004, pp. 374–381.

PHYSICS OF SEMICONDUCTOR DEVICES

Internal Optical Loss in Semiconductor Lasers

N. A. Pikhtin*, S. O. Slipchenko, Z. N. Sokolova, and I. S. Tarasov

Ioffe Physicotechnical Institute, Russian Academy of Sciences, St. Petersburg, 194021 Russia

**e-mail: nike@hpld.ioffe.ru*

Submitted July 21, 2003; accepted for publication July 22, 2003

Abstract—Internal optical loss in high-power semiconductor lasers based on quantum-well separate-confinement heterostructures was studied. Calculations show that the major portion of the internal optical loss occurs in the active region and emitters. Making the laser waveguide thicker and the cavity longer reduces the internal optical loss. Two possible approaches to the design of laser heterostructures are considered, and optimal solutions are suggested. The difference in the internal optical loss between lasers on InP and those on GaAs substrates is attributed to the larger cross section of photon absorption by holes in InP. Good agreement between the calculated and experimental values of the internal optical loss in lasers on InP and GaAs substrates is obtained. © *2004 MAIK "Nauka/Interperiodica".*

1. INTRODUCTION

Semiconductor heterolasers emit light in the spectral range from the visible to the far-infrared. These lasers are used in fiber optic communication, information recording and reading systems, duplication technology, material processing, pumping of solid-state and fiber amplifiers, medicine, ecology, spectroscopy, and so on. In a variety of applications, heterolasers must have a high emission power. Raising the power of coherent emission is associated with the development of lasers with a high quantum efficiency of stimulated emission [1–3], low temperature sensitivity [2, 4, 5], maximum accessible driving current [3, 6, 7], and finally, high differential quantum efficiency [3, 6, 7]. These lasers can be produced only on the basis of heterostructures with low internal optical loss [1, 7–9]; thus the minimization of the internal optical loss is a critical condition in the design of high-power semiconductor lasers. Quantum-well separate-confinement double heterostructures (SC DHS) have proved to be most promising for this task [1, 2, 6, 7]. However, the advantages of these heterostructures show their worth only in lasers with a long cavity, i.e., with low external optical loss [8, 10, 11]. The reduction of length of SC DHS laser diodes causes an increase in the external optical loss and a rise in the threshold current density [8, 10, 11]. The reduction of internal optical loss with simultaneous reduction of the output loss (increasing the cavity length) results in the retention of a high differential quantum efficiency and raises the maximum accessible driving current, which is necessary for the fabrication of high-power semiconductor lasers [1–7].

In this paper, we analyze internal optical loss in separate-confinement laser heterostructures on GaAs and InP substrates (the emission wavelength $\lambda \approx 1$ μm and $\lambda \approx 1.58$ μm, respectively). The dependences of optical loss on the configuration and structural parameters of laser diodes, in particular, on the cavity length and the thickness of the waveguide layer, are studied.

2. BASIC DEFINITIONS

Total optical loss, α, in a semiconductor laser includes two principal terms:

$$\alpha = \alpha_{ext} + \alpha_{int}. \quad (1)$$

The external ("useful") optical loss is $\alpha_{ext} = (1/L)\ln(1/R)$, where $R = 0.3$ is the reflectivity of naturally cleaved mirrors of the laser cavity and L is the cavity length.

The internal optical loss, α_{int}, is a combination of losses related to the free-carrier absorption in different layers of a heterostructure:

$$\alpha_{int} = \sum \alpha_i, \quad \alpha_i = \Gamma_i \alpha_i^l, \quad (2)$$

where α_i^l is the internal optical loss coefficient for a single layer of a laser heterostructure and Γ_i is the optical confinement factor (fraction of the electromagnetic emission) in a layer of a laser heterostructure (Γ_{QW}, in the active region; Γ_w, in the waveguide; and Γ_{cl}, in the emitters).

The free-carrier absorption of light causes electron and hole transitions within a single band, and it increases as the free-carrier density and the wavelength of the absorbed light increases. In view of the law of conservation of momentum, transitions within a single band are possible only with interaction with a third particle (phonon or impurity). The type of particles participating in the momentum scattering defines the exponent K in the dependence of the free-carrier absorption coefficient on the emission wavelength: $\alpha_i \propto \lambda^K$ [12]. For the case of momentum scattering by the acoustic deformation potential, $K = 1.5$; for scattering by polar

optical phonons, $K = 2.5$; and for scattering by ionized impurities, $K = 3.5$ [12]. Therefore, the free-carrier absorption should be stronger in long-wavelength lasers with heavily doped epitaxial layers.

In lightly doped semiconductors (with momentum scattering by phonons prevailing), the coefficient of absorption by free carriers depends linearly on their density, and in heavily doped ones, quadratically [13]. In lightly doped semiconductors, the optical loss coefficient is expressed by [14]

$$\alpha_i^l = \sigma_n n + \sigma_p p, \quad (3)$$

where n, p are the 3D-densities of electrons and holes and σ_n, σ_p, the free-electron and free-hole absorption cross sections, which are defined experimentally. In the calculations of the absorption coefficient in GaAs at room temperature for photon energies in the vicinity of the GaAs energy gap [14], the values $\sigma_n = 3 \times 10^{-18}$ cm^2 and $\sigma_p = 7 \times 10^{-18}$ cm^2 were used. Experimental dependences of the free-carrier absorption coefficient in *p*-InP and *n*-InP as functions of the wavelength for different carrier densities at room temperature are presented in [15]. It is worth noting that a sharp minimum in this dependence is observed in *n*-InP at a emission wavelength of 1.6 μm [15]. The free-hole absorption is several tens of times stronger than that by free electrons, which is related to the larger absorption cross section σ_p. In *p*-InP, at a wavelength of 1.5 μm, $\sigma_p = 20 \times 10^{-18}$ cm^2 [15]. The free-carrier absorption cross sections in InGaAs (bandgap $E_g = 1.214$ eV) and InGaAsP ($E_g = 1.458$ eV) solid solutions at a wavelength of 0.98 μm are given in [16]: $\sigma_p = 14 \times 10^{-18}$ cm^2 and $\sigma_n = 6 \times 10^{-18}$ cm^2. The values of σ_n and σ_p from [14–16] are used in further calculations.

According to (3), the coefficient α_i^l depends on the density of electrons and holes; thus, to minimize optical loss, it is necessary to minimize the carrier density in different layers of a laser heterostructure, especially in *p*-regions. Therefore, the active region and waveguide layers are not doped intentionally. In order to inject carriers into the active region, we are forced to heavily dope the emitter layers. The density of injected carriers in the active region cannot be greatly reduced, because it is determined by the gain that is necessary to reach the lasing threshold; in other words, it is the threshold density. In separate-confinement lasers with a long cavity, the principal part of the threshold density is the transparency carrier density of the material, n_0, at which the gain is zero; i.e., the medium neither absorbs nor amplifies [17]. The value of n_0 depends on the properties of the material of the active region, the type of the laser heterostructure (double heterostructure, quantum-well separate-confinement heterostructure, or heterostructure with quantum dots), and the technological perfection of the epitaxial method used. In this study, we do not discuss the possibility of reducing n_0.

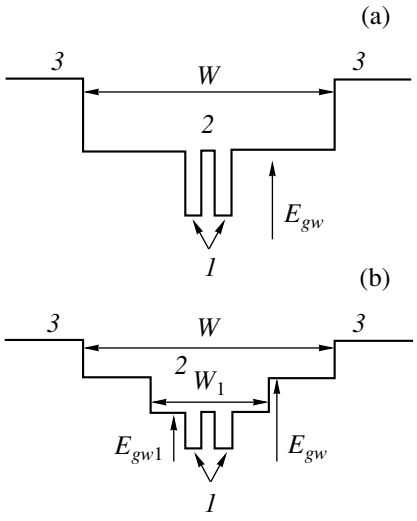

Fig. 1. Band diagrams of SC DHS lasers: (a) with an extended waveguide and (b) with an extended step-like waveguide. (*1*) Active region, (*2*) waveguide layers, (*3*) *p*- and *n*-emitters. (W, W_1) and (E_{gw1}, E_{gw}) are the waveguide thicknesses and band gaps, respectively.

3. OPTICAL CONFINEMENT FACTOR

In all the experiments concerning the development of high-power semiconductor lasers, we have used quantum-well separate-confinement heterostructures optimized for efficient lasing at the prescribed wavelength in a particular system of semiconductor solid solutions [1, 4, 7, 18]. The possibility of increasing the power of the laser optical emission is related to the reduction of the internal optical loss in epitaxial layers and, consequently, to the optimal distribution of the electromagnetic radiation within the layers. In the fabrication of SC DHSs, the most readily variable parameters are the thickness W and the composition of the waveguide layer (energy gap, E_{gw}). Below we present the calculated dependences of the optical confinement factor as functions of these parameters for three types of SC DHS lasers.

At first, the calculations were done for a model structure on an InP substrate (Fig. 1a). The structure comprised two 60-Å-thick strained quantum wells (QW) located at a distance of 120 Å from each other and emitting at a wavelength of 1.55 μm. The calculations were done for three compositions of the solid solution in the waveguide layer, InGaAs with $E_{gw} = 1.1$, 1.2, and 1.3 eV, for a layer thickness W in the range 0.1–2 μm (Fig. 2a, 2b). Evidently, in order to improve the laser performance parameters (to reduce the threshold current and raise the output power), it is necessary to raise the fraction of the electromagnetic emission (Γ-factor) in the active region and to reduce it in the emitters. The optimal thickness for narrow-gap waveguides ($E_{gw} \approx 1.1$ eV) is $W \approx 0.6$–0.7 μm, at which the Γ-factor in the active region, Γ_{QW}, is close to its

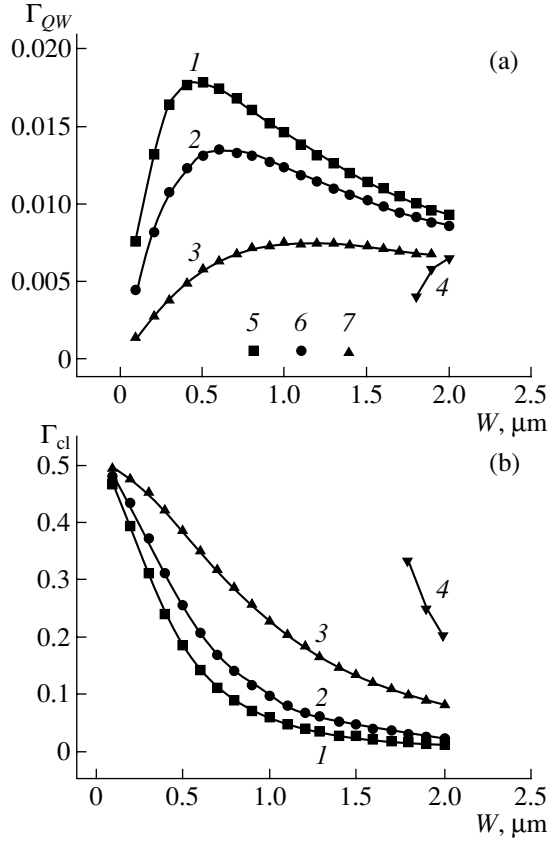

Fig. 2. Optical-confinement factors for (a) the active region, Γ_{QW}, and (b) a single emitter, Γ_{cl}, for even modes: (*1*–*3*) zeroth and (*4*) second, vs. the thickness of an InGaAsP waveguide, *W*, for three InGaAsP/InP SC DHSs (λ = 1.55 μm). Band gap of the solid solutions: (*1*, *4*, *5*) 1.1, (*2*, *6*) 1.2, and (*3*, *7*) 1.3 eV. Points *5*–*7* on the abscissa axis mark the waveguide thickness at which the first odd mode appears.

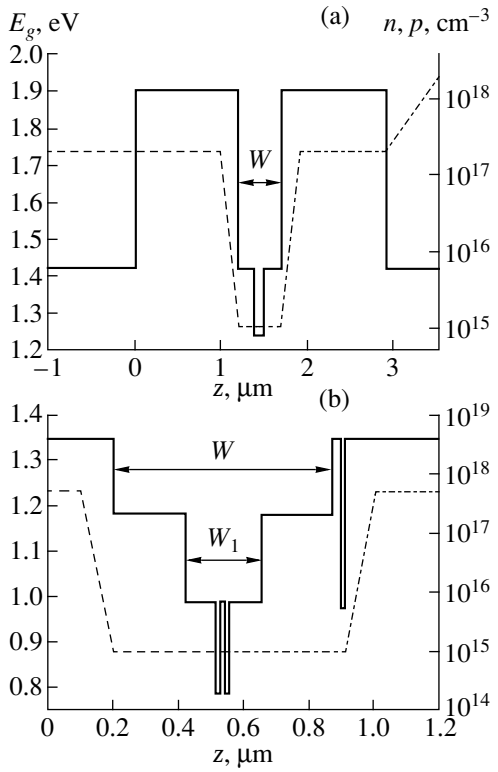

Fig. 3. Band diagrams of SC DHSs: (a) InGaP/GaAs/InGaAs (structure X-2582, λ = 1 μm); (b) InGaAs/InP (structure KP-1168, λ = 1.58 μm). Calculated doping profiles for: (dashed line) Si donor impurity; (dot–dash line) acceptor impurities: (a) Mg and (b) Zn. *z* is the structure growth coordinate.

maximum value (1.75%), and the Γ-factor of the emitter layer, Γ_{cl}, decreases to 10%. However, in this heterostructure electrons are emitted from QWs into the waveguide, which raises the threshold density of carriers and enhances the temperature sensitivity of laser diodes [1, 19, 20]. To reduce the emission of electrons from QWs, it is necessary to use a waveguide with wider energy gap, $E_{gw} \approx 1.2$ eV, and to reduce the "leak" of the waveguide mode to emitters; the waveguide thickness should exceed 1 μm. At the same time, the increase in the waveguide thickness reduces Γ_{QW} (Fig. 2a) and enhances the current leakage into the *p*-emitter [11, 20], which depresses the quantum efficiency of stimulated emission [3].

Our calculations have shown that no one single solution exists for the problem of optimal (in respect to Γ-factors) model heterostructures (Fig. 1). Therefore, the optimization must be performed for each particular laser heterostructure. Below we discuss two experimental structures [1, 7, 17, 18].

Structure X-2582 (Fig. 3a) was grown on a GaAs substrate, its waveguide layer consisted of undoped 0.52-μm-thick GaAs, and its configuration was similar to that of the first optimal model structure. The active region of structure X-2582 was a single strained QW of $In_xGa_{1-x}As$ (x = 20%) solid solution, 90 Å in thickness, emitting at a wavelength of 1 μm. The emitter layers were fabricated from $In_{0.51}Ga_{0.49}P$ solid solution. Optical-confinement factors for similar structures were calculated as functions of the waveguide thickness *W* in the range 0.1–0.7 μm (Figs. 4a, 4b). A limitation on the wavelength thickness appears because of the appearance of a second even (not fundamental) mode at W = 0.8 μm. For the fundamental mode, the optical confinement factor in the QW, Γ_{QW}, reaches its maximum at W = 0.2 μm (Fig. 4a); the optical confinement factor in the *p*-emitter, Γ_{pcl}, decreased as *W* increased (Fig. 4b); thus, the penetration of the field into the heavily doped *p*-emitter decreased.

The configuration of the second experimental laser heterostructure KP-1168 (Fig. 3b), which emitted at a wavelength of 1.58 μm, was similar to the second optimal model structure (Fig. 1b). Structure KP-1168 had a double-step extended waveguide [7, 17], InP emitter layers, and two strained 60-Å-thick QWs of $In_{1-x}Ga_xAs_{1-y}P_y$ solid solution. The step waveguide was comprised of

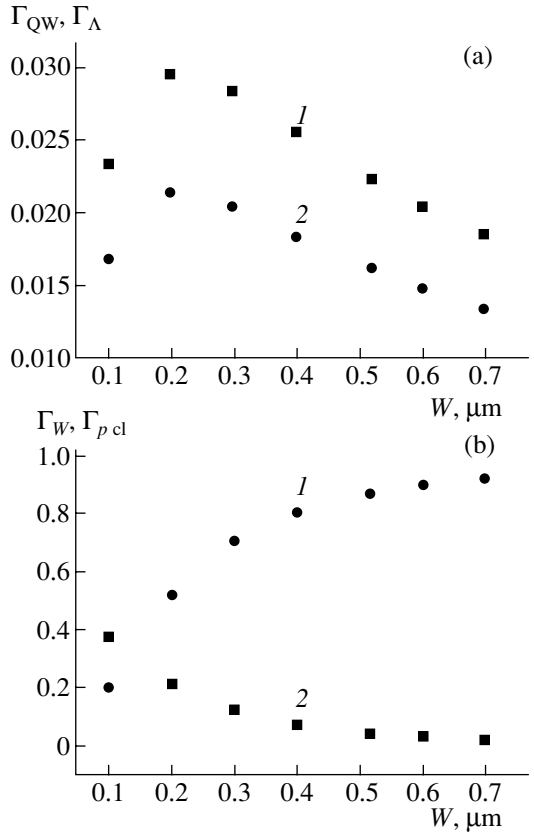

Fig. 4. Optical-confinement factors vs. the thickness of a GaAs waveguide, *W*, in an InGaP/GaAs/InGaAs SC DHS, similar to structure X-2582. (a): (*1*) Γ_{QW} (active region) and (*2*) Γ_Λ (Coulomb potential well). (b): (*1*) Γ_W (waveguide) and (*2*) Γ_{pcl} (*p*-emitter).

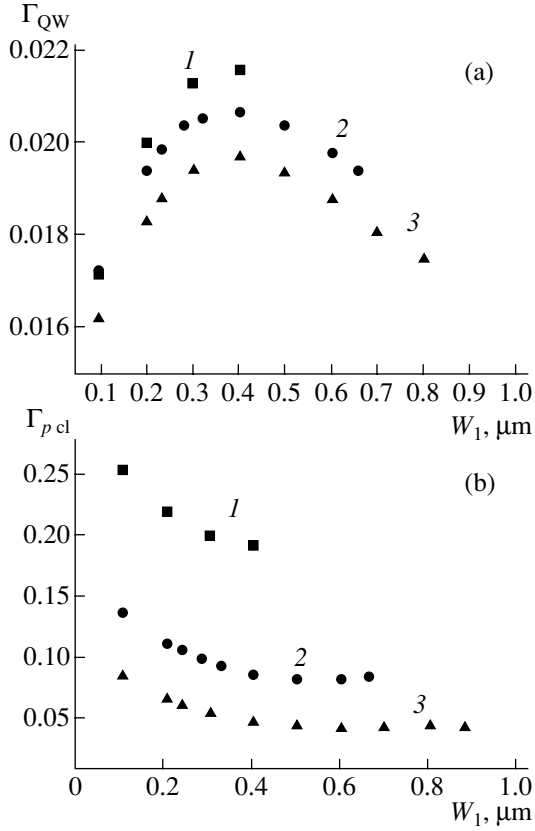

Fig. 5. Optical-confinement factors vs. the thickness of a narrow-gap waveguide, W_1, in a structure similar to KP-1168. (a) Γ_{QW} (active region) and (b) Γ_{pcl} (*p*-emitter). The thickness of the wide-gap waveguide, *W*: (*1*) 0.4, (*2*) 0.672, and (*3*) 0.9 μm.

two layers of InGaAsP solid solution. The thickness of the narrow-gap waveguide layer W_1 = 0.232 μm (energy gap E_{gw1} = 0.992 eV); for the wide-gap layer, W = 0.672 μm (E_{gw} = 1.181 eV). The dependences of the optical-confinement factors of the *p*-emitter and active region as functions of the thickness of the narrow-gap waveguide W_1 were calculated for three values of the wide-gap waveguide thickness (W = 0.4, 0.672, and 0.9 μm). For all the values of *W*, the optical confinement factor as a function of W_1 exhibits a peak at $W_1 \approx$ 0.4 μm and decreases with a further increase in the thickness of the narrow-gap waveguide W_1, as well as the optical confinement factor of the heavily doped region of the *p*-emitter (Figs. 5a, 5b).

The run of the dependences of the optical confinement factor in epitaxial layers of the laser heterostructures used in the experiment coincides with the corresponding dependences calculated for the model laser heterostructure (Fig. 2). The optical confinement factor of the active region, represented as a function of the waveguide thickness, exhibits a maximum and then decreases by a factor of 1.5–2, depending on the refractive indices of the waveguide and emitter layers (Figs. 2a, 4a, 5a). The increase in the waveguide layer thickness reduces the fraction of the electromagnetic radiation in heavily doped emitter layers for all the versions of the separate-confinement laser heterostructures (Figs. 2b, 4b, 5b).

4. FREE-CARRIER DENSITY IN THE LAYERS OF LASER HETEROSTRUCTURES

As mentioned in Section 2, in order to reduce the optical loss it is necessary to minimize the carrier density in different layers of a laser heterostructure. Modern MBE and MOCVD techniques allow the fabrication of layers with a residual level of dopant concentration as low as 10^{13} cm^{-3}. In the structures under study, KP-1168 (λ = 1.58 μm) and X-2582 (λ = 1 μm), the doping level in the waveguide layers was (2–3) × 10^{15} cm^{-3}. In the calculation of the internal optical loss, the carrier density in the waveguide and emitters was assumed to be equal to the calculated doping level.

In structure KP-1168 (Fig. 3b), the concentration of Si dopant in the 0.8-μm-thick *n*-type emitter was 5 × 10^{17} cm^{-3}, and in the *n*-substrate it was 2 × 10^{18} cm^{-3}. In the 1.24-μm-thick *p*-emitter, the concentration of the acceptor Zn impurity increased from 10^{17} to 5 × 10^{17} cm^{-3} at a distance of 0.13 μm from the waveguide.

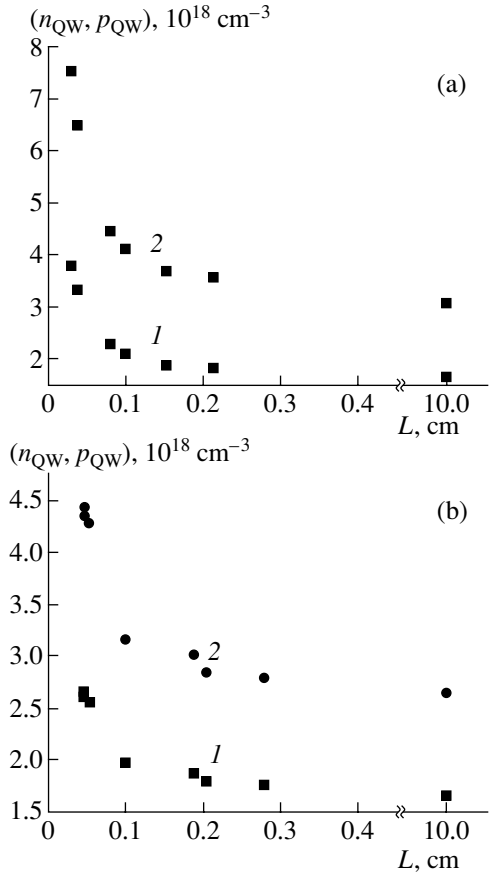

Fig. 6. Density of (*1*) electrons, n_{QW}, and (*2*) holes, p_{QW}, in the active region vs. the cavity length of a laser diode, L. (a) Structure KP-1168 and (b) structure X-2582.

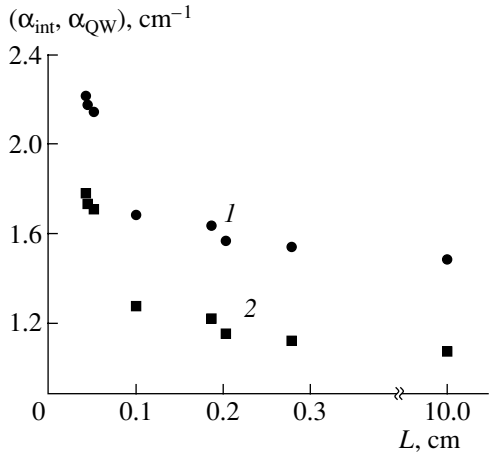

Fig. 7. (*1*) Total internal optical loss, α_{int}, and (*2*) optical loss in the active region, α_{QW}, vs. the cavity length of a laser diode, L. Structure X-2582; waveguide thickness $W = 0.52$ μm.

In undoped QWs of the active region, the free-carrier density equals the threshold density, which is necessary to ensure the stimulated emission in a laser diode. In structure KP-1168, the threshold density of holes appeared to be twice as high as the threshold density of electrons. This is related to the fact that holes in the active region are strongly localized in a deep QW, whereas electrons are weakly localized in a shallow QW (the binding energy of these electrons at room temperature is less than kT). Electrons are emitted into the waveguide, which is confirmed by our experimental data [11, 20].

Owing to the attraction between the electrons emitted into the waveguide and holes that are strongly localized in a deep QW, a Coulomb potential well with characteristic width Λ = 120–140 Å is formed in the waveguide; it confines the electrons emitted into the waveguide to the vicinity of the QW. The ratio between the density of electrons emitted into the waveguide, n_W, and that of electrons in the strained QW, n_{QW}, for structure KP-1168 was determined from the experimental data [17], using the model in [21]. The emission of electrons into the waveguide raised the threshold density of holes in the active region, because, in accordance with the electrical neutrality principle, the density of holes in a QW, p_{QW}, equals the sum of the electron densities in a QW and in the waveguide:

$$p_{QW} = n_{QW} + n_W. \quad (4)$$

Figure 6a shows the calculated densities of electrons and holes in the active region of this structure as functions of the cavity length L of a laser diode.

In the laser structure X-2582 (Fig. 3a), the binding energy of electrons in the QW of the active region was $2kT$. Nevertheless, electrons were emitted into the waveguide, and the threshold density of holes exceeded that of electrons by a factor of about 1.5 (Fig. 6b).

In the *n*-emitter of structure X-2582, the concentration of the Si donor impurity was 2.5×10^{17} cm^{-3}, and the concentration of the Mg acceptor impurity in the *p*-emitter was also 2.5×10^{17} cm^{-3} (Fig. 3a).

5. FREE-CARRIER LOSS

In the calculation of internal optical loss, the choice of absorption cross sections is important, because they may introduce large errors into the calculated data. In the calculations for structure X-2582, we used the following values of the absorption cross sections: $\sigma_n = 6 \times 10^{-18}$ cm^2 and $\sigma_p = 14 \times 10^{-18}$ cm^2 [15]. Figure 7 shows the dependences of total internal optical loss and loss in the active region vs. the cavity length of a laser diode with a fixed waveguide thickness W = 0.52 μm. The loss in the region of the Coulomb potential well was ~0.15 cm^{-1}; in the emitters, ~0.2 cm^{-1}. Despite the fact that the electromagnetic field is concentrated mainly in the waveguide ($\Gamma_W \approx 0.86$), the loss in the waveguide outside the region of the Coulomb potential well was only 0.016 cm^{-1}. The active region makes the main contribution to the optical loss on free carriers. The enhancement of the cavity length of a laser diode

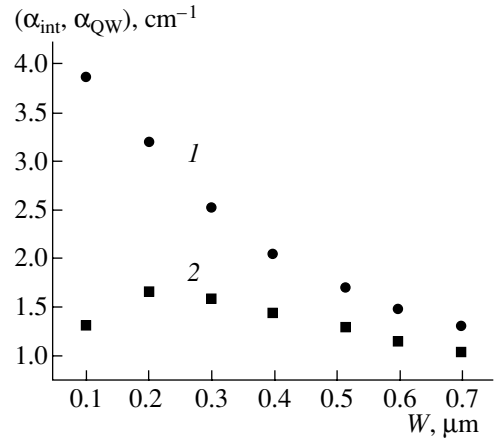

Fig. 8. (*1*) Total internal optical loss, α_{int}, and (*2*) optical loss in the active region, α_{QW}, vs. the waveguide thickness, *W*, in a structure similar to X-2582. Cavity length of a laser diode L = 1 mm.

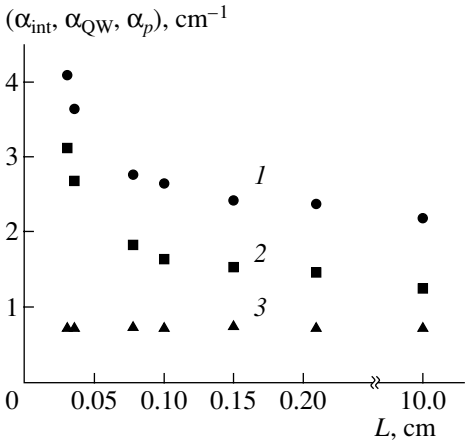

Fig. 9. (*1*) Total internal optical loss, α_{int}, (*2*) optical loss in the active region, α_{QW}, and (*3*) optical loss in the *p*-emitter, α_p, vs. the cavity length of a laser diode, *L*, for structure KP-1168.

reduces the threshold density in the active region and, consequently, the internal optical loss.

In [18], the internal optical loss in heterolasers based on structure X-2582 was determined experimentally; it was 1.3–1.8 cm^{-1}.

To reveal the effect of the waveguide thickness *W* on the total internal optical loss, model SC DHS lasers based on structure X-2582 were studied, with *W* varied from 0.1 to 0.7 μm with fixed cavity length L = 1 mm (Fig. 8). In the calculation, the variation in the threshold density in the active region of structures with different *W* was disregarded; according to our estimates, this assumption is admissible. The total optical loss decreases as the waveguide thickness increases, owing to the reduction of loss in heavily doped emitters.

In the calculation of internal optical loss in the structure with a double-step waveguide (KP-1168), the value $\sigma_p = 20 \times 10^{-18}$ cm^2 was used for the absorption cross section for holes. The cross section for electrons was determined from the experimental dependences presented in [15]. Figure 9 shows the calculated internal optical loss as a function of the cavity length for a laser diode for structure KP-1168 (waveguide thicknesses: W = 0.672 μm, W_1 = 0.232 μm). Regardless of the cavity length, the main contribution to the total optical loss in this structure is made by the loss in the active region. The loss was only 0.045 cm^{-1} in the narrow-gap waveguide outside the region of the Coulomb potential well, 0.1–0.05 cm^{-1} in the region of the Coulomb potential well (for different cavity lengths), 0.105 cm^{-1} in both parts of the wide-gap waveguide, 0.032 cm^{-1} in the *n*-emitter, and 0.214 cm^{-1} in the lightly doped and 0.526 cm^{-1} in the heavily doped part of the *p*-emitter. These values were virtually independent of the cavity length. One should stress that the loss in the active region surpasses the loss in the Coulomb potential well, though the optical-confinement factors are equal for both cases. The density of both types of carriers is high in the active region, whereas in the Coulomb well only the electron density is high. At the same time, the absorption of light by free holes is tens of times stronger than by electrons. Increasing the cavity length of a laser diode reduces the threshold current density and, consequently, the contribution of the internal optical loss related to the absorption in the active region.

One should note the great scatter (between 3.6 cm^{-1} [7] and 9 cm^{-1}) in the experimental values of the internal optical loss, obtained from the dependence of the reciprocal of the external differential quantum efficiency, $1/\eta_d$, on the cavity length L [17]. This is indicative of the existence of optical loss in the structure, which was not considered in calculations. Furthermore, this fact is related to the difficulty of determining the cross section of the free-carrier absorption in InGaAsP solid solutions and, consequently, the inaccuracy of the available values.

To reveal the effect of the thickness of a double-step waveguide on the total internal loss, model SC DHS lasers were investigated. Figure 10 shows the calculated internal optical loss as a function of the thickness of the narrow-gap waveguide, W_1, for three values of the thickness of the wide-gap waveguide, *W*, for the laser cavity length L = 0.77 mm. The variation of the threshold density in the active region of laser diodes was disregarded in the calculations.

The internal optical loss in a step-waveguide laser is significantly reduced when the thickness of the wide-gap waveguide, *W*, increases, and it is only slightly reduced with an increase in the thickness of the narrow-gap waveguide, W_1 (Fig. 10). As *W* increases, the penetration of the electromagnetic wave into the heavily doped region of the *p*-emitter and the loss on free carriers in this region are considerably reduced.

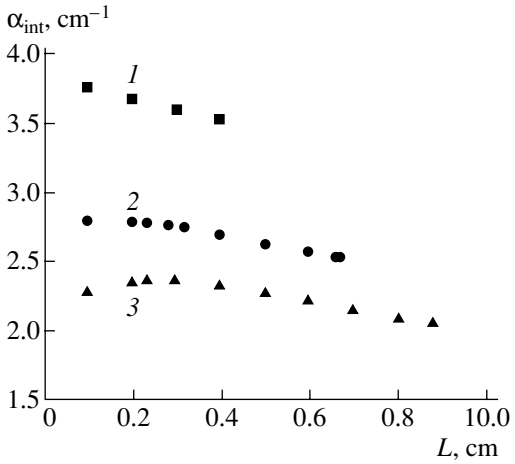

Fig. 10. Total internal optical loss, α_{int}, vs. the thickness of a narrow-gap waveguide, W_1, in a structure similar to KP-1168. Cavity length of a laser diode L = 0.77 mm. Thickness of a wide-gap waveguide, W: (*1*) 0.4, (*2*) 0.672, and (*3*) 0.9 μm.

6. CONCLUSION

Our study has shown that, in quantum-well separate-confinement heterostructures, most of the losses related to the free-carrier absorption occur in the active region and in heavily doped *p*-emitters. To reduce the internal loss in laser heterostructures, especially those on InP substrates, it is necessary to reduce the density of nonequilibrium carriers in the layers, as well as the fraction of the electromagnetic field in heavily doped layers, especially in *p*-emitters.

Two approaches are possible. The first involves an increase in the abrupt change in the refractive index across the interface between the waveguide and emitter, and, therefore, a decrease in the penetration of the electromagnetic field into emitter layers, with the reduction of the optical loss in these layers. In this case, the optical confinement factor in the active region is maximal, which ensures a low threshold density and low internal optical loss in the active region. Coincident with the minimum internal optical loss, the maximum internal quantum efficiency of stimulated emission is provided, because the leakage current from the waveguide to the *p*-emitter is lower in a relatively thin and narrow-gap waveguide [11, 20]. The assortment of semiconductor solid solutions used in the design of laser heterostructures is most commonly limited by the list of starting compounds and the requirement of lattice matching. As a result, given a sufficient change in the refractive index across the interface between the waveguide and the emitter, the depth of the QW in the active region is insufficient for an effective confinement of electrons. The small depth of a QW results in an incomplete collection of injected carriers and raises the temperature sensitivity of the threshold current density.

The second approach to the design of laser heterostructures with low internal loss is to increase the width of the wide-gap waveguide layer, with a small change in the refractive index across the waveguide–emitter interface. In this case, the internal optical loss in the structure is reduced, because the part of the emission entering the emitter layers is reduced. The expansion of the waveguide is limited by the condition that higher order modes appear. To reach the maximum internal quantum efficiency of the stimulated emission, it is necessary to use an expanded step-like waveguide [7].

One should note that the expansion of the waveguide results in a relative increase in the threshold current density, because the optical confinement factor in the active region is reduced. However, the optimization of a quantum-well heterostructure for a high-power semiconductor laser is directed to minimize the total internal optical loss, which decreases as the waveguide thickness increases.

It has been shown that most of the internal optical loss in an optimized quantum-well heterostructure occurs in the active region. Thus, a significant decrease in the threshold current density, e.g., the use of an array of quantum dots in the active region [22, 23], should reduce the internal optical loss and significantly increase the emitted optical power. However, the optimization of a laser structure with quantum dots must also be performed with minimization of the internal optical loss.

ACKNOWLEDGMENTS

The authors are grateful to I.D. Zalevskiĭ, E.G. Golikova, Ya.A. Ryaboshtan, A.A. Marmalyuk, and M.V. Kovalenko for their effective cooperation in the design of laser heterostructures. The authors are grateful to laboratory colleagues A.V. Lyutetski, D.A. Vinokurov, V.A. Kapitonov, A.Yu. Leshko, A.L. Stankevich, N.V. Fetisova, T.A. Nalet, T.N. Drokina, N.F. Kadoshchuk, N.A. Rudova, and V.V. Vasil'ieva for assistance in structure fabrication, sample preparation, and measurements.

This study was supported in part by the Russian Foundation for Basic Research and by the "Technology of Low-Dimensional Objects and Systems" program.

REFERENCES

1. D. A. Livshits, A. Yu. Egorov, I. V. Kochnev, *et al.*, Fiz. Tekh. Poluprovodn. (St. Petersburg) **35**, 380 (2001) [Semiconductors **35**, 365 (2001)].
2. P. V. Bulaev, V. A. Kapitonov, A. V. Lyutetskiĭ, *et al.*, Fiz. Tekh. Poluprovodn. (St. Petersburg) **36**, 1144 (2002) [Semiconductors **36**, 1065 (2002)].
3. G. V. Skrynnikov, G. G. Zegrya, N. A. Pikhtin, *et al.*, Fiz. Tekh. Poluprovodn. (St. Petersburg) **37**, 243 (2003) [Semiconductors **37**, 233 (2003)].
4. E. G. Golikova, V. A. Kureshov, A. Yu. Leshko, *et al.*, Fiz. Tekh. Poluprovodn. (St. Petersburg) **34**, 886 (2000) [Semiconductors **34**, 853 (2000)].

5. S. O. Slipchenko, A. V. Lyutetskiĭ, N. A. Pikhtin, *et al.*, Pis'ma Zh. Tekh. Fiz. **29** (3), 65 (2003) [Tech. Phys. Lett. **29**, 115 (2003)].
6. D. A. Livshits, I. V. Kochnev, V. M. Lantratov, *et al.*, Electron. Lett. **36**, 1848 (2000).
7. E. G. Golikova, V. A. Kureshov, A. Yu. Leshko, *et al.*, Pis'ma Zh. Tekh. Fiz. **26** (10), 40 (2000) [Tech. Phys. Lett. **26**, 913 (2000)].
8. V. P. Evtikhiev, D. Z. Garbuzov, Z. N. Sokolova, *et al.*, Fiz. Tekh. Poluprovodn. (Leningrad) **19**, 1420 (1985) [Sov. Phys. Semicond. **19**, 873 (1985)].
9. M. R. Gokhale, J. C. Dries, P. V. Studenkov, *et al.*, IEEE J. Quantum Electron. **33**, 2266 (1997).
10. D. Z. Garbuzov, S. V. Zaĭtsev, Yu. V. Il'in, *et al.*, Pis'ma Zh. Tekh. Fiz. **16** (5), 50 (1990) [Sov. Tech. Phys. Lett. **16**, 343 (1990)].
11. D. Z. Garbuzov, A. V. Ovchinnikov, N. A. Pikhtin, *et al.*, Fiz. Tekh. Poluprovodn. (Leningrad) **25**, 928 (1991) [Sov. Phys. Semicond. **25**, 560 (1991)].
12. K. Seeger, *Semiconductor Physics* (Springer, Berlin, 1974; Mir, Moscow, 1977).
13. V. I. Fistul', *Introduction to the Physics of Semiconductors* (Vysshaya Shkola, Moscow, 1975).
14. N. C. Casey, Jr. and M. B. Panish, *Heterostructure Lasers* (Academic, New York, 1978; Mir, Moscow, 1981), Part 1.
15. S. Adachi, *Physical Properties of III–V Semiconductor Compounds* (Wiley, New York, 1992).
16. R. F. Nabiev, E. C. Vail, and C. J. Chang-Hasnain, IEEE J. Sel. Top. Quantum Electron. **1**, 234 (1995).
17. N. A. Pikhtin, S. O. Slipchenko, Z. N. Sokolova, and I. S. Tarasov, Fiz. Tekh. Poluprovodn. (St. Petersburg) **36**, 365 (2002) [Semiconductors **36**, 344 (2002)].
18. D. A. Vinokurov, V. A. Kapitonov, D. N. Nikolaev, *et al.*, Fiz. Tekh. Poluprovodn. (St. Petersburg) **35**, 1380 (2001) [Semiconductors **35**, 1324 (2001)].
19. E. G. Golikova, V. A. Gorbylev, N. Yu. Davidyuk, *et al.*, Pis'ma Zh. Tekh. Fiz. **26** (6), 5 (2000) [Tech. Phys. Lett. **26**, 295 (2000)].
20. A. Yu. Leshko, A. V. Lyutetskiĭ, N. A. Pikhtin, *et al.*, Fiz. Tekh. Poluprovodn. (St. Petersburg) **34**, 1457 (2000) [Semiconductors **34**, 1397 (2000)].
21. L. V. Asryan, N. A. Gunko, A. S. Polkovnikov, *et al.*, Semicond. Sci. Technol. **15**, 1131 (2000).
22. G. T. Liu, A. Stinz, H. Li, *et al.*, IEEE J. Quantum Electron. **36**, 1272 (2000).
23. G. Park, O. B. Shchekin, D. L. Huffaker, and D. G. Deppe, IEEE Photonics Technol. Lett. **13**, 230 (2000).

Translated by D. Mashovets